

https://dspace.org/

Novel pH triggered fluorescent mesoporous silica nanoparticles for theranostic applications in cancer intervention

Freidus, Lara Gaby

2020
https://hdl.handle.net/10539/31816

Downloaded from a DSpace repository. https://dspace.org/

Novel pH triggered fluorescent mesoporous silica nanoparticles for theranostic applications in cancer intervention

LARA GABY FREIDUS

A thesis submitted to the Faculty of Health Sciences, University of the Witwatersrand, Johannesburg, South Africa in fulfilment of the requirements for the degree of

Doctor of Philosophy



WITS
UNIVERSITY

Supervisor:

Professor Viness Pillay

Department of Pharmacy and Pharmacology, University of the Witwatersrand, Johannesburg, South Africa

Co-Supervisors:

Professor Yahya E. Choonara
Associate Professor Pradeep Kumar

Department of Pharmacy and Pharmacology, University of the Witwatersrand, Johannesburg, South Africa

November 2020

DECLARATION

I, Lara Gaby Freidus, declare that this thesis is my own work. It is being submitted for the degree of Doctor of Philosophy in the Faculty of Health Sciences at the University of the Witwatersrand, Parktown, Johannesburg, South Africa. It has not been submitted before for any other degree or examination at this or any other university.



……

Signed this 5 day of November 2020

Copyright © 2020 University of the Witwatersrand All rights reserved

ANIMAL ETHICS DECLARATION

I, Lara Gaby Freidus confirm that the study entitled “Study to evaluate the theranostic applications of the novel nanosystem MSN_CurNQ for cancer intervention in BALB/c nude mice” received the approval from the Animal Ethics Screening Committee of the University of the Witwatersrand (AESC) with clearance certificate number 2018/11/55/C (Appendix A).

RESEARCH ACCOLADES

1. Faculty of Health Sciences Research Day – Best Student Oral Presentation (2018) – Novel pH-triggered, Fluorescent, Mesoporous Silica Nanoparticles for Potential Theranostic Applications in Cancer Intervention - Podium Presentation, Faculty of Health Sciences Research Day, University of the Witwatersrand, Faculty of Health Sciences, Parktown Johannesburg South Africa, 6 September 2018

2. Academy of Pharmaceutical Sciences Young Scientist award – Runner up (2018) – Can cancer be simultaneously targeted, detected and treated? Explaining novel pH-triggered, Fluorescent, Mesoporous Silica Nanoparticles for Potential Theranostic Applications in Cancer Intervention - Podium Presentation, Kleinkaap Boutique Hotel, Centurion, South Africa, 9 – 11 October 2019

3. Life Sciences Imaging Facility Research Day – Best Overall Oral Presentation (2019) – Fluorescent Properties of the Novel pH-triggered Mesoporous Silica Nanoparticles, MSN_CurNQ – Podium Presentation, Emoyeni Conference Center, Parktown, Johannesburg South Africa, 21 November 2019

RESEARCH OUTPUTS AS CONFERENCE PROCEEDINGS

1) 2018 Controlled Release Society Annual Meeting, New York Hilton Midtown Manhattan, New York City, New York, USA, 22-24 July 2018 – *Poster Presentation*

2) Faculty of Health Sciences Research Day, University of the Witwatersrand, Faculty of Health Sciences, Parktown Johannesburg South Africa, 6 September 2018 - *Podium Presentation.*

3) Academy of Pharmaceutical Sciences, annual conference on pharmaceutical sciences, incorporating the 40th AGM of the Academy of Pharmaceutical Sciences, Kleinkaap Boutique Hotel, Centurion, South Africa, 9-11 October 2019 – *Podium Presentation*

4) Life Sciences Imaging Facility Annual Research Day, Emoyeni Conference Center, Parktown, Johannesburg South Africa, 21 November 2019 - *Podium Presentation*

5) 2020 Controlled Release Society Annual Meeting, International Virtual Conference. 29June -2 July 2020 – *Poster presentation*

6) Controlled Release Society Asia Meeting, Biopolis, Singapore, 24 - 25 September 2018 –- *Poster Presentation* (Presented by Priyamvada Pradeep)

7) University of The Witwatersrand 9th Cross Faculty Postgraduate Symposium, Braamfontein, Johannesburg South Africa, 29-30 October 2018 - *Podium Presentation*

PUBLICATIONS

1) Lara G. Freidus, Priyamvada Pradeep, Pradeep Kumar, Yahya E. Choonara and Viness Pillay. Alternative fluorophores designed for advanced molecular imaging, Drug Discovery Today. 2018; 23(1), 115-133

2) Lara G. Freidus, Pradeep Kumar, Thashree Marimuthu, Priyamvada Pradeep, Viness Pillay and Yahya E. Choonara. Synthesis and Properties of CurNQ for the Theranostic Application in Ovarian Cancer Intervention. Molecules. 2020; 25 (19), 4471

3) Lara G. Freidus, Yahya E. Choonara, Pradeep Kumar, Thashree Marimuthu, Priyamvada Pradeep and Viness Pillay (2020) Novel Theranostic Mesoporous Silica Nanoparticles for Cancer Targeting, Diagnostic and Treatment Applications. To be submitted to International Journal of Pharmaceutics.

DEDICATION

To My Parents

To my parents Ava and Lewis Freidus, everything I have ever accomplished is owed to you. I am eternally grateful for your ceaseless love, guidance, encouragement, and support. You are my greatest supporters through life, my role models, my pillars of strength, everything is thanks to you. Without you, this thesis would have not been possible.

IN MEMORY OF

Professor Viness Pillay

This thesis is dedicated in memory of the late Professor Viness Pillay, my supervisor who passed away during the writing of this thesis. Prof Pillay was a giant in his field, a mentor who inspired a love of science and instilled a desire for academic excellence. He will be sorely missed. Without him this thesis would not have been possible.

ACKNOWLEDGMENTS

First and foremost, I would like to thank my supervisor Professor Viness Pillay who passed away during the final stages of writing this thesis and offer this thesis in his memory. He was a true mentor who instilled a passion for science and excellence. If it wasn't for you, I would not have been inspired to pursue research. You were a giant in your field I am so honoured to have had the opportunity to have been mentored by you and to have been a part of your world class research group.

To my co-supervisor, Professor Yahya Choonara, thank you for your expert opinions, your guidance throughout, and for helping to transform my work into a scientifically sound thesis.

To my co-supervisor Professor Pradeep Kumar, thank you for being a mentor, a sounding board, for offering endless guidance, advice, support and scientific direction. You always knew what to say to encourage me when failures in the lab happened. If it wasn't for you, I would have wanted to give up multiple times throughout this process, but somehow you always knew the right things to say to keep me motivated and feeling positive. I am eternally grateful for your mentorship.

Dr Priya Pradeep, words cannot thank you enough for the enormous role you have played in my research. Thank you for always being there to help, give advice, and for seeing every hurdle that I faced as your own hurdle and more than anything, thank you for being a friend!

Dr Thashree Marimuthu, thank you for your continuous outstanding scientific advice and guidance. Thank you for always having an open door and for the endless help that you continuously offered and for always going out of your way to help and offer support.

A big thank you to the all the people behind the scenes at WADDP, Sello, KB, Bafana, Busi and Pride. Thank you for offering the support we need to allow us to do our research. Thank you to the staff at the CAS. Thembeka, Mdu, Patrick, Lorraine and

Amelia, your passion and dedication to what you do is highly appreciated. Thank you for all the help provided.

A massive thank you to Zakkiyya Cassim. You went above and beyond anything expected to assist with my animal study. You were completely dedicated to my study, the extent to which was remarkable. Thank you for being the most wonderful person and for the countless hours you dedicated to helping me, it is so highly appreciated, thank you! To Kate, Vanessa and Abu, your assistance with my animals is greatly appreciated, thank you, thank you!

To the post-docs at WADDP, Mershen, Sunaina, Femi, Sam and Phil, thank you for always having an open door and always being happy to discuss my research and offer advice. You all offered continuous inspiration and support, thank you.

To my friends and colleagues at the WADDP, you all made this process enjoyable, fun and always were available for emotional support. To my friends, Kate, Zakkiyya, Johnel, Hillary, Azraa, Jolanda, Gillian, Yasar, Lusanda, Gretta, Patrick, Anwary, Zainul, Mpume, and Rabia, our friendships will always be cherished. Thank you for playing such a large part in making my experience at the WADDP a memorable one.

To my parents, Ava and Lewis Freidus, this thesis is dedicated to you. I owe everything that I have ever accomplished to you and I am the person who I am because of the two of you. My greatest supporters through life, my role models, my pillars of strength, everything is thanks to you.

An enormous thank you to my husband and best friend Justin. Thank you for pushing me to follow my dreams and for always being there to support me, day in and day out. Without your encouragement and endless support this entire journey would have felt impossible, with you by my side everything is possible.

Lastly, I would like to heartfully thank the National Research Foundation of South Africa and the University of the Witwatersrand postgraduate merit award for funding my postgraduate degree and my research.

Abstract

Cancer is set to become the leading cause of death globally and is the biggest impediment to increased life expectancy in the 21st century, as the global incidences and mortality rates are forever increasing. The ability to simultaneously target, detect and treat cancer would reduce patient mortality as a result of early disease detection and immediate targeted treatment.

Two highly studied phytochemicals namely curcumin and lawsone were selected for use in this study owing to their established anti-cancer properties and their innate fluorescence; however, their clinical applications are hindered by several limiting factors. This study aimed to improve the biopharmaceutical properties of curcumin and lawsone to further exploit their purported therapeutic properties by synthesising a novel therapeutically stable molecule with appropriate bioavailability, chemotherapeutic properties and innate fluorescence. In addition, the new combined molecule was designed to have pH-responsivity based on the known acidification of the extra cellular matrix during malignant transformation, enabling pH specific cancer targeting.

A novel molecule (2,2'-((((1E,3Z,6E)-3-hydroxy-5-oxohepta-1,3,6-triene-1,7-diyl)bis(2-methoxy-4,1-phenylene))bis(oxy))bis(naphthalene-1,4-dione) was synthesised through a Williamson ether synthesis reaction between curcumin and lawsone and was termed CurNQ. The structure of CurNQ was evaluated through ^{1}H and ^{13}C NMR, HRMS-ESI and FTIR and physiochemical characterisation was performed through PXRD and DSC. The loading of CurNQ onto a nanoplatform aimed to allow for enhanced delivery and enable *in vitro* and *in vivo* imaging and detection applications. To this end, mesoporous silica nanoparticles (MSN) were synthesised (size = 108 d.nm, Zeta potential -42 mV, PDI= 0.150) and were impregnated with CurNQ, forming the novel nanosystem MSN_CurNQ. The MSN nanoplatform aimed to enable passive tumour targeting owing to the EPR effect and for sustained release of CurNQ at the tumour site.

CurNQ was shown to have pH specific solubility, allowing for pH mediated cancer targeting owing to the Warburg effect. The saturation solubility of CurNQ increased

from 11.15 µM at pH 7.4 to 20.7 µM at pH 6.8. CurNQ release from the MSN mimicked this solubility switch whereby after 96 hours 31.5% of CurNQ was released at pH 7.4 compared to 57% release at pH 6.8. The large statistically significant pH specific shift in solubility (p=0.000) coincides with the shift in pH that occurs upon malignant transformation and allows for potential cancer targeting applications.

The fluorescent nature of MSN_CurNQ was evaluated using confocal and fluorescent microscopy. The microscopy images demonstrate MSN_CurNQ to have highly precise, distinctive high intensity innate fluorescence, with a high target to background ratio, low fluorescent blur, a long fluorescent lifetime and fluorescent stability, all of which demonstrate MSN_CurNQ to be a potentially powerful diagnostic and imaging agent.

CurNQ and MSN_CurNQ induced cytotoxicity to several cancer cell lines. CurNQ reduced cell viability to the ovarian cancer cell lines OVCAR-5 and SKOV3 to below 50% with a potent IC_{50} value of 4.048 µM observed for the OVCAR-5 cell line. Additionally, MSN_CurNQ induced a reduction in cell viability to below 50% in OVCAR-5, CACO-2, CHLA and MCF-7 cell lines demonstrating chemotherapeutic potential to a variety of cancer cell types. Furthermore, both CurNQ and MSN_CurNQ were less toxic to the healthy fibroblast cell line 3T3 compared to the toxicity displayed towards several cancer cell lines (p=0.001, 0.000); thus, demonstrating cancer selective toxicity further extending its novelty and its appropriateness as a potential chemotherapeutic agent.

The promising *in vitro* results prompted the commencement of a preclinical trial in a female MF-1 nude mice model. The preclinical trial demonstrated CurNQ and MSN_CurNQ to be well tolerated, inducing low overall toxicity and to be safe at an administered dosage of 10 mg/kg. OVCAR-5 tumour xenografts were successfully established in MF-1 nude mice and the potential efficacy of CurNQ and MSN_CurNQ as a chemotherapeutic agent was evaluated. Preliminary results suggested CurNQ and MSN_CurNQ may induce tumour necrosis and may reduce tumour growth rates; hence these results were highly promising and warrant the continuation of further *in vivo* studies.

Indeed, nano-enabled CurNQ acts as a promising theranostic nanosystem potentially allowing for simultaneous cancer targeting, detection and treatment.

Table of Contents

Declaration ii

Animal Ethics Declaration..... iii

Research Accolades..... iv

Research Outputs As Conference Proceedings v

Publications vi

Dedication vii

In Memory Of..... viii

Acknowledgments ix

Abstract xi

List of Figures i

List of Tables i

List of Schemes..... i

Chapter 1: Introduction 1

1.1 Background 1

1.2 Rationale for this Study 5

1.3 Problem statement 12

1.4 Aim and Objectives 13

1.4.1 *Aim:* 13

1.4.2 Objectives: 13

1.5 Novelty of this Study..... 14

1.6 Overview of thesis 15

1.7 References 16

Chapter 2: Alternative fluorophores designed for advanced molecular imaging..... 22

2.1 Abstract 22

2.2 Introduction 23

2.3 NIR fluorophores 25
2.4 Smart fluorophore conjugates as molecular probes 30
2.4.1 Biothiol probes 30
2.4.2 Amyloid-β-plaque-binding probe 34
2.4.3 Peroxynitrite detection probe 35
2.5 Fluorophores based on Förster resonance energy transfer 37
2.6 Fluorophores based on two-photon absorption 39
2.7 Fluorophores used in two-photon imaging 40
2.7.1 Squaraine dyes 40
2.7.2 Triphenylamines 41
2.7.3 BODIPY derivatives 41
2.8 Fluorophores based on rotor mechanism 42
2.8.1 Acedan 45
2.8.2 Carboranes 46
2.9 Chromophores exhibiting aggregation-induced emission 46
2.10 Three-photon absorption fluorescent dyes 48
2.11 Single-molecule imaging 49
2.11.1 Cell membrane probes 50
2.11.2 Lysosomal imaging 51
2.12 Super-resolution microscopy 52
2.12.1 Fluorophores used in super-resolution microscopy 54
2.13 Concluding remarks and future perspectives 58
2.14 References 60
Chapter 3: Exploring the chemistry and analysis of CurNQ for potential cancer theranostics 67
3.1 Introduction 67
3.2 Materials and Methods 70

3.2.1 Materials 70
3.2.2 Methods 70
3.3 Results and Discussion 75
3.3.1 Synthesis and structural evaluation of novel molecule CurNQ 75
3.3.2 Physiochemical characterisation of CurNQ 78
3.3.3 Fluorescent characterisation of CurNQ 81
3.3.4 pH responsivity of CurNQ 82
3.3.5 High Content Imaging and in-depth Cytotoxicity studies of CurNQ, Cur and BrNQ 82
3.4 Conclusions 91
3.5 References 91
Chapter 4: Theranostic Mesoporous Silica Nanoparticles for Potential Cancer Targeting, Diagnostic and Treatment Applications 96
4.1 Introduction 96
4.2 Materials and Methods 98
4.2.1 Materials 98
4.2.2 Mesoporous silica nanoparticle synthesis 98
4.2.3 Determination of MSN size and zeta potential 99
4.2.4 MSN morphological characterisation 100
4.2.5 Loading of CurNQ into MSN to create novel nanosystem 100
4.2.6 Determination of Encapsulation efficiency of CurNQ within MSN 100
4.2.7 Determination of CurNQ release profile from MSN at varied pH 101
4.2.8 In vitro determination of chemotherapeutic potential of MSN_CurNQ 101
4.2.9 Cytotoxicity studies through MTT assays 102
4.2.10 Determination of Fluorescent properties of MSN_CurNQ using Confocal microscopy 102
4.2.11 Cytotoxicity studies using High Content Imaging System 103
4.3 Results and Discussion 103

4.3.1 Synthesis and characterisation of mesoporous silica nanoparticles 103
4.3.2 Impregnation of MSN with CurNQ 105
4.3.3 Evaluation of pH-responsiveness of MSN_CurNQ 106
4.3.4 Evaluating the innate fluorescence of MSN_CurNQ and its detection capabilities 109
4.3.5 Evaluating the chemotherapeutic properties of MSN_CurNQ through high content imaging 118
4.3.6 In vitro cytotoxicity assay – MTT 119
4.3.7 Potential in vivo cytotoxic effects of MSN_CurNQ 128
4.4 Conclusions 130
4.5 References 131
Chapter 5: Preclinical studies to evaluate the safety, tolerability, toxicity and potential efficacy of CurNQ and MSN_CurNQ for cancer intervention in MF-1 nude mice ... 134
5.1 Introduction 134
5.2 Methods and Materials 135
5.2.1 Materials 135
5.2.2 Part A -Selection of appropriate dose 135
5.2.3 MF-1 female nude mice 137
5.2.4 Part A - Administration of CurNQ and MSN_CurNQ, Health monitoring, Euthanasia and Histopathology 137
5.2.5 Part B -Tumour xenograft establishment 138
5.2.6 Part B- Evaluation of chemotherapeutic potential of CurNQ and MSN_CurNQ 138
5.3 Results and Discussion 139
5.3.1 Part A – Safety Tolerability and Toxicity of CurNQ and MSN_CurNQ ... 139
5.3.2 Part B – OVCAR-5 tumour xenograft establishment and efficacy evaluation of CurNQ and MSN_CurNQ in MF-1 nude mice 144
5.4 Conclusions 153

5.5 References 154
Chapter 6: Conclusions and Future perspectives 157
6.1 Conclusions 157
6.2 Limitations 160
6.3 Future recommendations 160

List of Figures

Figure 1.1: Graphical explanation of leaky tumour vasculature resulting in the EPR effect..... 3
Figure 1.2: Beneficial properties of mesoporous silica nanoparticles 4
Figure 1.3: Main chemical constituents of curcuminoids……6
Figure 1.4: Curcumin interacts with several molecular targets and signalling pathways. 7
Figure 1.5: Degradation products of curcumin……...9
Figure 1.6: Lawsone interacts with multiple molecular pathways involved in oncogenesis. 11
Figure 1.7: Structure of novel molecule CurNQ……..13
Figure 2.1: Near-infrared (NIR) fluorophores. (**a**) The novel fluorophore ZW800-1 attached to a RGD peptide [16]. (**b**) Synthesis of fluorescent polymers pDA [8]. (**c**) Chemical structure of BF2–azadipyrromethene [19]. 28
Figure 2.2: Characterizations of pDA-PEG nanoparticle. (a) A schematic of the pDA-PEG nanoparticle showing a hydrophobic polymer core and a hydrophilic PEG shell. (b) A typical AFM image of pDA-PEG nanoparticles deposited on a silicon substrate. (c) Absorption and emission spectra of pDA-PEG, featuring a large Stokes shift of B400 nm. (d) A NIR-II fluorescence image of an aqueous solution of pDA-PEG taken in the range of 1.0–1.7 mm NIR-II window under an excitation of 808 nm. (e) Fluorescence stability of pDA-PEG in different media including water, PBS and serum. (f) Photostability curves of pDA-PEG in water, PBS and serum under continuous 808 nm illumination. pDA-PEG in serum exhibits the lowest degree of photobleaching among the three [8] (Reproduced with permission from Nature Publishing Group 2014)….. 32
Figure 2.3: Fluorophores used as molecular probes. (a) The chemical structures of biothiols (i) cystine, (ii) homocystine and (iii) glutathione. (b) Mechanism-of-action of biothiol detection probe based on a malonitrile and coumarin conjugate produced by [21]. (c) Biothiol turn-on probe [20]. (d) Chemical structure of amyloid-β-plaque-binding probe [23]. (e) *In vivo* synthesis of peroxynitrite. 34
Figure 2.4: Schematic explaining the mechanism of FRET. 36
Figure 2.5: Fluorophores designed using FRET. (a) The three chemical isoforms of tetrazine. (b) Schematic demonstrating dyad synthesis [34]. 38

Figure 2.6: Schematic explaining the mechanism of two-photon absorption 40
Figure 2.7: Fluorophores used in two-photon microscopy. (**a**) Chemical structure of squaraine. (**b**) Squaraine enclosed in a rotaxane molecule. (**c**) Structure of triphenylamine. (**d**) Structure of BTVPA [47]. (**e**) Structure and rotational ability of HJVPI [49]. (**f**) Structure of acedan and acedan derivatives [51]. (**g**) Synthetic route for the triphenylamine derivative (E)-3-(4-(4-(diphenylamino)styryl)-phenyl)acrylonitrile [56]. (**h**) Chemical structure of AIE fluorophore CTPE-Tau. (**i**) Chemical structure of GMP in the absence of zinc (1) and in the presence of zinc (2) [59]. 44
Figure 2.8: Schematic illustrating the effects of aggregation-induced emission. 49
Figure 2.9: Cellular-uptake-responsive near-infrared (NIR) fluorophore. (**a**) Simplified endocytosis of a responsive NIR fluorophore. Numbers represent the approximate pH of the corresponding organelles. (**b**) Three observable stages of the path of the pH-responsive fluorophore in the cellular environment: uptake, trafficking and efflux [66] (reproduced with permission from Nature Publishing Group under Creative Commons Licence). 52
Figure 3.1: Spectral analysis of synthesised molecule **A)** ^{1}H NMR of CurNQ in d-DMSO ^{1}H NMR (500 MHz, DMSO-d 6) δ 8.11 – 8.04 (m, 2H), 8.04 – 7.97 (m, 2H), 7.94 – 7.85 (m, 4H), 7.74 (s, 2H), 7.55(d, J = 15.8 Hz, 2H), 7.32 (d, J = 2.0 Hz, 2H), 7.15 (dd, J = 8.3, 2.0 Hz, 2H), 6.83 (d, J = 8.2 Hz, 2H), 6.75 (d, J =15.8 Hz, 2H), 6.06 (s, 1H), 3.85 (s, 6H). **B)** ^{13}C NMR of CurNQ in d-DMSO δ 183.1 (C=O), 182.8 (C=O), 178.1(C=O), 149.4, 148.3, 141.0, 140.5, 139.6, 134.96, 134.7, 131.7, 131.0, 127.5, 126.7, 126.6, 123.4, 121.5, 116.0, 111.5, 101.3, 56.0 (OCH_3). **C)** HRMS-ESI spectrum of CurNQ77
Figure 3.2: Structural Characterisation of CurNQ and comparison with Cur and BrNQ ***A*)** FTIR spectra **B)** PXRD spectra. **C)** DSC thermograms. The spectral characteristics of CurNQ was elucidated through FTIF, DSC and PXRD and these spectral characteristics were compared to those of Cur and BrNQ. 80
Figure 3.3: Fluorescence properties and pH specific properties of CurNQ **A)** Excitation and emission spectra of 1,5 µM solution of CurNQ **B)** Saturation solubility of a I,5 µM solution of CurNQ at pH 7.4 and 6.8. 81
Figure 3.4: Cell viability assays were performed using a High Content Imaging System. Three cell lines were utilised, 2 OC cell lines and 1 healthy fibroblast cell line. **A)** OVCAR-5 **B)** SKOV3 **C)** 3T3. Each cell line was treated with varying concentrations of Cur, CurNQ and BrNQ and treatments where incubated for 24- and 48-hour intervals. 84

Figure 3.5: Brightfield Microscopy images overlaid on fluorescent microscopy images with DAPI staining. Acquired through High Content Imaging……..89
Figure 3.6: Cell morphology analysis of OVCAR-5 cells subsequent to Cur, CurNQ and BrNQ treatment. Cell morphology data obtained on the CELENA® X. **A)** Eccentricity **B)** Compactness **C)** Form Factor 90
Figure 4.1: Reaction scheme for the synthesis of MSN..... 99
Figure 4.2: Size, morphology and zeta potential analysis of synthesised MSN. **A)** Size of MSM determined to be 108d.nm through dynamic light scattering (N=3) **B)** Zeta potential of MSN obtained using the ZetaSizer and determined to be -42mV (N=3) **C)** SEM microscopy image of the surface of MSN to evaluate surface morphology. .. 105
Figure 4.3: Release assay of CurNQ and Cur from MSN at pH 7.4 and pH 6.8 over a 96-hour period. 107
Figure 4.4: Confocal microscopy images of MSN_CurNQ in OVCAR-5 cells after 24 hours. Blue fluorescence is DAPI nuclear staining and red fluorescence is MSN_CurNQ. 112
Figure 4.5: Confocal microscopy images of MSN_CurNQ in OVCAR-5 cells after 24 hours. Blue fluorescence is DAPI nuclear staining, green fluorescence is Phalloidin-Atto 488 actin stain and red fluorescence is MSN_CurNQ. 113
Figure 4.6: Fluorescent microscopy images acquired on the CELENA® X High Content Imaging System of OVCAR-5 cells incubated with MSN_CurNQ for 24 hours. Blue fluorescence is DAPI nuclear staining and red fluorescence is MSN_CurNQ. D) Cells given no treatment (control). No red fluorescence is present in the control group, confirming fluorescence is from MSN_CurNQ. 115
Figure 4.7: Confocal microscopy images demonstrating that CurNQ is required to be loaded into a delivery vehicle to allow for fluorescence detection and tracking. OVCAR-5 cells treated with CurNQ for 24 hours (no MSN), nuclear DAPI staining, phalloidin 488 actin stain. 118
Figure 4.8: Nuclei count and MSN count of OVCAR-5 cells treated with varying concentrations of MSN_CurNQ for 24-hours. Nuclei and MSN count were quantitively obtained using a high content imaging system. 119
Figure 4.9: Cytotoxicity of MSN_CurNQ and MSN_Cur to OVCAR-5 and CACO-2 cell lines. MSN_CurNQ and MSN_Cur treatments were administered at a range of concentrations over a 72-hour period and the reductions in cell viability were

determined through an MTT assay. Large reductions in cell viability towards MSN_CurNQ treatment were observed..... 123
Figure 4.10: Cytotoxicity of MSN_CurNQ and MSN_Cur to MCF-7 and CHLA cell lines. MSN_CurNQ and MSN_Cur treatments were administered at a range of concentrations over a 72-hour period and the reductions in cell viability were determined through an MTT assay. Moderate reductions in cell viability towards MSN_CurNQ treatment were observed..... 124
Figure 4.11: Cytotoxicity of MSN_CurNQ and MSN_Cur to Ht-29 and HeLa cell lines. MSN_CurNQ and MSN_Cur treatments were administered at a range of concentrations over a 72-hour period and the reductions in cell viability were determined through an MTT assay. Low reductions in cell viability towards MSN_CurNQ treatment were observed..... 125
Figure 4.12: Cytotoxicity of MSN_CurNQ and MSN_Cur to the healthy fibroblast cell line 3T3. MSN_CurNQ and MSN_Cur treatments were administered at a range of concentrations over a 72-hour period and the reductions in cell viability were determined through an MTT assay. Very minor reductions in cell viability towards MSN_CurNQ treatment were observed..... 127
Figure 4.13: A comparative analysis of the reduction in cell viability to a variety of cell lines in response to MSN_CurNQ treatment at 300 ng/mL after 48 hours..... 127
Figure 4.14: Cell viability in response to concentration of MSN_CurNQ after **A)** 24 hours and **B)** 48 hours in 6 cancer cell lines and in 1 healthy fibroblast cell line. ... 128
Figure 4.15: Cell viability assay of OVCAR-5 cells treated with CurNQ and Cur alone after 24-hour incubation..... 129
Figure 5.1: IC_{50} value of CurNQ in OVCAR-5 cells..... 136
Figure 5.2: Weight changes of mice receiving CurNQ and MSN_CurNQ over Part A of the preclinical trial..... 140
Figure 5.3: Xenograft tumour growth in nude mice over a 4-week period. 145
Figure 5.4: Weight changes of tumour bearing mice treated with 10mg/kg CurNQ, 10mg/kg MSN_CurNQ and 25mg/kg MSN_CurNQ over part B of the preclinical trial. 148
Figure 5.5 A) Average tumour size and **B)** average tumour growth rate of mice treated with 10mg/kg CurNQ, 10mg/kg MSN_CurNQ and 25mg/kg MSN_CurNQ over a 4-week period. The control group was required to be excluded from the results as 2 of the mice in the control group did not develop tumours and the development of fully grown

tumours did not occur in the remaining 2 mice, therefore all obtained results are considered as preliminary..... 149
Figure 5.6: Necrosis factor of tumours in experimental groups. The necrosis factor is rated from 0 to 3, with 0 being no necrosis occurring and 3 being >50% of section viewed. 151
Figure 5.7: The Mitotic rate of the tumours in the three experimental groups..... 152

List of Tables

Table 2.1: Summary table for fluorophores discussed in this review 24
Table 2:2: Comparison between novel Si-Q-rhodamine fluorophores and an Alexa647-phalloidin conjugate [85] 57
Table 5:1: Histopathology of mice organs from preclinical trial part A. Three mice were allocated to each experimental group, and histopathology samples are presented for each mouse. 142

List of Schemes

Scheme 3.1: Reaction scheme for CurNQ synthesis. 71

Chapter 1: Introduction

1.1 Background

Phytochemicals are naturally occurring compounds found in fruit, vegetables, plants, spices and other food products. They have been used for centuries to treat and prevent a variety of illnesses [1-3]. The extensive use of phytochemicals in traditional medicines has prompted scientific research to be performed to elucidate the potential medicinal properties of many of these compounds [2]. The scientific exploration into phytochemicals has skyrocketed in the last two decades and several of these compounds have been shown to have potent bioactive moieties and some to even have promising anti-cancer activities [1-5]. Phytochemicals have been shown to modulate several diverse biochemical pathways and processes and to interact with numerous pathways which have been associated with oncogenesis [1-5]. The use of phytochemicals in cancer therapeutics in place of traditional chemotherapeutics is highly advantageous owing to their low overall toxicity [3]. The highly toxic nature of chemotherapy has given rise to the ongoing search for new and improved anti-cancer drugs which allow for targeted treatment as well as having low systemic toxicity [1-4].

Theranostics is the field of research combining both diagnostic and therapeutic elements into a single platform to occur simultaneously [6,7]. Theranostic agents are highly advanced systems that can monitor the accumulation of nanomedicine compounds at the target site, quantify triggered drug release, assess therapeutic efficacy, visualize biodistribution, indicate the premise location of malignant cells and deliver a chemotherapeutic agent to the target site [8,9]. Much research has been applied in the field of theranostics as it offers a smart approach to cancer diagnostics and treatment [7,8]. The ability to simultaneously detect and treat cancer will reduce patient mortality through early detection and immediate treatment [10].

The prevalence and mortality rate associated with cancer has instigated a global health crisis as currently cancer is globally the second leading cause of death [11]. Clearly, there is an immediate need for effective cancer diagnostics and treatment. The non-specific nature of traditional cancer treatment limits its efficacy. The unavailability of

early detection systems and targeted treatment options further hinders cancer treatment success. Approximately 60% of patients are diagnosed subsequent to tumour metastasis, this critically increases patient mortality [12]. The earlier the malignancy is detected, and treatment commences, the better the prognosis [10]. Accordingly, research into new and improved ways of detecting and treating cancer at an early stage is of vital importance. Furthermore, available chemotherapeutic agents target healthy cells to the same degree as malignant cells [13,14]. To improve cancer treatment outcome, the specific targeting of a tumour is essential [15–17]. This can be achieved through advanced drug delivery methods which target specific features unique to that of a tumour [18–20].

Cell survival is reliant on the highly dynamic nature of cellular behaviour. Homeostasis involves multiple signalling events which translate an extracellular signal to a cellular response such as protein expression. This highly complex system hinges on the interaction between multiple cytoplasmic signalling constituents [21]. The transformation of a cell into a malignant state cannot be a result of one mutation event alone; rather, the culmination of multiple cellular mutations allows for oncogenesis. Signalling ablations may be cancer promoting if proliferative checkpoints and apoptotic signals are bypassed [22]. Thus, the oncogenic phenotype is characterised by multiple perturbations of the genetic material and multiple different growth and proliferation pathways are affected with the dysregulation of several signalling pathways [23,24].
Malignant transformation involves an increase in the cell's glycolytic rate which supports constant cell growth and proliferation [25]. The metabolism of a cancer cell is unique in that it produces lactate under oxygenated conditions. This process is referred to as aerobic glycolysis or the 'Warburg effect' [26]. This feature of cancerous cells can be exploited to differentiate between cancerous and healthy cells and thus can be used for tumour targeting and detection.

Leaky tumour vasculature is a hallmark feature of cancer. This induces nanoparticles to leak out of tumour blood vessels [27]. This phenomenon does not occur in heathy vessels owing to well-organised branching and regularly spaced capillary beds. This highly structured vessel is not apparent in tumour vasculature on account of rapid tumour growth, allowing for the leaking of nanoparticles into the tumour interstitium. Concurrently, poor tumour lymphatic drainage enables nanoparticle accumulation and

enhanced retention [28,29]. The automatic accumulation of nanoparticles in tumour tissue has been well documented and is referred to as the Enhanced Permeation and Retention (EPR) effect [27]. This effect has been the rationale behind the field of nanomedicine for cancer intervention. EPR allows for the passive targeting of nanoparticles to tumour tissue [30]. The addition of an active targeting strategy in conjunction with EPR can allow for enhanced tumour targeting capabilities.

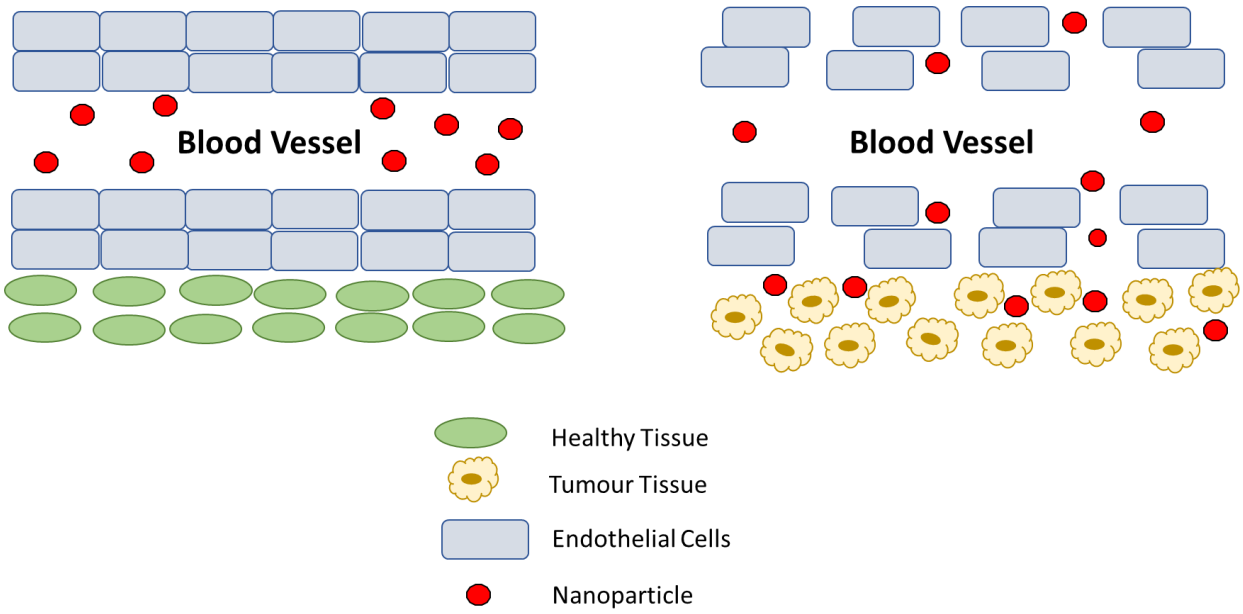


Figure 1.1: Graphical explanation of leaky tumour vasculature resulting in the Enhanced Permeation and Retention (EPR) effect.

Mesoporous silica nanoparticles (MSN) are a class of nanoparticles that have been widely studied for drug delivery applications. Silica is one of the most abundant natural resources and has been deemed safe and is widely used in food additives, pharmaceutical products and cosmetics. With the explosion into nanomedicine research, silica has been the focus of an abundance of research, mainly in terms of drug delivery [31,32]. MSN have numerous features that make them ideal for advanced drug delivery. These features include their solid framework, high surface to volume ratio, them being mesoporous thereby allowing for drug loading, their chemically inert nature, along with their biocompatibility, biodegradability and that they show no toxicity *in vitro* [33–37]. Moreover, their hydrophilic silanol surface is ideal for the delivery of low solubility drugs and allows for easy surface functionalisation [36]. The large pores evenly distributed over the surface of MSN are ideal for drug loading, especially for the

loading of hydrophobic drugs. The loading of hydrophobic drugs into MSN has become a standard approach in the delivery of hydrophobic drug molecules. The poor solubility of these drugs is overcome as the EPR effect delivers these loaded drugs directly into the tumour [10].

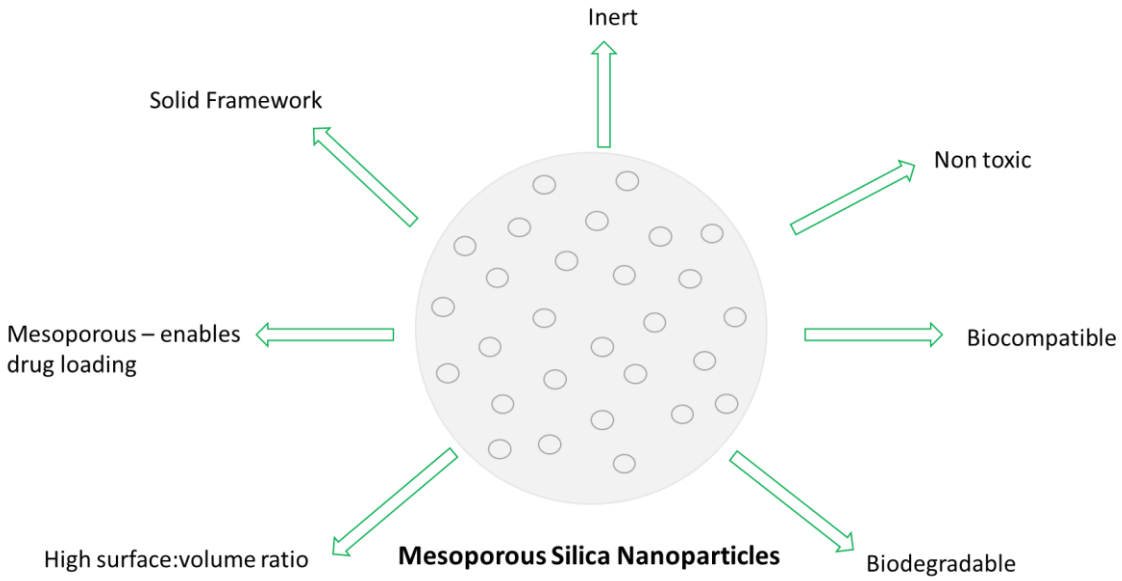


Figure 1.2: Beneficial properties of mesoporous silica nanoparticles

Ovarian Carcinoma (OC) is the sixth most common cancer amongst females and is the leading cause of death from gynaecological cancers [38]. Epithelial OC is the most common OC, accounting for 90% of ovarian tumours. Its lack of initial symptoms results in overall late diagnosis and patients are usually only diagnosed at stage III and IV [39,40]. This in conjunction with the highly metastatic nature of the disease is responsible for low patient survival rates [41]. The mortality rate is approximately 60%, and this mortality rate has not improved in the past three decades. Moreover, OC has a high rate of chemoresistance, and relapse readily occurs [3]. Clearly, new therapies targeting epithelial OC is of immediate concern.

1.2 Rationale for this Study

Curcumin (1,7-bis(4-hydroxy-3-methoxyphenyl)-1,6-heptadiene-3,5-dione) is a natural polyphenol found in the rhizomes of Curcuma longa (turmeric) and this bright yellow/orange compound was first isolated in 1815 [42]. The rhizome of turmeric is crushed into a powder and this powder has been used in Indian and Chinese cooking, medicine, cosmetics and as a dye for more than 2000 years. In Indian traditional medicine, crushed turmeric extract has been used to treat multiple ailments including, respiratory ailments, dysentery in children, dental diseases, digestive disorders, ulcers, and is used for wound healing [42]. The active ingredient in turmeric extract has been identified as curcumin (Cur).

The use of Cur in traditional medicine has instigated an abundance of scientific research into Cur bioactivity, including anti-inflammatory, anti-oxidant, chemopreventative, chemotherapeutic, antiangiogenic and it ability to target a variety of diseases including diabetes, cardiovascular diseases, Alzheimer's disease, arthritis, inflammatory bowel disease, lung fibrosis, HIV, nephrotoxicity, psoriasis and gall stone formation [42–46].

Structurally, Cur is comprised of two aromatic rings with phenolic rings which are bound together by an α,β-unsaturated-β-diketone, with the β-diketone structure undergoing keto-enol tautomerism in solution. However, the enolic conformation is predominant at room temperature [42–46]. Turmeric extract typically contains curcumin (typically 60−70% of a crude extract), demethoxycurcumin (20−27%), and bisdemethoxycurcumin (10−15%) as well as secondary metabolites and by-products; this mixture is often referred to as curcuminoids. The chemical constituents present in curcuminoids are illustrated in Figure 1.3 [42].

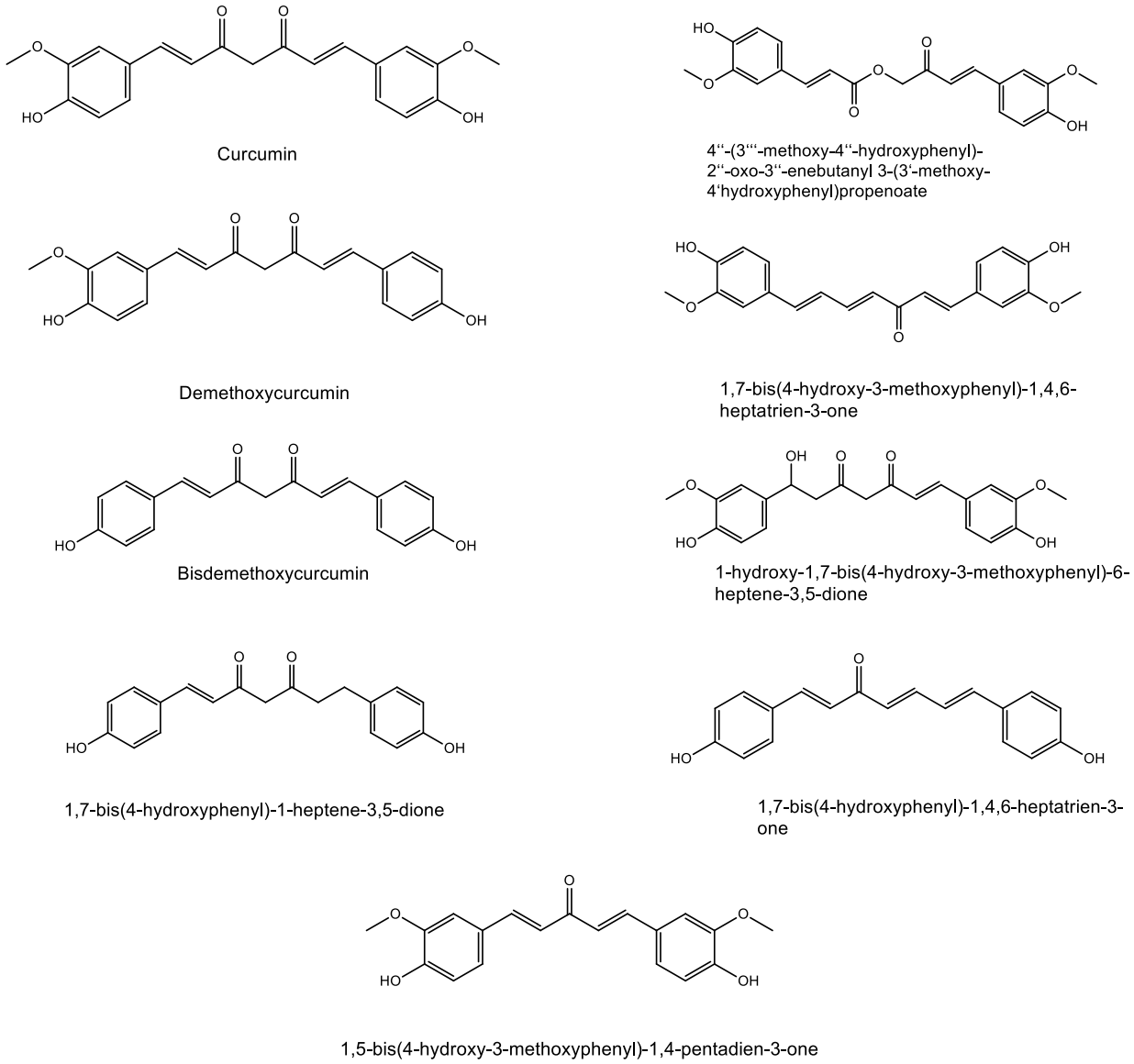


Figure 1.3: Main chemical constituents of curcuminoids.

Multiple studies indicate that Cur modulates numerous signalling pathways and has multiple anti-cancer mechanisms. Cur has numerous anti-cancer properties including the ability to reduce proliferation and metastasis, induce apoptosis and has antiangiogenic, anti-inflammatory and antioxidant properties [42,47]. Cur has been shown to affect multiple different signalling pathways including NF-κB, PI3K/AKT, EGFR, Nrf2, Notch 1, Wnt/β-catenin, and HIF-1. This rare multi action ability of Cur suggests potential for it to be used as an anti-cancer agent [43–46].

Cur interacts with various signalling pathways in OC. Lysophosphatidic acid (LPA) stimulates tumour development, progression, motility and metastasis when overexpressed. LPA overexpression has been detected in 98% of ovarian tumours. Thus, the overexpression of LPA is a critical factor in the establishment, survival and progression of OC. LPA induces the activity of activators of transcription 3 (STAT3) and Interleukin 6 and 8 (IL6 and IL8). STAT3, IL6 and IL8 all enhance the motility of cells, and motility is the most important property allowing for metastasis. Cur has been shown to inhibit LPA, which reduces the expression of STAT3, IL6 and IL8, thus reducing motility and subsequent metastasis [41,48].

NF-κB is the master switch in inflammation. NF-κB stimulates cytokines inducing inflammation and acts as a transcription factor stimulating cell growth. NF-κB is responsible for the transcription of multiple genes involved in the regulation of cell proliferation, survival, migration, and apoptosis [49]. The continuous activation of NF-κB has been reported as the origin of many cancers. The inhibition of NF-κB induces apoptosis through multiple pathways. Research has shown the ability of Cur to inhibit NF-κB, thereby inducing apoptosis. Moreover, NF-κB has an antagonistic relationship, when NF-κB is inhibited, p53 is activated which induces apoptosis. The ability of Cur to inhibit NF-κB suggests that Cur has potential to be a potent anti-cancer agent [3,49–51].

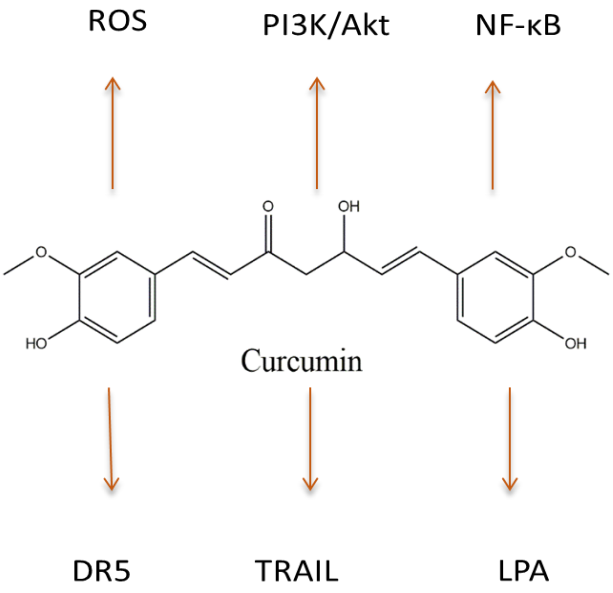


Figure 1.4: Curcumin interacts with several molecular targets and signalling pathways.

Additionally, Cur interacts with the Tumour necrosis factor (TNF) α-related apoptosis-inducing ligand (TRAIL) pathway. OC cells become resistant to TRAIL induced apoptosis and through this resistance, cancer cells bypass apoptosis resulting in continued survival and cancer progression. Cur induces the production of reactive oxygen species (ROS), ROS then stimulates the expression of death receptor 5 (DR5) on the cell surface. The increased expression of DR5 sensitizes the cells to TRAIL, resulting in TRAIL mediated apoptosis and cell death. The increase in ROS also results in the disruption of the mitochondrial membrane and the release of cytochrome c, thereby activating the caspase cascade and apoptosis. Moreover, Cur further sensitizes cells to TRAIL through the inhibition of NF-κB [52,53].

Further research has demonstrated that Cur disrupts the PI3K/AKT pathway. The PI3K pathway is a critical pathway in cell proliferation, cell cycle progression and invasion, as it controls multiple transcription factors. The PI3K pathways has been shown to be involved in OC development and the deactivation of this pathway has proven to be an effective therapy for OC [54]. Cur inhibits this PI3K pathway in OC cells, as increased levels of phospho-AKT and caspase-3 are observed in response to Cur treatment, with a reduction on Bcl-2 expression, all of which result in apoptosis [43,49,54].

It is unique for a single molecule to be able to interact with multiple different signalling pathways, all of which contribute to the oncogenic state. It is this synergistic mechanism that has attracted the attention of many researches to Cur potential as a highly promising anti-cancer agent.

In addition to its clinical applications, Cur has fluorescent properties. Cur has two distinct absorption peaks, the first of which is in the UV region at 265nm and the second is in the visible region and occurs between 408-430 nm [55]. The fluorescent intensity and quantum yield of Cur greatly depends on the solvent in which it is dissolved [55,56]. However, Cur has been shown to have a short fluorescent lifetime, a low quantum yield, rapidly photo bleaches and the quantum yield significantly decreases in the presence of an aqueous solution making its fluorescent intensity low at physiological pH [57]. Clearly, Cur is not suitable as an *in vivo* imaging agent.

Contrary to the multiple promising anti-cancer properties of Cur, Cur has several limitations to successful clinical implementation. Numerous studies have demonstrated Cur's low solubility, low bioavailability and inherent instability. Cur undergoes rapid hydrolysis and molecular fragmentation at physiological pH, and 90% of Cur is degraded within 30 minutes when in PBS [58]. Cur degrades into at least 5 different metabolites, some of which are thought to have anti-cancer properties of their own and some of which do not. These metabolites include trans-6-(4′-hydroxy-3′-methoxyphenyl)-2,4-dioxo-5-hexenal, ferulic aldehyde, ferulic acid, feruloyl methane, vanillin and other smaller metabolites (Figure 1.5) [59].

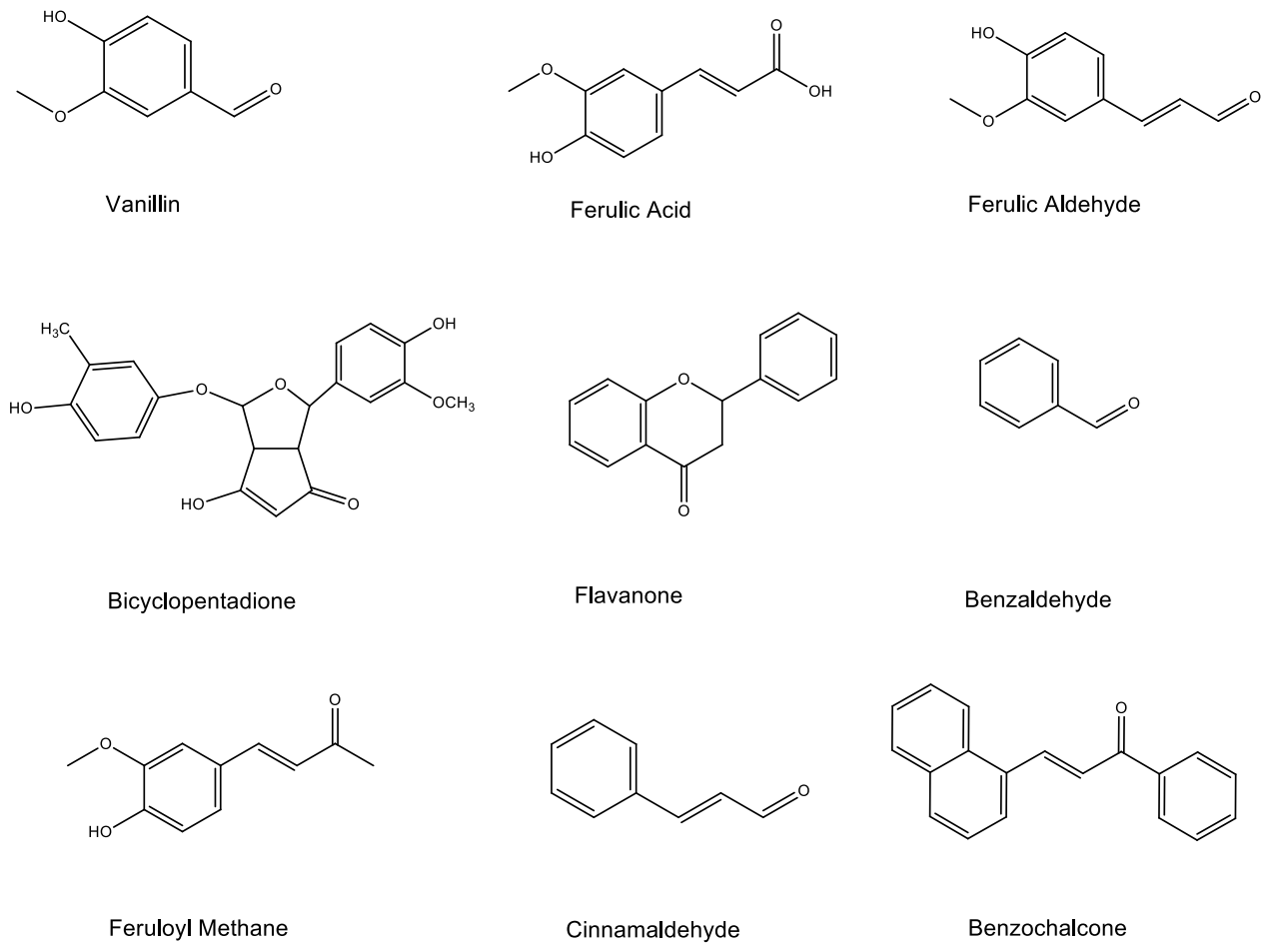


Figure 1.5: Degradation products of curcumin

Cur is sensitive to light and undergoes rapid photodegradation. This photodegradation has been observed in solution as well as in the solid form and multiple degradation products are formed, the number of which is dependent on the wavelength of light Cur

is exposed to [57]. Additionally, Cur has been observed to degrade completely in cell culture media within 8 hours [58]. Furthermore, studies which evaluated Cur levels after *in vivo* administration, were unable to detect Cur in serum or tissue [60]. These findings are alarming considering the numerous studies which regard Cur to be a highly promising drug candidate yet fail to address these several severe limitations. Numerous studies do however focus on increasing Cur's solubility and bioavailability through multiple avenues; yet these avenues are unable to completely solve all the issues plaguing Cur's applications *in vivo*.

Lawsone (2-hydroxy-1,4-naphthoquinone) is the major chemical constituent of the plant Lawsonia inermis (henna). Henna is mostly widely known for its staining ability and is commonly used as a dye and in body art painting. Lawsone has numerous therapeutic attributes and has been demonstrated to have antioxidant, anti-inflammatory, antibacterial and anti-cancer activities [61]. The 1,4-naphthoquinone pharmacophore has been at the centre of numerous studies and has well documented biological activity. Its biological activity is owing to the gain of one or two electrons, creating a dianion species or radical anion [61]. Quinone moieties are found in several anti-cancer drugs including daunorubicin, doxorubicin and mitoxantrone [62] and many derivatives synthesised from 2-hydroxy-1,4-naphthoquinone have been demonstrated to have anti-cancer activities. These anti-cancer activities result from redox cycling, arylation, intercalation, induction of DNA strand breaks, generation of free radicals and alkylation via quinone methide formation [63].

The potent anti-cancer activity of lawsone can be attributed to its interaction with various signalling pathways. It has been well established that 1,4-naphthoquinone induces the rapid formation of ROS which induces DNA damage and leads to cell death. Numerous studies have reported 1,4-naphthoquinone to kill several human cancer cell lines through this induction of ROS generation [62,64,65]. Su, *et al*, [66] showed lawsone derivatives to induce G(2)/M cell cycle arrest and to upregulate Bax with the simultaneous downregulation of Bcl-2 and induced the activation of p38 MAPK. Moreover, Chien, *et al*, [67] demonstrated that a lawsone derivative suppressed the PI3K/AKT pathway and suppression of the expression of downstream targets of AKT were observed. In addition, cytochrome c was released resulting in the activation of the

caspase cascade and the induction of apoptosis [67]. Clearly, this phytochemical elicits potent anti-cancer effects through its interaction with multiple oncogenic pathways.

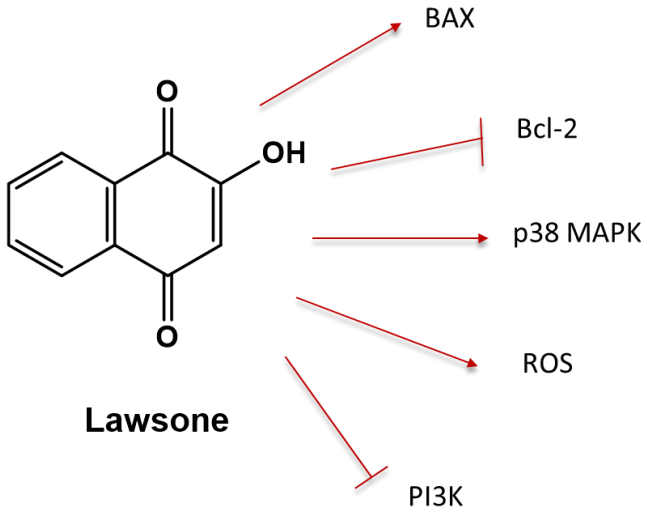


Figure 1.6: Lawsone interacts with multiple molecular pathways involved in oncogenesis.

Lawsone's major structure is that of a quinone. Quinones are widespread in nature and are a class of organic molecules which contain a fully conjugated cyclic dione structure [68]. Quinones are formed through the reaction of aromatic compounds with electron donating substituents which increase the nucleophilicity of the ring. This addition creates a large redox potential which enables the breaking of aromaticity [69]. Quinones are widely known for their fluorescent properties and many quinone derivatives are widely used as dyes and fluorescent labels [70]. Thus, lawsone exhibits inherent fluorescent properties owing to its structure.

The rationale of this research was to combine an imaging and a therapeutic agent into a single platform by synthesising a novel theranostic compound that combines Cur and lawsone in order to take advantage of the anti-cancer properties (therapeutic) as well as the fluorescent properties particularly of lawsone (diagnostic). Although both phytochemicals have independently been shown to elicit anti-cancer activity, each have several limiting factors to advance their clinical application. These limiting factors include molecular instability, rapid degradation and poor bioavailability. This work aimed to overcome some of these limitations by the synthesis of a stable molecule with appropriate bioavailability, targeting capabilities and innate fluorescence. In addition, to facilitate the new theranostic system to function as an anti-cancer passive targeting

system, the new combined molecule was designed to have pH-responsivity based on the known acidification of the extra cellular matrix (ECM) during malignant transformation. Moreover, the inclusion of a nanosystem would passively enhance targeted delivery of the novel compound to the tumour owing to the EPR effect and would allow for advanced delivery strategies. A Williamson ether synthesis reaction between Cur and lawsone was used as the chemical synthesis route to produce the novel theranostic compound termed CurNQ [2,2'-((((1E,3Z,6E)-3-hydroxy-5-oxohepta-1,3,6-triene-1,7-diyl)bis(2-methoxy-4,1-phenylene))bis(oxy))bis(naphthalene-1,4-dione)].

The non-specific nature of traditional cancer treatment limits its efficacy. The unavailability of early detection systems and targeted treatment options further hinders cancer treatment success. Approximately 60% of patients are diagnosed subsequent to tumour metastasis, this critically increases patient mortality [12]. The earlier the malignancy is detected, and treatment commences, the better the prognosis [10]. Accordingly, research into new and improved ways of detecting and treating cancer at an early stage is of vital importance.

1.3 Problem statement

Late detection and non-specific treatment are substantial problems plaguing traditional cancer treatment. An early detection system that incorporate targeted treatment would greatly enhance the field of oncology and reduce patient mortality. A simple system simultaneously allowing for the detection, targeting and treatment of cancer would revolutionise cancer diagnostics and therapeutics.

Current research utilising lawsone and Cur independently are plagued with the intrinsic limiting factors of these two molecules such as molecular instability, rapid degradation and poor bioavailability. Yet, these two molecules possess many properties that make them promising therapeutic candidates. Thus, the challenge presented was to circumvent the limitations of these two molecules whilst retaining both their favourable properties, and to create an intrinsically fluorescent molecule with anti-cancer properties.

1.4 Aim and Objectives

1.4.1 *Aim:*

The aim of the research was to synthesise a novel theranostic nanosystem for targeted cancer intervention through the synthesis of a pH responsive fluorescent compound designed to be solubilised at the pH specific to that of the malignant microenvironment thereby allowing for simultaneous cancer detection and targeting applications.

The envisioned pH stimulated solubility with accompanying fluorescence aimed to allow for simultaneous detection and targeting of the tumour microenvironment owing to the acidic tumour microenvironment. To further enhance targeting applications, the inclusion of mesoporous silica nanoparticles aimed to enable passive tumour targeting owing to the EPR effect as well as enable sustained delivery at the tumour site. Furthermore, the novel compound aimed to have chemotherapeutic properties allowing for therapeutic applications. Indeed, the aim of this research was to synthesise a novel nanosystem for the simultaneous targeting, detection and treatment of cancer.

1.4.2 *Objectives:*

1. The synthesis of the novel theranostic molecule CurNQ [2,2'-((((1E,3Z,6E)-3-hydroxy-5-oxohepta-1,3,6-triene-1,7-diyl)bis(2-methoxy-4,1-phenylene))bis(oxy))bis(naphthalene-1,4-dione)] and the elucidation of its structure and physiochemical properties through the use of ^{1}H, ^{13}C NMR, HRMS-ESI, FTIR, DSC and X-RD.

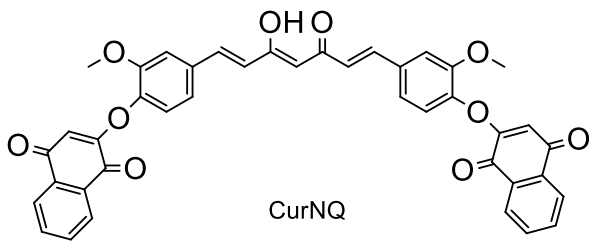


Figure 1.7: Structure of novel molecule CurNQ

2. Synthesis of mesoporous silica nanoparticles (MSN) with appropriate size and zeta potential attributes and confirmation of successful synthesis through physiochemical characterisation.
3. Impregnation of MSN with CurNQ, confirmation of loading and determination of encapsulation efficiency.
4. Confirm proposed pH responsive solubility through the analysis of the saturation solubility at physiological and malignant pH and evaluate the release profile of CurNQ from MSN at pH 7.4 and 6.8 over a 96-hour period.
5. Investigate fluorescent properties and cellular uptake of CurNQ and MSN_CurNQ in OVCAR-5 cells using fluorescent and confocal microscopy.
6. In-depth *in vitro* cytotoxicity analyses of CurNQ and MSN_CurNQ on 7 cell lines namely OVCAR-5, SKOV3, MCF-7, HeLA, CACO-2, CHLA and HT-29 and on the healthy fibroblast cell line 3T3 and the use of advanced techniques such as High Content Imaging to further *in vitro* characterisation of CurNQ through the quantification of cellular morphological changes and toxicity induced in response to CurNQ treatment.
7. Preclinical study evaluating safety, toxicity, tolerability and potential efficacy of CurNQ and MSN_CurNQ in female MF-1 nude mice.

1.5 Novelty of this Study

The novelty of this study lies in the multifaceted nature of the novel molecule CurNQ, a single molecule to that allows for theranostic applications. Theranostic systems are usually a combination of two or more elements that enable theranostic applications; however, in this study we report on a single molecule with flexible theranostic properties. Moreover, the pH responsiveness of CurNQ is highly sensitive and robust; the shift in pH upon malignant transformation is small, yet this small change in pH elicits a large solubility response, with CurNQ's saturation solubility having a 25% increase in solubility with a 0.6-point pH change. The novelty lies in CurNQ having simultaneous cancer targeting, detection and treatment capabilities.

1.6 Overview of thesis

Chapter 1 is the introduction to the thesis. A background to the relevance of the study is discussed and the rationale behind the synthesis of the novel molecule is explained. The aim, objectives and novelty of the research are presented, and an overview of the is thesis given.

Chapter 2 is comprised of the published review article entitled “Alternative fluorophores designed for advanced molecular imaging” and is published in Drug Discovery Today, Volume 23, Issue 1, January 2018, Pages 115-133 and outlines the use of alternative fluorophores for molecular imaging applications thereby highlighting the relevance and robust applications where CurNQ could be applied.

Chapter 3 of the thesis describes in detail the synthesis, physiochemical characterisation and in-depth *in vitro* cytotoxicity studies of CurNQ. The structure of CurNQ was evaluated through ^{1}H and ^{13}C NMR, HRMS-ESI and FTIR and physiochemical characterisation was performed through PXRD and DSC. CurNQ was shown to have pH specific solubility, allowing for pH mediated cancer targeting owing to the Warburg effect. The saturation solubility of CurNQ increased from 11.15 µM at pH 7.4 to 20.7 µM at pH 6.8. High content imaging was utilised to ascertain the effects of CurNQ, Cur and BrNQ on cell viability and cell morphology at a variety of concentrations at 24 and 48 hours. CurNQ reduced cell viability to the OC cell lines OVCAR-5 and SKOV3 to below 50% with a potent IC_{50} value of 4.048 µM observed for the OVCAR-5 cell line and morphological changes depict the induction of apoptosis.

Chapter 4 of this thesis incorporates CurNQ onto a nanoplatform. Mesoporous silica nanoparticles were synthesised and characterised through size and zeta potential analysis and scanning electron microscopy. MSN were impregnated with CurNQ to form the novel nanosystem MSN_CurNQ. CurNQ release from the MSN mimicked the solubility switch demonstrated in chapter 3 whereby after 96 hours 31.5% of CurNQ was released at pH 7.4 compared to 57% release at pH 6.8, thereby confirming pH-responsivity. Confocal and fluorescent microscopy images demonstrated the highly precise, distinct and specific innate fluorescence of MSN_CurNQ and demonstrate its potential to act as a powerful diagnostic and imaging agent. MSN_CurNQ induced a reduction in cell viability to below 50% in OVCAR-5, CACO-2, CHLA and MCF-7 cell lines demonstrating chemotherapeutic potential to a variety of cancer cell types.

Chapter 5 of this thesis presents the preclinical study in female MF-1 nude mice. The preclinical trial demonstrated CurNQ and MSN_CurNQ to be well tolerated, induce low overall toxicity and to be safe at an administered dose of 10mg/kg. OVCAR-5 tumour xenografts were successfully established in MF-1 nude mice and preliminary efficacy results suggested CurNQ and MSN_CurNQ may induce tumour necrosis and may reduce tumour growth rates.

Chapter 6 is the concluding chapter, the overall conclusions found as well as future recommendations are proposed, and future work is discussed.

1.7 References

1. Veeresham C. Natural products derived from plants as a source of drugs. J Adv Pharm Technol Res. 2012;3(4):200—201.
2. Rizwanullah M, Amin S, Mir SR, Fakhri KU, Rizvi MMA. Phytochemical based nanomedicines against cancer: current status and future prospects. J Drug Target. 2018;26(9):731–52.
3. Rais J, Jafri A, Siddiqui S, Tripathi M, Arshad M. Phytochemicals in the treatment of OC. Front Biosci. 2017;9:67–75.
4. Panda AK, Chakraborty D, Sarkar I, Khan T, Sa G. New insights into therapeutic activity and anti-cancer properties of curcumin. J Exp Pharmacol. 2017;9:31–45.
5. Butt AS, Nisar N, Mughal T. A review: Therapeutics potentials of phytochemical drugs and their loading in pH specific degradable nano-drug carrier targeting colorectal cancer. J Pak Med Assoc. 2018;68(4):607–14.
6. Ma Z, Wan H, Wang W, Zhang X, Uno T, Yang Q, et al. A theranostic agent for cancer therapy and imaging in the second near-infrared window. Nano Res. 2019;12(2):273–9.
7. Saroj S, Rajput SJ. Composite smart mesoporous silica nanoparticles as promising therapeutic and diagnostic candidates: Recent trends and applications. J Drug Deliv Sci Technol. 2018;44:349–65.
8. Chen H, Zhang W, Zhu G, Xie J, Chen X. Rethinking cancer nanotheranostics. Nat Rev Mater. 2017;2(1):1–36.
9. Wicki A, Witzigmann D, Balasubramanian V, Huwyler J. Nanomedicine in cancer therapy: Challenges, opportunities, and clinical applications. J Control Release. 2015;200:138–57.
10. Feng Y, Panwar N, Tng DJH, Tjin SC, Wang K, Yong KT. The application of mesoporous silica nanoparticle family in cancer theranostics. Coord Chem Rev. 2016;319:86–109.
11. Smith RA, Manassaram-Baptiste D, Brooks D, Doroshenk M, Fedewa S, Saslow D, et

al. Cancer Screening in the United States, 2015: A Review of Current American Cancer Society Guidelines and Current Issues in Cancer Screening. CA Cancer J Clin. 2015;65:30–54.

12. Bohunicky B, Mousa SA. Biosensors: The new wave in cancer diagnosis. Nanotechnol Sci Appl. 2011;4(1):1–10.
13. Steichen SD, Caldorera-Moore M, Peppas NA. A review of current nanoparticle and targeting moieties for the delivery of cancer therapeutics. Eur J Pharm Sci. 2013; 48(3): 416–427.
14. Rosenblum D, Joshi N, Tao W, Karp JM, Peer D. Progress and challenges towards targeted delivery of cancer therapeutics. Nat Commun. 2018;9(1):1410.
15. Prabhu RH, Patravale VB, Joshi MD. Polymeric nanoparticles for targeted treatment in oncology: Current insights. Int J Nanomedicine. 2015; 2(10):1001-18.
16. Xu X, Ho W, Zhang X, Bertrand N, Farokhzad O, Hospital W, et al. Cancer Nanomedicine: From Targeted Delivery to Combination Therapy. Trends Mol Med. 2015;21(4):223–32.
17. Zhang RX, Wong HL, Xue HY, Eoh JY, Wu XY. Nanomedicine of synergistic drug combinations for cancer therapy – Strategies and perspectives. J Control Release. 2016;240:489–503.
18. Danhier F, Feron O, Préat V. To exploit the tumor microenvironment : Passive and active tumor targeting of nanocarriers for anti-cancer drug delivery. J Control Release. 2015;148(2):135–46.
19. Biswas S, Torchilin VP. Nanopreparations for organelle-specific delivery in cancer. Adv Drug Deliv Rev. 2014;66:26–41.
20. Yang G, Xu L, Xu J, Zhang R, Song G, Chao Y, et al. Smart Nanoreactors for pH-Responsive Tumor Homing, Mitochondria-Targeting, and Enhanced Photodynamic-Immunotherapy of Cancer. Nano Lett. 2018;18(4):2475–84.
21. Uings IJ, Farrow SN. Cell receptors and cell signalling. J Clin Pathol - Mol Pathol. 2000;53(6):295–9.
22. McCormick F. Signalling networks that cause cancer. Trends Genet. 1999;15(12):53–6.
23. Kolch W, Halasz M, Granovskaya M, Kholodenko BN. The dynamic control of signal transduction networks in cancer cells. Nat Rev Cancer. 2015;15(9):515–27.
24. Sever R, Brugge JS. Signal transduction in cancer. Cold Spring Harb Perspect Med. 2015;5(4):a006098.
25. DeBerardinis RJ, Lum JJ, Hatzivassiliou G, Thompson CB. The Biology of Cancer: Metabolic Reprogramming Fuels Cell Growth and Proliferation. Cell Metab. 2008;7(1):11–20.
26. Warburg O. The Metabolism of Carcinoma Cells. J Cancer Res. 1925;9(1):148–63.

27. Shi J, Kantoff PWJ, Wooster R, Farokhzad OC. Cancer nanomedicine: progress, challenges and opportunities. Nat Rev Cancer. 2017;17(1):20–37.
28. Tran S, DeGiovanni PJ, Piel B, Rai P. Cancer nanomedicine: a review of recent success in drug delivery. Clin Transl Med. 2017;6(1):1-21.
29. Baeza A, Manzano M, Colilla M, Vallet-Regí M. Recent advances in mesoporous silica nanoparticles for antitumor therapy: Our contribution. Biomater Sci. 2016;4(5):803–13.
30. Ivey JI, Bonakdar M, Kanitkar A, Davalos RV, Verbridge SS. Improving cancer therapies by targeting the physical and chemical hallmarks of the tumor microenvironment. Cancer Lett. 2016;380(1):330–9.
31. Watermann A, Brieger J. Mesoporous silica nanoparticles as drug delivery vehicles in cancer. Nanomaterials. 2017;7(7):189.
32. Moreira AF, Dias DR, Correia IJ. Stimuli-responsive mesoporous silica nanoparticles for cancer therapy: A review. Microporous Mesoporous Mater. 2016;236:141–57.
33. Liu J, Luo Z, Zhang J, Luo T, Zhou J, Zhao X, et al. Hollow mesoporous silica nanoparticles facilitated drug delivery via cascade pH stimuli in tumor microenvironment for tumor therapy. Biomaterials. 2016;83:51–65.
34. Yang KN, Zhang CQ, Wang W, Wang PC, Zhou JP, Liang XJ. pH-responsive mesoporous silica nanoparticles employed in controlled drug delivery systems for cancer treatment. Cancer Biol Med. 2014;11(1):34-43.
35. Argyo C, Weiss V, Bra C, Bein T. Multifunctional Mesoporous Silica Nanoparticles as a Universal Platform for Drug Delivery. Chem Mater. 2013;26:435–51.
36. Mai WX, Meng H. Mesoporous silica nanoparticles: A multifunctional nano therapeutic system. Integr Biol. 2013;5:19–28.
37. Ma'mani L, Nikzad S, Kheiri-manjili H. Chemistry Curcumin-loaded guanidine functionalized PEGylated I3ad mesoporous silica nanoparticles KIT-6 : Practical strategy for the breast cancer therapy. Eur J Med Chem. 2014;83:646–54.
38. Helleman J, Jansen MPHM, Burger C, van der Burg MEL, Berns EMJJ. Integrated genomics of chemotherapy resistant OC: A role for extracellular matrix, TGFbeta and regulating microRNAs. Int J Biochem Cell Biol. 2010;42(1):25–30.
39. He M, Wang D, Zou D, Wang C, Lopes-Bastos B, Jiang WG, et al. Re-purposing of curcumin as an anti-metastatic agent for the treatment of epithelial OC: In vitro model using cancer stem cell enriched OC spheroids. Oncotarget. 2016;7(52):86374–87.
40. Li P, Xin H, Liu W. Lawsone Inhibits Cell Growth And Improves The Efficacy Of Cisplatin In Skov-3 OC Cell Lines. African J Tradit Complement Altern Med. 2017;14(5):8–17.
41. Seo JH, Jeong KJ, Oh WJ, Sul HJ, Sohn JS, Kim YK, et al. Lysophosphatidic acid induces STAT3 phosphorylation and OC cell motility: Their inhibition by curcumin. Cancer Lett. 2010;288(1):50–6.

42. Perrone D, Ardito F, Giannatempo G, Dioguardi M, Troiano G, Russo LLO, et al. Biological and therapeutic activities, and anti-cancer properties of curcumin (Review). Exp Ther Med. 2015;10:1615–23.
43. Kasi PD, Tamilselvam R, Skalicka-Woźniak K, Nabavi SF, Daglia M, Bishayee A, et al. Molecular targets of curcumin for cancer therapy: An updated review. Tumor Biol. 2016;37(10):13017–28.
44. Kunnumakkara AB, Bordoloi D, Harsha C, Banik K, Gupta SC, Aggarwal BB. Curcumin mediates anti-cancer effects by modulating multiple cell signaling pathways. Clin Sci. 2017;131:1781–99.
45. Mirzaei H, Shakeri A, Rashidi B, Jalili A, Banikazemi Z, Sahebkar A. Phytosomal curcumin: A review of pharmacokinetic, experimental and clinical studies. Biomed Pharmacother. 2017;85:102–12.
46. Rauf A, Imran M, Orhan IE, Bawazeer S. Health perspectives of a bioactive compound curcumin: A review. Trends Food Sci Technol. 2018;74:33–45.
47. Wilken R, Veena MS, Wang MB, Srivatsan ES. Curcumin : A review of anti-cancer properties and therapeutic activity in head and neck squamous cell carcinoma. Mol Cancer. 2011;10(12):1–19.
48. Sun K, Duan X, Cai H, Liu X, Yang Y, Li M, et al. Curcumin inhibits LPA-induced invasion by attenuating RhoA/ROCK/MMPs pathway in MCF7 breast cancer cells. Clin Exp Med. 2016;16(1):37–47.
49. Sabarwal A, Kumar K, Shyanti R, Singh RP. Curcumin in Cancer Prevention. In: Yadav RVU. ed 1. Functional Food and Human Health. Singapore: Springer; 2018:329–74.
50. Banik U, Parasuraman S, Adhikary AK, Othman NH. Curcumin: The spicy modulator of breast carcinogenesis. J Exp Clin Cancer Res. 2017;36(1):1–16.
51. Deng Y, Verron E, Rohanizadeh R. Molecular mechanisms of anti-metastatic activity of curcumin. Anti-cancer Res. 2016;36(11):5639–47.
52. Yang X, Li Z, Wu Q, Chen S, Yi C, Gong C. Trail and curcumin codelivery nanoparticles enhance trail-induced apoptosis through upregulation of death receptors. Drug Deliv. 2017;24(1):1526.
53. Jung EM, Lee TJ, Park JW, Choi KS, Kwon TK. Curcumin sensitizes tumor necrosis factor-related apoptosis-inducing ligand (TRAIL)-induced apoptosis through reactive oxygen species-mediated upregulation of death receptor 5 (DR5). Carcinogenesis. 2005;26(11):1905–13.
54. Yu Z, Wan Y, Liu Y, Yang J, Li L, Zhang W. Curcumin induced apoptosis via PI3K/Akt-signalling pathways in SKOV3 cells. Pharm Biol. 2016;54(10):2026–32.
55. Baglole KN, Boland PG, Wagner BD. Fluorescence enhancement of curcumin upon inclusion into parent and modified cyclodextrins. J Photochem Photobiol A Chem.

2005;173:230–7.

56. Chignell CF, Bilski P, Reszka KJ, Motten AG, Sik RH, Dahl TA. A Spectral and photochemical properties of curcumin. Photochem Photobiol. 1994;59(3):295–302.
57. Priyadarsini KI. Photophysics, photochemistry and photobiology of curcumin: Studies from organic solutions, bio-mimetics and living cells. J Photochem Photobiol C Photochem Rev. 2009;10(2):81–95.
58. Wang YJ, Pan MH, Cheng AL, Lin LI, Ho YS, Hsieh CY, et al. Stability of curcumin in buffer solutions and characterisationof its degradation products. J Pharm Biomed Anal. 1997;15(12):1867–76.
59. Priyadarsini KI. The chemistry of curcumin: From extraction to therapeutic agent. Molecules. 2014;19(12):20091–112.
60. Shen L, Ji HF. The pharmacology of curcumin: Is it the degradation products? Trends Mol Med. 2012;18(3):138–44.
61. Oliveira AS de, Brighente IMC, Lund RG, Llanes LC, Nunes RJ, Bretanha LC, et al. Antioxidant and Antifungal Activity of Naphthoquinones Dimeric Derived from Lawsone. J Biosci Med. 2017;5:39–48.
62. Pereyra CE, Dantas RF, Ferreira SB, Gomes LP, Silva FP. The diverse mechanisms and anti-cancer potential of naphthoquinones. Cancer Cell Int. 2019;19(1):1–20.
63. Kanaan YM, Das JR, Bakare L, Enwerem NM, Berhe S, Beyene D, et al. Biological evaluation of 23-dichloro-5,8-dimethoxy-1,4-naphthoquinone as an anti-breast cancer agent. Anti-cancer Res. 2009;29(1):191–9.
64. Zhang Q, Dong J, Cui J, Huang G, Meng Q, Li S. Cytotoxicity of Synthesized 1,4-Naphthoquinone Oxime Derivatives on Selected Human Cancer Cell Lines. Chem Pharm Bull. 2018;66(6):612–9.
65. Zhang Y, Luo YH, Piao XJ, Shen GN, Wang JR, Feng YC, et al. The design of 1,4-naphthoquinone derivatives and mechanisms underlying apoptosis induction through ROS-dependent MAPK/Akt/STAT3 pathways in human lung cancer cells. Bioorganic Med Chem. 2019;27(8):1577–87.
66. Su JC, Lin KL, Chien CM, Tseng CH, Chen YL, Chang LS, et al. Furano-1,2-naphthoquinone inhibits EGFR signaling associated with G2/M cell cycle arrest and apoptosis in A549 cells. Cell Biochem Funct. 2010;28(8):695–705.
67. Chien CM, Lin KL, Su JC, Chuang PW, Tseng CH, Chen YL, et al. Naphtho[1,2-b]furan-4,5-dione induces apoptosis of oral squamous cell carcinoma: Involvement of EGF receptor/PI3K/Akt signaling pathway. Eur J Pharmacol. 2010;636(1–3):52–8.
68. Kishore N, Binneman B, Mahapatra A, Van De Venter M, Du Plessis-Stoman D, Boukes G, et al. Cytotoxicity of synthesized 1,4-naphthoquinone analogues on selected human cancer cell lines. Bioorganic Med Chem. 2014;22(17):5013–9.

69. Dias GG, King A, De Moliner F, Vendrell M, Da Silva Júnior EN. Quinone-based fluorophores for imaging biological processes. Chem Soc Rev. 2018;47(1):12–27.
70. Dabiri M, Tisseh ZN, Bazgir A. Synthesis of fluorescent hydroxyl naphthalene-1,4-dione derivatives by a three-component reaction in water. Dye Pigment. 2011;89(1):63–9.

Chapter 2: Alternative fluorophores designed for advanced molecular imaging

Chapter 2 has been published in Drug Discovery Today and is cited as follows:
Freidus LG, Pradeep P, Kumar P, Choonara YE, Pillay V. Alternative fluorophores designed for advanced molecular imaging, Drug Discov Today.2018;23(1):115-133

2.1 Abstract

Fluorescent molecular imaging has advanced drastically over the past decade. With the development of high-resolution microscopy techniques and the ability to visualize intracellular molecular events, there is a growing need for new fluorophores to accompany these fast-developing techniques. Therefore, there has been substantial development of alternative fluorophores for single-molecule detection and molecular imaging. These rationally designed fluorophores have infinite possibilities and novel fluorophores are constantly being produced for different applications. This review focuses on the recent developments in novel fluorophores designed for molecular imaging and single-molecule detection. Here, single-molecule imaging, smart fluorescent probes, two photon microscopy, Förster resonance energy transfer (FRET) and super resolution microscopy are discussed in detail.

2.2 Introduction

Molecular imaging is a technique that enables the real-time visualization and characterisation of cellular structures, events and pathways in living organisms at the molecular level [1]. Molecular imaging offers the opportunity to elucidate cellular behaviour at the molecular level, aiding in drug discovery, the evaluation of therapy efficacy and early diagnosis of several diseases [2–4]. Real-time *in vivo* imaging is the current goal of much research and the realization of this technique would increase medical discoveries and scientific breakthroughs that have boundless applications [5]. Molecular imaging utilizing fluorescent molecules is the focus of current molecular imaging research. The use of fluorescent molecules in imaging is advantageous because of high-resolution images, high sensitivity and precision, non-invasiveness, cost-effectiveness and no perturbation with cellular functions [6]. In recent years, the field of molecular imaging has emerged considerably, because the ability for site-specific and molecule specific imaging enables countless applications and opportunities with wide reaching effects [5]. The application of molecular imaging in a clinical setting requires improvements in the fluorescent dyes used in terms of background:target ratios, specificity, quantum yields, absorption and emission wavelengths, water solubility, cell permeability and fluorescent lifetimes [7]. Moreover, the production of fluorophores that are in the near-infrared (NIR) range and that have low toxicity is required for *in vivo* applications [8]. To fulfil this need, alternative fluorophores need to be developed. This review provides an overview of novel organic fluorophores that have recently been designed and employed for molecular imaging and single molecule detection. Over the past two decades, there has been an abundance of research on the development of novel and alternative fluorophores for *in vivo* imaging. Owing to the enormity of research available on this topic, only organic fluorophores created in the current decade are reviewed (Table 1).

Table 2.1: Summary table for fluorophores discussed in this review

Fluorophore	Intended application
ZX800-1	NIR fluorophore for image guided surgery
pDA	polymer fluorophore for blood flow imaging
azadipyrromethene fluorophores	NIR fluorophore for glycoprotein imaging
coumarin-malonitrile conjugate	Biothiol detection
triphenylamine and maleimide conjugate	Biothiol detection
RealThiol	GSH detection
naphthyl aldehyde and malononitrile	Aβ plaque detection
HK yellow	peroxynitrile detection
Dyad of chloroalkoxytetrazine and naphthalimide	FRET fluorophore
TY-1	FRET fluorophore for Cu^{2+} detection
Squarine dyes	fluorophore for TPM
BTVPA	fluorophore for TPM
BODIPY derivatives	NIR and TMA fluorophore for mitochondrial imaging
HJVPI	NIR and TMA fluorophore for mitochondrial imaging
Acedan derivatives	Aβ plaque detection and water soluble dye for TPM
carborane-triphenylamine conjugate	fluorophore for TPM
Triphenylamine derivative	AIE chromophore
CTPE-Tau	ROS detection through AIE
Pyrene-fluorescein conjugate	AIE fluorophore for live cell imaging
GMP	3PA fluorophore for Zinc detection
push-pull probe	cell membrane probe
BF2 chelated azadipyrromethane	lysosomal imaging
pentamethine dyes	pH responsive dye for lysosomal imaging
cyanine dye conjugate	photoswitching fluorophore
JF549	single molecule labelling and intracellular imaging
naphthalimide azindine derivative	super resolution microscopy
Si-Q-rhodamine	imaging for F-actin

2.3 NIR fluorophores

It has been well established that fluorophores designed for molecular imaging should aim to be in the NIR or second NIR window. Utilizing fluorophores in this wavelength range is superior overusing fluorophores in the visible window because NIR or second NIR fluorophores enable a reduction of photon absorption in biological tissue, autofluorescence and increasing resolution and penetration depth [9]. However, drawbacks to these fluorophores currently exist, such as low fluorescent quantum yield and possible toxicity. Thus, current research is trying to tackle these problems and develop ideal NIR fluorophores for molecular imaging and single molecule detection to afford better imaging resolution. Numerous fluorescent dyes are available; however, there is much room for the optimization of dye properties to produce an ideal dye for *in vivo* imaging. An ideal dye would have low background noise and unspecific binding, excellent optical properties, display optical and physical stability, have no cytotoxicity, be soluble in an aqueous media and have the ability to be easily conjugated onto a targeted ligand. For this reason, substantial research is currently being undertaken to develop a dye with all the aforementioned properties [10].

Cyanines, a subclass of polymethine dyes, are a newer class of traditional fluorescent dyes displaying fluorescence in the visible and NIR wavelengths and they constitute the main class of NIR dyes used currently. Structurally, they consist of two nitrogen centers conjugated to methine carbons forming a polymethine bridge [11]. This bridge connects the electron donor to the electron acceptor, which are located on opposite ends of the molecule and induce the delocalization of the p electrons resulting in a positive charge existing over the nitrogen atoms [11]. The variety of cyanine dyes available offers a broad range of absorption maxima that are dependent on the length of the polymethine chain, thus allowing multiple derivatives to be produced in multiple avenues [12,13]. They are advantageous because they are brighter, have low degrees of quenching, display high quantum yields, have large molar extinction coefficients, have a broad wavelength tunability and have better photostabilities than other traditional dyes. Additionally, they are easily linked to biomolecules and exhibit strong fluorescence when conjugated, enabling them to be used as probes [14]. Although cyanine dyes are substantially better than traditional fluorophores, they also have

drawbacks such as low water solubility owing to their hydrophobic nature and a high propensity for dye aggregation [15]. Hydrophilicity has traditionally been increased through the addition of sulfo and carboxyl groups, thus imparting a negative charge [15]. Although this has been successful in increasing hydrophilicity and reducing aggregation, anionic cyanine dyes display high levels of nonspecific uptake in a variety of organs as well as a reduction in lipophilicity, thus impeding cell membrane penetration [10].

Choi and co-workers created a much improved NIR fluorophore by introducing zwitterionic properties to the commonly used indocyanine dye, which is hydrophobic in nature. The charged species were equally distributed across the fluorophore, thus hiding the hydrophobic heptamethine core. This dye was termed ZX800-1 (Figure 1). Rapid update of hydrophobic fluorophores by the liver is a major limitation to their application. This rapid uptake is accompanied by an increase in dye concentration in the bile and gastrointestinal tract. This nonspecific uptake hinders *in vivo* imaging specificity and increases background fluorescence. The researchers found that by alternating charged molecules across the surface of the fluorophore the hydrophobic nature of the fluorophore was shielded, allowing minimum interaction with serum proteins and difficulty in crossing cellular membranes thus reducing nonspecific binding and tissue and/or organ uptake and liver clearance [10]. A further limitation of hydrophobic dyes is the difficulty of conjugating them to ligands, enabling specific targeting. This zwitterionic dye incorporated a carboxylic acid moiety for amide bond linkage to a targeted ligand. Choi *et al*. further extended their work by conjugating their dye (ZX800-1) onto an RGD peptide to enable integrin targeting (Figure 2.1). To assess the improved properties, the zwitterionic nature of ZX800-1, they conjugated two common dyes, namely IRDye 800-CW and Cy5.5, with RGD peptides for a comparative analysis. XZ800-1 outperformed the commercially available dyes in all tests performed by exhibiting substantially lower background noise, nonspecific binding and better optical properties [16]. The researchers later demonstrated their zwitterionic fluorophore to be effective as a NIR fluorophore for dual colour channel image-guided surgery. In a clinical setting, the tumour and normal tissue such as nerve and blood vessels should be visible, reducing surgical mistakes and unnecessary damage of healthy tissue upon tumour resection. The research group undertook various *in vitro* and *in vivo* assays to evaluate the clinical application of a NIR fluorophore for image-

guided surgery. *In vivo* studies showed that the fluorophore exhibited a long half-life of 45 min in a pig model, compared with the short half-life of 3.6 min for Indocyanine green (ICG). The long half-life allowed sufficient time for imaging applications before urine excretion, yet the half-life was short enough to avoid nonspecific binding and toxicity [17]. This work is significant because the precision and effectiveness of surgical procedures can be vastly improved using such a fluorophore.

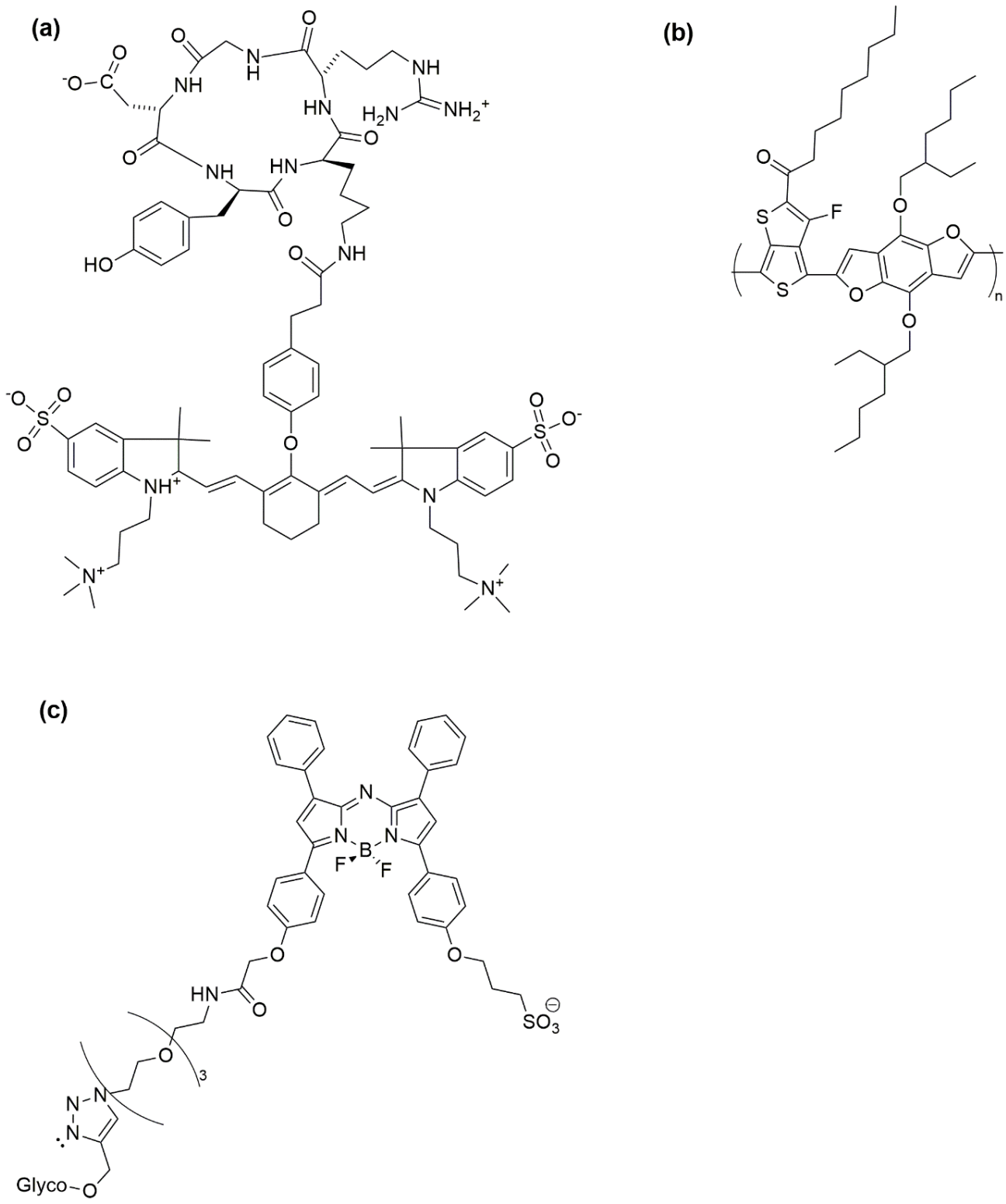


Figure 2.1: Near-infrared (NIR) fluorophores. (**a**) The novel fluorophore ZW800-1 attached to a RGD peptide [16]. (**b**) Synthesis of fluorescent polymers pDA [8]. (**c**) Chemical structure of BF2–azadipyrromethene [19].

Hong *et al*. demonstrated a unique way in which a novel NIR fluorophore can be used for *in vivo* imaging. A conjugated fluorescent polymer was produced through the copolymerization of alternating electron donating and electron accepting molecules. The copolymerization process allows bandgap energy to be tunable to NIR wavelengths because optical properties can be optimized by manipulating the structure of the donor–acceptor structures and length of the polymers. The electron donating monomer benzo[1,2-b:3,4-b0]difuran and the electron accepting monomer fluorothieno-[3,4-b]thiophene were conjugated onto the alternating electron-donating–accepting fluorescent polymer poly(benzo[1,2-b:3,4-b0]difuran-alt-fluorothieno-[3,4-b]thio-phene and the resultant molecule was termed pDA (Figure 2.1). The addition of fluorine enabled the tuning of fluorescence to longer wavelengths; furthermore, the addition of polyethylene glycol (PEG) afforded water solubility and biocompatibility. pDA exhibited a large Stokes shift of 400 nm, an emission wavelength of 1050 nm and a high quantum yield of 1.7%. Their method of copolymerization enabled fluorescence emission to be increased to over 1000 nm (Figure 2.2). The majority of NIR fluorophores exhibit fluorescence emission below 900 nm, this substantial bathochromic shift is advantageous for *in vivo* imaging [8]. The researchers demonstrated that rapid blood flow changes can be visualized in real space and in real time using pDA. They managed to achieve a high quantum yield with substantially lower doses than typically administered. This, taken together with the increase in emission wavelength, offers a salient advantage in the field of fluorescent *in vivo* imaging.

Ease of bioconjugation is a significant factor that should be considered during fluorophore design. The ability to covalently link a fluorophore to a biological molecule is fundamentally important in the field of live cell imaging [18]. Limited chemical coupling routes have been explored. Most coupling techniques are either ester–amine or maleimide–thiol based. A copper catalyzed azide–alkyne cycloaddition reaction (CuAAC) was explored by Wu and co-workers for fluorophore bioconjugation because the mild reaction conditions afford greater biocompatibility. This technique was explored in glycoprotein imaging. Boron-chelated aza-dipyrromethenes were used as the fluorescent core owing to their favourable spectral properties, including a high quantum yield, emission in the NIR range (696 nm) and high photostability. The two aryl rings present on the BF2–azadipyrromethene core were each functionalized in two

alternate manners: an alkylsulfonic acid group, which would impart aqueous solubility, was functionalized onto one of the aryl rings; whereas the other aryl ring was functionalized with an oligoether spacer with a terminal azide group that would enable CuAAC chemical modification through the separation of the fluorophore and conjugation reaction site [19]. The research group successfully used this conjugation method in producing a fluorescent glycoconjugate with good photophysical properties and effective cellular uptake and imaging (Figure 2.1).

Indeed, the development of NIR fluorophores has advanced the field of live imaging. Clearly, a fluorophore that is to be used in *in vivo* imaging applications would need to be excited and emitted in the NIR range. The need for long wavelength emitting fluorophores has clearly been established in the literature. The development of new NIR fluorophores is simply not enough. Scores of these fluorophores have already been developed, thus NIR fluorophores with novel features are the focus of forthcoming research.

2.4 Smart fluorophore conjugates as molecular probes

Fluorophore conjugates are being produced for various functions. The combination of two fluorophores or the conjugation of a fluorophore onto another molecule has become common place. Many of these conjugates have unique capabilities that deem them extremely useful in a variety of assays. Fluorescent conjugates are being designed as probes to detect a variety of biological molecules or events *in vivo*. Below are a few examples of fluorescent probes.

2.4.1 *Biothiol probes*

Biothiols encompass molecules such as cysteine (Cys), homocysteine (Hcy) and glutathione (GSH) (Figure 2.3). Biothiols are implicated in a variety of biological functions and diseases such as cancer, liver disease, edema, weakness, lethargy, hair depigmentation, loss of muscle and fat, skin lesions and AIDS [20]. Therefore, *in vivo* levels for biothiols are of clinical significance. Kwon and co-workers developed a coumarin–malonitrile conjugate to fluorescently detect biothiols (Figure 2.3). Coumarin is a commonly used fluorophore that exhibits fluorescence in the UV–VIS spectrum at

524 nm. Malonitrile is nonfluorescent and acts as a fluorescent quencher when attached to coumarin via a double bond and is also an electrophile. The nucleophilic properties of biothiols induce the breaking of the double bond between coumarin and malonitrile. Therefore, when the probe encounters a thiol, the conjugate is separated, coumarin is no longer quenched and fluorescence is observed. This probe was demonstrated to be effective *in vitro* and ex vivo for detecting Cys, Hcy and GSH. Amino acids with similar structures such as methionine and serine did not induce the fluorescence of the probe. Additionally, acidic and basic amino acids did not induce fluorescence either. Thus, the coumarin– malonitrile probe was thiol specific [21].

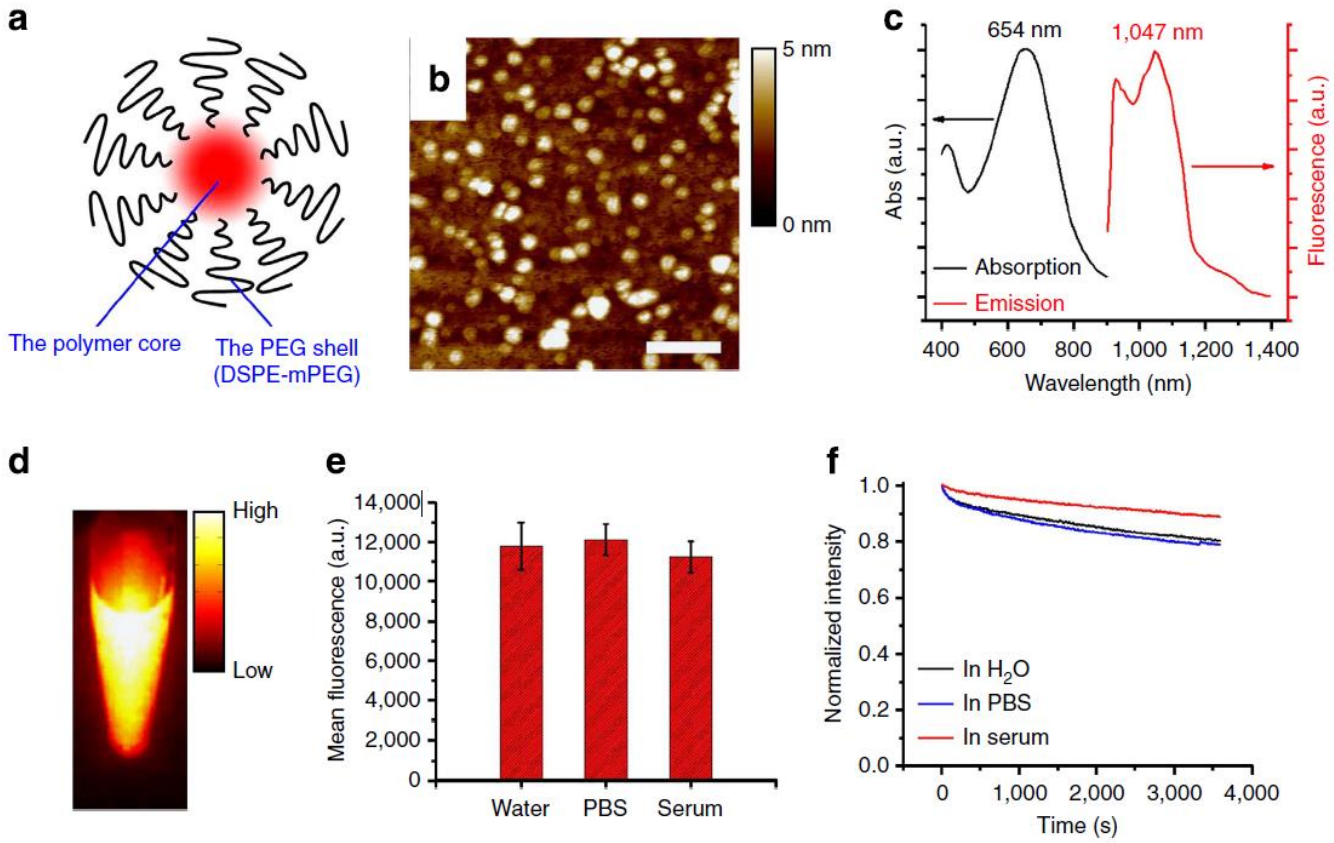


Figure 2.2: Characterizations of pDA-PEG nanoparticle. (a) A schematic of the pDA-PEG nanoparticle showing a hydrophobic polymer core and a hydrophilic PEG shell. (b) A typical AFM image of pDA-PEG nanoparticles deposited on a silicon substrate. (c) Absorption and emission spectra of pDA-PEG, featuring a large Stokes shift of 400 nm. (d) A NIR-II fluorescence image of an aqueous solution of pDA-PEG taken in the range of 1.0–1.7 mm NIR-II window under an excitation of 808 nm. (e) Fluorescence stability of pDA-PEG in different media including water, PBS and serum. (f) Photostability curves of pDA-PEG in water, PBS and serum under continuous 808 nm illumination. pDA-PEG in serum exhibits the lowest degree of photobleaching among the three [8] (Reproduced with permission from Nature Publishing Group 2014).

A similar 'turn-on' probe for biothiol detection was developed by Lui and co-workers. The probe was a triphenylamine and maleimide conjugate (Figure 2.3). Maleimide reacts selectively with thiols via a Michael addition reaction involving the electrondeficient C=C double bond. Like the work of Kwon and co-workers, this probe experienced fluorescent quenching when in the conjugated form and experienced fluorescent enhancement upon the detection of thiols. Another similarity exists in that the probe was specific to thiols and no fluorescence emission was observed in response to other similar amino acids. *In vitro* cell studies successfully showed the turn-

on and imaging ability of the probe owing to the probe's cell permeability and specificity toward thiols in living cells. However, a limitation of the probe designed by Lui *et al*. was that the emission spectrum was at 480 nm and thus is not in the NIR range optimal for live cell imaging. Therefore, a future aim of this research group should be to red shift the emission spectrum to enable *in vivo* applications [20].

Jiang and co-workers took the principle of a Michael addition reaction to produce a GSH fluorescent probe. This probe was termed RealThiol (RT) and could quantitatively monitor GSH dynamics in living cells. GSH, which is the most abundant thiol in cells, along with its oxidative partner GSSG, is instrumental in maintaining cellular redox homeostasis, acts as a molecule by directly activating gene expression and is involved in several other fundamental cellular processes. These functions are governed by the concentration and distribution of GSH in the cell. Current methods enable GSH concentration levels to be determined; however, they do not enable the intracellular dynamics to be accessed, which is a crucial component of GSH function. Using a Michael addition reaction, they produced a reversible real time GSH probe with an appropriate equilibrium dissociation constant and rapid reaction kinetics. They designed their fluorophore to have a four membered azetidine ring which increased the quantum yield and improved photostability. Furthermore, they included a cyano group which enabled rapid reaction kinetics and two carboxylic acid groups which allowed aqueous solubility. Through the rational design of a novel fluorophore they were successfully able to produce a GSH specific fluorescent probe that reacts in real time to fluctuations in intracellular GSH concentrations and dynamics, thus enabling the elucidation of the effect of GSH on redox perturbance in a cell, all of which is crucial in understanding cellular dynamics and chemistry [22].

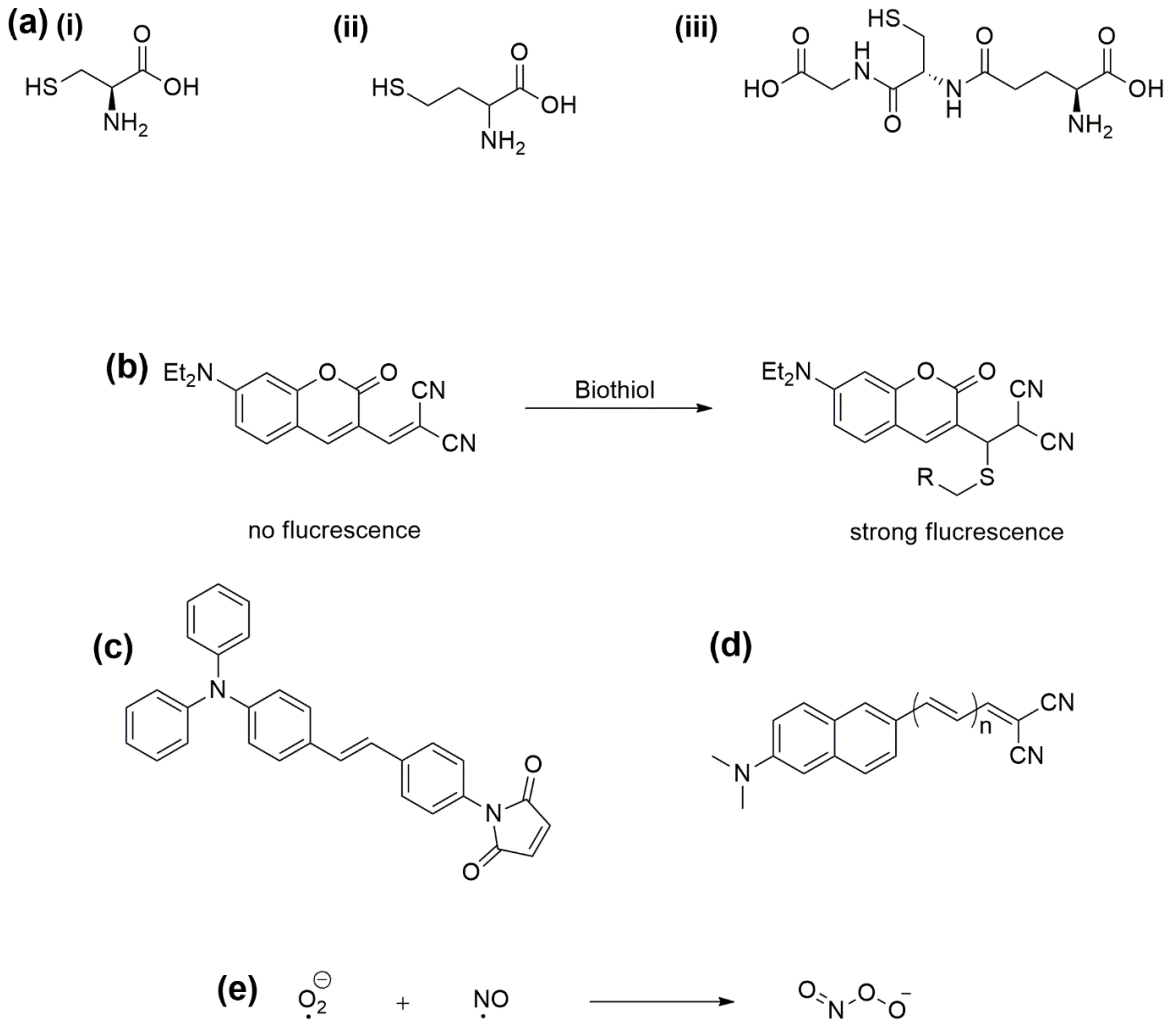


Figure 2.3: Fluorophores used as molecular probes. (a) The chemical structures of biothiols (i) cystine, (ii) homocystine and (iii) glutathione. (b) Mechanism of action of biothiol detection probe based on a malonitrile and coumarin conjugate produced by [21]. (c) Biothiol turn-on probe [20]. (d) Chemical structure of amyloid-β plaque binding probe [23]. (e) *In vivo* synthesis of peroxynitrite.

2.4.2 *Amyloid-β-plaque-binding probe*

Alzheimer's disease is a disease characterized by extracellular accumulation of amyloid-β plaques in the brain. Current methods lack sufficient resolution for early stage detection or are accompanied with excessive radiation. Fluorescent imaging offers a non-invasive, radiation free, real time imaging system for the detection of amyloid-β plaques. The rationale design of NIR fluorophores allows the blood–brain barrier (BBB) to be crossed [23]. Fu *et al*. developed a NIR fluorophoric probe based on a donor–acceptor p-conjugated system. The probes were formed from naphthyl

aldehydes and malononitrile (Figure 2.3). By lengthening the polyenic chain, the emission maxima were increased pushing the fluorophore into the NIR range. However, this lengthening procedure had drawbacks, such as a decrease in quantum yield owing to an increase in the photo induced charge delocalization and induced structural changes. Thus, the polyenic chain could only be increased to a certain degree, limiting the extent the fluorophore absorption spectrum could be lengthened [23]. The probe produced displayed turn-on properties, meaning it demonstrated an increase in quantum yield in response to amyloid-β plaque binding. This turn-on feature is necessary for *in vivo* probes to circumvent background fluorescence and to increase probe sensitivity [23]. The probe was successfully shown to selectively bind to (and to enable effective detection of) amyloid-β plaques *in vivo*. Furthermore, the probe was shown to readily cross the BBB and to have a long emission lifetime. The use of a fluorophoric probe is a novel mechanism to detect Alzheimer's in a cost effective, non-invasive manner and enables earlier detection than the conventional detection methods [23].

2.4.3 *Peroxynitrite detection probe*

Peroxynitrite is an important reactive oxygen species (ROS) produced through the reaction of superoxide and nitric oxide [24] (Figure 2.3). It interacts with various biologically important molecules such as DNA, proteins and lipids and induces irreparable damage through direct oxidation or via radical mediated reactions [24]. Peroxynitrite has been implicated in several diseases such as and induces irreparable damage through direct oxidation or via radical mediated reactions [24]. Peroxynitrite has been implicated in several diseases such as neurodegeneration, cancer, inflammation, circulatory shock and ischemia–reperfusion injury [25]. The small concentrations in which it exists has made its detection challenging. Recently, Peng and co-workers rationally designed a fluorescent probe for peroxynitrite detection. The properties of two rhodamine fluorophores, namely rhodamine B and x-rhodamine, were evaluated. It was observed that the julolidine moiety of x-rhodamine, which offers water solubility, was not stable toward peroxynitrite owing to the exposed lone pair of nitrogen electrons. By contrast, the N, N-diethylaniline moiety from rhodamine B was protected from peroxynitrite attack because its lone pair of nitrogen electrons were protected by an ethyl group; however, this renders rhodamine B insoluble and thus ineffective for

peroxynitrite detection. Indeed, the combination of the desirable moieties from each rhodamine and the exclusion of the undesirable moieties enables the synthesis of a fluorophore specialized for peroxynitrite detection [26]. This novel fluorophore was termed HKyellow. The addition of acetoxymethyl ester onto HKyellow enabled *in vivo* applications, because acetoxymethyl ester imparted a neutral charge and allowed diffusion across the cell membrane. This acetoxymethyl ester group was then removed intracellularly through the action of esterases. Cell culture studies demonstrated the specificity toward peroxynitrite and the applicability of the novel fluorophore for *in vivo* studies. Further research involving animal studies is required to access the suitability of the fluorophore for live cell imaging [26].

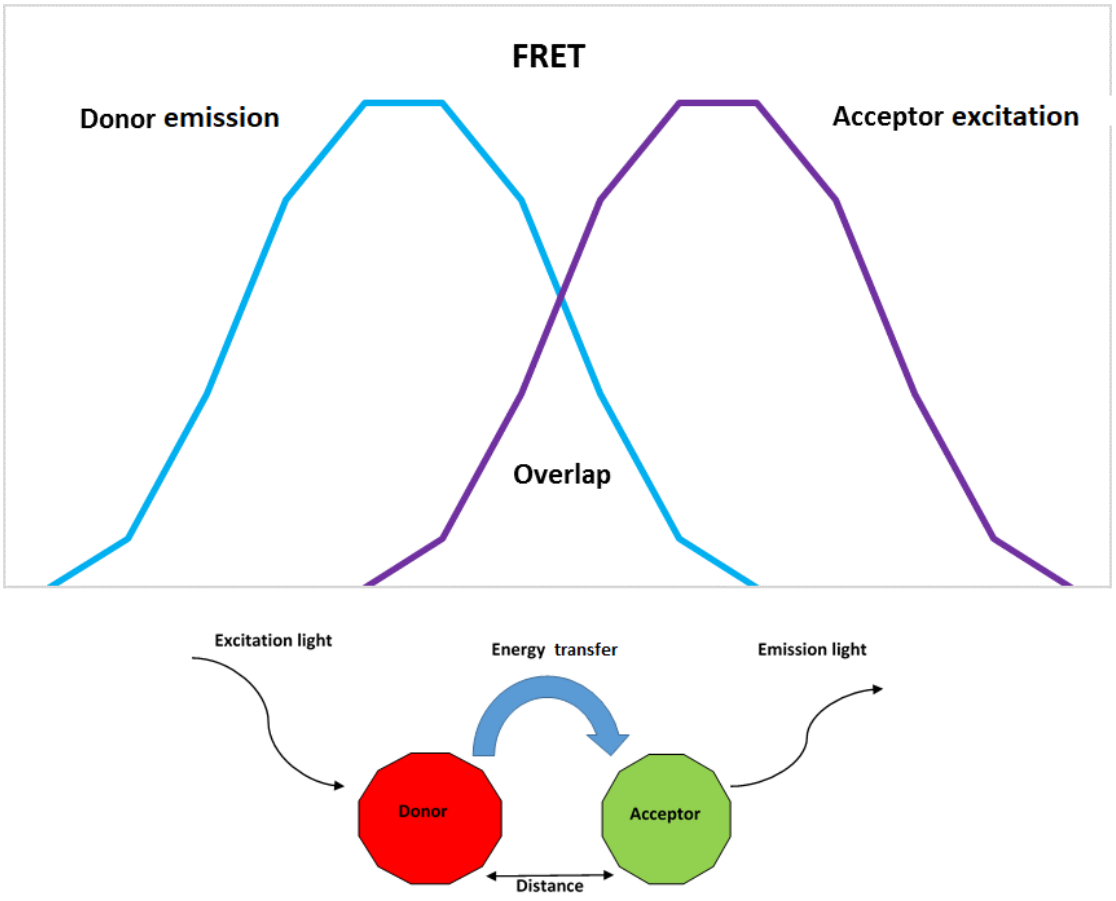


Figure 2.4: Schematic explaining the mechanism of FRET.

2.5 Fluorophores based on Förster resonance energy transfer

Förster resonance energy transfer (FRET) is a process where light energy is transferred between two light sensitive molecules. Once in an excited state, a donor fluorescent molecule transfers energy to an acceptor fluorescent molecule that is in close range through nonradiative dipole–dipole interactions [27,28] (Figure 2.4). FRET can be used to determine distances between two molecules at angstrom diameters. A requirement for FRET to occur is that the emission wavelength of the donor fluorophore and the excitation wavelength of the acceptor fluorophore overlap. The distance between the donor and the acceptor fluorophore and the orientation of the transition dipole moment are key parameters in FRET and have been extensively exploited in the development of novel fluorescent molecules [27–29].

Tetrazines comprise four electronegative nitrogen atoms on an aromatic ring. They have a high electron affinity and can be reduced at high potentials. s-Tetrazines exist as many derivatives that differ by the substituents attached to the aromatic ring [30] (Figure 2.5). The lifetime, quantum yield and colour of fluorescence are all dependent on the substituents present. s-Tetrazines are electron poor nitrogen heterocycles and their photophysical properties are highly dependent on their redox state. Tetrazines have a low molar absorption coefficient of around 500 l/mol/cm and tetrazines exhibit fluorescence switching depending on the redox state [31]. They absorb light at 520 nm and are efficient fluorescent quenchers when near a fluorophore through the mechanism of FRET [32]. Conversely, tetrazines can also function as a fluorophore. However, their low extinction coefficient prevents a high fluorescence intensity. This has been overcome by linking tetrazines to a chromophore such as a naphthalimide, which allows energy transfer between the two chromophores, resulting in tetrazine fluorescence. The fluorescence intensity increase is inversely proportional to the inter-chromophore distance of the dyad, with this increase in fluorescence intensity being dependent solely on the inter-chromophore distance; moreover, the quenching efficiency was also dependent on the inter-chromophore distance. [33]. Qing and co-workers prepared a dyad consisting of chloroalkoxytetrazine linked to a naphthalimide (Figure 2.5). The substitution of s-tetrazines with heteroatoms led to unique fluorescent properties such as fluorescence stemming from a n-p* transition. The long fluorescent lifetime (100 ns) of chloroalkoxytetrazine and its ability to detect electron rich pollutants

owing to its highly oxidizing character make them attractive molecules for fluorescent detection applications. However, these molecules display low molecular extinction coefficients and are poor at absorbing, thus limiting their applications. In the work performed by Qing *et al*. the conjugation of naphthalimide onto a chloroalkoxytetrazine substantially increased the fluorescent intensity of the dye. Naphthalimide efficiently absorbed light and simultaneously transferred the energy to tetrazine with a 95% efficiency. However, to reap the rewards of this fluorescent enhancement, the dyad was required to be excited at 355 nm which was selective of the imide moiety, instead of 517 nm which was selective of the tetrazine moiety. This short wavelength required for enhanced fluorescence does not allow *in vivo* imaging applications, because this wavelength incites autofluorescence. However, the rationale behind this dyad can be utilized in future in producing a long living fluorophore with high fluorescent intensity [34].

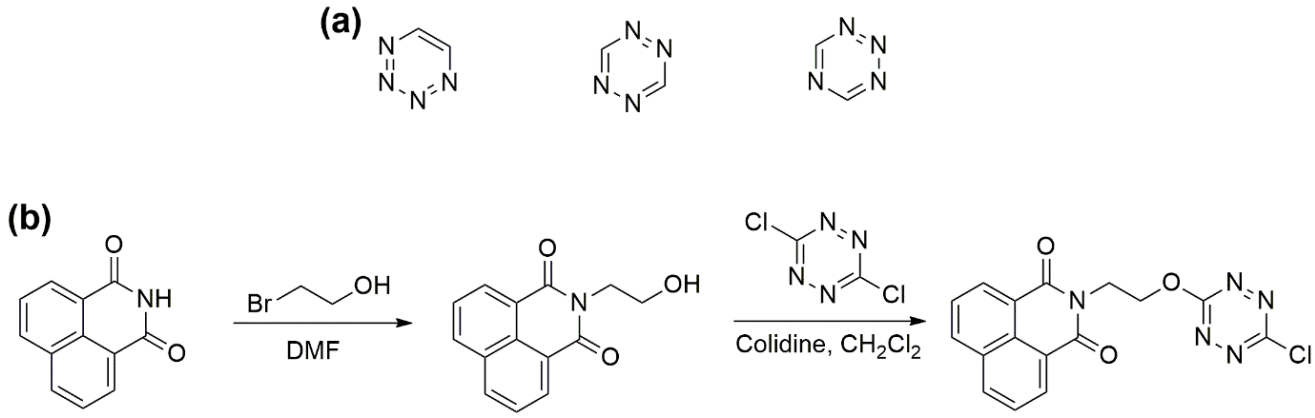


Figure 2.5: Fluorophores designed using FRET. (a) The three chemical isoforms of tetrazine. (b) Schematic demonstrating dyad synthesis [34].

A FRET probe for the ratiometric detection of Cu2+ was developed by Ge and co-workers. Rhodamine B was used as the acceptor molecule owing to its favourable photophysical properties and pyrido[1,2-a]-benzimidazole was used as the donor molecule. Furthermore, piperazine was used as a linker and a hydrazine functional group was added as the Cu2+ reaction site. This novel probe was termed TY-1. When no metal ion was present no FRET could occur and this resulted in a colourless solution. Upon the probe's detection of Cu2+ FRET occurred and a significant observable colour change to pink occurred. The FRET probe has a large Stokes shift

of 190 nm, is highly sensitive and selective, has a low detection limit of 42 nM and has a fast response rate of 2 min. Additionally, the probe was shown to be cell permeable thus allowing intracellular Cu2+ levels to be imaged and monitored [35].

2.6 Fluorophores based on two-photon absorption

Two-photon absorption (TPA) is a linear optical process where a single fluorophore is excited by two photons, both of which are lower in energy than the single photon that is required to excite the fluorophore. The fluorophore simultaneously absorbs two photons and becomes excited, inducing fluorescence [36]. The sum of the energies of the two photons is required to be greater than the energy gap between the ground and excited state of the fluorophore. These fluorophores are usually in the NIR range. This phenomenon has been exploited in the use of two-photon microscopy (TPM) which enables live cell imaging with high resolution and low background fluorescence [37]. TPM is superior to confocal microscopy for live cell imaging because it enables greater penetration depths, reduced background fluorescence and a high resolution [38] (Figure 2.6).

The advantages of TPA are caused by several phenomena that are unique to TPA fluorophores. The increase in resolution corresponding to TPA results from the fact that TPA will only occur where the laser is most concentrated, which is close to the laser's focal point. Thus, nonspecific fluorescence is reduced which significantly improves resolution. Additionally, a light source of lower intensity is required in TPM; therefore, less tissue scattering is induced, corresponding to lower background fluorescence and large material penetration [39]. Furthermore, TPM reduces photo damage because there is a limited excitation volume and a reduction in tissue scattering. Thus, TPM is ideal for *in vivo* imaging applications. The probability of a TPA event occurring and the efficiency of absorbed photons to fluorescence emission conversion is referred to as the two-photon cross section. This value is an important parameter for evaluating and comparing the ability and efficiency of TPA dyes [36,40]. Fluorophores that are typically used in confocal microscopy are not ideal for TPM because they have low TPA cross-sections and many do not fluoresce in response to the two-photon mechanism. Therefore, a distinct class of fluorophores with high TPA cross-sections are required for TPM [40,41]. The presence of electron donating and accepting moieties substituted

on a p-conjugated system is required for a molecule to possess TPA. TPA dyes can be improved through the incorporation of heteroaromatic rings into the p-conjugated system. This incorporation enables a dye to have increased fluorescence emission and precise optical properties [42]. The sizes of the TPA cross sections are dependent on several properties including the efficiency and dimensionality of the intramolecular charge transfer, vibronic coupling, molecular planarity, conjugation length and the efficiency of the donating and withdrawing abilities of the electron donor and acceptor groups of the dye [43].

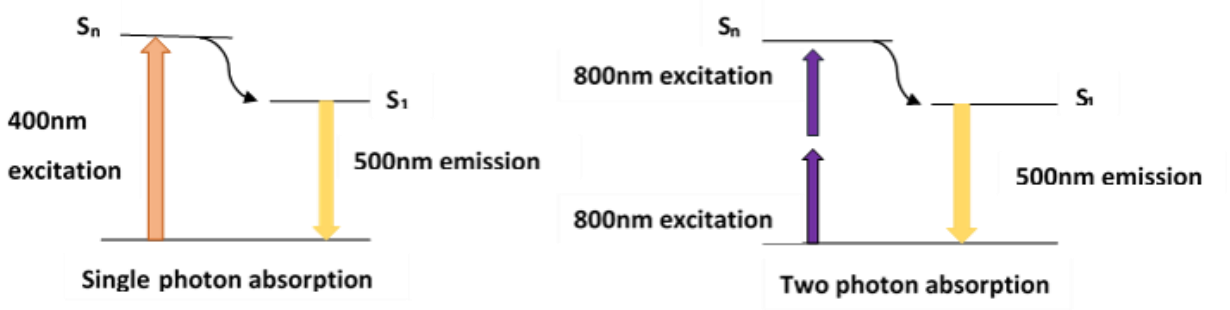


Figure 2.6: Schematic explaining the mechanism of two-photon absorption

2.7 Fluorophores used in two-photon imaging

2.7.1 *Squaraine dyes*

Squaraine dyes are a class of organic NIR fluorophores derived from squaric acid that have undergone a condensation reaction with an electron rich aromatic compound (Figure 2.7). Squaraine dyes show sharp absorbance in the NIR region and are thus attractive for biological applications. The four membered ring system is highly sensitive to nucleophilic attack, owing to its electron deficient nature. The nucleophilic attack of squaraine in solution greatly impedes its photostability [44]. Additionally, squaraine dyes are prone to self-aggregation which induces self-quenching. These problems have been overcome by surrounding the squaraine in a molecular casing called a rotaxane. This molecular architecture is designed to protect the squaraine dye from nucleophilic attack and self-aggregation, thus improving its photo and chemical stability (Figure 2.7). Additionally, their encapsulation prohibits the dye from partaking in cellular pathways, a key requirement for a dye that is to be used in *in vivo* imaging [7]. The typical absorption and emission maxima of squaraine are approximately 630 nm and

650 nm, respectively. Squaraine becomes excited through the absorption of two photons, thus allowing squaraine dyes to be used in TPM [45]. Squaraines exhibit strong optical properties for TPM compared with other commonly used dyes such as Alexa FluorTM. Podgorski and co-workers compared a squaraine–rotaxane derivative, SeTau-647 to Alexa FluorTM 488. SeTau-647 emitted 110 times the number of photons compared with Alexa FluorTM 488. Additionally, SeTau-647 displayed a greater photobleaching time constant and proved to be less reactive in the intracellular environment than Alexa FluorTM 488 [7]. Johnson *et al*. demonstrated that squaraine dyes were 20 times more photostable and have a five times greater half-life than cyanine dyes [46]; hence demonstrating the ideal nature of squaraine dyes as fluorophores in TPM and imaging technologies.

2.7.2 *Triphenylamines*

Triphenylamine has been demonstrated to be effective as a TPA fluorophore core molecule owing to its strong electron donor character, and its ability to be branched (Figure 2.7). Branching increases the cross section values of the fluorophore, thereby increasing its TPA capabilities and results in improved fluorescence. This ability has resulted in many researchers producing fluorophores that comprise triphenylamine [47]. Feng and co-workers developed a novel triphenylamine-based membrane-permeable TPA fluorescent probe: 4-((e)-2-(benzo[d]thiazol-2-yl)- vinyl)-N-(4-((e)-2-(benzo[d]thiazol-2-yl)vinyl)phenyl)-N-phenyla-niline (BTVPA). This novel fluorophore possessed a cross-section of 1700 GM, a quantum yield of 0.88, a Stokes shift of 80 nm and a molecular extinction coefficient (e) of 128 000 (Figure 2.7). Compared with fluorescein, rhodamine and coumarin, the TPA cross sections of BTVPA were 45-, 8- and 90 times greater, respectively [47]. Clearly, the BTVPA dye is highly efficient and ideal as a fluorescent dye.

2.7.3 *BODIPY derivatives*

The field of *in vivo* imaging is advancing at a rapid rate. Simultaneously, the demands on the imaging capabilities are constantly increasing. The imaging of specific organelles is now a reality; however, this advanced imaging technique requires novel TPA fluorophores. Zhang and co-workers developed such fluorophores through the

creation of BODIPY derivatives. Their aim was to design a NIR TPA fluorophore for mitochondrial imaging. The extension of p conjugations and creating moderate intramolecular charge transfer are common methods for extending dyes into the NIR region [48]. Zhang *et al*. combined these two methods through the addition of a carbazole group to the BODIPY core. In addition, this optimized the optical properties of the dye and enabled further conjugation procedures. Furthermore, the addition of chlorides onto the second and sixth positions of the BODIPY core further extended the excitation and emission wavelengths into the NIR region [48]. Importantly, the advantageous properties of the BODIPY parent dye were maintained in the novel fluorophores. The fluorophores were demonstrated to have high quantum yields, good photostabilities, high molar extinction coefficients and displayed cross section values ranging from 250 to 1200 GM depending on the derivative [48]. These fluorophores were unique in that they combined the theory of two-photon excitation and long wavelength emissions. Thus, these dyes are considerably more effective for *in vivo* imaging than a dye that singularly exploits the concept of two-photon excitation or NIR wavelengths independently. One of the derivatives was compared to Cy5 to evaluate its effectiveness as a NIR TPA fluorophore. The results demonstrated that the novel fluorophore exhibited greater photostability, a longer life-time, higher emission rates and a lower level of photobleaching than Cy5, thus showing its effectiveness as a novel fluorophore. This fluorophore was successfully utilized for mitochondrial imaging [48].

2.8 Fluorophores based on rotor mechanism

In a later work by Zhang *et al*., a different TPA NIR dye used for mitochondrial imaging was produced (Figure 2.7). This probe was based on a rotor mechanism where fluorescence was quenched in low viscosity media and in highly viscous media fluorescence was intensified [49]. A fluorophore that contains a rotatable conjugated moiety is referred to as a rotor. The presence of intramolecular rotational relaxation and free rotation inhibits fluorescence; however, if this intramolecular rotational relaxation is constrained fluorescence is allowed. In a non-viscous environment, there is no constraint on the intramolecular rotation resulting in fluorescent quenching, whereas the opposite is true in a viscous environment. Therefore, in terms of mitochondrial imaging, the high viscosity of the double membrane bound organelle

induces significant fluorescence, yet only upon entering the mitochondria [49]. This turn-on ability increases the target:background ratio and offers greater specificity.

Using this mechanism, Zhang *et al*. developed a NIR mitochondrial probe designed for two-photon microscopy. The fluorophore termed HJVPI was formed through the modification of the traditional rotor 9-(dicyanovinyl)julolidine (DCVJ). DCVJ was modified through the replacement of the two nitrile groups with cationic pyridnium, which allowed mitochondrial accumulation owing its specific membrane potential (Figure 2.7) [49]. Furthermore, hydrophilicity was enabled through the presence of a hydroxyl group. HJVPI was successfully shown to exhibit mitochondrial specific fluorescence and enabled effective imaging using TPM in cell studies. Moreover, HJVPI was demonstrated to possess a large Stokes shift, good membrane permeability, high photostability, low toxicity and the ability to be effective in the presence of other organelle stains, thus allowing the imaging of multiple organelles simultaneously using different colours [49]. Indeed, this technique still requires further testing to evaluate whether the same imaging capabilities seen in *in vitro* studies will translate to *in vivo* studies.

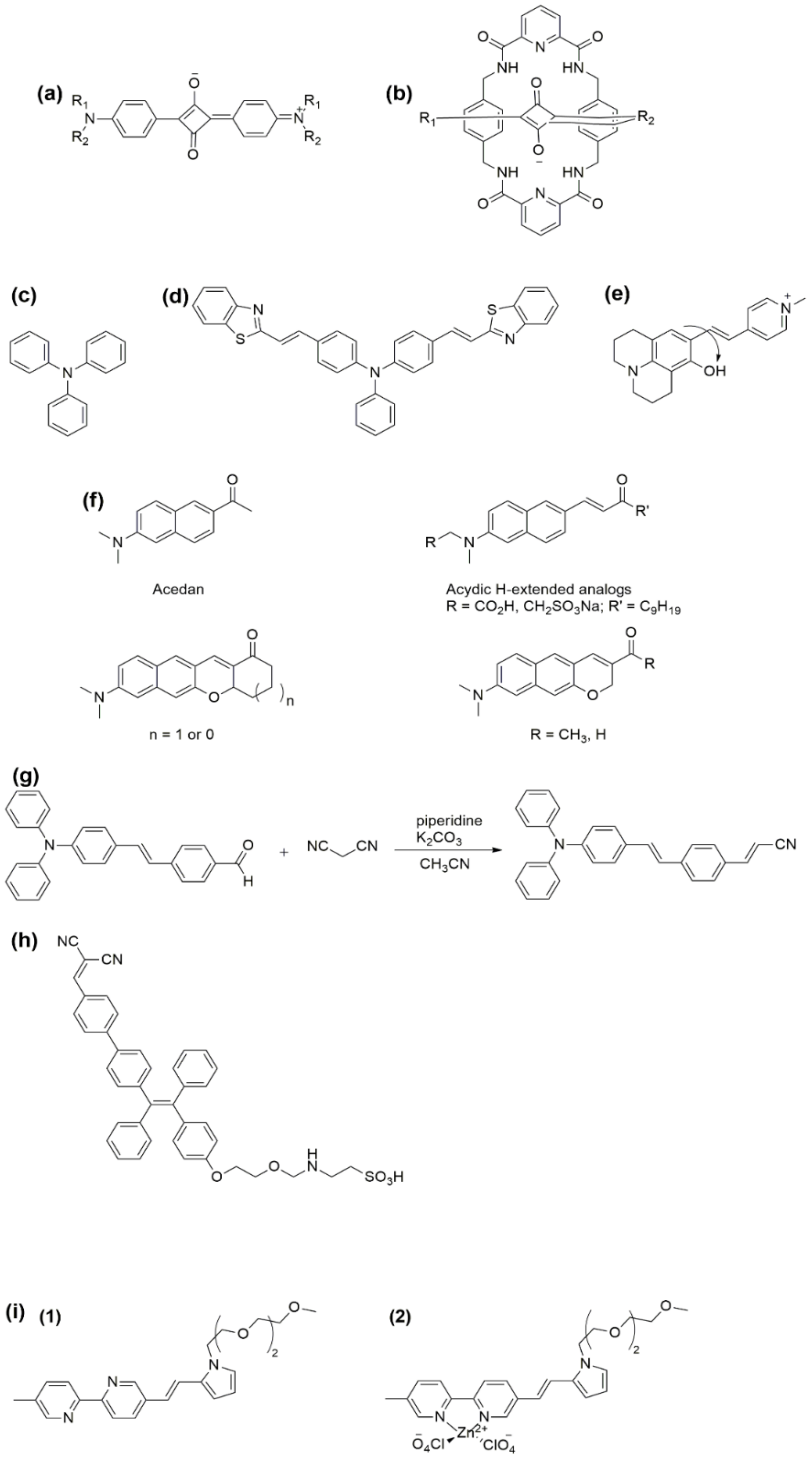


Figure 2.7: Fluorophores used in two-photon microscopy. (**a**) Chemical structure of squaraine. (**b**) Squaraine enclosed in a rotaxane molecule. (**c**) Structure of triphenylamine. (**d**) Structure of BTVPA [47]. (**e**) Structure and rotational ability of HJVPI [49]. (**f**) Structure of acedan and acedan derivatives [51]. (**g**) Synthetic route for the triphenylamine derivative (E)-3-(4-(4-(diphenylamino)styryl)-phenyl)acrylonitrile [56]. (**h**) Chemical structure of AIE fluorophore CTPE-Tau. (**i**) Chemical structure of GMP in the absence of zinc (1) and in the presence of zinc (2) [59].

2.8.1 *Acedan*

Acedan, 6-acetyl-2-(dimethylamino)naphthalene, is a commercially available donor–acceptor dipolar dye. Acedan has a sufficient TPA cross section and is easily modified for various uses [50]. The electron donating group of acedan is a 6-dimethylamino and has a 2-acetyl electron-accepting group (Figure 2.7). Intramolecular charge transfer (ICT) occurs through p-electron delocalization. However, the dye has short absorption and emission wavelengths (in the region of 364 nm and 484 nm, respectively, in ethanol) and emits weakly in aqueous solutions [50]. These short absorption and emission wavelengths result in substantial autofluorescence when applied for *in vivo* imaging. This in combination with low aqueous solubility renders them inappropriate for live cell imaging purposes [51,52]. The research of Kim *et al*. aimed to extend the absorption and emission wavelengths of acedan into the NIR range. Their modification of acedan involved the addition of a carbon–carbon double bond between the naphthalene ring and acetyl group, which locked the double bond into the trans conformation (Figure 2.7). This modification enabled the dye to be excited at 900 nm, which is the optical wavelength for tissue imaging [51]. The new dye produced was environmentally sensitive and fluorescence intensity was dependent on the polarity of the solvent. This sensitivity enabled this dye to be used as a probe. In particular, it was demonstrated as a successful probe for amyloid-β plaques in Alzheimer's disease. The probe was shown to be photochemically stable, biocompatible, soluble, have an adequate TPA cross section and could cross the BBB allowing effective imaging of amyloid-β plaques [51]. Low solubility in aqueous solutions precludes acedan's use in biological systems. Therefore, Singha and co-workers modified acedan in such a way as to improve its fluorescent emission in water. Their rationale when designing the novel acedan derivative was to impede the phenomenon that induces fluorescent quenching in water but not in organic media. It was concluded that H-bonding between the amine nitrogen and water reduces the transition dipole moment and induces a reduction in fluorescent intensity. Through the addition of a hydrophobic N-substituent, the accessibility of water molecules to nitrogen will become obstructed and H-bonding will not occur [52]. Therefore, the researchers modified acedan through the addition of an N-alkyl group. In addition to blocking H-bonding, the internal rotational freedom of the amino group was hindered, which reduced nonradiative decay and enhanced

fluorescence (Figure 2.7). This modification resulted in a fivefold increase in TPA, and a six-fold increase in the fluorescence quantum yield of the dye in water [52].

2.8.2 *Carboranes*

Dicarboclosododecaboranes, or carboranes, are 3D pseudo aromatic compounds consisting of two carbon and ten boron atoms and exist in three alternate geometrical isomers. Carboranes have unique electron properties, in that they can be electro withdrawing and electron donating [53]. Carboranes themselves are not emissive; however, their addition to a fluorescent core molecule greatly enhances the TPA cross-section and the fluorescence quantum yield of the fluorophore to which they are conjugated [54]. Carboranes increase TPA properties through the suppression of nonradiative decay through the inhibition of vibrational relaxation and the internal conversion process (S1-S0), these are the main contributing factors to nonradiative decay [55]. Uebe *et al*. increased the TPA cross section of triphenylamine through carborane substitution. This was achieved by utilizing the principle that when an excited molecule is in an emitting state owing to excitation between a pair of molecular orbitals then, if one delocalizes one of the molecular orbitals over the entire molecule and localizes the other molecular orbital over the nonfluorescent core molecular unit, nonradiative decay will be suppressed owing to the inhibition of vibronic interactions [55]. The addition of a nonfluorescent carborane substituent to triphenylamine through p conjugation limited the distribution of only the highest occupied molecular orbital (HOMO) in the nonfluorescent parent p-conjugated core, yet this partial delocalization had no effect on the lowest unoccupied molecular orbital (LUMO). This phenomenon prohibited the internal conversion process [55]. This intuitive method substantially increased the quantum yield and TPA cross section of triphenylamine, thus resulting in fluorescent enhancement [55].

2.9 Chromophores exhibiting aggregation-induced emission

Organic chromophores have several properties that make them ideal in bioimaging applications. However, there is a common problem existing with these molecules in that they experience aggregation induced fluorescent quenching. This quenching negatively impacts their application in bioimaging [55–58]. Therefore, the development

of an organic chromophore that exhibits aggregation-induced emission (AIE) would be highly advantageous. Through the manipulation of preparation procedures Kong and co-workers as well as Wang and co-workers independently formulated an organic chromophore exhibiting AIE. This AIE state is the result of the restriction of intramolecular rotations that are induced through the steric interactions in the aggregated state; this then inhibits nonradiative decay and allows emission. The greater the extent of aggregation the greater the quantum yield and TPA cross section of the organic chromophore [56,57]. Using this rationale, Kong *et al*. formulated a triphenylamine derivative: (E)-3-(4-(4-(diphenylamino)styryl)-phenyl)acrylonitrile. The tri-phenylamine group attached to the C¼C double bond of benzene was used as the electron donor, whereas the cyano group was used as the electron acceptor (Figure 2.7) [56]. It has been shown that an additive substance in the solution such as metal ions greatly contributes to the optical properties of AIE chromophores. The strong binding between the metal ions and chromophore results in an increase in the degree of aggregation. Here, the researchers utilized cadmium and copper ions. The incorporation of these metal ions changed the growth direction, electronic structure, the ICT process, the aggregation degree and induced an energy transfer to occur between the components [56]. Collectively, this greatly altered the linear and nonlinear optical properties and greatly enhanced its ability to act as a live cell imaging dye. Moreover, the derivative was shown to have a high quantum yield, an enhanced lifetime, high photostability, no photobleaching and have a high TPA cross section. This novel fluorophore offers a unique method for *in vivo* imaging applications owing to its AIE and ideal optical properties [56].

More recently, Singh and colleagues aimed to produce a pyrene– fluorescein AIE fluorophore. The use of a hydrophobic and hydrophilic molecule was designed to enable aggregation in an aqueous environment. A conjugate of pyrene and fluorescein produced a fluorophore with a high quantum yield, cell permeability and no toxicity. To prove this fluorophore displayed AIE, they measured fluorescent intensity in samples with increasing water concentrations. Upon the increase in water concentration, a bathochromic shift occurred with an enhancement of emission intensity. This was thought to occur owing to J-type aggregation in response to the hydrophobic effect, which induces the opening of the lactam ring of fluorescein. This aggregation restricts molecular rotation which leads to fluorescence emission enhancement. Furthermore,

the fluorescence intensity was shown to increase over time [58]. These optical and physical properties are highly advantageous for live cell imaging (Figure 2.8).

The work of Wang and co-workers proposed the design of a ROS probe utilizing the theory of AIE. They conjugated the ROS scavenger, taurine (Tau) onto the AIE fluorophore CTPE through a carbamate bond (Figure 2.7). This ROS probe exhibited optimal optical properties, such as high photostability, large Stokes shift (thus avoiding self-quenching) and excitation and emission bands in the NIR range. The addition of Tau improved the water solubility and cellular uptake ability of the conjugate [57]. Owing to the hydrophobic nature of the conjugate that Tau induced, no aggregation occurred in the aqueous intercellular environment and therefore no fluorescence emission. Upon entering the cell, esterase enzymes cleaved the carbamate bond, thus separating the fluorophore from Tau. The fluorophore then became hydrophobic and thus induced aggregation of the fluorophore molecules in the polar cellular environment thereby inducing fluorescence. The Tau moiety was then free to perform ROS scavenging and acted as an antioxidant. Hence, fluorescence emission served as a fluorescent reporter of biochemical events, in addition to allowing intracellular cell imaging [57].

2.10 Three-photon absorption fluorescent dyes

A recent extension of the TPA theory is the development of three-photon absorption (3PA) fluorescent dyes. 3PA follows the same behaviour as TPA, yet three photons are absorbed instead of two. These 3PA fluorophores utilize nonlinear optics and enable deep tissue penetration and strong spatial confinement, thus enabling images of high contract and resolution [59]. Phillips and co-workers designed a donor–acceptor (D-p-A)-based 3PA fluorophore comprising a bipyridine acceptor attached to a pyrole donor through a vinyl linker molecule. Furthermore, the addition of an oxyethylene moiety afforded water solubility and biocompatibility [59]. The 3PA fluorophore was designed as a probe for intracellular zinc (Zn2+) detection. Zn2+ is the second most abundant element in the body and high concentrations of free Zn2+ have been linked to several pathological states such as Parkinson’s disease, epilepsy and Alzheimer’s disease [60]. Therefore, a probe that could detect and determine the concentration of free Zn2+ is of clinical interest. The probe was based on the theory that the binding of Zn2+ to

the bipyridine group allows improvements in the nonlinear optical properties through the extension of charge separation, which rigidifies the chromophore [59]. The resultant chromophore was termed GMP (Figure 2.7). Before Zn2+ binding, the probe had absorption and emission spectra of 370 nm and 530 nm, respectively. Upon GMP binding to Zn2+ the absorption spectra shifted to 400 nm and the emission spectra shifted to 600 nm. This shift in bands in response to Zn2+ binding enabled the ratiometric determination of Zn2+ concentration [59]. GMP exhibited a 3PA cross-section two orders in magnitude greater than previously demonstrated by other 3PA fluorophores. Moreover, GMP displayed a high quantum yield, good cell permeability and no cytotoxicity. The Zn2+ detection capabilities of GMP were demonstrated on cell lines and on rat brain hippocampal slices. The successful detection and imaging of Zn2+ ions intracellularly at a high resolution and deep tissue penetration offers novel abilities for multitudes of health applications [59].

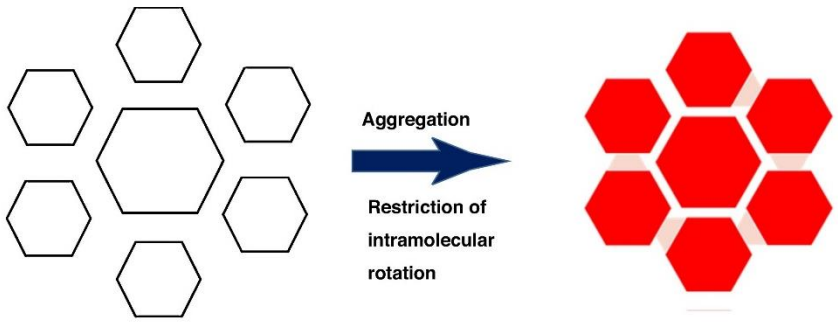


Figure 2.8: Schematic illustrating the effects of aggregation-induced emission.

2.11 Single-molecule imaging

In vivo imaging is moving toward visualization of cellular components rather than the cell in its entirety. Single molecule imaging can provide information on a variety of biological processes and offers extensive possibilities for diagnostics, treating disease states and for studying cellular events [61]. Several fluorescent probes have been designed for single molecule imaging utilizing fluorescence as the means of visualization. Here, some of these fluorescent probes will be discussed in greater detail.

2.11.1 *Cell membrane probes*

Previously, membrane structures were imaged using electron microscopy. However, this technique has limited applications, because live cells cannot be subjected to electron microscopy. Membranes are highly dynamic in nature and consistently undergo remodelling. Thus, dynamic membrane systems cannot be visualized using traditional electron microscopy [62,63]. To overcome this obstacle, fluorescent probes have been produced to allow live cell and real-time imaging of membranous structures. Cell membrane specific optical probes are required to possess a hydrophilic head group and a hydrophobic tail. An amphiphilic design enables the probe to anchor into the cell membrane and still retain its water solubility. The membrane potential in living cells complicates probe design because the membrane potential should not disturb the functionality of the probe. By combining the two nonlinear optical processes of TPA and second harmonic generation, Barsu and co-workers created an optical push–pull probe consisting of pyridine dicarboxamide electron acceptor, a fluorenethynyl p-conjugated bridge and a dialkylamino electron donor (Figure 2.9) [64]. To further assist in membrane docking the researchers added two carbohydrate groups onto the probe, thus aiming to mimic a glycoprotein. A delicate balance between the hydrophilicity and hydrophobicity was required so that the probe did not permeate into the cell nor was it retained in the extracellular matrix but, instead, it was docked into the membrane [64]. Shim *et al*. furthered the concept of membrane imaging utilizing the alternate imaging concept of super-resolution imaging. This research involved the creation of photoswitchable dyes. Several photoswitchable dyes were created using the traditional fluorescent dyes: cyanine, rosamine (a rhodamine derivative) and BODIPY. In this study, these dyes were used to image membranous structures including mitochondria, the endoplasmic reticulum and the plasma membrane. All dyes were induced to perform photoswitching, yet the way photoswitching occurred differed between the dyes [65]. Using this mechanism of super-resolution imaging, high-resolution dynamic images of membranous structures of a cell were achieved. Limitations to this technique do exist, in particular motion blur. The probe was subject to diffusion once retained in the membrane. Additionally, certain organelles such as mitochondria experience movement. These movements resulted in motion blur which reduced the resolution of the images recorded. By reducing the timeframe this blur can be reduced. However, more work is required to completely negate the effects of motion blur [65].

2.11.2 *Lysosomal imaging*

Imaging of intracellular compartments or organelles is the latest focus of *in vivo* imaging. Intracellular molecular events can be monitored in real time using highly specific fluorescent probes. The development of a lysosomal and endosomal specific probe by Grossi and co-workers allowed the real-time imaging of cellular uptake, trafficking and reflux events. BF2-chelated azadipyrro-methane was functionalized with an ortho-nitro phenolic group (Figure 2.9). The BF2-chelated azadipyrromethane core was used owing to its straightforward synthesis, ease of structural manipulation and excellent photophysical properties [66]. The rationale that allowed lysosome and endosome specificity was a pH responsive turn-on probe. The added phenolic group imparted pH responsiveness. The lower pH present in the lysosome and endosome enabled their differentiation from the remaining intracellular space (Figure 2.10). At a neutral pH, the ionized phenolic group dominates owing to the non-emissive intramolecular charge transfer excited state imparted by the electro withdrawing ortho-nitro group. This induced fluorescent quenching. In an acidic environment, protonation occurred giving rise to the neutral phenolic species, thus allowing fluorescent enhancement. The more acidic the environment the greater the fluorescent enhancement. This difference between fluorescent intensity allowed the distinction between endosome and lysosome [66]. The probe displayed decent photophysical properties. The absorption and emission spectra were 696 nm and 727 nm, respectively, thus enabling NIR emission. A high aqueous quantum yield of 0.3–0.4 was observed. Furthermore, the probe was demonstrated to have a good photostability, and photobleaching occurred after 2 h of emission [66]. To validate the effectiveness of the probe, cell culture and animal *in vivo* studies were performed. These studies indicated the ability of the probe to experience cellular uptake through endocytosis as well as the probe's site-specific turn-on feature in the acidic microenvironment of the endosome and lysosome [66].

Wycisk and co-workers developed a water-soluble pH-sensitive dye to allow precise cellular uptake studies. Currently available dyes such as indocyanine green function as 'always on' dyes, thereby generating substantial background signal. The development of environmentally sensitive dyes, whereby an environmental cue amplifies the fluorescent signal, is ideal for single molecule imaging. Wycisk *et al*. developed a new

fluorophore through the addition of three sulfonate groups and a carboxy group to a cyanine precursor. The sulfonate groups allowed water solubility and a reduction in dye aggregation and the carboxy group allowed the fluorophore to be conjugated to carriers or target molecules. The new fluorophores were then conjugated onto the iron binding plasma protein transferrin (tf) and the monoclonal IgG antibody ctx. These ligands enter the cell through receptor mediated endocytosis; tf is recycled and transported back to the ECM whereas ctx binds to the epidermal growth factor (EGF) receptor, which after time will end up in the lysosome. The ctx–dye conjugate accumulates in the lysosome and there is an increase in fluorescent signal owing to the acidic pH, whereas no fluorescent enhancement is expected for the tf–dye conjugate because it is not destined for an acidic cellular compartment. These novel water-soluble, pH-sensitive cyanine fluorophores allowed precise visualization and understanding of cellular uptake processors and demonstrated the ability to fine tune the pH dependence of dyes [67].

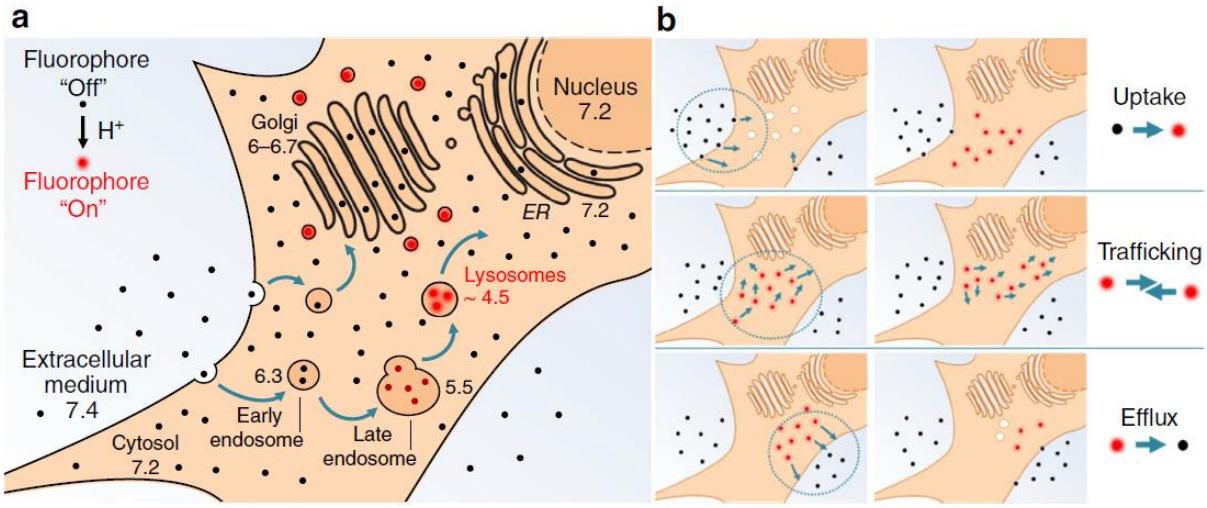


Figure 2.9: Cellular uptake responsive near infrared (NIR) fluorophore. (**a**) Simplified endocytosis of a responsive NIR fluorophore. Numbers represent the approximate pH of the corresponding organelles. (**b**) Three observable stages of the path of the pH responsive fluorophore in the cellular environment: uptake, trafficking and efflux [66] (reproduced with permission from Nature Publishing Group under Creative Commons Licence).

2.12 Super-resolution microscopy

The study of biological processes is continually enhanced by improvements in microscopy. Biological systems are highly dynamic and therefore static images are

limited to the amount of information they can provide [1]. Imaging technologies that afford the possibility to provide high-resolution dynamic images are of great interest in the scientific community. The development of super-resolution microscopy greatly fulfils this need [62,68]. Optical imaging instruments are unable to distinguish between two objects where the distance between them is less than half the wavelength of the incident light. This is known as the diffraction limit [1]. As the aperture of a lens decreases diffraction increases, which limits the degree to which two objects in close proximity can be resolved. The diffraction limit applies to light which must travel a distance exceedingly greater than its wavelength; thus, by placing the light source in a close proximity to the object of interest, can improve resolution by overcoming the diffraction limit [1,62,68–71]. However, for biological samples this close proximity cannot be achieved. The diffraction limit impedes the imaging of nanostructures and for the imaging of nanostructures to occur the diffraction limit needs to be overcome [62]. Super-resolution microscopy enables imaging at a higher resolution than the diffraction limit.

Imaging molecular species requires microscopy techniques that allow images of enhanced resolution. Super-resolution imaging aims to focus the emitting fluorescence by turning the fluorescence signal of individual fluorophores on and off [70]. Through the excitation of a single subset of a single molecule, while the remaining subsets are dark, and repeating this procedure, a mathematical estimation can be drawn about the structure of the molecule producing a super-resolution image and can determine the location of the molecule with high accuracy [1,69]. The turn on/off feature is an important requirement for super-resolution imaging because it means the images do not overlap, which would result in blur, and form individual distinct images. The localization of single emitters is a requirement of super-resolution microscopy. A single emitter must be adequately separate from neighbouring emitters within a diffraction-limited area to allow successful localization of emitters [71]. Furthermore, the occurrence of a released photoburst, where a single emitter releases multiple photons simultaneously, allows a clearer distinction between on and off fluorescent molecules. Additionally, the photoburst allows the localization of the fluorescent molecule as well as the surrounding molecules. This clear distinction between emitters is what enables the diffraction limit to be overcome and for super-resolution images [69,71]. When excited at a certain wavelength, the fluorescent dyes used for super-resolution

microscopy will enter a long-lived dark state. Once in this state, the dye cannot be excited to the fluorescent state, and thus cannot fluoresce upon irradiation. This phenomenon is termed reversible saturable optical linear fluorescence transitions (RESOLFT). This allows structures that are spatially close together to be resolved [68,72]. These special fluorophores require a high triplet yield or need to be in the presence of oxygen removing species. Molecular oxygen is responsible for photobleaching through the direct interaction with a fluorophore, or indirectly through the production of radical oxygen species [73]. Hence, fluorophore probes often include an oxygen scavenger to enhance photostability and the fluorescent lifetime of the fluorophore [74]. Additionally, molecular oxygen and radical oxygen species are toxic to biological systems and irreversibly damage fluorophores; therefore, their removal is vital for efficient live cell imaging [73].

Super-resolution microscopy can be conceived through two processes. The first being where fluorescence is emitted non-simultaneously from an excited fluorophore. Stimulated emission depletion (STED) microscopy, RESOLFT theory and saturated structured illumination microscopy (SSIM) all fit into this first category [70]. The second process is where individual subsets of a fluorophore are excited individually [75]. This category includes stochastic optical reconstruction microscopy (STORM), photoactivated localization microscopy (PALM) and fluorescence photo-activation localization microscopy (FPALM). In both events, subdiffraction limit images can be obtained through individual fluorophores monitoring and controlling the state of neighbouring fluorophores, thus allowing individual fluorophores to be resolved [76,77].

2.12.1 *Fluorophores used in super-resolution microscopy*

Photoswitchable fluorescent compounds are ideal for super-resolution microscopy. These fluorophores can be switched on at one wavelength and then switched off at a second wavelength. This offers a controllable switching mechanism [68]. Single-molecule fluorophores that contain a photochromic and fluorophore unit connected via a linker enable a photoswitchable process. An example for this is cyanine dyes, of which one cyanine dye is a reporter dye and the other an activator dye. Different activator dyes allow different subsets of the reporter dye to be activated. This allows multicolour super-resolution images [71]. Here, photo-switching occurs from the

reversible addition of a thiol group. Photoswitchable dyes can also be realized by adding a quencher onto an established fluorophore. Upon the radiation of a certain wavelength, the quencher detaches from the fluorophore inducing fluorescence [71]. Furthermore, cyanine dyes can be utilized for super-resolution microscopy employing an alternate technique for photoswitching. This technique involves the use of intracellular enzymes to switch the dye between an on and off state. Hydrogenation of cyanine dyes by sodium borohydride converts them into the nonfluorescent form. This process is reversible through a reaction with a superoxide or a hydroxyl radical [71]. A controversial method in super-resolution microscopy is utilization of the triplet state. Every so often the excitation of a fluorophore results in the fluorophore entering the triplet state. In this state, no fluorescence occurs. If oxygen is present in this environment, oxygen quenches the triplet state and the triplet state is short lived and cannot be distinguished. The removal of oxygen from the immediate environment using oxygen scavengers allows the triplet state to last milliseconds [78]. Once returning from the triplet state the fluorophore can once again emit fluorescence. Chemicals such as b-mercaptoethanol and Trolox (a vitamin E analogue) can quench the triplet state and induce triplet-state blinking. Through the combination of oxygen scavengers and b-mercaptoethanol or Trolox the observation time of the triplet state can be extended [74]. Entering the triplet state induces fluorescence blinking which results in fluorescence fluctuations and can promote various chemical reactions. In many cases this triplet state is avoided through the incorporation of molecular oxygen or radical oxygen species that have undesirable effects as previously mentioned. Conversely, the triplet state creates a definitive on/off state thus fulfilling the requirements for super-resolution microscopy. Therefore, several research projects have extended the triplet state to assist in photoswitching and have thus chosen to take advantage of the triplet state instead of eliminating it [79].

An obstacle in the development of new fluorophores for intra-cellular labelling and imaging is retaining cell permeability and allowing rapid labelling kinetics. Several novel fluorophores are ideal for extracellular imaging, yet cannot be applied to intracellular imaging owing to their highly polar structures that prohibit cell membrane penetration. For this reason, most intracellular labelling dyes have been based on coumarin and rhodamine scaffolds. However, these dyes exhibit poor brightness and photostability. These poor optical properties are thought to arise from a twisted internal charge

transfer (TICT) which induces rapid non-radiative decay and formation of a highly reactive chemical species owing to no photon being released when the excited state of TICT relaxes (Figure 2.11) [80,81]. Grimm and co-workers envisioned to mitigate the effects of TICT through replacing the N,N-dimethyl group of tetramethylrhodamine (TRM) with the four membered nitrogen containing azetidine ring. The addition of two carbon atoms increased the quantum yield and lifetime of the dye, while retaining its cell permeability. This novel fluorophore was termed JF549 (Figure 2.11). The incorporation of a ligand resulted in the ability for single molecule labelling and intracellular imaging [80]. Furthermore, the reducing intracellular environment allowed reversible photoswitching of the dye and thus it was an effective dye for dSTORM and enables super-resolution imaging. The intracellular labelling and super-resolution imaging abilities of JF549 were successfully demonstrated. Furthermore, the researchers extended this rationale to other dyes such as coumarin, naphthalimide, oxazine and rhodol, creating a plethora of super-resolution cell permeable fluorophores [80].

The work of Liu and co-workers was based on the research performed by Grimm *et al*. and further extended the concept of prohibiting TICT through the addition of a four membered azetidine ring. However, Liu and co-workers demonstrated that a three membered aziridine ring was more effective in suppressing TICT than a four membered azetidine ring. The three membered ring was demonstrated to improve brightness, photostability and result in an enlarged Stokes shift [81]. This concept was demonstrated on a naphthalimide derivative and was based on the theory that the TICT state is energetically unfavourable owing to the steric repulsion caused by the presence of amino arms that resulted in a large energy barrier between the excited and TICT state (Figure 2.11) [81]. Indeed, this energetically unfavourable transition enabled TICT resistance. The naphthalimide aziridine derivative possessed good chemical stability and a large Stokes shift, thus allowing multicolour super-resolution imaging. However, this fluorophore exhibited a low molar extinction coefficient and a hypochromic shift [81]. Thus, further modifications are required to allow *in vivo* imaging, yet this novel dye offers significant improvements to the real-life applications of super-resolution microscopy. The addition of a photolabile group onto a fluorophore allows the formation of a caged fluorophore.

The photolabile group can be removed through short wavelength illumination; thus, fluorescence emission is stimulated through a photochemical reaction. This enables precise and controlled turn on emission of individual molecules, thus easing the photoswitching procedure [82]. Caged fluorophores also offer higher photon counts allowing better localization precision. Grimm *et al*. continued their research into novel fluorophores for super-resolution microscopy. They designed a caged Q-rhodamine fluorophore encompassing a nitroveratryl oxycarbonyl (NVOC) caging group. To formulate the fluorophore a reduced leuko-rhodamine was used as a synthetic intermediate. Subsequently, the xanthene oxygen was substituted for a (CH3)2Si moiety, forming Si-Q-rhodamine (Figure 2.11) [83]. The absorption/emission spectra were 637 nm and 654 nm, respectively, with a molar extinction coefficient of 7.7 _ 104 M_1cm_1 and a quantum yield of 0.38. To test its ability to act as a fluorophore for super-resolution microscopy, the Si-Q-rhodamine was utilized to image F-actin in COS-7 cells and it was compared to the Alexa 647-phalloidin conjugate. It was further established that the addition of the vitamin E analogue Trolox greatly enhanced the fluorescent properties of the fluorophore. A comparison of the photophysical properties is displayed in Table 2. The unique fluorophore circumvents the need for the use of reducing buffers to induce photoswitching, hence improving the possibility for *in vivo* use. Conversely, improvements in biocompatibility, increased water solubility and labelling strategies are required to propel the technology for the use in live molecular imaging [83].

Table 2.2: Comparison between novel Si-Q-rhodamine fluorophores and an Alexa647-phalloidin conjugate [85]

Fluorophore	**Photon count**	**Localisation precision (nm)**
Alexa647-phalloidin conjugate	5547	5.7
Si-Q-rhodamine	9145	6.2
Si-Q-rhodamine-Trolox	14944	5.3

Super-resolution microscopy offers tremendous advances in the field of molecular imaging and has enabled the visualization of nanoscale molecular species in real time and allows their activities to be observed. The future of *in vivo* imaging, in particular single molecule imaging, will be through super-resolution imaging [84]. However,

several advances are still needed to propel this technique into human *in vivo* imaging. Highly powerful photoswitchable fluorophores that are site-specific as well as the development of specialized equipment are required to allow clinical applications. The field of super-resolution imaging is still in its infancy and it is expect that significant enhancements in the field are still to transpire [1].

2.13 Concluding remarks and future perspectives

Microscopy and imaging techniques are the cornerstones of modern medical discoveries, and without these technologies' numerous scientific knowledge and medical procedures would not be possible. In a short few years, large strides have been made in advancing imaging technologies [3]. Real-time nanoscale imaging is a non-pareil tool for scientific enhancement. Being able to view cellular behavioural events and molecular interactions would be a transformative technique allowing numerous significant scientific contributions [1]. Current technologies are limited in their clinical applications. The majority of the research discussed here was demonstrated in tissue culture studies. Although these *in vitro* studies are fundamentally important, they cannot replace *in vivo* studies. Furthermore, only a few studies have been taken to clinical trials wherein only fluorophore-guided surgeries have utilized novel fluorophores in a clinical setting [17]. Hence, strides in this research field are still required to fully grasp the enormity of potential applications. Novel fluorophores can be applied in numerous settings and possible applications are boundless. Some possible applications could include: a fluorophore being attached onto a drug delivery platform and fluorescent activity could indicate effective drug delivery as well as dosage delivered [1]. Moreover, novel fluorophores could be incorporated into theranostic systems, whereby detection and treatment would be undertaken simultaneously using one platform [85]. Other applications could include: the detection of pathogenic organisms and determining the extent of an infection, as well as the effectiveness of treatment [86,87]. Alternatively, gene editing technologies can be visualized and monitored using fluorescent molecules, thus improving outcomes [88]. Furthermore, uncertainty remains about signalling intermediates in various molecular signalling cascades. Dissecting this information through the use of single molecule imaging utilizing novel fluorophores would yield beneficial information in understanding cellular behaviour and several diseased states, which are required for tackling diseases at the

molecular level [2]. Indeed, scientific understanding and medical advances could be greatly enhanced through the application of detailed molecular imaging. Moreover, current practices utilizing these novel fluorophores can improve established practices exponentially, thus underscoring the importance of the development of rationally designed novel fluorophores [84].

A new field creating smart fluorescent probes has emerged since the advent of advanced fluorophores. Bioorthogonal probes allow *in vivo* labelling and targeted delivery of imaging agents as well as drugs. Furthermore, the issue of excess probe present is circumvented through their use because only probe at the targeted region is visible, thus improving target:background ratios and specificity. Numerous smart bioorthogonal probes have been designed to detect various *in vivo* states. Much research has been performed on this topic, and the reader is referred to additional reviews for more detail [89,90]. Additionally, significant advances have been made in live cell imaging through the application of quantum dots. Quantum dots offer many advantages over organic fluorophores such an increased circulation time and strong fluorescent activity; yet several disadvantages also exist such as toxicity issues. Advanced organic fluorophores were the focus of this review and therefore quantum dots have not been discussed. Reviews are available on quantum dots and are recommended reading [91,92]. Future research should aim to design fluorophores that incorporate numerous scientific principles such as NIR absorption and emission, having photoswitching capabilities allowing super-resolution microscopy and utilizing FRET to enhance the photo-physical properties. An ideal fluorophore should incorporate all the aforementioned techniques. Furthermore, the aim of future research should be applying these novel fluorophores to clinical applications and envisioning novel uses for these fluorophores. Current research needs to be propelled into a clinical setting through appropriate clinical trials, thereby making this new technology accessible to the health sector.

2.14 References

1. Yang Z, Sharma A, Qi J, Peng X, Lee DY, Hu R, et al. Super-resolution fluorescent materials: an insight into design and bioimaging applications. Chem Soc Rev. 2016;9:413–20.
2. Geertsema HJ, Schulte AC, Spenkelink LM, McGrath WJ, Morrone SR, Sohn J, et al. Single-molecule imaging at high fluorophore concentrations by local activation of dye. Biophys J. 2015;108(4):949–56.
3. Swedlow JR. Innovation in biological microscopy: Current status and future directions. BioEssays. 2012;34(5):333–40.
4. Zhao J, Jin G, Weng G, Li J, Zhu J, Zhao J. Recent advances in activatable fluorescence imaging probes for tumor imaging. Drug Discov. Today. 2017;04(006):1359–6446.
5. Specht EA, Braselmann E, Palmer AE. A Critical and Comparative Review of Fluorescent Tools for Live-Cell Imaging. Annu Rev Physiol. 2017;79:93–117.
6. Boustany NN, Boppart SA, Backman V. Microscopic imaging and spectroscopy with scattered light. Annu Rev Biomed Eng. 2010;12(732):285–314.
7. Podgorski K, Terpetschnig E, Klochko OP, Obukhova OM, Haas K. Ultra-Bright and -Stable Red and Near-Infrared Squaraine Fluorophores for In Vivo Two-Photon Imaging. PLoS One. 2012;7(12):1–7.
8. Hong G, Zou Y, Antaris AL, Diao S, Wu D, Cheng K, et al. Ultrafast fluorescence imaging in vivo with conjugated polymer fluorophores in the second near-infrared window. Nat Commun. 2014;5:4206.
9. Hong G, Antaris AL, Dai H. Near-infrared fluorophores for biomedical imaging. Nat Biomed Eng. 2017;1:1–22.
10. Choi HS, Nasr K, Alyabyev S, Feith D, Lee JH, Ashitate Y, et al. Synthesis and In Vivo Fate of Zwitterionic Near-Infrared Fluorophores. Angew Chem Int Ed Engl. 2011;50(28):6258–63.
11. Henary M, Paranjpe S, Owens EA. Synthesis and applications of benzothiazole containing cyanine dyes. Heterocycl Commun. 2013;19(1):1–11.
12. Fei X, Gu Y. Progress in modifications and applications of fluorescent dye probe. Prog Nat Sci. 2009;19(1):1–7.
13. Mojzych M, Henary M. Synthesis of Cyanine Dyes. In: Strekowski L, ed 1. Heterocyclic Polymethine Dyes: Synthesis, Properties and Applications. Berlin, Heidelberg: Springer; 2008;1–9.
14. Shindy HA. Basics, Mechanisms and Properties in the Chemistry of Cyanine Dyes: A Review Paper. Mini Rev Org Chem. 2012;9(4):352–60.
15. Podrugina TA, Temnov VV, Doroshenko IA, Kuzmin VA, Nekipelova CTD, Proskurnina

MV. Synthesis of advanced fluorescent probes — water soluble symmetrical tricarbocyanines with phosphonate groups. Russ Chem Bull Int Ed. 2016;65(11):2722–3.

16. Choi HS, Gibbs SL, Lee JH, Kim SH, Liu F, Hyun H, et al. Optical Imaging. Nat Biotechnol. 2013;31(2):1–16.
17. Hyun H, Henary M, Gao T, Narayana L, Owens EA, Lee JH, et al. 700-nm Zwitterionic Near-Infrared Fluorophores for Dual-Channel Image-Guided Surgery. Mol Imaging Biol. 2016;18(1):52–61.
18. Sapsford KE, Berti L, Medintz IL. Materials for fluorescence resonance energy transfer analysis: Beyond traditional donor-acceptor combinations. Angew Chemie - Int Ed. 2006;45(28):4562–88.
19. Wu D, Cheung S, Daly R, Burke H, Scanlan EM, O'Shea DF. Synthesis and Glycoconjugation of an Azido-BF2-Azadipyrromethene Near-Infrared Fluorochrome. European J Org Chem. 2014;2014(31):6841–5.
20. Liu T, Huo F, Yin C, Li J, Chao J, Zhang Y. Dyes and Pigments A triphenylamine as a fluorophore and maleimide as a bonding group selective turn-on fluorescent imaging probe for thiols. Dye Pigment. 2016;128:209–14.
21. Kwon H, Kim H, Lee K, Kim H. Coumarin-malonitrile conjugate as a fluorescence turn-on probe for biothiols and its cellular expression. Chem Commun. 2011;47(6):1773–5.
22. Zhang C, Song X, Carroll SL, Jiang X, Chen J, Bajic A, et al. Quantitative real-time imaging of glutathione. Nat Commun. 2017;1–12.
23. Fu H, Cui M, Zhao L, Tu P, Zhou K, Dai J, et al. Highly Sensitive Near-Infrared Fluorophores for in Vivo Detection of Amyloid-β Plaques in Alzheimer's Disease. J Med Chem. 2015;58(17):6972–83.
24. Radi R. Peroxynitrite, a stealthy biological oxidant. J Biol Chem. 2013;288(37):26464–72.
25. Pacher P, Beckman JS, Liaudet L. Nitric oxide and peroxynitrite in health and disease. Physiol Rev. 2007;87(1):315–424.
26. Peng T, Chen X, Gao L, Zhang T, Wang W, Shen J, et al. A rationally designed rhodamine-based fluorescent probe for molecular imaging of peroxynitrite in live cells and tissues. Chem Sci. 2016;7(8):5407–13.
27. Ding S, Cargill AA, Das SR, Medintz IL, Claussen JC. Biosensing with förster resonance energy transfer coupling between fluorophores and nanocarbon allotropes. Sensors. 2015;15(6):14766–87.
28. Sasaki S, Drummen GPC, Konishi G. Recent advances in twisted intramolecular charge transfer (TICT) fluorescence and related phenomena in materials chemistry. J Mater Chem C. 2016;4(14):2731–43.

29. Sekar RB, Periasamy A. Fluorescence resonance energy transfer (FRET) microscopy imaging of live cell protein localizations. J Cell Biol. 2003;160(5):629–33.
30. Guermazi R, Clavier G, Hedhli A, Audebert P. Functionalization of s-tetrazine: Preparation of new compounds with high synthetic potential. J Tunis Chem Soc. 2016;18:8–13.
31. Quinton C, Alain-Rizzo V, Dumas-Verdes C, Miomandre F, Audebert P. Tetrazine-triphenylamine dyads: Influence of the nature of the linker on their properties. Electrochim Acta. 2013;110:693–701.
32. Liu DS, Tangpeerachaikul A, Selvaraj R, Fox JM. Diels-Alder Cycloaddition for Fluorophore Targeting to Specific Proteins inside Living Cells. J Am Chem Soc. 2012;134(2):792–5.
33. Wieczorek A, Buckup T, Wombacher R. Rigid tetrazine fluorophore conjugates with fluorogenic properties in the inverse electron demand Diels-Alder reaction. Org Biomol Chem. 2014;12(24):4177–85.
34. Qing Z, Audebert P, Clavier G, Méallet-Renault R, Miomandre F, Tang J. Bright fluorescence through activation of a low absorption fluorophore: the case of a unique naphthalimide–tetrazine dyad. New J Chem. 2011;35(8):1678.
35. Ge Y, Zheng X, Ji R, Shen S, Cao X. A new pyrido [1 , 2- a] benzimidazole-rhodamine FRET system as an efficient ratiometric fluorescent probe for Cu2þ in living cells. Anal Chim Acta. 2017;965:103–10.
36. Pawlicki M, Collins HA, Denning RG, Anderson HL. Two-photon absorption and the design of two-photon dyes. Angew Chemie - Int Ed. 2009;48(18):3244–66.
37. Aparicioixta L, Rodriguez M, Ramosortiz G. Organic Nanomaterials with Two-Photon Absorption Properties for Biomedical Applications. In: Contemporary Optoelectronics. Netherlands:Springer; 2016: 25–50.
38. Raposo MMM, Herbivo C, Hugues V, Clermont G, Castro MCR, Comel A, et al. Synthesis , Fluorescence , and Two-Photon Absorption Properties of Push – Pull 5-Arylthieno [3 , 2- b] thiophene Derivatives. European J Org Chem. 2016;5263–73.
39. Ge X, Gan X, Yao S, Wang K, Zhu W, Yu J, et al. Rationally designed two-photon absorption compounds based on benzoxazole derivatives: structure–property relationships and bio-imaging applications. J Mater Chem B. 2016;4(16):2785–93.
40. Yao S, Belfield KD. Two-photon fluorescent probes for bioimaging. European J Org Chem. 2012;(17):3199–217.
41. Mulligan S, MacVicar B. Two-photon fluorescence microscopy: basic principles, advantages and risks. Mod Res Educ Top Microsc. 2007;881–8.
42. Terenziani F, Katan C, Badaeva E, Tretiak S, Blanchara-Desce M. Enhanced two-photon absorption of organic chromophores: Theoretical and experimental

assessments. Adv Mater. 2008;20(24):4641–78.
43. Tian X, Zhang Q, Zhang M, Uvdal K, Wang Q, Chen J, et al. Probe for simultaneous membrane and nucleus labeling in living cells and in vivo bioimaging using a two-photon absorption water-soluble Zn(II) terpyridine complex with a reduced π-conjugation system. Chem Sci. 2017;8:142-149.
44. Hrobáriková V, Hrobárik P, Gajdoš P, Fitilis I, Fakis M, Persephonis P, et al. Benzothiazole-based fluorophores of donor-π-acceptor-π-donor type displaying high two-photon absorption. J Org Chem. 2010;75(9):3053–68.
45. Kitova S, Stoyanova D, Dikova J, Kandinska M, Vasilev A, Angelova S. Optical modeling of bulk-heterojunction organic solar cells based on squarine dye as electron donor. J Phys Conf Ser. 2015;15(2):19-23.
46. Lambert C, Scherpf T, Ceymann H, Schmiedel A, Holzapfel M. Coupled Oscillators for Tuning Fluorescence Properties of Squaraine Dyes. J Am Chem Soc. 2015;137(10):3547–57.
47. Johnson JR, Fu N, Arunkumar E, Leevy WM, Gammon ST, Piwnica-Worms D, Smith BD. Squaraine-Rotaxanes: Superior Substitutes for Cy-5 in Molecular Probes for Near-Infrared Fluorescence Cell Imaging. Angew Chem Int Ed Engl. 2007;46(29):5528–31.
48. Feng R, Sun Y, Tian M, Zhang G, Zhang R, Guo L, et al. Large Two-Photon Excited Fluorescence Action. J Mater Chem B. 2015;3:8644–9.
49. Zhang X, Xiao Y, Qi J, Qu J, Kim B, Yue X, et al. Long-wavelength, photostable, two-photon excitable BODIPY fluorophores readily modifiable for molecular probes. J Org Chem. 2013;78(18):9153–60.
50. Zhang G, Sun Y, He X, Zhang W, Tian M, Feng R, et al. Red-Emitting Mitochondrial Probe with Ultrahigh Signal-to-Noise Ratio Enables High-Fidelity Fluorescent Images in Two-Photon Microscopy. Anal Chem. 2015;87(24):12088–95.
51. Moon H, Jun W, Kim D, Ryu G, Wang T. A Dipolar Anthracene Dye: Synthesis, Optical Properties and Two-photon Tissue Imaging. Chem - A Eur J. 2016;11:2518–23.
52. Kim D, Moon H, Baik SH, Singha S, Jun YW, Wang T, et al. Two-photon absorbing dyes with minimal autofluorescence in tissue imaging: Application to in vivo imaging of amyloid-β plaques with a negligible background signal. J Am Chem Soc. 2015;137(21):6781–9.
53. Singha S, Kim D, Roy B, Sambasivan S, Moon H, Rao AS, et al. A structural remedy toward bright dipolar fluorophores in aqueous media. Chem Sci. 2015; 6: 4335-4342.
54. Ferrer-Ugalde A, González-Campo A, Viñas C, Rodríguez-Romero J, Santillan R, Farfán N, et al. Fluorescence of new o-carborane compounds with different fluorophores: Can it be tuned? Chem - A Eur J. 2014;20(32):9940–51.
55. Zhu L, Lv W, Liu S, Yan H, Zhao Q, Huang W. Carborane enhanced two-photon

absorption of tribranched fluorophores for fluorescence microscopy imaging. Chem Commun. 2013;49(90):10638–40.

56. Uebe M, Ito A, Kameoka Y, Sato T, Tanaka K. Fluorescence enhancement of non-fluorescent triphenylamine: A recipe to utilize carborane cluster substituents. Chem Phys Lett. 2015;633:190–4.
57. Kong L, Tian Y, Chen Q, Zhang Q, Wang H, Tan D, et al. Self-assembly of metal ion induced highly emissive fluorophore-triphenylamine nanostructures: enhanced two-photon action cross-section for bioimaging applications. J Mater Chem C. 2015;3(3):570–81.
58. Wang J, Wu Y, Zeng F, Huang S, Wu S. AIE fluorophore with enhanced cellular uptake for tracking esterase-activated release of taurine and ROS scavenging. Faraday Discuss. 2017;196:335–50.
59. Singh VK, Prasad R, Koch B, Hasan SH, Dubey M. Pyrene–fluorescein-based colour-tunable AIE-active hybrid fluorophore material for potential live cell imaging applications. New J Chem. 2017;41:5114–20.
60. Philips DS, Sreejith S, He T, Menon NV, Anees P, Mathew J, et al. A Three-Photon Active Organic Fluorophore for Deep Tissue Ratiometric Imaging of Intracellular Divalent Zinc. Chem - An Asian J. 2016;11(10):1523–7.
61. Grabrucker AM, Rowan M, Garner CC. Brain-Delivery of Zinc-Ions as Potential Treatment for Neurological Diseases: Mini Review. Drug Deliv Lett. 2011;1(1):13–23.
62. Juette MF, Terry DS, Wasserman MR, Zhou Z, Altman RB, Zheng Q, et al. The bright future of single-molecule fluorescence imaging. Curr Opin Chem Biol. 2014;20(1):103–11.
63. Leung BO, Chou KC. Review of super - Resolution fluorescence microscopy for biology. Appl Spectrosc. 2011;65(9):967–80.
64. Owen DM, Gaus K. Imaging lipid domains in cell membranes: the advent of super-resolution fluorescence microscopy. Front Plant Sci. 2013;4:503.
65. Barsu C, Cheaib R, Chambert S, Queneau Y, Maury O, Cottet D, et al. Neutral push-pull chromophores for nonlinear optical imaging of cell membranes. Org Biomol Chem. 2010;8(1):142–50.
66. Shim SH, Xia C, Zhong G, Babcock HP, Vaughan JC, Huang B, et al. Super-resolution fluorescence imaging of organelles in live cells with photoswitchable membrane probes. Proc Natl Acad Sci. 2012;109(35):13978–83.
67. Grossi M, Morgunova M, Cheung S, Scholz D, Conroy E, Terrile M, et al. Lysosome triggered near-infrared fluorescence imaging of cellular trafficking processes in real time. Nat Commun. 2016;7:10855.
68. Wycisk V, Achazi K, Hillmann P, Hirsch O, Kuehne C, Dernedde J, et al. Responsive

Contrast Agents: Synthesis and Characterisationof a Tunable Series of pH-Sensitive Near-Infrared Pentamethines. ACS OMEGA. 2016;1:808–17.

69. Hell SW, Sahl SJ, Bates M, Zhuang X, Heintzmann R, Booth MJ, et al. The 2015 super-resolution microscopy roadmap. J Phys D Appl Phys. 2015;48(44):443001.
70. Sahl SJ, Moerner WE. Super-resolution fluorescence imaging with single molecules. Curr Opin Struct Biol. 2013;23(5):778–87.
71. Molle J, Raab M, Holzmeister S, Schmitt-Monreal D, Grohmann D, He Z, et al. Superresolution microscopy with transient binding. Curr Opin Biotechnol. 2016;39:8–16.
72. Vogelsang J, Steinhauer C, Forthmann C, Stein IH, Person-Skegro B, Cordes T, et al. Make them blink: Probes for super-resolution microscopy. ChemPhysChem. 2010;11(12):2475–90.
73. Hoyer P, Medeiros G De, Norlin N, Besir C, Hanne J, Engelhardt J, et al. Breaking the diffraction limit of light-sheet fluorescence microscopy by RESOLFT. Proc Natl Acad Sci. 2016;113(3):3442–6.
74. Zheng Q, Jockusch S, Zhoua Z, Blanchard SC. The Contribution of Reactive Oxygen Species to the Photobleaching of Organic Fluorophores. Photochem Photobiol. 2014;90(2):448–54.
75. Ha T, Tinnefeld P. Photophysics of Fluorescence Probes for Single Molecule Biophysics and Super-Resolution Imaging. Annu Rev Phys Chem. 2012;63(2):595–617.
76. Sednev MV, Belov VN, Hell SW. Fluorescent dyes with large Stokes shifts for super-resolution optical microscopy of biological objects: a review. Methods Appl Fluoresc. 2015;3(4):042004.
77. Huang B, Babcock H, Zhuang X. Breaking the diffraction barrier: Super-resolution imaging of cells. Cell. 2010;143(7):1047–58.
78. Small A, Stahlheber S. Fluorophore localization algorithms for super-resolution microscopy. Nat Methods. 2014;11(3):267–79.
79. Godin AG, Lounis B, Cognet L. Super-resolution microscopy approaches for live cell imaging. Biophys J. 2014;107(8):1777–84.
80. van de Linde S, Heilemann M, Sauer M. Live-cell super-resolution imaging with synthetic fluorophores. Annu Rev Phys Chem. 2012;63:519–40.
81. Grimm JB, English BP, Chen J, Slaughter JP, Zhang Z, Revyakin A, et al. A general method to improve fluorophores for live-cell and single-molecule microscopy. Nat Methods. 2015;12(3):244–50.
82. Liu X, Qiao Q, Tian W, Liu W, Chen J, Lang MJ, et al. Aziridinyl Fluorophores Demonstrate Bright Fluorescence and Superior Photostability by Effectively Inhibiting Twisted Intramolecular Charge Transfer. J Am Chem Soc. 2016;138(22):6960–3.
83. Kolmakov K, Wurm C, Sednev MV, Bossi ML, Belov VN, Hell SW. Masked red-emitting

carbopyronine dyes with photosensitive 2-diazo-1-indanone caging group. Photochem Photobiol Sci. 2012;11(3):522–32.

84. Grimm JB, Klein T, Kopek BG, Shtengel G, Hess HF, Sauer M, et al. Synthesis of a Far-Red Photoactivatable Silicon-Containing Rhodamine for Super-Resolution Microscopy. Angew Chemie - Int Ed. 2016;55(5):1723–7.
85. Coelho M, Maghelli N, Tolić-Nørrelykke IM. Single-molecule imaging in vivo: the dancing building blocks of the cell. Integr Biol (Camb). 2013;5(5):748–58.
86. Chinen AB, Guan CM, Ferrer JR, Barnaby SN, Merkel TJ, Mirkin CA. Single-molecule imaging in vivo. Chem Rev. 2015;115(19):10530–74.
87. Xiong LH, Cui R, Zhang Z.L, Yu X, Xie Z, Shi Y.B, et al. Uniform Fluorescent Nanobioprobes for Pathogen Detection Ling-Hong. ACS Nano. 2014;8(5):5116–24.
88. Wen C, Hu J, Zhang Z, Tian Z, Ou G, Liao Y, et al. One-Step Sensitive Detection of Salmonella typhimurium by Coupling Magnetic Capture and Fluorescence Identification with Functional Nanospheres. Anal Chem. 2013;85:1223–30.
89. Crosetto N, Bienko M, van Oudenaarden A. Spatially resolved transcriptomics and beyond. Nat Rev Genet. 2015;16(1):57–66.
90. Cserép GB, Herner A, Kele P. Bioorthogonal fluorescent labels: a review on combined forces. Methods Appl Fluoresc. 2015;3(4):042001.
91. Shieh P, Bertozzi CR. Design strategies for bioorthogonal smart probes. Org Biomol Chem. 2014;12(46):9307–20.
92. Vu TQ, Lam WY, Hatch EW, Lidke DS, Health O. Quantum dots for quantitative imaging: from single molecules to tissue. Cell Tissue Researh. 2015;360(1):71–86.
93. Wegner KD, Hildebrandt N. Quantum dots: bright and versatile in vitro and in vivo fluorescence imaging biosensors. Chem Soc Rev. 2015;44(14):4792–834.

Chapter 3: Exploring the chemistry and analysis of CurNQ for potential cancer theranostics

3.1 Introduction

Natural compounds provide a significant database of potential drug candidates and play a pivotal role in drug discovery [1,2]. Phytochemicals are naturally occurring compounds and have been used for centuries to treat and prevent many illnesses [1-5]. Several phytochemical compounds have been shown to have potent bioactive moieties, with a few even showing promise as anti-cancer molecules [1-4] through modulation of several biochemical pathways and processes associated with oncogenesis [3-5].

An interesting concept of late in anti-cancer interventions are theranostic systems (i.e. combining diagnostic and therapeutic elements in a single platform) and chemically modified phytochemicals could play a significant role in the conception of such systems [6,7]. Theranostic agents are highly advanced systems that can function to monitor the accumulation of various compounds (including nanomedicines) at target sites, quantify triggered drug release, and detect malignant cells in order to deliver a chemotherapeutic agent to the targeted site [7,8]. The ability to simultaneously target, detect and treat cancer would reduce patient mortality as a result of early disease detection and immediate treatment [9].

Epithelial ovarian carcinoma (OC) is the most common type of OC accounting for 90% of ovarian tumours. Symptoms of OC are detected late resulting in diagnosis at stages III and IV [10,11]. In addition, the highly metastatic nature of OC results in low patient survival with a mortality of approximately 60% [12]. A high rate of chemoresistance and relapse has also been associated with OC [13]. Therefore, newer interventions are urgently required to provide earlier detection of OC and provide a more targeted form of chemotherapy. The metabolism of a cancer cell is unique in that it undergoes aerobic glycolysis (the Warburg effect) [14]. This phenomenon can therefore be exploited to design a targeted theranostic system for the detection and treatment of OC.

In order to harness the benefits of utilising a phytochemical in the design of a theranostic system for OC, Curcumin (Cur) (diferuloylmethane), a natural polyphenol was selected based on multiple studies that reported on Cur to modulate signalling pathways in OC as an anti-cancer molecule (including NF-κB, PI3K/AKT, EGFR, Nrf2, Notch 1, Wnt/β-catenin, and HIF-1intervention). In addition, studies have demonstrated Cur to reduce proliferation and metastasis as well as induce apoptosis [15-21]. Specifically, in OC, lysophosphatidic acid (LPA) stimulates tumour development, progression, motility and metastasis when over-expressed and overexpression has been detected in 98% of OC tumours. Cur inhibits LPA, thus reducing OC cell motility [12,22]. In addition, studies have shown Cur to inhibit NF-κB and thereby reduce inflammation [4,23,24]. Other studies have reported Cur to induce ROS production which stimulates the expression of DR5 on the cell surface, resulting in TRAIL mediated apoptosis as well as sensitising cells to TRAIL via inhibition of NF-κB [25,26]. Furthermore, various researchers have demonstrated Cur to disrupt the PI3K/AKT pathway which is involved in OC development [19,27,28]. Cur is therefore a unique phytochemical that has been shown to interact with multiple signalling pathways in OC and to function as a chemotherapeutic agent.

In addition to its anti-cancer properties, Cur has fluorescent properties [29,30]. However, the fluorescent lifetime is short (degraded within 30 minutes with a low quantum yield) at physiological pH [31,32]. This impedes its suitability to be used as an *in vivo* imaging agent as part of a new theranostic system for OC. Moreover, Cur readily degrades in a variety of standard conditions, has negligible aqueous solubility and bioavailability, undergoes rapid metabolism, has poor photostability and has many PAINS characteristics [33,34]. Numerous studies have focussed on improving the solubility and bioavailability of Cur, but none have been successful in resolving the many stability and bioavailability issues faced *in vivo* [31-34]. Therefore, in addition to utilising Cur for the design of a new theranostic system in OC, this study aimed to improve the biopharmaceutical properties of Cur to further exploit the purported anti-cancer and therapeutic properties of the phytochemical, by synthesising a novel therapeutically stable molecule.

In order to achieve this, another natural molecule lawsone (2-hydroxy-1,4-naphthoquinone) (a chemical constituent of the plant Lawsonia inermis) was also

selected based on its demonstratable anti-cancer activity [35,36]. The 1,4-naphthoquinone pharmacophore has been at the centre of numerous studies and has reported biological activity via a dianion species or radical anion [36]. Quinone moieties are present in several anti-cancer drugs including daunorubicin, doxorubicin and mitoxantrone [37] and many derivatives synthesised from 2-hydroxy-1,4-naphthoquinone have been demonstrated to have anti-cancer activity [38] resulting from redox cycling, arylation, intercalation, induction of DNA strand breaks, generation of free radicals and alkylation via quinone methide formation [38]. The anti-cancer activity of lawsone (1,4 naphthoquinone) has been attributed to its interaction with various signalling pathways, via inducing the rapid formation of ROS, which induces DNA damage and leads to cell death. [39]. Quinones are widely known for their fluorescent properties and many quinone derivatives are used as dyes and fluorescent labels [40]. Thus, lawsone exhibits inherent fluorescent properties owing to its structure making it possible to be incorporated within a new anti-cancer theranostic system.

Therefore, this study focuses on combining an imaging and a therapeutic agent into a single platform, by synthesising a novel theranostic compound that combines Cur and lawsone in order to take advantage of their anti-cancer properties, [18,19,21,22,27,41](therapeutic) as well as the fluorescent properties, particularly of lawsone [40,42](diagnostic). Although both phytochemicals have independently been shown to elicit anti-cancer activity, each have several limiting factors to advance their clinical application. These limiting factors include molecular instability, rapid degradation and poor bioavailability; therefore, this work aims to overcome some of these limitations by the synthesis of a stable molecule with appropriate bioavailability, targeting capabilities and innate fluorescence. In addition, to facilitate the new theranostic system to function as an anti-cancer passive targeting system, the new combined molecule has been designed to have pH-responsivity based on the known acidification of the ECM during malignant transformation [14]. A Williamson ether synthesis reaction between Cur and lawsone was used as the chemical synthesis route to produce the novel theranostic compound termed CurNQ.

3.2 Materials and Methods

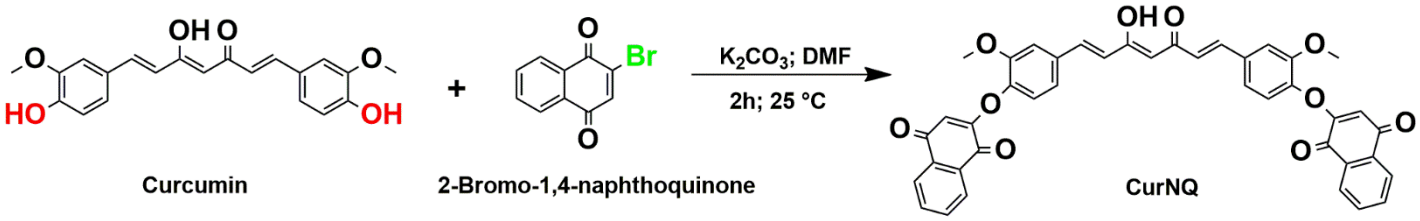
3.2.1 *Materials*

Curcumin (Cur) (95%) was received ex Gratia from Jiaherb Phytochem (China). 2-Bromo-1,4-naphthoquinone, 98%, dimethylformamide (DMF), DAPI, and sodium hydroxide pellets were procured from Sigma-Aldrich (Darmstadt, Germany) and potassium carbonate was purchased from ACE chemicals (Johannesburg, South Africa). All other solvents, including methanol, ethanol, ethyl acetate, hexane and salts were of analytical grade and were used as received. Silica Gel 60 (0.015-0.040mm) was purchased from Merck (Darmstadt, Germany) and thin layer chromatography plates were purchased from Macherey-Nagel (Düren, Germany) and were viewed under UV light (254 nm and 366 nm). Cell lines were purchased from Cell Biolabs Inc (San Diego USA) and Fox Chase Cancer Facility (Philadelphia, USA). Cell culture consumables including growth media and reagents were purchased from Thermo Fischer Scientific (Waltham, USA).

3.2.2 *Methods*

3.2.2.1 Synthesis of novel Cur derivative CurNQ

The hydroxy moiety of lawsone was replaced with a reactive bromine group allowing for reactivity at this moiety. For the purpose of ease, the lawsone derivative 2-Bromo-1,4-naphthoquinone (BrNQ) was purchased and utilised as received. In a fume hood shielded from light, one equivalent of Cur (50 mg, 1.36 mmols) was reacted with two equivalents of BrNQ (64 mg, 2.72 mmols) and two equivalents of potassium carbonate (37.6 mg, 2.72 mmols) in dry DMF (5 mL) as depicted in Scheme 3.1. The reaction was monitored continuously by thin layer chromatography (TLC) and after 2 hours the reaction was complete. The resulting reaction was quenched with dilute HCL solution and washed three times with ethyl acetate and water. The organic phase was collected, dried over anhydrous magnesium sulphate, filtered, and the organic solvent was removed under reduced pressure to obtain a crude product. The pure product was isolated via silica column chromatography using 30% (v/v) ethyl acetate:hexane eluent. The combined fractions were subjected to solvent evaporation and the resulting purified product CurNQ, was dried *in vacuo* and analysed.



Scheme 3.1: Reaction scheme for CurNQ synthesis.

3.2.2.2 Nuclear Magnetic Resonance - Structural determination

Multinuclear 1D, ^{1}H and ^{13}C NMR spectroscopy was performed to elucidate the structure of the synthesised molecule. ^{1}H and ^{13}C NMR spectroscopy was performed on the Bruker AVANCE II 500 MHz (Bruker Biospin, Germany) using deuterated dimethyl sulfoxide (DMSO) as a solvent at room temperature. All chemical shift values are reported in parts per million and coupling constants (J-values).

3.2.2.3 High Performance Liquid chromatography–mass spectrometry - Structural confirmation

The analysis of CurNQ was performed on a Bruker Compact electrospray ionization (ESI) Q-TOF high resolution compact mass spectrophotometer. 10 µL of the sample was injected into the HPLC and run through the C18 column (5-95% ACN). The solvent system was made up of solvent A, consisting of 0.1 % formic acid in H_2O (%v/v) and 50% solvent B, consisting of 0.1 % formic acid in Acetonitrile (%v/v). The samples were diluted to a concentration of approximately 10 ppm in a mixture of methanol and formic acid (1:1). The mass spectrum analysis was processed using the Bruker Daltonics data analysis program.

3.2.2.4 Fourier Transform infrared spectroscopy (FTIR)- characterisation of structural moieties

FTIR was performed using a single-reflection diamond MIRTGS detector on a PerkinElmer Spectrum 100, (PerkinElmer, Llantrisant, Wales, UK) to analyse the vibrational changes in the chemical structures which occurred during product formation. Through obtaining the spectra of Cur, BrNQ and CurNQ, the chemical structure of the product could be ascertained, as FTIR allows for functional group identification. All

samples were scanned from 4000-600 cm^{-1} at room temperature at a constant pressure of 120 psi.

3.2.2.5 Differential scanning calorimetry (DSC) – characterisation of thermal properties

Differential scanning calorimetry (DSC) was performed on the Mettler Toledo DSC-1 STARe system (Mettler Toledo, DSC1, STARe System, Swchwerzenback, Switzerland) to evaluate the heat flow required for phase transition and the thermal properties of the new molecule as well as both starting materials. Six mg of each sample was loaded and sealed into a 40 mL aluminium crucible pan and a small puncture was inserted into the top of the crucible and was heated at a rate of 10 °C/min from 10-350 °C under constant N_2 gas. The instrument was heat and enthalpically calibrated using indium metal (99.99 %).

3.2.2.6 Powder X-ray diffraction (PXRD) – crystallinity characterisation

Powder X-ray diffraction (PXRD) utilising a variable and fixed slit system was used to determine the crystallinity and atomic spacing and unit cell dimensions of the new molecule. This characterisation technique was performed on the Rigaku MiniFlex 600 Benchtop X-ray Diffractometer (Rigaku Corporation, Tokyo, Japan). A powdered sample was packed onto the sample holder and was analysed at a scanning rate of 15° per minute at a diffraction angle range of 3-90° with a degree step of 0.02, a voltage of 40 kV and a current of 15 mA.

3.2.2.7 Fluorescent and Absorbance – spectrofluorometric characterisation

The fluorescent and absorbance properties of CurNQ were evaluated to ascertain the fluorescent nature of CurNQ. The fluorescent properties of CurNQ were determined through obtaining the absorption and fluorescence spectra, which were measured and recorded on the Shimadzu UV-1800 spectrophotometer and Shimadzu RF-6000 spectrofluorophotometer (Maryland, USA) respectively.

3.2.2.8 Cell Culture

The ovarian carcinoma cancer cell lines OVCAR-5 and SKOV3 were purchased from Cell Biolabs, Inc (San Diego USA) and Fox Chase Cancer Facility (Philadelphia, USA)

respectively. The healthy fibroblast cell line 3T3 was utilised as a control. The cells were cultured in DMEM with the media being supplemented with 10% fetal bovine serum (FBS) and 1% penicillin-streptomycin. Cells were incubated at 37°C with 5% CO_2. Upon the cells reaching 70-80% confluency, the cells were washed, and sub-cultured by harvesting using trypsin/EDTA.

3.2.2.9 High Content Imaging – evaluation of cellular cytotoxicity

Cells were grown until 80% confluency prior to utilisation. Upon confluency, media was removed, and cells were washed twice in sterile PBS. Trypsin/EDTA was then added to the flasks and incubated at 37°C for 5 minutes, allowing the cells to detach from the bottom of the flask. These cells were then collected and centrifuged. The pellet was re-suspended, and the cells were counted using the trypan blue exclusion assay. A predetermined and equal number of cells were then added into each well of a 96 well plate. The cells were incubated overnight at 37°C and at 5% CO_2, allowing the cells to attached to the plates. The following morning, cells were treated with each sample (CurNQ, Cur and BrNQ) at concentrations of 5 µM, 10 µM, 20 µM, 50 µM and 100 µM. Each treatment was performed in quintuplicate. Treatments occurred for 24 and 48 h. Subsequent to this time period, media was removed, and cells were fixed with 5% formaldehyde in PBS for 20 minutes. Next, cells were incubated for 15 minutes in a 1 µg/mL solution of DAPI. The plates were then washed several times with PBS to remove all residual DAPI and to reduce background fluorescence. All plates were stored in the dark. Plates were then run on the Logos Biosystem CELENA® X High Content Imaging System and analyses were performed using their proprietary software. Using this software, a pipeline was set up to determine nuclei count, form factor, compactness and eccentricity. The following definitions were used:

Eccentricity = ratio of the distance between the foci of the ellipse and its major axis length.

Compactness = mean squared distance of the object's pixels from the centroid divided by the area.

Form Factor = $4*\pi*\text{Area}/\text{Perimeter}^2$

3.2.2.10 Statistical analysis

All experiments were performed in triplicate or quadruplet for statistical purchases and standard deviations were calculated. One-way ANOVA, three-way ANOVA and a Tukey's Test for Post-Hoc Analysis were performed on acquired data. Statistical analyses were all performed on Stata/IC15.1.

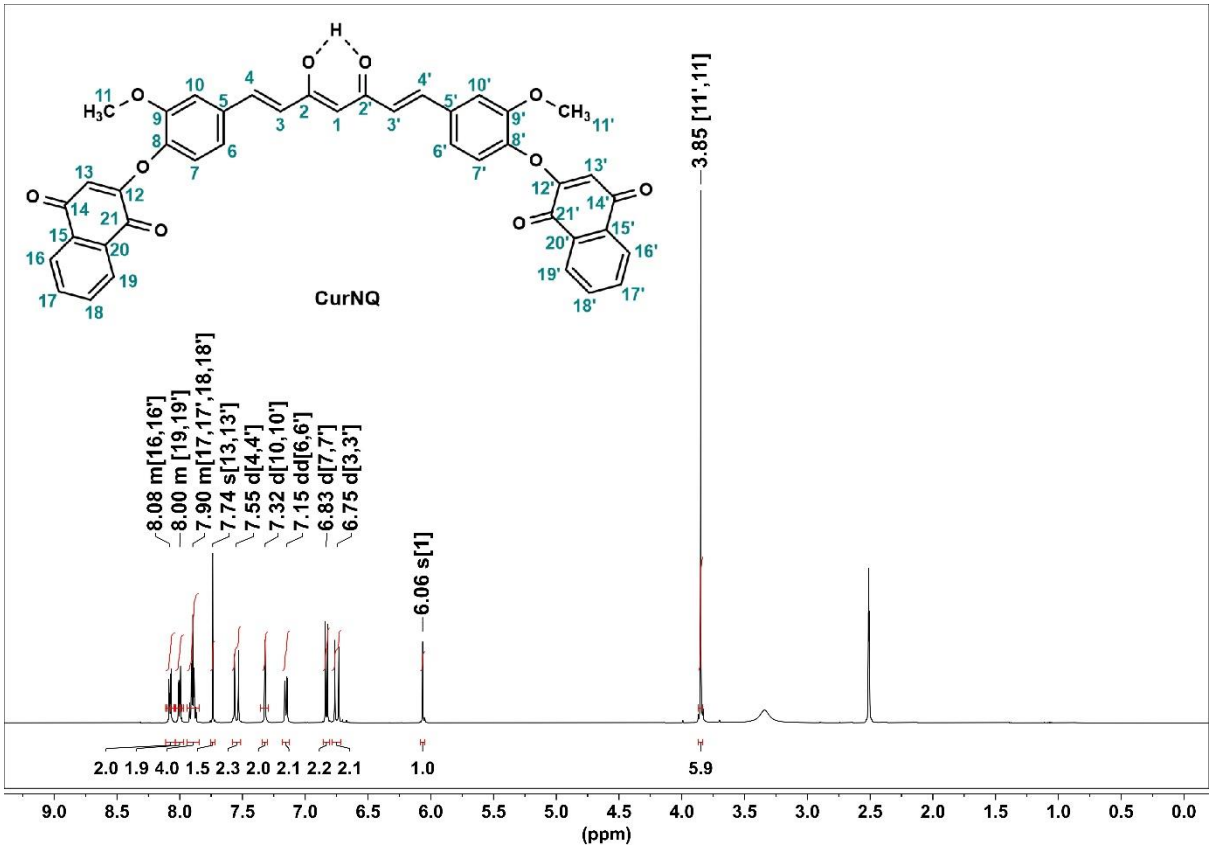
3.3 Results and Discussion

3.3.1 *Synthesis and structural evaluation of novel molecule CurNQ*

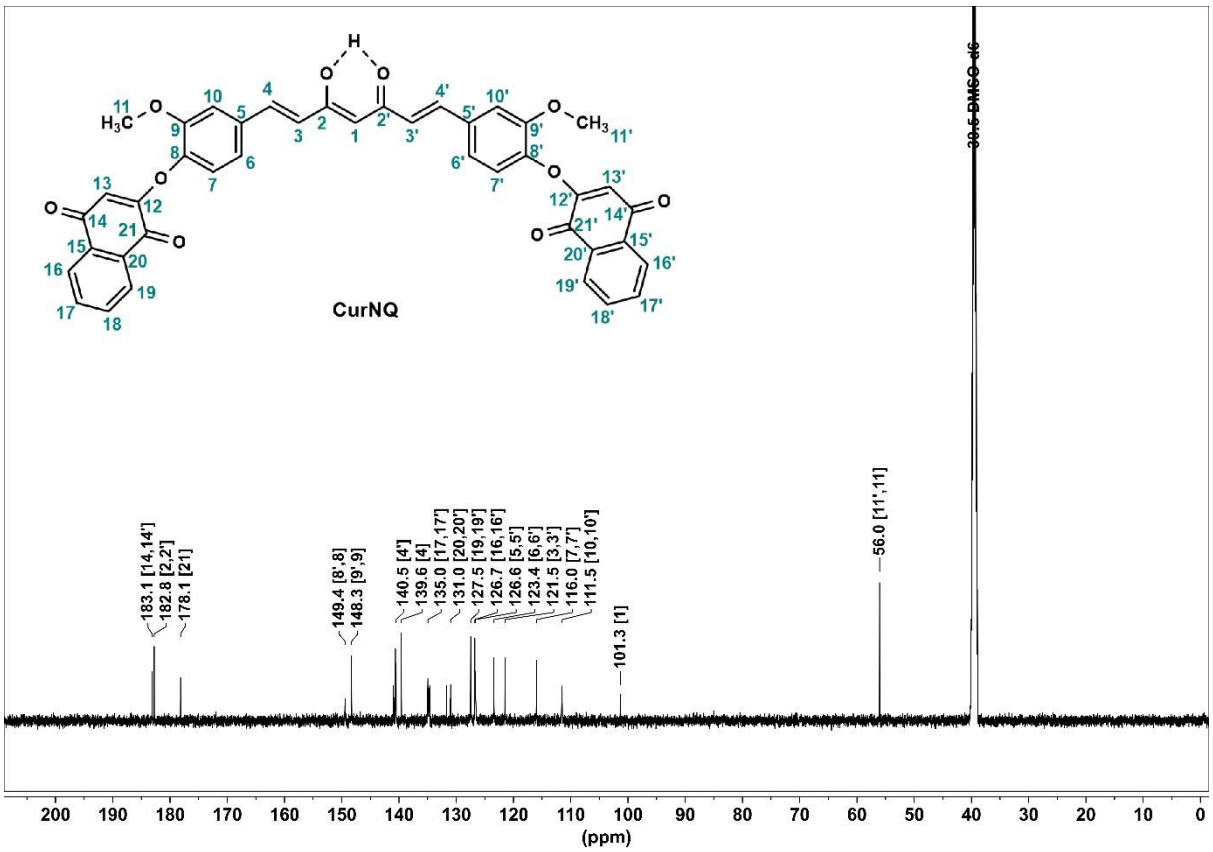
^{1}H and ^{13}C NMR spectra were obtained for the novel molecule (Figure 3.1). In the ^{1}H NMR (Figure 3.1A). The signal at 3.85 ppm which integrates to 6 protons was indicative of two methoxy groups (protons H11 and H11') on the Cur backbone. These methoxy groups have a similar spatial environment and because of this reason, the peaks for both appear at the same chemical shift. Moreover, doublets at 7.55(d, J = 15.8 Hz, 2H), and 6.75 (d, J =15.8 Hz, 2H) were characteristic of the alkenyl protons on Cur backbone. New multiplets centred around δ 8.08 (m, 2H), 8.00(m, 2H), and 7.90(m, 4H), were assigned to the aromatic phenyl protons and a singlet at 7.74 ppm was ascribed to the cyclic alkenyl proton which are indicative of the successful derivatisation of Cur with BrNQ.

In the ^{13}C NMR (Figure 3.1B) two significant peaks appear at 183.1 and 178.1 ppm, these were assigned to the carbonyl (C=O, ketones) at C14,14’ and C21,21’ respectively. Moreover, the keto/enol carbon present at 182.8 ppm represents the distinctive keto/enol system of Cur. In the mass spectrum (Figure 3.1C) a peak at 681.176 corresponded with is the exact mass of CurNQ with the addition of one hydrogen atom $[M+H]^{+}$. This analysis gives complementary characterisation and is also indicative of the successful synthesis and isolation of CurNQ.

A


CurNQ
8.08 m[16,16']
8.00 m [19,19']
7.90 m[17,17',18,18']
7.74 s[13,13']
7.55 d[4,4']
7.32 d[10,10']
7.15 dd[6,6']
6.83 d[7,7']
6.75 d[3,3']
6.06 s[1]
3.85 [11',11]
2.0 1.9 4.0 1.5 2.3 2.0 2.1 2.2 2.1
1.0
5.9
(ppm)

B


CurNQ
183.1 [14,14']
182.8 [2,2']
178.1 [21]
149.4 [8',8]
148.3 [9',9]
140.5 [4']
139.6 [4]
135.0 [17,17']
131.0 [20,20']
127.5 [19,19']
126.7 [16,16']
126.6 [5,5']
123.4 [6,6']
121.5 [3,3']
116.0 [7,7']
111.5 [10,10']
101.3 [1]
56.0 [11',11]
39.5 DMSO-d6
(ppm)

C

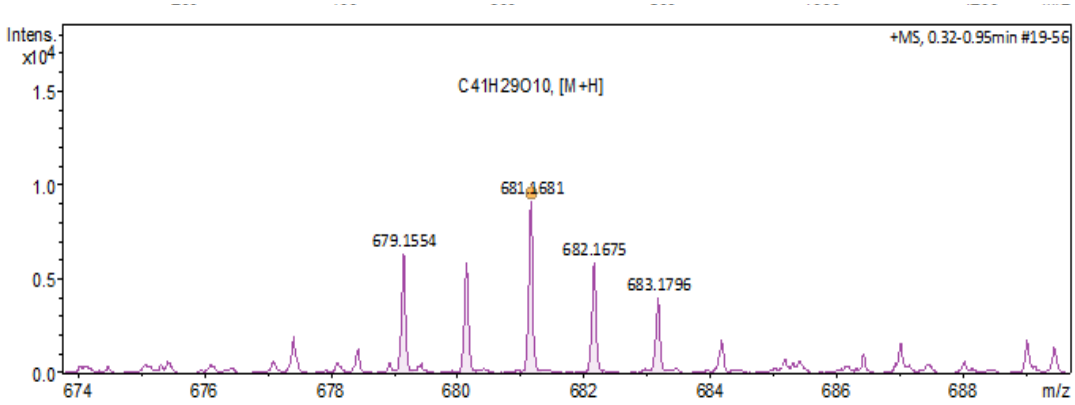


Figure 3.1: Spectral analysis of synthesised molecule **A)** ^{1}H NMR of CurNQ in d-DMSO ^{1}H NMR (500 MHz, DMSO-d 6) δ 8.11 – 8.04 (m, 2H), 8.04 – 7.97 (m, 2H), 7.94 – 7.85 (m, 4H), 7.74 (s, 2H), 7.55(d, J = 15.8 Hz, 2H), 7.32 (d, J = 2.0 Hz, 2H), 7.15 (dd, J = 8.3, 2.0 Hz, 2H), 6.83 (d, J = 8.2 Hz, 2H), 6.75 (d, J =15.8 Hz, 2H), 6.06 (s, 1H), 3.85 (s, 6H). **B)** ^{13}C NMR of CurNQ in d-DMSO δ 183.1 (C=O), 182.8 (C=O), 178.1(C=O), 149.4, 148.3, 141.0, 140.5, 139.6, 134.96, 134.7, 131.7, 131.0, 127.5, 126.7, 126.6, 123.4, 121.5, 116.0, 111.5, 101.3, 56.0 (OCH_3). **C)** HRMS-ESI spectrum of CurNQ

In the FTIR spectrum of Cur (Figure 3.2A), the phenolic O-H stretching molecular vibration was observed around 3508 cm^{-1} [43]. In comparison to the FTIR spectrum of CurNQ this absorption band was not observed, and this was indicative of the removal of this hydroxyl group, and the occurrence of a reaction as this site. Stretching vibrational band of the hydroxyl group of the keto-enol tautomerism (C2, 2') is present at 3347 cm^{-1} and is visible in both Cur and CurNQ spectra. The alkyl ether groups (C11, 11') of Cur are represented at wavenumber of 1155 cm^{-1}, which is slightly shifted relative to the spectrum of CurNQ spectra (1153 cm^{-1}) [44]. The aromatic ring of Cur and CurNQ (5,5'-10,10') are assigned to vibrational bands 1488 and 1511 cm^{-1} respectively. The sharp band at 2917 cm^{-1} in CurNQ and 3059 cm^{-1} in BrNQ are representative of aliphatic and aromatic C-H groups. The carbonyl functional groups of BrNQ (C14, 14', 21, 21') were present at 1677 cm^{-1} in the BrNQ spectrum and 1669 cm^{-1} in the CurNQ spectrum. Moreover, the sharper peaks at 1590 and 1587 cm^{-1} and the small peaks present at 1457 and 1430 cm^{-1} are attributed to the aromatic C=C groups in BrNQ and CurNQ respectively (C15-20, 15'-20') [45]. The presence of the carbonyl groups and the aromatic rings in CurNQ indicate the successful synthesis of the desired molecule, as BrNQ functional groups are present in CurNQ. Thus, the key functional groups of Cur and BrNQ are present in the FTIR spectrum of CurNQ.

3.3.2 *Physiochemical characterisation of CurNQ*

The thermal properties of Cur, BrNQ and CurNQ were measured from 10-350 °C under inert conditions with a nitrogen flow rate of 50 $mL.min^{-1}$ and with the temperature ramping at a rate of 10 °C per minute. DSC thermograms of the Cur, BrNQ and CurNQ were obtained and are presented in Figure 3.2C. Cur and BrNQ display sharp endothermic peaks at 182 °C and 131 °C respectively. These endothermic peaks represent the melting point of crystalline materials. Moreover, the peaks of these two endotherms agree with previously published data on the melting temperatures of both Cur and BrNQ respectively [46,47]. Moreover, the presence of a single peak as well as the sharpness of the peaks indicates Cur and BrNQ's high degree of purity.

The exothermic peak present in the CurNQ thermogram at 172 °C is representative of a crystallization peak, this crystallization peak is shortly followed by an endothermic peak at 200 °C which represents crystal melting. The presence of the exothermic crystallization peak further concurs with the PXRD results which indicate that CurNQ is an amorphous material. This release of energy represented by the exothermic peak is indicative of the ordering of the molecules to form a crystal which results in a release of energy, as the material enters a more ordered state. CurNQ requires a temperature of 172 °C to convert it from an amorphous material into a crystalline solid.

Powder X-ray diffraction (PXRD) was then performed on the three samples to ascertain the crystalline phases present in each sample and is presented in Figure 3.2. A change in crystalline phases indicates a unit cell transformation and thus a structural change. The PXRD of CurNQ takes the shape of a 90% amorph, in contrast to the highly crystalline structure of both Cur and BrNQ. This change to an amorphous nature is also verified by the broad exothermic peak of CurNQ in the DSC thermogram.

Overcoming low aqueous solubility has become a fundamental issue in drug discovery, as many new chemical entities are hydrophobic and display low aqueous solubility [48]. Multiple approaches to improve a drug's solubility exist, one of which is converting the crystalline drug to its amorphous form. Amorphous drug formulations have multiple favourable properties over crystalline formulations, the most important of which is

increased solubility and increased bioavailability. The amorphous state is the highest energy form of a solid material with no long-range molecular order. Amorphous materials have larger molecular motions and more favourable thermodynamic properties, compared to their crystalline counterparts owing to their high energy form [48]. Together, this results in amorphous materials displaying greater aqueous solubility thereby increasing bioavailability. Consequently, many researchers convert crystalline drugs into amorphous formulations to harness these favourable properties [49]. As evident in Figure 3.2, both Cur and BrNQ have high levels of crystallinity. On the contrary, CurNQ has a highly amorphous structure. The amorphous nature of CurNQ is confirmed through both the PXRD and the DSC spectra. Concerns exist relating to the re-crystallization of an amorphous formulation which would then decrease its solubility and bioavailability [50]. As seen in Figure 3.2, the crystallization peak of CurNQ occurs at 172°C. This temperature would not be reached *in vivo* and thus removes the possibility of crystallization subsequent to treatment or during storage. The naturally amorphous nature of CurNQ is highly favourable and it is expected this amorphous nature will enhance CurNQ`s bioavailability and further eludes to CurNQ to be a highly promising drug candidate.

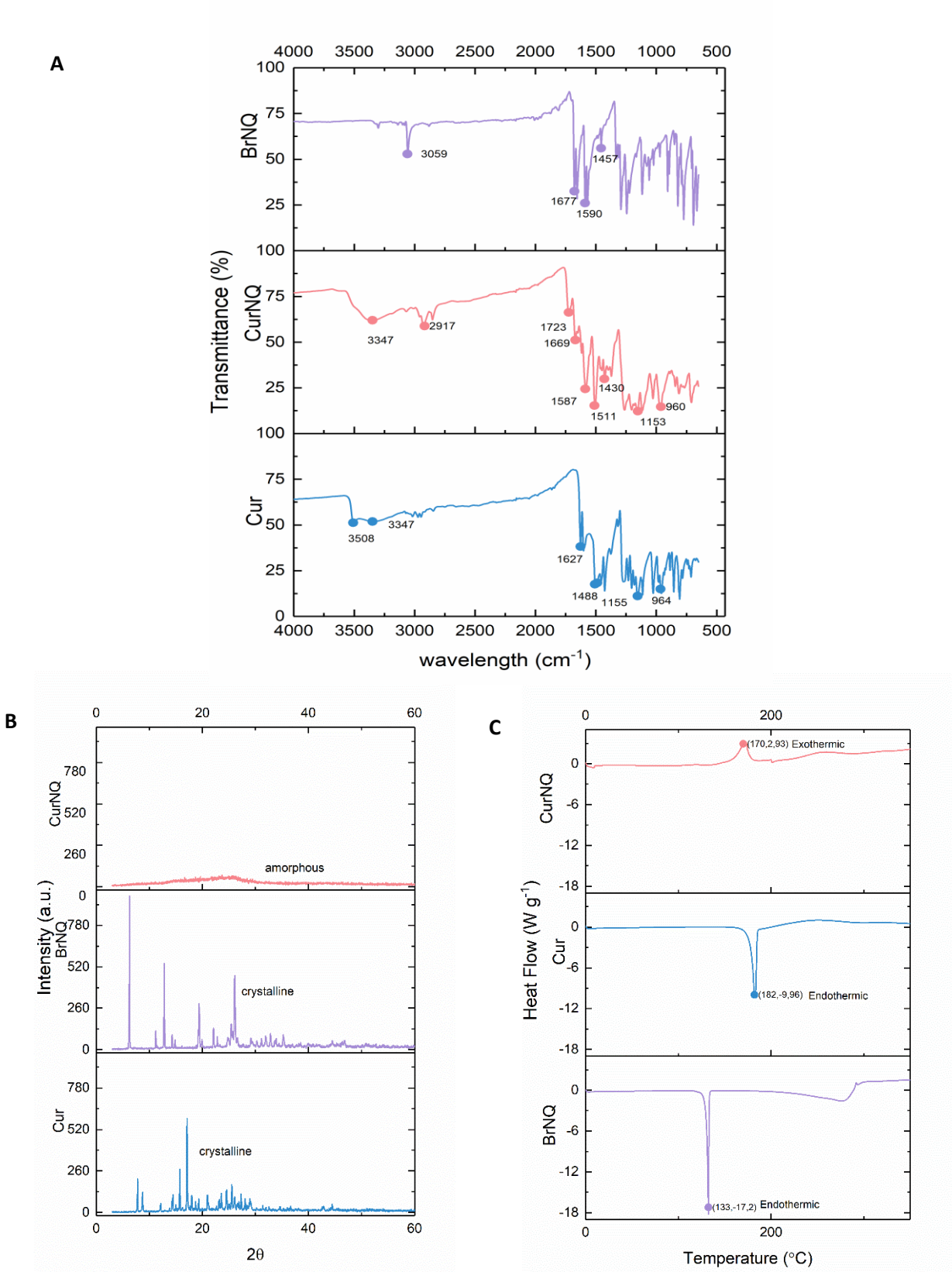


Figure 3.2: Structural Characterisation of CurNQ and comparison with Cur and BrNQ ***A)*** FTIR spectra **B)** PXRD spectra. **C)** DSC thermograms. The spectral characteristics of CurNQ was elucidated through FTIF, DSC and PXRD and these spectral characteristics were compared to those of Cur and BrNQ.

3.3.3 *Fluorescent characterisation of CurNQ*

The rationale behind this novel theranostic molecule was to synthesize a novel molecule that exhibits fluorescent and anti-cancer properties, along with cancer targeting abilities. CurNQ contains multiple aromatic groups. Aromatic groups are known to exhibit intense fluorescence [51]. Consequently, CurNQ was expected to exhibit intense fluorescence owing to its highly aromatic chemical structure. This property can be exploited for cancer diagnostics, as a fluorescent signal can be detected and tracked *in vivo*. The excitation and emission spectra of a 1.5 µM solution of CurNQ was ascertained using the Shimadzu RF-6000 spectrofluorophotometer. The excitation peak of CurNQ was determined to be at 595 nm with the emission peak at 670 nm. A high intensity peak was detected thus confirming the innate fluorescent nature of CurNQ and this fluorescent signal was further confirmed on the fluorescent microscope. Moreover, CurNQ displayed a large stokes shift of 75 nm. A large stokes shift is crucial for *in vivo* imaging applications as it reduces the overlap between the excitation and emission spectra thus reducing self-absorbance [52].

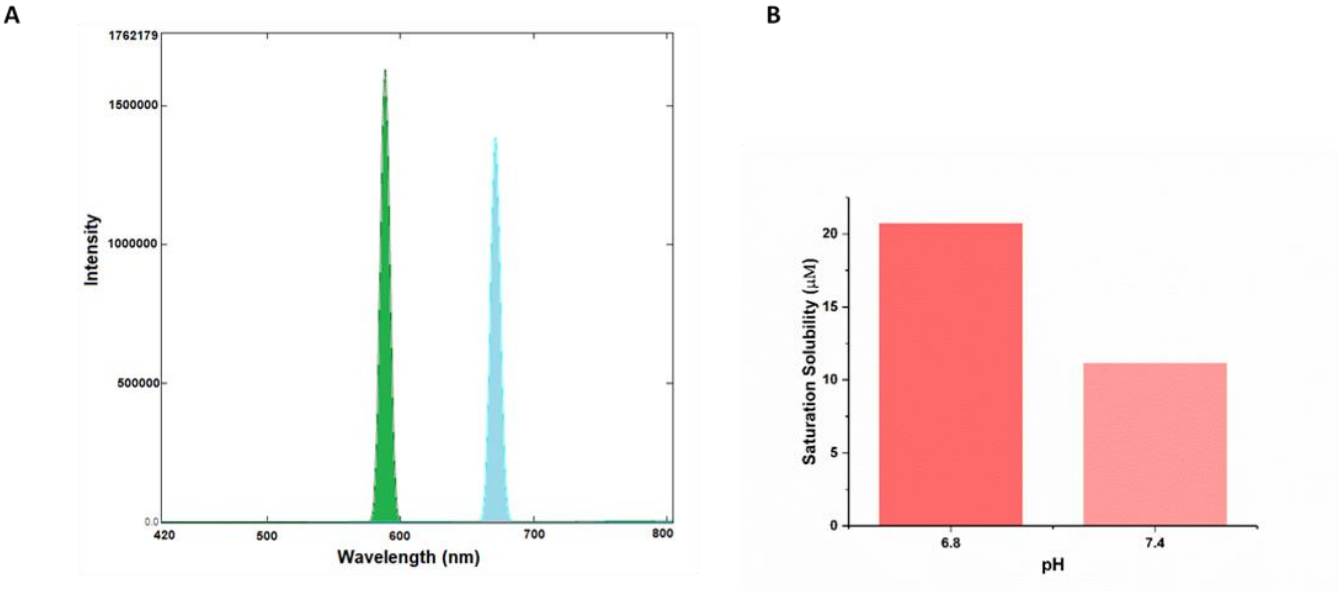


Figure 3.3: Fluorescence properties and pH specific properties of CurNQ **A)** Excitation and emission spectra of 1.5 µM solution of CurNQ **B)** Saturation solubility of a I.5 µM solution of CurNQ at pH 7.4 and 6.8.

3.3.4 *pH responsivity of CurNQ*

The non-specificity and untargeted nature of current chemotherapeutics is a major hindering factor to successful treatment, as unspecific treatment results in severe side effects and often displays poor efficacy. Consequently, cancer targeting and specific release of an active agent at the tumour location is essential. Multiple tactics can be employed to achieve this. Herein, the acidification of the tumour microenvironment that accompanies malignant transformation was exploited for targeted detection and treatment. As seen in Figure 3.3, CurNQ displays a low solubility at physiological pH (pH 7.4); with a small shift in pH from 7.4 to 6.8, CurNQ experiences a dramatic increase in solubility. The saturation solubility increased from 11.15 µM at pH 7.4 to 20.7 µM at pH 6.8. Hence, the saturation solubility almost doubled in response to this small change in pH. This establishes that CurNQ is highly pH responsive and demonstrates pH specific solubility. The slight acidification of the microenvironment surrounding a tumour is a hallmark feature of cancer and is termed the Warburg effect [14]. Therefore, CurNQ can detect this change in pH associated with malignant transformation resulting from its pH specific solubility. More than this, CurNQ displays bright fluorescence once soluble (Figure 3.3), thus the detection of the acidic microenvironment will be accompanied with a sharp increase in fluorescent intensity. Indeed, CurNQ demonstrates cancer targeting and detection abilities owing to its pH specific solubility and fluorescent properties.

3.3.5 *High Content Imaging and in-depth Cytotoxicity studies of CurNQ, Cur and BrNQ*

High content imaging is an advanced technique that combines high throughput techniques and fluorescent microscopy to obtain quantitative data from complex biological systems [53]. It is a robust method utilising an automated microscope that allows for rapid, high content image acquisition and analysis [54]. Multiple independent measurements can be collected from a single cell or a single cell population. High content imaging removes the limitations of other techniques which collect a single average value for a population of cells, this technique allows for individual cells to be monitored and the effects of a drug to be quantified independently and simultaneously. Furthermore, high content imaging allows for the full effect of a selected compound to be evaluated *in vitro* [53]. Herein, this advanced technique was employed and using

this technique, the toxicity and dose dependency of CurNQ, Cur and BrNQ on three cell lines at 24- and 48-hours intervals was evaluated. Moreover, the morphological changes associated with treatment were quantified and analysed.

OC was selected as the model cancer type for this study. To this end, two OC cell lines namely, OVCAR-5 and SKOV3 were utilised. The toxicity of CurNQ as well as any morphological changes that were induced through CurNQ treatment were ascertained using a high content imaging system. This high throughput imaging and screening method allows for an in-depth analysis of the effect CurNQ has on OC cells. The cells were also treated with equivalent concentrations of Cur and BrNQ. This acted as a comparative analysis, as previous studies have demonstrated the anti-cancer properties of these two compounds. Owing to the retention of active moieties of Cur and BrNQ in the novel molecule, it was expected that the viability results to resemble that of Cur and BrNQ; thus, all assays were performed with all three compounds.

All three compounds displayed considerable reductions in cell viability in both OVCAR-5 and SKOV3 cell lines. OVCAR-5 cell viability was greatly reduced in response to CurNQ treatment. Low concentrations of CurNQ reduced cell viability to below 40% after 24-hour incubation and cell viability reduction occurred in a dose dependent manner. After 48-hour incubation, cell viability increased slightly; however, this increase was not significant. The cell viability assay demonstrated that the toxicity of CurNQ to OVCAR-5 cells was in between that of Cur and BrNQ. Cur treatment did result in cytotoxicity, however, even at highest treated concentrations, cell viability did not reduce to below 30%.

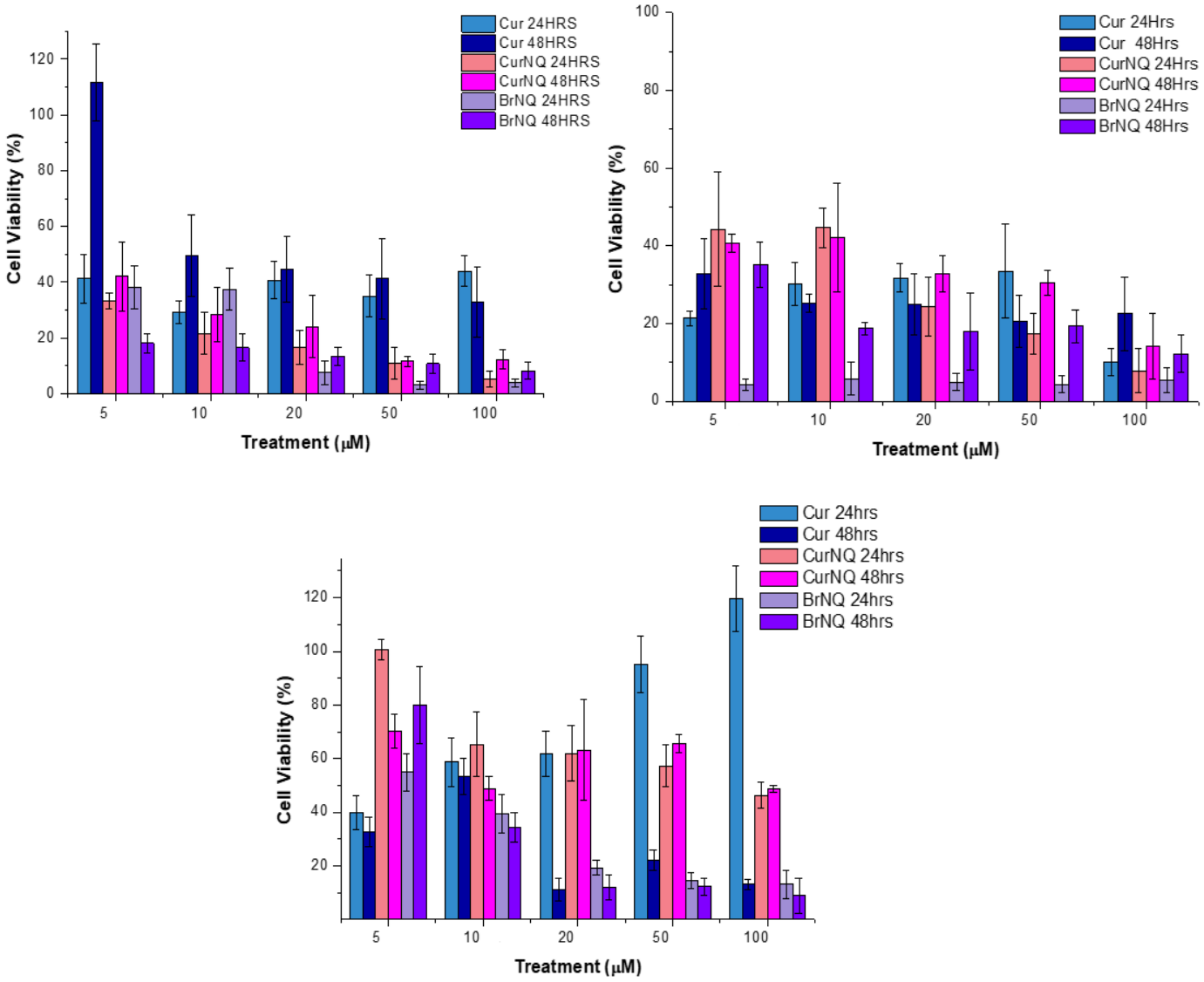


Figure 3.4: Cell viability assays were performed using a High Content Imaging System. Three cell lines were utilised, 2 OC cell lines and 1 healthy fibroblast cell line. **A)** OVCAR-5 **B)** SKOV3 **C)** 3T3. Each cell line was treated with varying concentrations of Cur, CurNQ and BrNQ and treatments where incubated for 24- and 48-hour intervals.

Additionally, reduction in cell viability in response to Cur treatment was not dose dependent, but an overall general decrease in cell viability was observed. This may be owing to Cur degradation in cell culture media [32]. BrNQ treatment exhibited a far more potent cytotoxic effect than Cur treatment to OVCAR-5 cells ($p = 0.000$). In addition, the cytotoxic nature of BrNQ is highly dose dependent. A 20 µM treatment of BrNQ resulted in cell viability being reduced to below 10% after 24 hours. Reductions in cell viability to CurNQ treatment were observed in both OVCAR-5 and SKOV3 cell lines, and no statistical difference was observed between these two cell lines to CurNQ

treatment (p = 0.743). Cell viability increased slightly after 48 hours for CurNQ treatment, but this increase was insignificant (p=0.8970). This sharp reduction in cell viability observed in response to CurNQ treatment in both OVCAR-5 and SKOV3 cell lines is promising data suggesting that CurNQ could act as a potent anti-cancer drug against OC.

The above assay was also performed on the healthy fibroblast line, 3T3. This acted as a control cell line and allowed for the effects of CurNQ on non-malignant cells to be ascertained. Traditional chemotherapeutics result in severe side effects owing to their non-specific toxicity, resulting in the equal death of healthy and malignant cells. The development of a treatment that is only toxic to cancerous cells would be highly advantageous and greatly enhance the clinical applications of such an anti-cancer agent. 3T3 cells did see a reduction in cell viability in response to CurNQ and BrNQ treatment (p=0.0185). BrNQ displayed severe toxicity to the healthy cells and cell viability dropped to below 15%; thereby, further demonstrating its clinical barriers to use as an anti-cancer agent. On the contrary, 3T3 cells did not experience severe toxicity to CurNQ treatment. Even at the highest tested concentration of CurNQ, the cell viability only dropped to 44%, although the reduction in cell viability was significant it was less severe than in response to BrNQ. These results are promising and indicate a lower overall toxicity of CurNQ to healthy cells. This would further accentuate CurNQ`s application as a cancer treatment as healthy cells will be affected to a far less extent than the malignant cells. On the contrary, the reduction in cell viability of 3T3 to Cur treatment was erratic and was not dose dependent. This further demonstrates the unreliability and unpredictability of Cur treatment owing to Cur instability and degradation.

A three-way ANOVA statistical analysis was performed with the above data using Stata/IC 15.1 software. Across the three cell lines, there was a statistically significant difference (p = 0.000) to Cur, CurNQ and BrNQ treatment on cell viability and the administered concentration was also significant (p = 0.0095). Interestingly, the incubation time applied (p = 0.8807) was not significant. Additionally, the cell line had a significant impact of the treatment outcome (p = 0.0000). A Tukey post-hoc test revealed that there was no statistical difference in reduction of cell viability between OVCAR-5 and SKOV3 cell lines to CurNQ treatment (p = 0.743), however both cell

lines cell viabilities were reduced to a significant difference compared to 3T3 (p= 0,001; 0,000). These statistics demonstrate that CurNQ is more effective in reducing cell viability in malignant cell lines than in a healthy fibroblast cell line.

It has been well established that Cur displays poor solubility and bioavailability and is highly unstable. Cur degrades rapidly in various conditions and has multiple confirmed metabolites. Wang *et al* [32] demonstrated that 90% of Cur degrades within 30 minutes in PBS as well as 90 % degradation in cell culture media supplemented with FBS after 8 hours. This rapid and complete degradation of Cur in PBS and cell culture media can explain the absence of dose dependent cell viability results to Cur treatment. All treatments were prepared in PBS and then added into the cell culture media. This would have resulted in the total degradation of Cur prior to the 24-hour incubation period. Cur degrades into at least 5 different metabolites, some of which are thought to have anti-cancer properties of their own and some of which do not (Figure 1.5) [33]. The unpredictability of Cur degradation precludes the results obtained to be highly accurate as each treatment event could have resulted in the formation of different metabolites as well as at varying proportions. This lack of stability and rapid degradation of Cur in aqueous solutions is greatly overlooked and is not considered in majority of research articles utilising Cur alone. These prohibitive properties preclude Cur's use as an anti-cancer agent.

Figure 3.5 displays microscopy images comprised of brightfield images overlaid on fluorescent images with DAPI staining. These images were acquired simultaneously using high content imaging. This combination of brightfield and fluorescent microscopy allows for a visual representation of the effect of treatments on OVCAR-5 cells morphology after 24 hours. Phenotypic changes that occurred in response to treatment can be visually monitored and qualitative data can be obtained. The reduction in cell count in response to an increased dosage of each treatment is clearly apparent and Figure 3.5 is a visual representation of the cell viability data displayed in Figure 3.4. As seen in Figure 3.5, cellular morphology becomes less consistent and variations in cell morphology are evident with increasing concentration of CurNQ. Importantly, the high content imaging software that was used to acquire these images also gives quantitative data on the morphology of the cells in these images, allowing for changes in morphology to be quantitatively assessed. This combination of qualitative and

quantitative data makes the high content imaging a powerful tool for drug discovery. The phenotypic changes in response to treatment can elucidate important cellular events and further reveal the mechanisms of action and effectiveness of a target compound. The use of machine learning to evaluate the morphological changes in response to a test compound is an advanced method to analyse the potential effectiveness of a novel compound. Cell morphology of OVCAR-5 cells in response to varying concentrations of Cur, CurNQ and BrNQ was quantified using the CELENA® X High Content Imaging System and their algorithm (Figure 3.6).

Apoptosis is characterised by chromatin condensation, disassembly of nuclear scaffold proteins and DNA fragmentation [55]. These events would lead to the condensing of the nucleus, thereby resulting in the nucleus to become more rounded. This rounding of the nucleus can be detected, and the extent of rounding can be quantified using High Content Imaging, consequently, allowing for apoptosis to be detected and quantified. Compactness is a measure of a spheroid's fullness. An equally filled circle will have a compactness of 1, with irregular objects or objects with holes having a value greater than 1. Therefore, in the context of cellular morphology, it would be expected that the compactness of healthy cells to be close to 1, and cells that are experiencing stress and that are undergoing apoptosis to have a compactness exceeding 1. Healthy cells would exhibit a compactness value close to 1, as a healthy nucleus is evenly "filled" with DNA. Apoptosis induces DNA fragmentation, thus reducing the amount of DNA evenly spread out across the area of the nucleus, thus a cell undergoing apoptosis would have a compactness exceeding 1 as DNA fragmentation would make the nucleus appear to have 'holes' or to appear irregular; the results concur with these assumptions. The compactness of all treated cells was greater than the control (Figure 3.6). This indicated that DNA fragmentation and nuclear distortion was occurring as the nuclei became irregular subsequent to treatment. This concurs with the results displayed in Figure 3.4 that demonstrated the substantial reduction of cell viability in response to treatment.

Moreover, the form factor and eccentricity values were obtained. These values indicate the level of circularity of an object. Form factor is calculated as $4*\pi*Area/Perimeter^2$ and equals 1 for a perfectly circular object. The eccentricity is the ratio of the distance between the foci of the ellipse and its major axis length. The value is between 0 and 1.

An ellipse with an eccentricity of 0 is a circle, while an ellipse with an eccentricity of 1 is a straight line. Chromatin condensation and DNA fragmentation is a hallmark of apoptosis [54]. Chromatin condensation causes the DNA to become dense, thereby condensing the nucleus into a more circular object. Therefore, a cell undergoing apoptosis would display a higher form factor and lower eccentricity.

As evident in Figure 3.6, the form factor was only greatly altered in cells treated with CurNQ and BrNQ greater than 50 µM, and this treatment induced a large increase in the form factor. Therefore, after 50 µM of CurNQ or BrNQ treatment, higher levels of apoptosis would be expected as chromatin condensation causes the nucleus to become more rounded. Indeed, this aligns with the cell viability results in Figure 3.4. Moreover, eccentricity decreased in a dose dependent manner in response to CurNQ treatment, and it was reduced to a greater extent than both Cur and BrNQ treated cells. A lower eccentricity value indicates the nucleus is becoming more rounded, thus implying chromatin condensation and apoptosis was occurring. All three indicators of cell morphology align in indicating that apoptosis was induced in response to Cur, CurNQ and BrNQ treatment. Nuclear morphology is altered, the nuclei becomes more irregular and circular in shape. This eludes to chromatin condensation and DNA fragmentation thus indicating the induction of apoptosis.

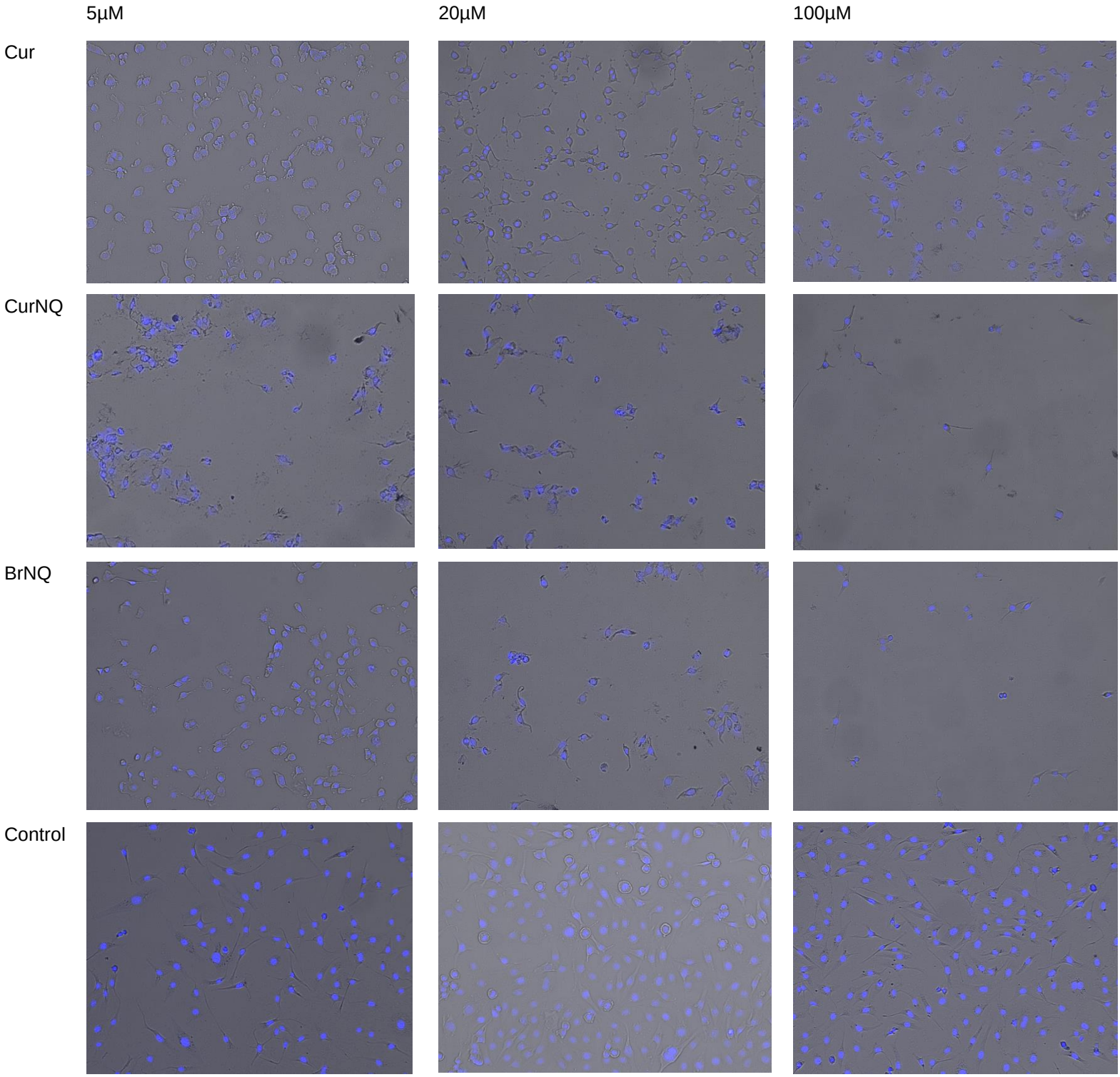


Figure 3.5: Brightfield Microscopy images overlaid on fluorescent microscopy images with DAPI staining. Acquired through High Content Imaging.

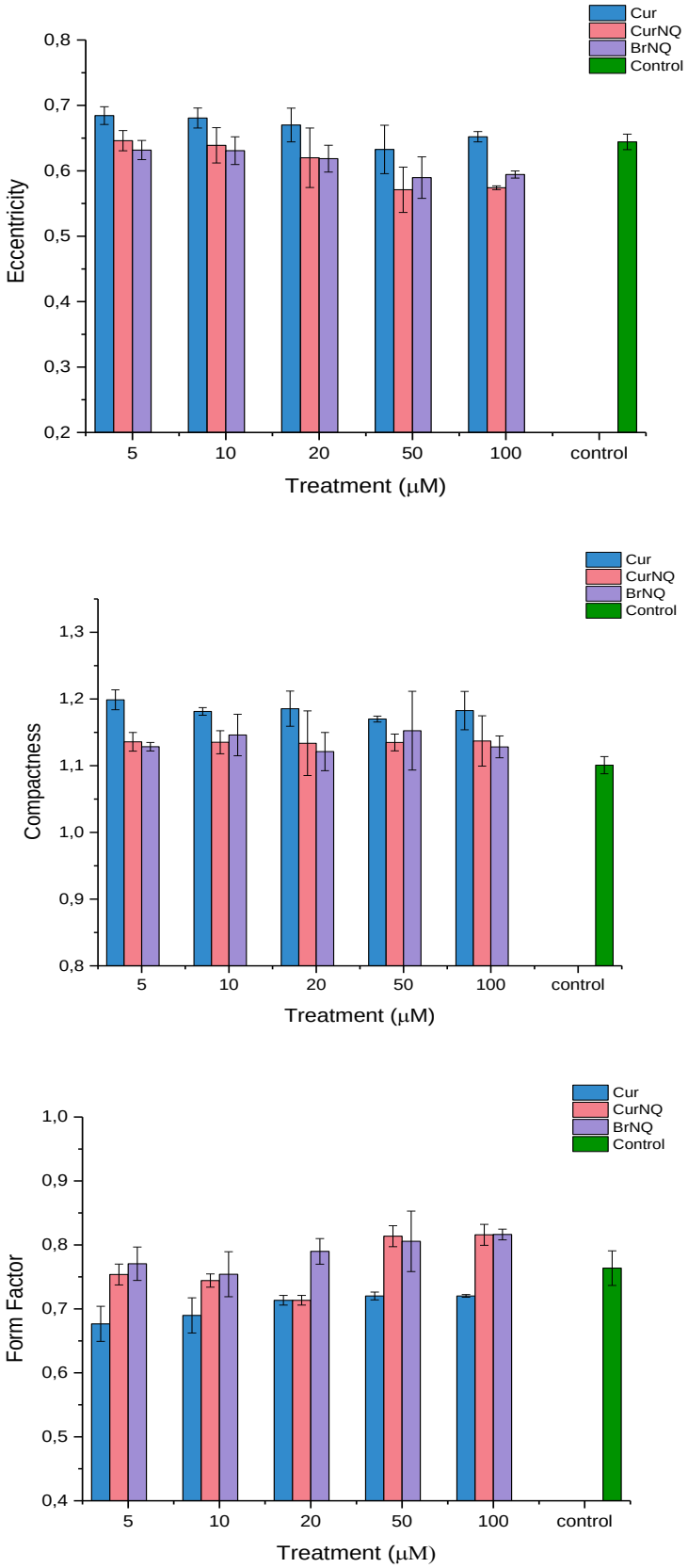


Figure 3.6: Cell morphology analysis of OVCAR-5 cells subsequent to Cur, CurNQ and BrNQ treatment. Cell morphology data obtained on the CELENA® X. **A)** Eccentricity **B)** Compactness **C)** Form Factor

3.4 Conclusions

A novel theranostic molecule (termed CurNQ) was synthesised through a Williamson ether synthesis reaction between the phytochemicals Cur and lawsone. The CurNQ structure was confirmed through ^{1}H and ^{13}C NMR and HRMS-ESI. CurNQ was found to be highly pH specific with preferential solubility at the pH of the tumour microenvironment enabling tumour targeting in OC. Moreover, CurNQ facilitated tumour detection once soluble at the tumour microenvironment due to its intense innate fluorescence. Furthermore, CurNQ was cytotoxic to two OC cell lines demonstrating its applicability as a potential chemotherapeutic agent. Clearly, CurNQ has theranostic properties and may have applications in the simultaneous targeting, detection and treatment of OC.

3.5 References

1. Veeresham C. Natural products derived from plants as a source of drugs. J Adv Pharm Technol Res. 2012;3(4):200—201.
2. Ho TT, Tran QT, Chai CL. The polypharmacology of natural products. Future Med Chem. 2018;10(11):1361–8.
3. Rizwanullah M, Amin S, Mir SR, Fakhri KU, Rizvi MMA. Phytochemical based nanomedicines against cancer: current status and future prospects. J Drug Target. 2018;26(9):731–52.
4. Rais J, Jafri A, Siddiqui S, Tripathi M, Arshad M. Phytochemicals in the treatment of OC. Front Biosci. 2017;9:67–75.
5. Panda AK, Chakraborty D, Sarkar I, Khan T, Sa G. New insights into therapeutic activity and anti-cancer properties of curcumin. J Exp Pharmacol. 2017;9:31–45.
6. Ma Z, Wan H, Wang W, Zhang X, Uno T, Yang Q, et al. A theranostic agent for cancer therapy and imaging in the second near-infrared window. Nano Res. 2019;12(2):273–9.
7. Saroj S, Rajput SJ. Composite smart mesoporous silica nanoparticles as promising therapeutic and diagnostic candidates: Recent trends and applications. J Drug Deliv Sci Technol. 2018;44:349–65.
8. Chen H, Zhang W, Zhu G, Xie J, Chen X. Rethinking cancer nanotheranostics. Nat Rev Mater. 2017;2(1):1–36.
9. Feng Y, Panwar N, Tng DJH, Tjin SC, Wang K, Yong KT. The application of mesoporous silica nanoparticle family in cancer theranostics. Coord Chem Rev. 2016;319:86–109.
10. He M, Wang D, Zou D, Wang C, Lopes-Bastos B, Jiang WG, et al. Re-purposing of

curcumin as an anti-metastatic agent for the treatment of epithelial OC: In vitro model using cancer stem cell enriched OC spheroids. Oncotarget. 2016;7(52):86374–87.

11. Li P, Xin H, Liu W. Lawsone Inhibits Cell Growth And Improves The Efficacy Of Cisplatin In Skov-3 OC Cell Lines. African J Tradit Complement Altern Med. 2017;14(5):8–17.
12. Seo JH, Jeong KJ, Oh WJ, Sul HJ, Sohn JS, Kim YK, et al. Lysophosphatidic acid induces STAT3 phosphorylation and OC cell motility: Their inhibition by curcumin. Cancer Lett. 2010;288(1):50–6.
13. Stakes SJ. OCS: Development of the Risk of OC Algorithm (ROCA) and ROCA screening trials. Int J Gynecol Cancer. 2012;22:45–64.
14. Warburg O. The Metabolism of Carcinoma Cells. J Cancer Res. 1925;9(1):148–63.
15. Kasi PD, Tamilselvam R, Skalicka-Woźniak K, Nabavi SF, Daglia M, Bishayee A, et al. Molecular targets of curcumin for cancer therapy: An updated review. Tumor Biol. 2016;37(10):13017–28.
16. Mirzaei H, Shakeri A, Rashidi B, Jalili A, Banikazemi Z, Sahebkar A. Phytosomal curcumin: A review of pharmacokinetic, experimental and clinical studies. Biomed Pharmacother. 2017;85:102–12.
17. Sasaki H, Sunagawa Y, Takahashi K, Imaizumi A, Fukuda H, Hashimoto T, et al. Innovative preparation of curcumin for improved oral bioavailability. Biol Pharm Bull. 2011;34(5):660–5.
18. Park SY, Kim DSHL. Discovery of natural products from Curcuma longa that protect cells from beta-amyloid insult: A drug discovery effort against Alzheimer's disease. J Nat Prod. 2002;65(9):1227–31.
19. Wen S, Zhu D, Huang P. Targeting cancer cell mitochondria as a therapeutic approach. Future Med Chem. 2013;5(1):53–67.
20. Perrone D, Ardito F, Giannatempo G, Dioguardi M, Troiano G, Lo Russo L, et al. Biological and therapeutic activities, and anti-cancer properties of curcumin (Review). Exp Ther Med. 2015;10:1615–23.
21. Kunnumakkara AB, Bordoloi D, Harsha C, Banik K, Gupta SC, Aggarwal BB. Curcumin mediates anti-cancer effects by modulating multiple cell signaling pathways. Clin Sci (Lond). 2017;131(15):1781-1799
22. Sun K, Duan X, Cai H, Liu X, Yang Y, Li M, et al. Curcumin inhibits LPA-induced invasion by attenuating RhoA/ROCK/MMPs pathway in MCF7 breast cancer cells. Clin Exp Med. 2016;16(1):37–47.
23. Deng Y, Verron E, Rohanizadeh R. Molecular mechanisms of anti-metastatic activity of curcumin. Anti-cancer Res. 2016;36(11):5639–47.
24. Arshad L, Areeful Haque M, Bukhari SNA, Jantan I. An overview of structure-Activity relationship studies of curcumin analogs as antioxidant and anti-inflammatory agents.

Future Med Chem. 2017;9(6):605–26.
25. Yang X, Li Z, Wu Q, Chen S, Yi C, Gong C. Trail and curcumin codelivery nanoparticles enhance trail-induced apoptosis through upregulation of death receptors. Drug Deliv. 2017;24(1):1526-36.
26. Jung EM, Lee TJ, Park JW, Choi KS, Kwon TK. Curcumin sensitizes tumor necrosis factor-related apoptosis-inducing ligand (TRAIL)-induced apoptosis through reactive oxygen species-mediated upregulation of death receptor 5 (DR5). Carcinogenesis. 2005;26(11):1905–13.
27. Sabarwal A, Kumar K, Shyanti R, Singh RP. Curcumin in Cancer Prevention. In: Yadav RVU. ed 1. Functional Food and Human Health. Singapore: Springer; 2018:329–74.
28. Yu Z, Wan Y, Liu Y, Yang J, Li L, Zhang W. Curcumin induced apoptosis via PI3K/Akt-signalling pathways in SKOV3 cells. Pharm Biol. 2016;54(10):2026–32.
29. Baglole KN, Boland PG, Wagner BD. Fluorescence enhancement of curcumin upon inclusion into parent and modified cyclodextrins. J Photochem Photobiol A Chem. 2005;173:230–7.
30. Chignell CF, Bilski P, Reszka KJ, Motten AG, Sik RH, Dahl TA. A Spectral and photochemical properties of curcumin. Photochem Photobiol. 1994;59(3):295–302.
31. Priyadarsini KI. Photophysics, photochemistry and photobiology of curcumin: Studies from organic solutions, bio-mimetics and living cells. J Photochem Photobiol C Photochem Rev. 2009;10(2):81–95.
32. Wang YJ, Pan MH, Cheng AL, Lin LI, Ho YS, Hsieh CY, et al. Stability of curcumin in buffer solutions and characterisationof its degradation products. J Pharm Biomed Anal. 1997;15(12):1867–76.
33. Nelson KM, Dahlin JL, Bisson J, Graham J, Pauli GF, Walters MA. The Essential Medicinal Chemistry of Curcumin. J Med Chem. 2017;60(5):1620–37.
34. Zhang Y, Khan AR, Fu M, Zhai Y, Yu A, Zhai G. The progresses in curcuminoids-based metal complexes: Especially in cancer therapy. Future Med Chem. 2019;11(9):1035–56.
35. Oliveira AS, Brighente IMC, Lund RG, Llanes LC, Nunes RJ, Bretanha LC, et al. Antioxidant and Antifungal Activity of Naphthoquinones Dimeric Derived from Lawsone. J Biosci Med. 2017;5:39–48.
36. Ouk S, Liou M-L, Liou H-C. Direct Rel/NF-κB inhibitors: structural basis for mechanism of action. Future Med Chem. 2009;1(9):1683–707.
37. Pereyra CE, Dantas RF, Ferreira SB, Gomes LP, Silva FP. The diverse mechanisms and anti-cancer potential of naphthoquinones. Cancer Cell Int. 2019;19(1):1–20.
38. Kanaan YM, Das JR, Bakare L, Enwerem NM, Berhe S, Beyene D, et al. Biological evaluation of 23-dichloro-5,8-dimethoxy-1,4-naphthoquinone as an anti-breast cancer

agent. Anti-cancer Res. 2009;29(1):191–9.

39. Dias GG, King A, De Moliner F, Vendrell M, Da Silva Júnior EN. Quinone-based fluorophores for imaging biological processes. Chem Soc Rev. 2018;47(1):12–27.
40. Dabiri M, Tisseh ZN, Bazgir A. Synthesis of fluorescent hydroxyl naphthalene-1,4-dione derivatives by a three-component reaction in water. Dye Pigment. 2011;89(1):63–9.
41. Lin YG, Kunnumakkara AB, Nair A, Merritt WM, Han LY, Armaiz-Pena GN, et al. Curcumin inhibits tumor growth and angiogenesis in ovarian carcinoma by targeting the nuclear factor-κB pathway. Clin Cancer Res. 2007;13(11):3423-30.
42. Penet MF, Mikhaylova M, Li C, Krishnamachary B, Glunde K, Pathak AP, et al. Applications of molecular MRI and optical imaging in cancer. Future Med Chem. 2010;2(6):975–88.
43. Kolev TM, Velcheva EA, Stamboliyska BA, Spiteller M. DFT and experimental studies of the structure and vibrational spectra of curcumin. Int J Quantum Chem. 2005;102(6):1069–79.
44. Sreelakshmi C, Goel N, Datta KKR, Addlagatta A, Ummanni R, Reddy BVS. Green synthesis of curcumin capped gold nanoparticles and evaluation of their cytotoxicity. Nanosci Nanotechnol Lett. 2013;5(12):1258–65.
45. Safie EN, Ludin AN, Su SM, Hamid HN, Sepeai S, Ibrahim AM, et al. Preliminary study of natural pigments photochemical properties of curcuma longa l. and lawsonia inermis l. as tio 2 photoelectrode sensitizer. Malaysian J Anal Sci. 2015;19(6):1243–9.
46. Rachmawati H, Yanda YL, Rahma A, Mase N. Curcumin-loaded PLA nanoparticles: Formulation and physical evaluation. Sci. Pharm. 2016; 84(1):191-202.
47. Van NT, Kimpe DN. Synthesis of 6H-naphtho[2,3-c]chromene-7,12-diones via palladium-catalyzed intramolecular cyclization of 2-bromo-3-aryloxymethyl-1,4-naphthoquinones. Tetrahedron. 2003;59(31):5941–6.
48. Laitinen R, Lőmann K, Strachan CJ, Grohganz H, Rades T. Emerging trends in the stabilization of amorphous drugs. Int J Pharm. 2013;453(1):65–79.
49. Rumondor ACF, Dhareshwar SS, Kesisoglou F. Amorphous Solid Dispersions or Prodrugs: Complementary Strategies to Increase Drug Absorption. J Pharm Sci. 2016;105(9):2498–508.
50. Trasi NS, Taylor LS. Dissolution performance of binary amorphous drug combinations - Impact of a second drug on the maximum achievable supersaturation. Int J Pharm. 2015;496(2):282–90.
51. Duuren BLV. The Fluorescence Spectra of Aromatic Hydrocarbons and Heterocyclic Aromatic Compounds. Anal Chem. 1960;32(11):1436–42.
52. Qi Y, Huang Y, Li B, Zeng F, Wu S. Real-Time Monitoring of Endogenous Cysteine Levels in Vivo by near-Infrared Turn-on Fluorescent Probe with Large Stokes Shift. Anal

Chem. 2018;90(1):1014–20.
53. Zanella F, Lorens JB, Link W. High content screening: Seeing is believing. Trends Biotechnol. 2010;28(5):237–45.
54. Zock J. Applications of High Content Screening in Life Science Research. Comb Chem High Throughput Screen. 2009;12(9):870–6.
55. Robertson JD, Orrenius S, Zhivotovsky B. Review: Nuclear events in apoptosis. J Struct Biol. 2000;129(2–3):346–58.

Chapter 4: Theranostic Mesoporous Silica Nanoparticles for Potential Cancer Targeting, Diagnostic and Treatment Applications

4.1 Introduction

Leaky tumour vasculature is a hallmark feature of cancer. This induces nanoparticles to leak out of tumour blood vessels [1]. This phenomenon does not occur in heathy vessels owing to well-organized branching and regularly spaced capillary beds. This highly structured vessel is not apparent in tumour vasculature on account of rapid tumour growth, allowing for the leaking of nanoparticles into the tumour interstitium. Concurrently, poor tumour lymphatic drainage enables nanoparticle accumulation and enhanced retention [2,3]. The automatic accumulation of nanoparticles in tumour tissue has been well documented and is referred to as the Enhanced Permeation and Retention (EPR) effect [1]. This effect has been the rationale behind the field of nanomedicine for cancer intervention. EPR allows for the passive targeting of nanoparticles to tumour tissue [4]. The addition of an active targeting strategy in conjunction with EPR can allow for enhanced tumour targeting capabilities.

Mesoporous silica nanoparticles (MSN) are a class of nanoparticles that have been widely studied for drug delivery applications. Silica is one of the most abundant natural resources and has been deemed safe and is widely used in food additives, pharmaceutical products and cosmetics. With the explosion into nanomedicine research, silica has been the focus of an abundance of research, mainly in terms of drug delivery [5,6]. MSN have numerous features that make them ideal for advanced drug delivery. These features include their solid framework, high surface to volume ratio, them being mesoporous thereby allowing for drug loading, their chemically inert nature, along with their biocompatibility, biodegradability and that they show no toxicity *in vitro* [7–11]. Moreover, their hydrophilic silanol surface is ideal for the delivery of low solubility drugs and allows for easy surface functionalization [10]. The large pores evenly distributed over the surface of MSN are ideal for drug loading, especially for the loading of hydrophobic drugs. The loading of hydrophobic drugs into MSN has become a standard approach in the delivery of hydrophobic drug molecules. The poor solubility

of these drugs is overcome as EPR delivers these loaded drugs directly into the tumour [12]. These properties of MSN make them ideal for the delivery of the novel molecule CurNQ. Consequently, MSN were selected as the nanoparticle of choice for CurNQ delivery.

New cancer therapies should circumvent the issues that plague current chemotherapeutics, some of which include: high toxicity, non-specificity, cancer resistance and the lack of early detection systems [2,13]. One of the current trends in cancer research is the development of advanced platforms using nanotechnology that allows for simultaneous diagnostics and treatment, this field of research is referred to as theranostics [14]. Concurrent diagnostics and treatment would allow for earlier detection and treatment of malignancy, resulting in improved prognosis and lower mortality rates [15].

Theranostic intervention is often achieved using nanotechnology. Nanomedicine has become of great interest in the field of cancer research on account of enhancements to drug delivery mechanisms [1]. A significant barrier to cancer treatment is the non-specificity of treatment which induces severe side effects and reduces treatment efficacy [13,16]. The targeting of treatment to cancer cells would reduce systemic toxicity and increase treatment effectiveness and thus is of immense interest [15]. The tuneable and controllable drug delivery that can be achieved using nanomedicine has propelled this field forward into the spotlight of cancer intervention [17].

The novel theranostic molecule described in the previous chapter was designed for the purpose of simultaneous cancer targeting, detection and treatment and was termed CurNQ (Chapter 3). The aim of this chapter was to enhance the theranostic capabilities of the novel molecule through advanced drug delivery techniques through the formation of a detectable fluorescent nanoparticle. The inclusion of MSN aimed to allow for the fluorescence of CurNQ to be detected and tracked. Moreover, MSN aimed to enhance the targeting capabilities on account of the EPR effect. Chapter 4 presents the synthesis of the complete nanosystem and explores its theranostic properties *in vitro*. Chapter 4 demonstrates the synthesis of MSN with an average size of 108 d.nm, a zeta potential of -42 mV and a PDI of 0.150. MSN were impregnated with CurNQ to form the novel nanosystem MSN_CurNQ. MSN_CurNQ was demonstrated to have pH-

responsivity whereby after 96 hours, at pH 7.4 31.5% of CurNQ was released from the MSN compared to 57% release at pH 6.8, corresponding to an 25.5% increase in release with a 0.6 pH drop. The innate fluorescence was then characterised through confocal and fluorescence microscopy. Microscopy images illustrated the clear, distinct, specific, high intensity innate fluorescence of MSN_CurNQ which also demonstrated a high background to target ratio, thus confirming detection capabilities and potentially extending MSN_CurNQ's application to molecular imaging purposes. Moreover, the chemotherapeutic potential of MSN_CurNQ was demonstrated as cell viability was reduced to below 50% in OVCAR-5, CACO-2, CHLA and MCF-7 cell lines. Furthermore, MSN_CurNQ displayed tumour specific toxicity whereby the cell viability was reduced to a far greater extent in the cancer cell lines compared to a healthy fibroblast cell line (p=0.000). Indeed, the novel MSN_CurNQ nanosystem has potential for applications in cancer targeting, detection and treatment.

4.2 Materials and Methods

4.2.1 *Materials*

Hexadecyltrimethylammonium bromide (CTAB; MW- 364.45), Pluronic F-127 (MW – 12600), Tetraethyl orthosilicate (TEOS; MW - 208.33), Phalloidin-Atto 488 (MW- 1472) and 4′,6-Diamidine-2′-phenylindole dihydrochloride (DAPI, MW- 350.25) were purchased from Merck/Sigma Aldrich (Darmstadt, Germany) and were used as received. High purity solvents (>98%) were purchased from ACE chemicals (Johannesburg, South Africa) and were also used as received. Cell lines were all purchased from Cell Biolabs Inc (San Diego, USA) and from Fox Chase Cancer Center (Philadelphia, USA). Cell culture consumables, 3- [4,5- dimethylthiazol-2-yl]-2,5-diphenyl tetrazolium bromide (MTT), and other cell culture reagents were purchased from Thermo Fischer Scientific (Waltham, USA).

4.2.2 *Mesoporous silica nanoparticle synthesis*

Mesoporous silica nanoparticles (MSN) were synthesised using a modified method originally reported by Yang and co-workers (Figure 4.1) [18]. Briefly, 1 g of cetrimonium bromide and 1 g of Pluronic F-127 was added to 480 mL of deionised water and was mixed at room temperature until a clear solution was obtained. To this, 3.5 ml of 2M

sodium hydroxide was added and the temperature was slowly increased to 80 °C. Once this temperature was kept constant, 6 mL of tetraethyl orthosilicate (TEOS) was added dropwise to the stirring solution at a constant drop rate. The solution was then allowed to stir rapidly for 2 hours. The solution was then filtered and dried at room temperature for 24 hours to obtain a white powder. This white powder was then calcined in a furnace at 550 °C for 5 hours to remove the unwanted surfactants.

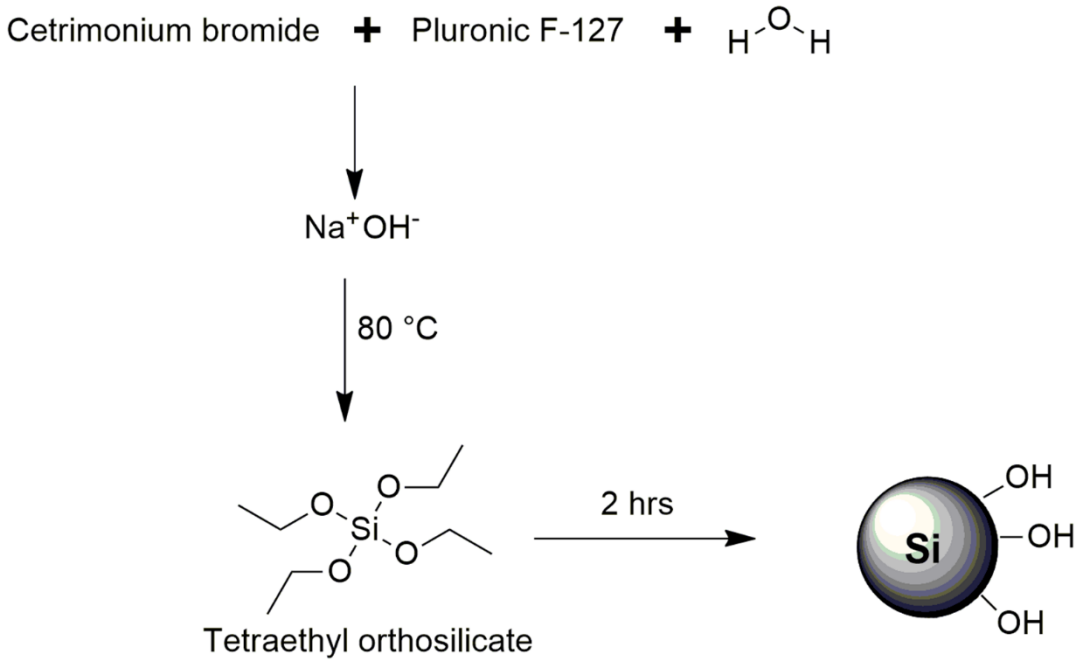


Figure 4.1: Reaction scheme for the synthesis of MSN

4.2.3 *Determination of MSN size and zeta potential*

The size and zeta potential of the synthesised silica nanoparticles were analysed using the Zetasizer Nano ZS (Malvern, UK.). Dilute 10 mL suspensions of nanoparticles were sonicated for 30 minutes at room temperature to reduce particle aggregation. 2 mL of the dispersed samples were filtered into disposable cuvettes and the size, polydispersity index (PDI) and zeta potential values were recorded at 25°C on the ZetaSizer Nano ZS.

4.2.4 *MSN morphological characterisation*

Scanning electron microscopy (SEM) using a FEI Nova Nanolab 600 SEM was performed to determine nanoparticle morphology as well as offered a confirmation of the size determined through dynamic light scattering (obtained on the Zeta Sizer). Powdered sample of the nanoparticles was placed onto an aluminium specimen stub covered with a double-sided carbon adhesive disc and placed under a vacuum, flushed with argon, evacuated and sputter coated with gold for 4 minutes at 20kV. SEM images were obtained on a FEI Nova Nanolab 600 FEG-SEM/FIB.

4.2.5 *Loading of CurNQ into MSN to create novel nanosystem*

MSN were impregnated with CurNQ and were designated MSN_CurNQ. To achieve this, the methodology previously utilised by Jambhrunkar *et al* [19] to load Cur into MSN was followed owing to similarity. Here 40mg of CurNQ was dissolved in methanol and mixed with 160 g of MSN particles (1:4 ratio) rapidly for 24 hours at room temperature protected from light. The solvent was then slowly removed under reduced pressure using a rotary evaporator, further encouraging CurNQ entrapment. The particles were washed thrice with ethanol and twice with deionised water to remove unentrapped CurNQ and loaded particles were collected via centrifugation at 5000 rpm for 10 minutes. The particles were then dried in an oven overnight at 37 °C. The above procedure was repeated with Cur to produce MSN_Cur, which was to be used for comparative analyses.

4.2.6 *Determination of Encapsulation efficiency of CurNQ within MSN*

A mixture containing 40 mg of CurNQ and 160 mg of MSN was added to methanol and was stirred rapidly, allowing for loading to occur [19]. The UV absorbance of the solution was measured at 429 nm at varying time points over 48 hours.

$$Abs\ at\ start\ of\ experiement - Abs\ after\ 48\ hours = Abs\ corresponding\ to\ drug\ uptake$$

A decrease in absorbance over 48 hours was recorded and the concentration of drug uptake was calculated using a standard curve of concentration versus UV absorbance at 429 nm (R^2=0.99).

Encapsulation efficiency was then calculated using the formula:

$$\frac{drug\ uptake}{Total\ drug} \times 100$$

Entrapment efficiency values of 54.54% and 32.5% were computed for CurNQ and Cur, respectively. A decrease in UV absorbance indicated successful entrapment owing to CurNQ being impregnated into MSN thereby being removed from the solution.

4.2.7 *Determination of CurNQ release profile from MSN at varied pH*

CurNQ release from the MSN nanoparticles was measured at pH 7.4 and 6.8 at 37 °C for both MSN_CurNQ and MSN_Cur. One mg/mL of CurNQ-loaded nanoparticles were immersed in a PBS/CTAB solution and the pH of each sample was adjusted to mimic both physiological conditions (pH 7.4) and at the tumour microenvironment (pH 6.8). Samples were incubated and stirred on an orbital shaker incubator at a rate of 50rpm at 37 °C. At 12-hour intervals, 1 mL of buffer was removed, and UV absorbance was measured through UV/Vis spectroscopy at 429nm. Total CurNQ release was then calculated using a standard curve (R^2=0.99) for both CurNQ and Cur respectively. The experiment was performed in triplicate to ensure statistical reliability (N=3). The experiment was concluded after 96-hours as no more CurNQ was released after this time.

4.2.8 *In vitro determination of chemotherapeutic potential of MSN_CurNQ*

Multiple cell lines were used to determine the cytotoxic effects of MSN_CurNQ and MSN_Cur on a variety of cancer types. The following cell lines were cultured namely: OVCAR-5, 3T3, MCF-7, HeLa, CACO-2, HT-29 and CHLA. The cell lines were cultured using standard tissue culture techniques. Cells were either grown in RMPI 1640 or DMEM, depending on the guidelines specified by the cell line supplier. All media was supplemented with 10% foetal bovine serum (FBS) and 1% Streptomycin and penicillin [20]. Cells were incubated at 37ºC at 5% CO_2 atmospheric pressure. Once cells reached 80% confluency, cells were detached and sub-cultured using trypsin (0.05% w/v) and EDTA (0.01% w/v).

4.2.9 *Cytotoxicity studies through MTT assays*

Seven cell lines were cultured and the cytotoxicity of MSN_CurNQ and MSN_Cur was evaluated on all 7 cell lines. This allowed for an in-depth analysis of the cytotoxic effect of the loaded nanoparticles on a variety of cancer types. Cells were cultured as per above conditions. Upon the cells reaching 70-80% confluency, the cells were washed, and sub-cultured by harvesting using trypsin/EDTA. Thereafter, 1.5×10^4 cells (counted using trypan blue exclusion dye method) were plated in each well of a 96 well dish and were incubated at 37°C in 5% CO_2 for 24 hours, allowing for cell attachment. Subsequently, cells were treated with varying concentrations of MSN_CurNQ and MSN-Cur. Cells were incubated in treatments for 24, 48, and 72-hour time period. After which, 3- [4,5- dimethylthiazol-2-yl]-2,5-diphenyl tetrazolium bromide (MTT) reagent was added and left for 4 hours, subsequently, the MTT reagent was removed and DMSO was added to solubilize the formazan crystals. All samples were performed in quadruplicate for statistical reliability. Absorbance readings were then recorded on a Perkin Elmer Victor X3 2030 multilabel reader at 570 nm and 690 nm.

4.2.10 *Determination of Fluorescent properties of MSN_CurNQ using Confocal microscopy*

OVCAR-5 cells were cultured on coverslips and allowed to reach 70% confluency. Cells were then treated with MSN_CurNQ for 24 hours, thereby allowing for cellular uptake to occur. After this, Phalloidin-Atto 488 was added, and staining occurred over 30 minutes. Cells were then washed and fixed through incubation in 5% formaldehyde in PBS for 20 minutes. After fixation, DAPI stain was added at a concentration of 1 µg/mL and samples were left to incubate for 15 minutes in the dark. Hereafter, samples were washed thoroughly with PBS to remove unstained DAPI. Coverslips were stored in the dark in PBS. Coverslips were viewed on the Zeiss Laser Scanning Confocal Microscope (LSM) 780 (Oberkochen, Germany). Super resolution microscopy was performed using Airyscan technology as an add on feature to the LSM confocal microscope.

4.2.11 *Cytotoxicity studies using High Content Imaging System*

High content imaging is an advanced technique that combines high throughput techniques and fluorescent microscopy to obtain quantitative data from complex biological systems [21]. It is a robust method utilising an automated microscope that allows for rapid, high content image acquisition and analysis [22]. Cells were grown until 80% confluency prior to utilisation. Upon confluency, media was removed, and cells were washed twice in sterile PBS. Trypsin/EDTA was then added to the flasks and incubated at 37°C for 5 minutes, allowing the cells to detach from the bottom of the flask. These cells were then collected and centrifuged. The pellet was resuspended, and the cells were counted using the trypan blue exclusion assay. A predetermined and equal number of cells were then added into each well of a 96 well plate. The cells were incubated overnight at 37°C and at 5% CO_2, allowing the cells to attached to the plates. The following morning, cells were treated with each sample (MSN_CurNQ and MSN_Cur) at varying concentrations for 24 hours. Each treatment was performed in quintuplicate. After this time period, media was removed, and cells were fixed with 5% formaldehyde in PBS for 20 minutes. Next, cells were incubated for 15 minutes in a 1 µg/mL solution of DAPI. The plates were then washed several times with PBS to remove all residual DAPI and to reduce background fluorescence. All plates were stored in the dark. Plates were then run on the Logos Biosystem CELENA® X High Content Imaging System and analyses were performed using their proprietary software (Geonggi-do, South Korea).

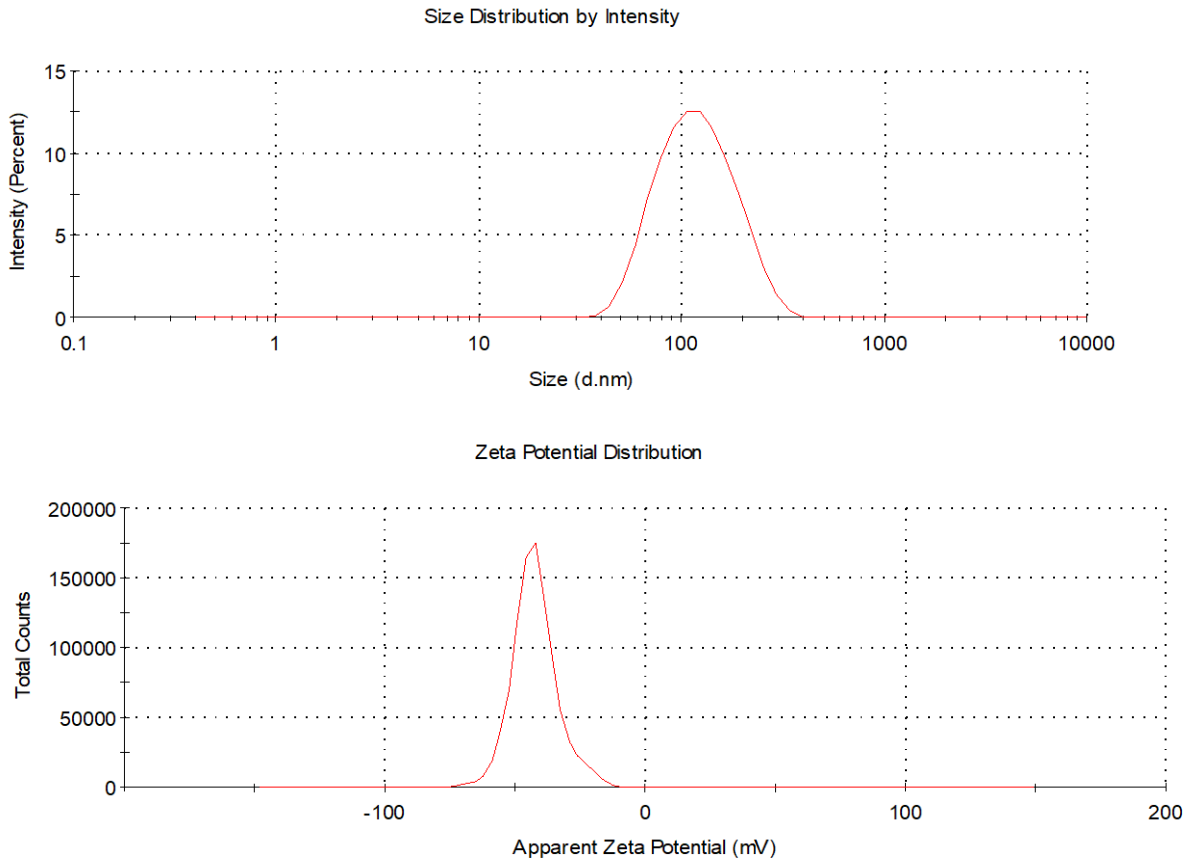
4.3 Results and Discussion

4.3.1 *Synthesis and characterisation of mesoporous silica nanoparticles*

Mesoporous silica nanoparticles (MSN) were synthesised and were aimed to act as a delivery platform for CurNQ [18]. Multiple methods for MSN synthesis were performed with their products being evaluated in terms of size, zeta potential ease of synthesis and reproducibility. A summary of synthesis routes performed is presented in Appendix C. Small particles with an average size around 100 d.nm with a substantial negative zeta potential were desired, allowing for the EPR effect as well as for the colloidal stability of the particles. A modified method from Yang, et al, allowed for the synthesis of MSN with the desired characteristics [18].

As shown in Figure 4.1, the average size of the synthesised MSN was determined to be 108 d.nm with a polydispersity index (PDI) of 0.150. Moreover, the zeta potential of the nanoparticles was determined to be -42 mV, confirming the colloidal stability of the nanoparticles with reduced potential for aggregation. Synthesis and particle evaluation were performed in triplicate to confirm reproducibility of desired MSN synthesis.

The particle size was further confirmed, and the morphology determined through scanning electron microscopy (SEM). This allowed for the surface of the nanosystem to be characterised and to ascertain if the morphology of the nanosystem was uniform. As seen in Figure 4.1, the particles displayed a uniform morphology, being oval in shape and the average size of the particles observed through the SEM concurred with the zeta analysis results, with an average approximate size of 108 d.nm. (Figure 4.1). This uniformity was expected owing to the low PDI value which indicated an overall low polydispersity of the sample.



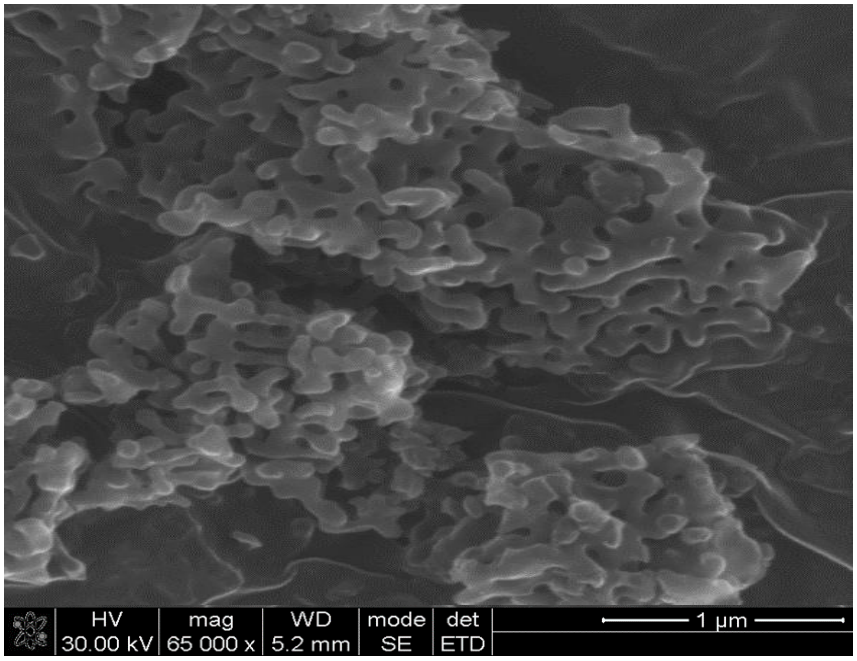


Figure 4.2: Size, morphology and zeta potential analysis of synthesised MSN. **A)** Size of MSM determined to be 108 d.nm through dynamic light scattering (N=3) **B)** Zeta potential of MSN obtained using the ZetaSizer and determined to be -42 mV (N=3) **C)** SEM microscopy image of the surface of MSN to evaluate surface morphology.

4.3.2 *Impregnation of MSN with CurNQ*

Following MSN synthesis and calcination, MSN was impregnated with CurNQ and Cur individually to create the nanosystems MSN_CurNQ and MSN_Cur respectively. This was achieved through rapid mixing of the MSN and CurNQ in a small volume of methanol protected from light at room temperature for 48 hours, allowing for CurNQ to be impregnated in the pores of the MSN. Successful loading of MSN with CurNQ was confirmed through UV/Vis absorbance readings. The absorbance readings were taken before, during and after the 48-hour period. A decline in absorbance readings corresponded to the uptake of the drug into the pores of the nanoparticles, thereby leaving the solution and reducing the absorbance of the solution. This uptake was quantified, and the encapsulation efficiency was calculated. Moreover, to further confirm successful CurNQ encapsulation the size of the loaded nanoparticles was measured and compared to the empty nanoparticles. As expected, the size of the CurNQ loaded particles increased upon drug loading from an average of 108 d.nm to 214 d.nm. This increase in size was owing to the pores of the particles being

impregnated with the product. The above process was repeated for the loading of Cur into MSN, thereby acting as a control. The entrapment efficiencies were calculated to be 54,54% and 32,5% for CurNQ and Cur respectively.

4.3.3 *Evaluation of pH-responsiveness of MSN_CurNQ*

To support constant cell growth and proliferation, a cancer cell increases glycolysis and bypasses oxidative phosphorylation, this allows for the rapid production of ATP and for cellular proliferation to continue unabated [21]. This phenomenon is known as the 'Warburg effect' and is a hallmark feature of oncogenesis. This increase in glycolysis induces the acidification of the ECM, owing to the production of lactate [21]. This results in the slight acidification of the tumour microenvironment and allows for the differentiation between cancerous and healthy tissue [21]. However, this overall pH reduction is slight. Therefore, exploiting this pH reduction to detect and target malignant cells would require a robust detection system which is highly pH sensitive and would elicit a large response to a small change in pH. As discussed in chapter 3, CurNQ displays pH-responsive solubility within the pH change that occurs during malignant transformation and demonstrated a substantial increase in solubility with a shift in pH from 7.4 to 6.8. Moreover, CurNQ was demonstrated to have high fluorescent intensity thereby releasing a strong fluorescent signal once soluble. It was thought that this shift in solubility and concurrent fluorescence could act as a molecular switch allowing for potential tumour targeting and detection applications.

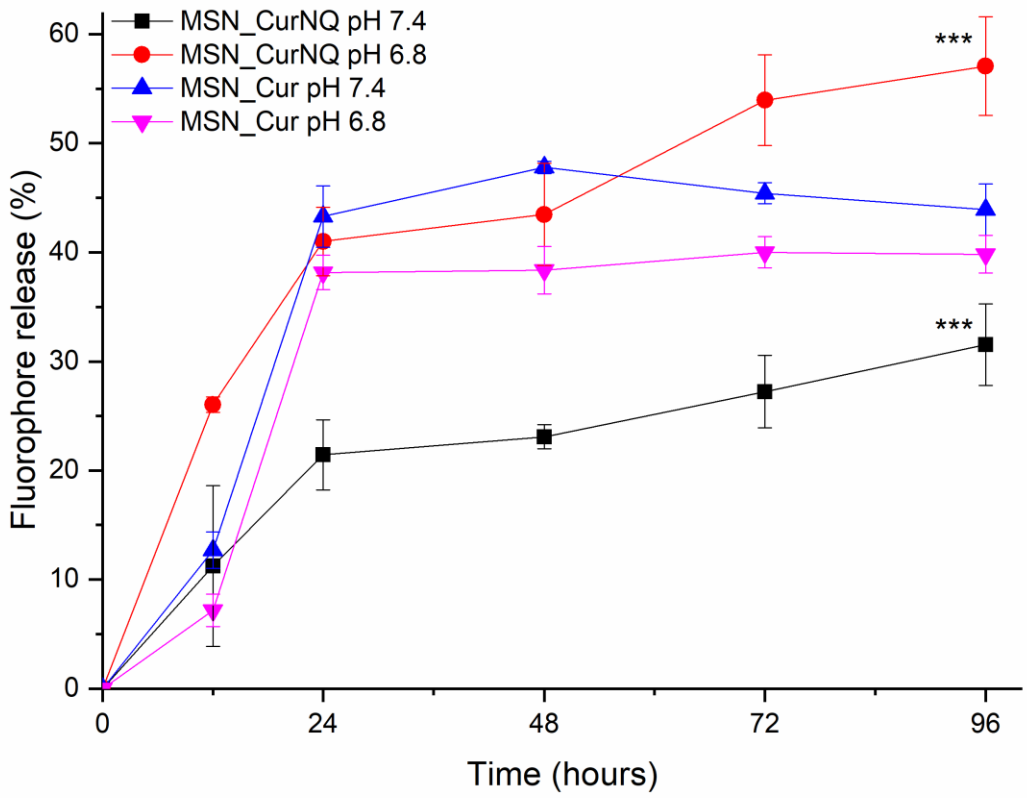


Figure 4.3: Release assay of CurNQ and Cur from MSN at pH 7.4 and pH 6.8 over a 96-hour period.

It was of interest to determine if this molecular switch occurred when CurNQ was loaded onto MSN and if this molecular switch could be exploited for cancer targeting; therefore, a release assay of CurNQ from the MSN was performed at pH 7.4 and pH 6.8. This assay again included MSN_Cur acting as a comparison and allowed for the novelty of this pH switch to be highlighted. As seen in Figure 4.3, there was a large difference between the release profile of CurNQ at pH 7.4 compared to at pH 6.8, as well as a highly statistically significant different release profile between MSN_CurNQ and MSN_Cur ($p=0.0001$). The release of CurNQ at pH 6.8 is just less than double its release at pH 7.4. At physiological pH (7.4), there was only 10% release within the first 12 hours, with it reaching 20% after 24 hours and peaking at 31,5% at 96 hours.

This was in stark contrast to the release profile of MSN_CurNQ at pH 6.8. With this small reduction in pH, the novel nanosystem released 43,45% after 48 hours, with the release peaking at 57% at 96 hours. This equates to a 25,5% increase in release occurring in response to a 0.6 reduction in pH. Consequently, the release of CurNQ at

pH 6.8 was almost double the release at pH 7.4. This difference in release between the two pH values was highly statistically significant with a corresponding p-value of 0.000. This highly significant p-value confirms the effects of pH on the release of CurNQ from the MSN, verifying the pH responsivity and specificity of the nanosystem. Moreover, this highly statistically significant p-value emphasizes the robust nature of CurNQ pH-responsivity. Clearly, the change in pH associated with malignant transformation acts as a solubility switch for CurNQ. This pH specificity was not observed for MSN_Cur (p=0.31), and notably MSN_Cur exhibited a slightly greater release at physiological pH, thereby indicating its non-specific pH solubility and its inability to act as a tumour targeting agent.

The synthesis of CurNQ saw the addition of two quinone moieties and the substantial pH dependent release profile difference between Cur and CurNQ can be attributed to the addition of these quinone moieties. Quinones undergo a reversible two-electron redox reaction and the corresponding redox potential is strongly pH dependent. At acidic pH, reduction occurs and is a single step two-electron two-proton process and this reduction forms a hydroquinone and this hydroquinone form has a greater solubility than the quinone form [22]. Thus, this redox reaction accounts for the switch in solubility and the pH dependent release.

The release profile aligns with the saturation solubility results presented in chapter 3. At pH 7.4 CurNQ's saturation solubility was determined to be 11.5 µM, compared to 20.7 µM at pH 6.8. This drastic increase in solubility in response to a small change in pH is what would allow CurNQ to act as a cancer targeting molecule through a pH specific solubility switch. Figure 4.3 confirms that this solubility switch occurs once CurNQ was loaded into MSN as the release of CurNQ from the MSN occurred in a pH dependant manner.

Furthermore, Figure 4.3 demonstrated the increase of release of CurNQ over a period of 96 hours thereby demonstrating sustained release of CurNQ from the MSN. This sustained release is imperative to allow for the fluorescent detection of a tumour and to offer effective treatment upon release, owing to sustained exposure to the anti-cancer agent. Again, this sustained release is not evident in MSN_Cur, as after 48

hours, there is no longer further release of Cur, further highlighting the novelty and applicability of the novel nanosystem.

Targeting the slightly acidic tumour microenvironment for tumour targeting, detection and specific drug release has been of great interest for cancer theranostic applications. Several strategies have been investigated by several researchers to achieve this. Such strategies have included the modification of nanoparticles whereby their surface was modified with a pH sensitive compound such as glycol chitosan or through the introduction of protonatable groups. Other avenues include using polymers whereby acid labile bonds are introduced or through an amphiphilic polymer triggered prodrug. Other researchers have used calcium carbonate nanocrystals loaded with cancer drugs that disassociate at the tumour microenvironment, thereby releasing the drug at the desired location [23–24]. Moreover, many of these strategies utilise the acidic pH of the exosome or lysosome that allows for drug uptake, as the pH in the exosome or lysosome is substantially different to the pH of the cytosol or the microenvironment, thus pH differentiation is easier to achieve compared to the highly sensitive system that is required to detect the change to a slightly acidic microenvironment that accompanies malignancy [23–24].

The realisation of pH-responsiveness in this study differs to all the strategies mentioned above. To best of our knowledge we are not aware of any active compound that intrinsically offers robust pH sensitivity without the addition of nanomaterials or pH sensitive groups. The simplicity of the pH-responsive solubility of the active compound is unique and is highly novel, especially owing to the sensitivity and alignment to the pH change that occurs during malignancy. Not only is the molecule highly pH specific which is rare, but it offers this specificity at the exact change in pH that is stimulated in response to oncogenesis. Clearly, this is an exceptional finding and can be exploited for tumour targeting and detection applications.

4.3.4 *Evaluating the innate fluorescence of MSN_CurNQ and its detection capabilities*

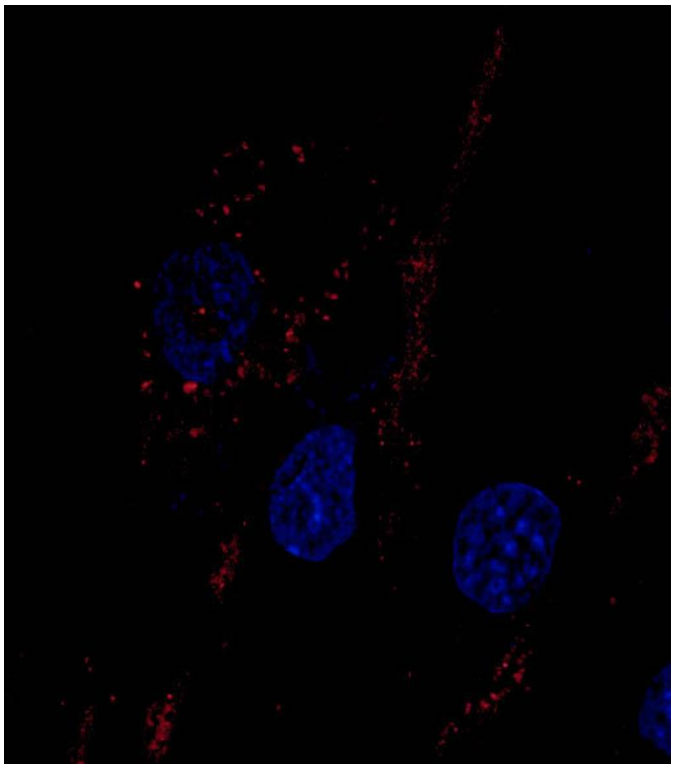
As discussed in detail in chapter 2, the need for novel fluorophores for imaging applications is immense and there is a wide range of possible applications for *in vivo* imaging and detection devices. The synthesis of a fluorescent compound that is ideal

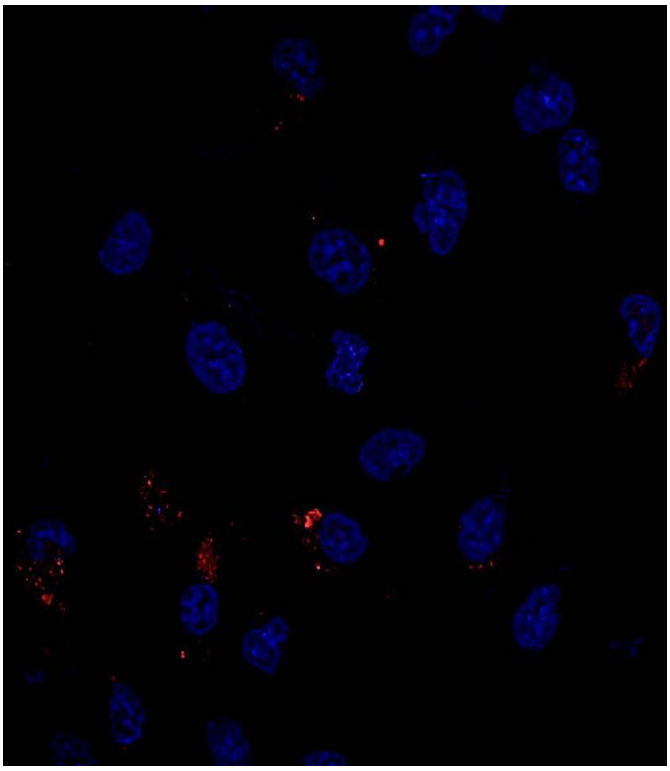
for imaging applications is a large area of research. Here, the aim was to extend previous research in the synthesis of a novel fluorescent compound that possesses additional theranostic attributes. The considerations when designing a new fluorescent compound that is ideal for imaging applications is immense. An ideal fluorophore for imaging applications should have an appropriate background to target ratios, high specificity, appropriate absorption and emission wavelengths to avoid tissue autofluorescence, appropriate solubility and fluorescence stability, exhibit cell permeability and have a long fluorescent lifetime. The synthesis of a fluorophore that fulfils these requirements is a large task and is a vast area of research (Chapter 2).

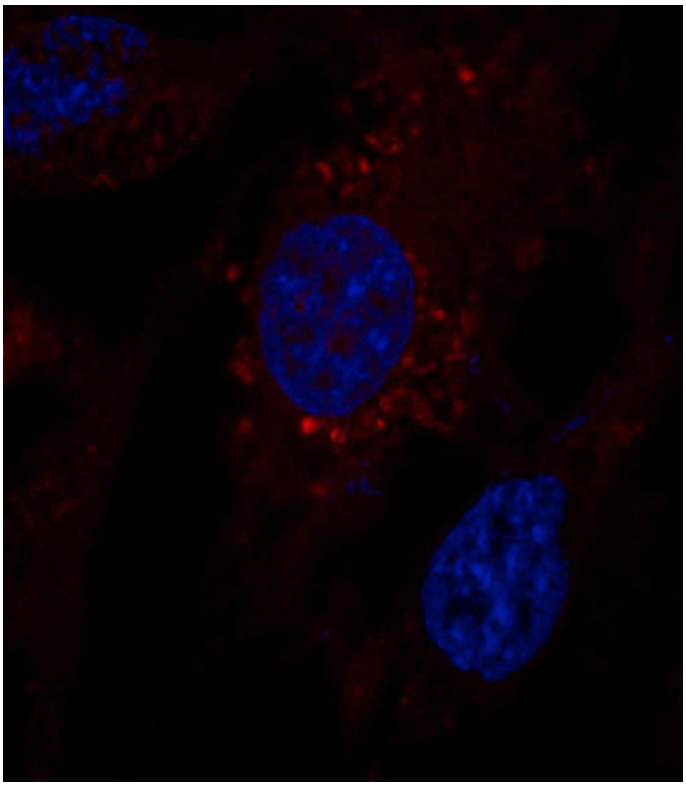
As presented in chapter 3, CurNQ has a high fluorescence intensity and as discussed above its pH-responsive solubility would allow it to release a fluorescent signal at the pH of the tumour microenvironment. However, without the loading of CurNQ onto a nanoparticle, the fluorescence of CurNQ cannot properly be traced and visualised, as generalised fluorescence is difficult to pinpoint *in vitro* and *in vivo*. Therefore, the loading of CurNQ onto a delivery vehicle is crucial to exploit its fluorescent capabilities for detection applications. In order to explore these fluorescent capabilities and to determine if MSN_CurNQ can be used for detection and imaging applications, confocal microscopy utilising super resolution Airyscan technology and fluorescent microscopy on the CELENA® X High Content Imaging System were performed.

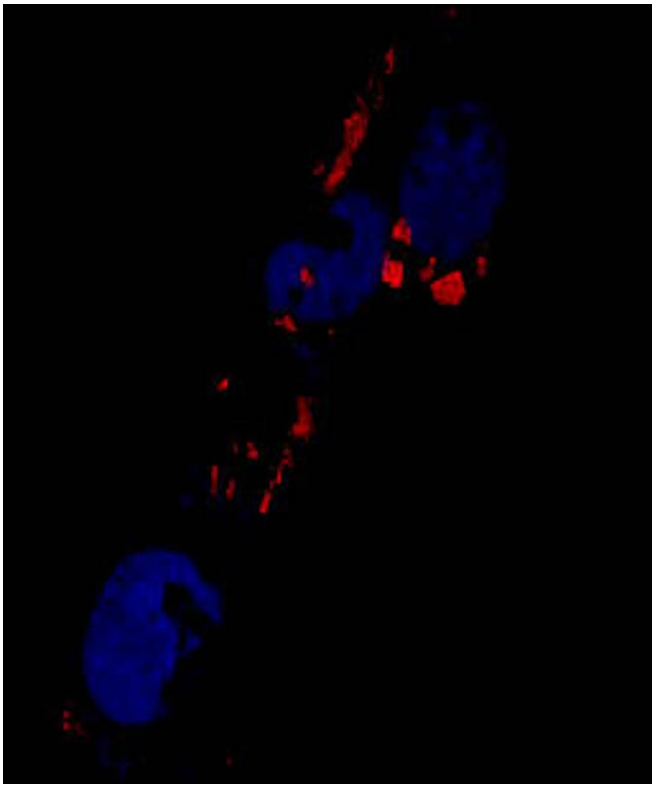
These assays were used to verify fluorescence and to determine whether the loaded nanoparticles could be accurately detected and visualised using the innate fluorescent properties of CurNQ; moreover, cellular uptake could be evaluated. Cellular uptake is important as for an active compound to exert its desired effect, it is required to enter the cell. The OC cell line OVCAR-5 was utilised for this assay. This cancer cell line was selected owing to the promising results which were observed in chapter 3, and consequently OC was used throughout as the model cell line to evaluate the novel theranostic molecule.

Cells were incubated with MSN_CurNQ for 24 hours, to allow for cellular uptake to occur. Subsequently, cells were fixed in formaldehyde and stained with DAPI. The cells were then viewed under the Zeiss LSM 780 confocal microscope (Figure 4.4 and 4.5) as well as the CELENA® X High Content Imaging System (Figure 4.6).









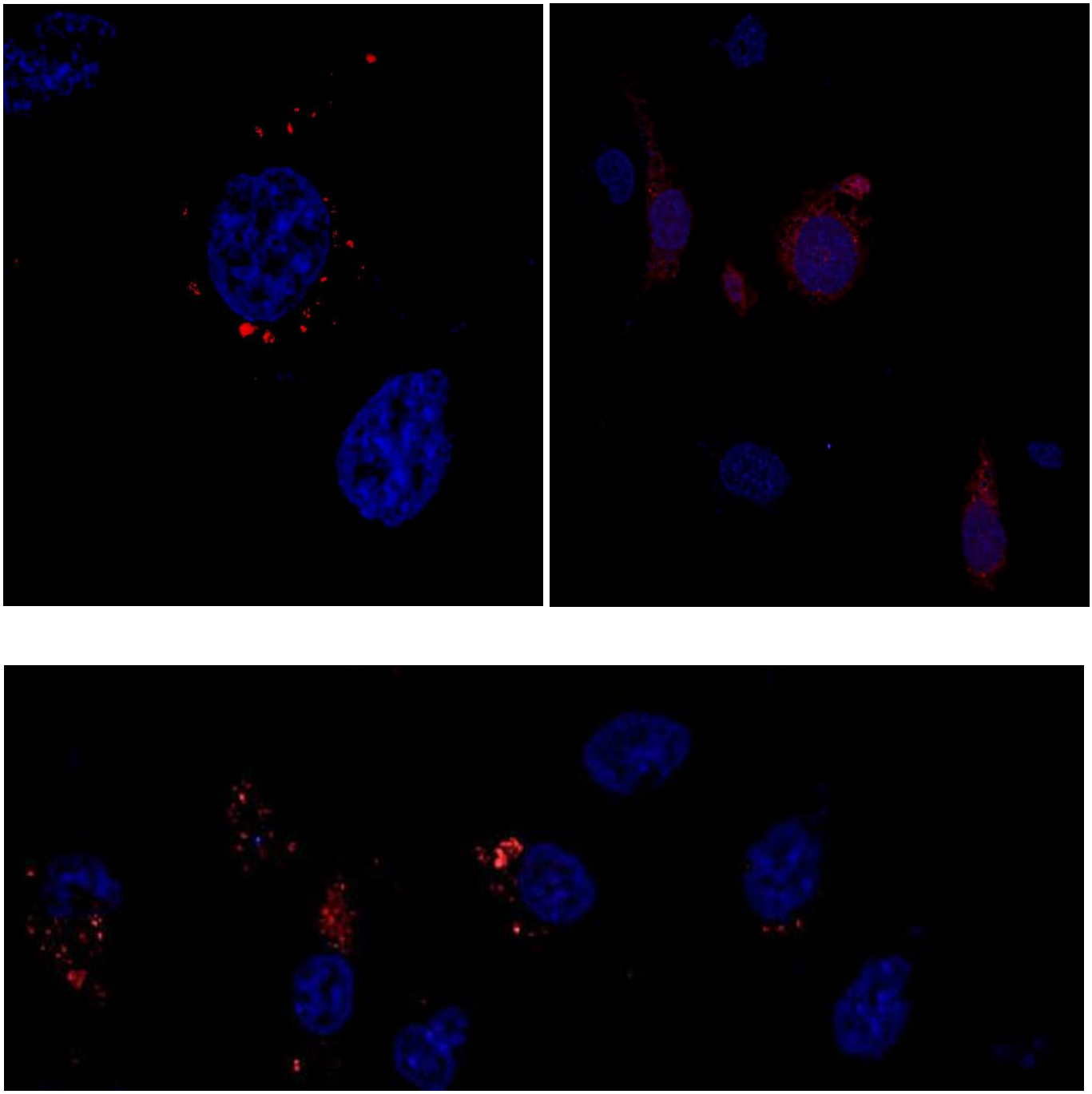


Figure 4.4: Confocal microscopy images of MSN_CurNQ in OVCAR-5 cells after 24 hours. Blue fluorescence is DAPI nuclear staining and red fluorescence is MSN_CurNQ.

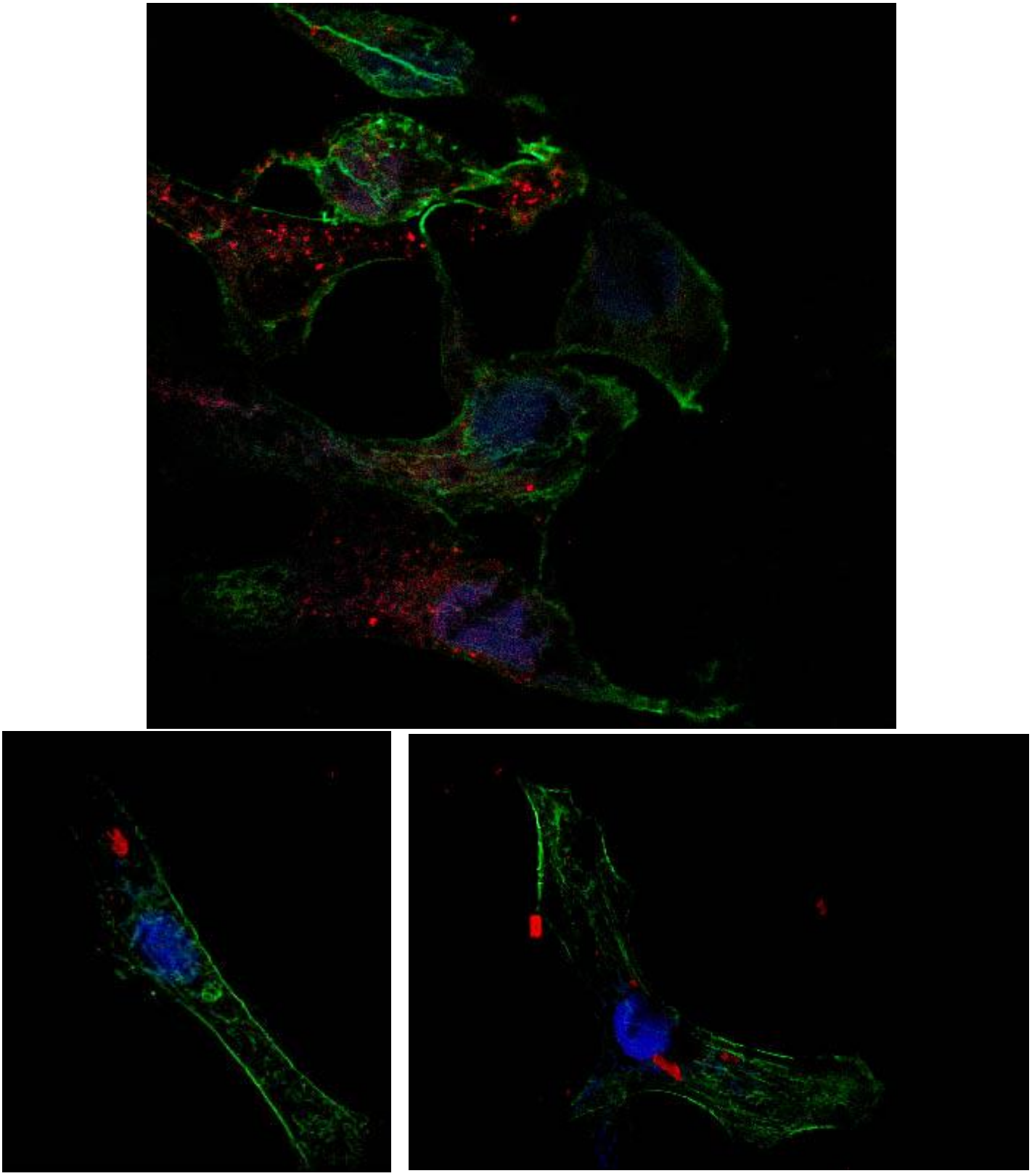
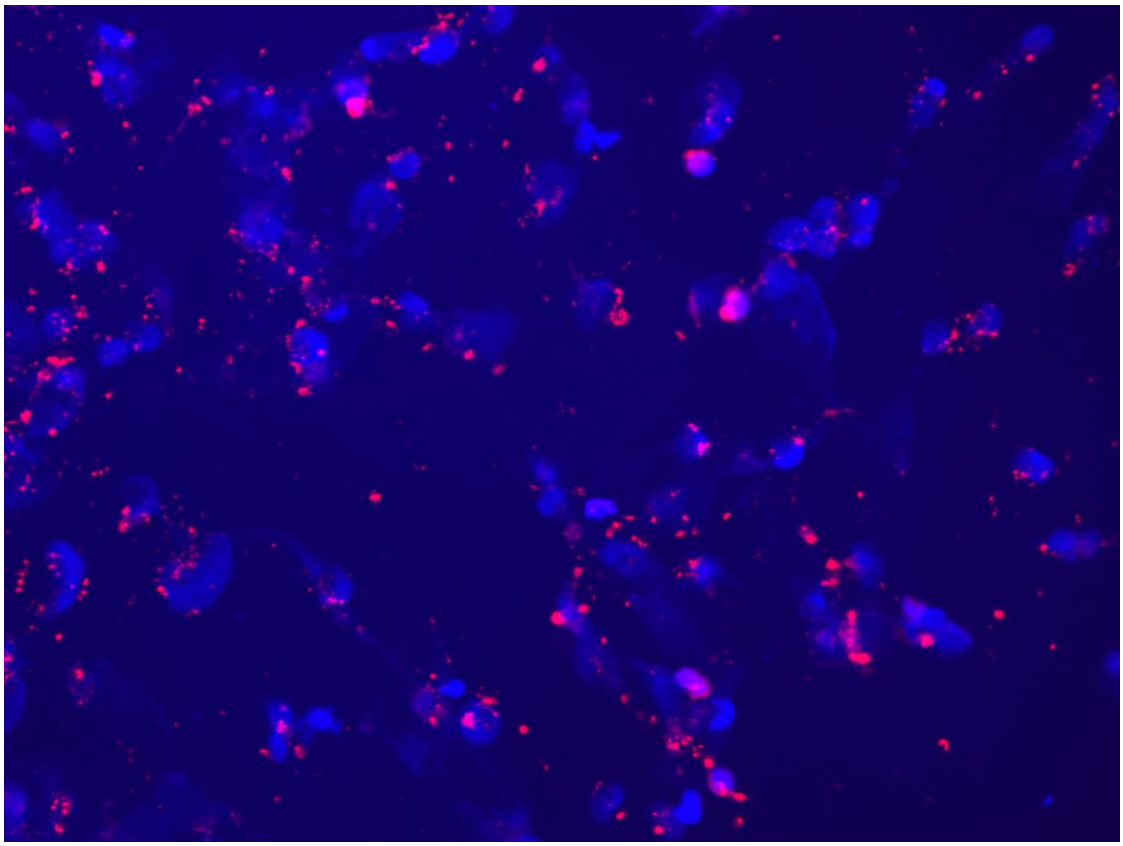
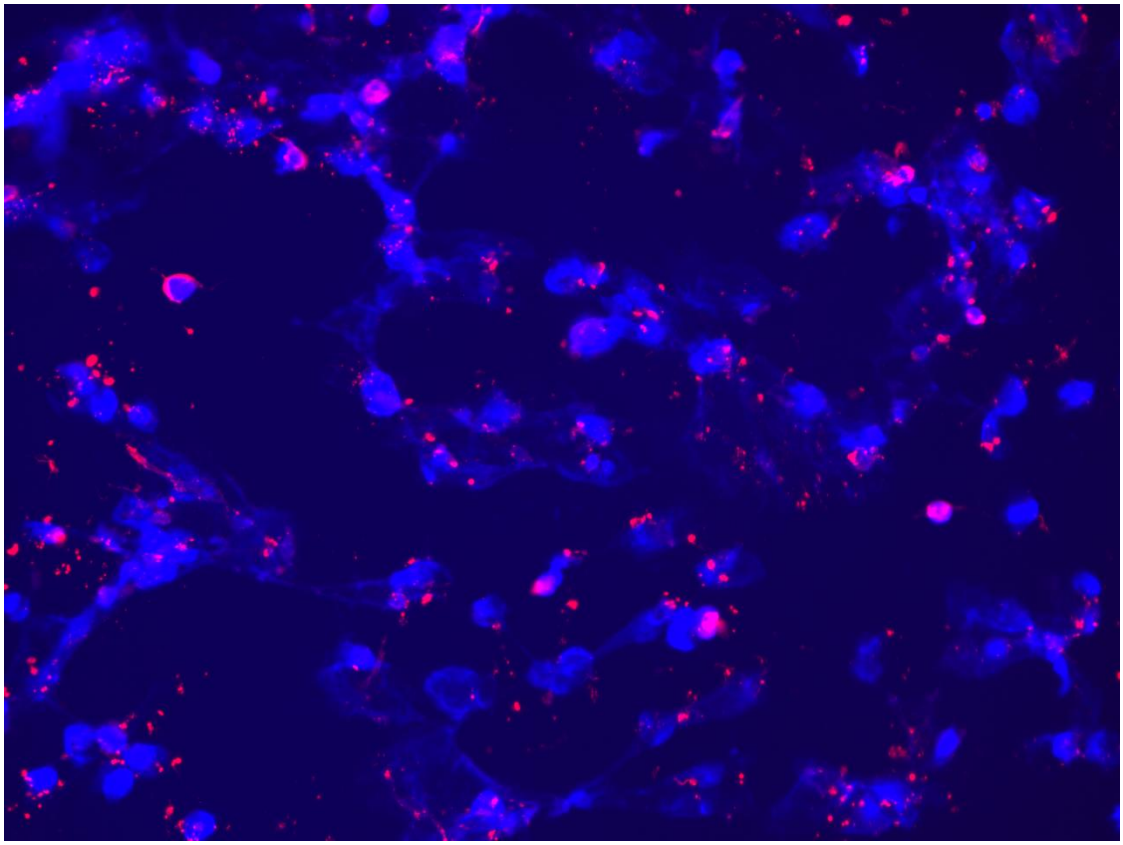


Figure 4.5: Confocal microscopy images of MSN_CurNQ in OVCAR-5 cells after 24 hours. Blue fluorescence is DAPI nuclear staining, green fluorescence is Phalloidin-Atto 488 actin stain and red fluorescence is MSN_CurNQ.

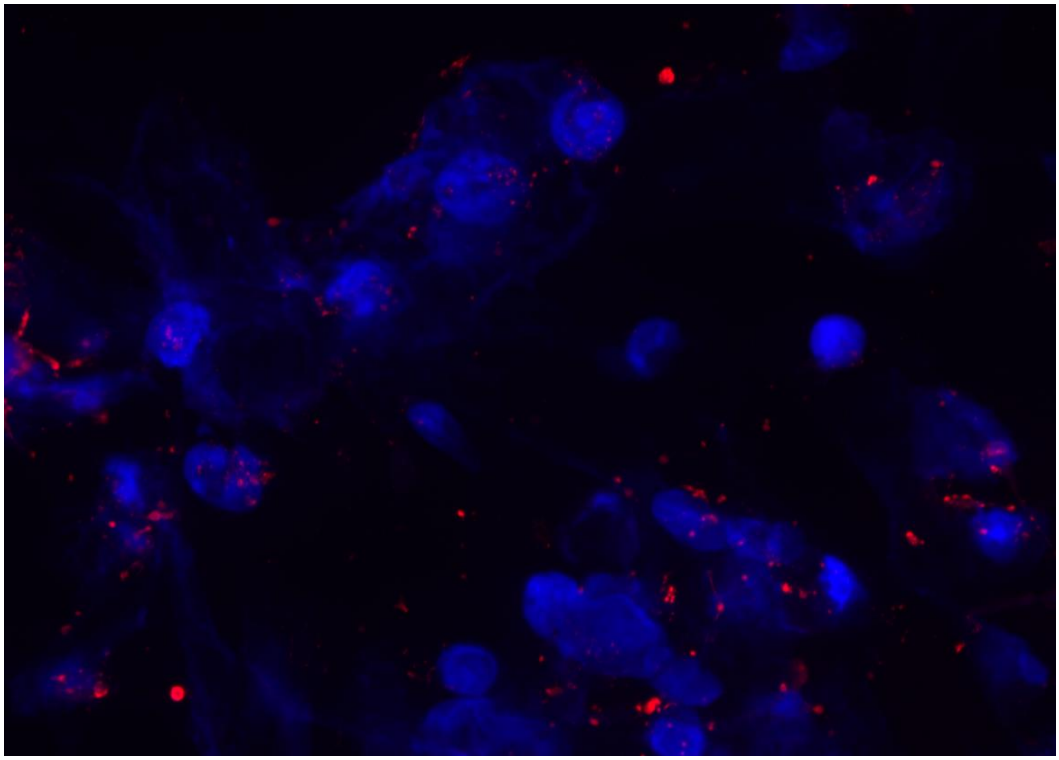
A



B



C



D

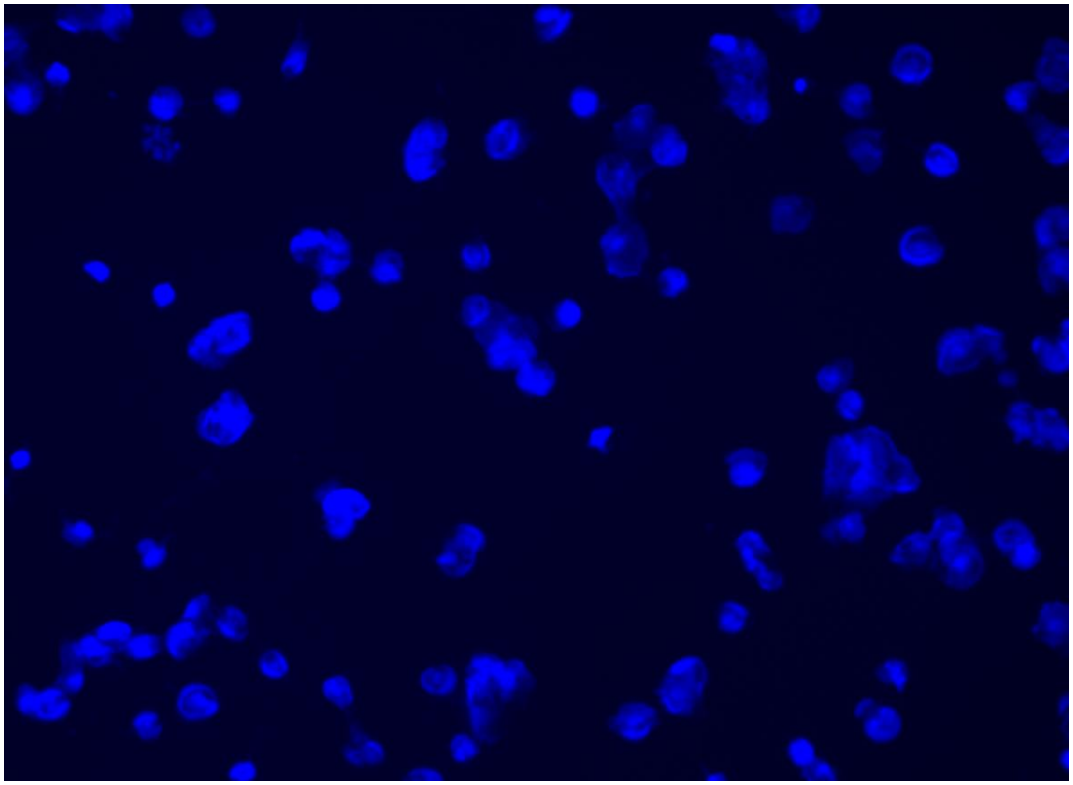


Figure 4.6: Fluorescent microscopy images acquired on the CELENA® X High Content Imaging System of OVCAR-5 cells incubated with MSN_CurNQ for 24 hours. Blue fluorescence is DAPI nuclear staining and red fluorescence is MSN_CurNQ. **D)** Cells given no treatment (control). No red fluorescence is present in the control group, confirming fluorescence is from MSN_CurNQ.

As seen in the microscopy images, MSN_CurNQ displayed clear, distinctive, high intensity fluorescence. The fluorescence was distinctive enough to pinpoint small clusters of nanoparticles, with almost no fluorescent blur. Moreover, an exceptionally high target to background ratio was observed with almost no background or unspecific fluorescence. This is a crucial requirement for a fluorophore effective for *in vivo* imaging. Hence, this distinctive and precise fluorescence with low background poses MSN_CurNQ as a potentially powerful imaging agent. Cell permeability is critical to allow for internal cellular imaging, as well as required for therapeutic applications; as seen in the above images, MSN_CurNQ exhibited cell permeability, and was evenly distributed throughout the cytoplasm. No loss of fluorescent intensity was observed after repetitive imaging over time using the same sample, therefore MSN_CurNQ has a long fluorescent lifetime, has stable fluorescence as was not easily photodegraded or photobleached. These fluorescent properties potentially offer the opportunity to extend the use of MSN_CurNQ for molecular imaging applications.

Moreover, the fluorescent images demonstrate that there was cellular uptake of MSN_CurNQ, but not nuclear uptake. The nanoparticles can be observed to cluster around the nucleus, yet they do not enter the nucleus. Cellular uptake is of great importance, as for a drug to elicit its response, it is required to enter the cell. Clearly, cellular uptake occurs allowing for MSN_CurNQ to elicit its potential anti-cancer effects. Cellular uptake may occur through endocytosis or membrane permeation; however; the method of uptake cannot be determined through the above microscopy images.

As discussed above, it was expected that the inclusion of a nanosystem would be required to realise the potential detection and imaging applications of CurNQ. Therefore, it was of interest to visualise cells treated with the loaded nanosystem MSN_CurNQ and CurNQ treatment alone. As seen in Figure 4.7, no red fluorescence is observable in cells treated with CurNQ alone, this indicates that CurNQ needs to be loaded onto a nanoplatform for detection capabilities to be realised.

One of the main objectives of this research as to synthesise a molecule with appropriate fluorescent properties to allow for detection and imaging applications. Cur cannot be used for detection or imaging applications owing to its short fluorescent lifetime and its low quantum yield. Furthermore, it undergoes rapid photo bleaching and has a low

quantum yield and fluorescent intensity in aqueous solution [25]. Therefore, it was a challenge to improve these fluorescent properties with Cur's core structure being present in CurNQ and to develop a fluorescent molecule having suitable properties for fluorescence detection applications. Cur has an excitation and emission spectra of 450 nm and 550 nm and these wavelengths would induce tissue autofluorescence if used in *in vivo* applications, therefore a longer excitation wavelength is required to avoid autofluorescence. The synthesis of CurNQ resulted in the excitation and emission wavelengths being significantly red shifted compared to Cur. CurNQ had an excitation and emission wavelength of 595 nm and 670 nm respectively, this equates to a red shift of 145 nm. This is noteworthy, as excitation at 595 nm would substantially reduce tissue autofluorescence and would allow for effective *in vivo* imaging. Moreover, CurNQ displayed a large stokes shift of 75 nm. A large stokes shift is crucial for *in vivo* imaging applications as it reduces the overlap between the excitation and emission spectra thus reducing self-absorbance [26].

The microscopy images demonstrated MSN_CurNQ to have highly precise, distinctive and high intensity fluorescence. Moreover, a high target to background ratio, low fluorescent blur, a long fluorescent lifetime and fluorescent stability indicate MSN_CurNQ to be a potentially powerful diagnostic and imaging agent.

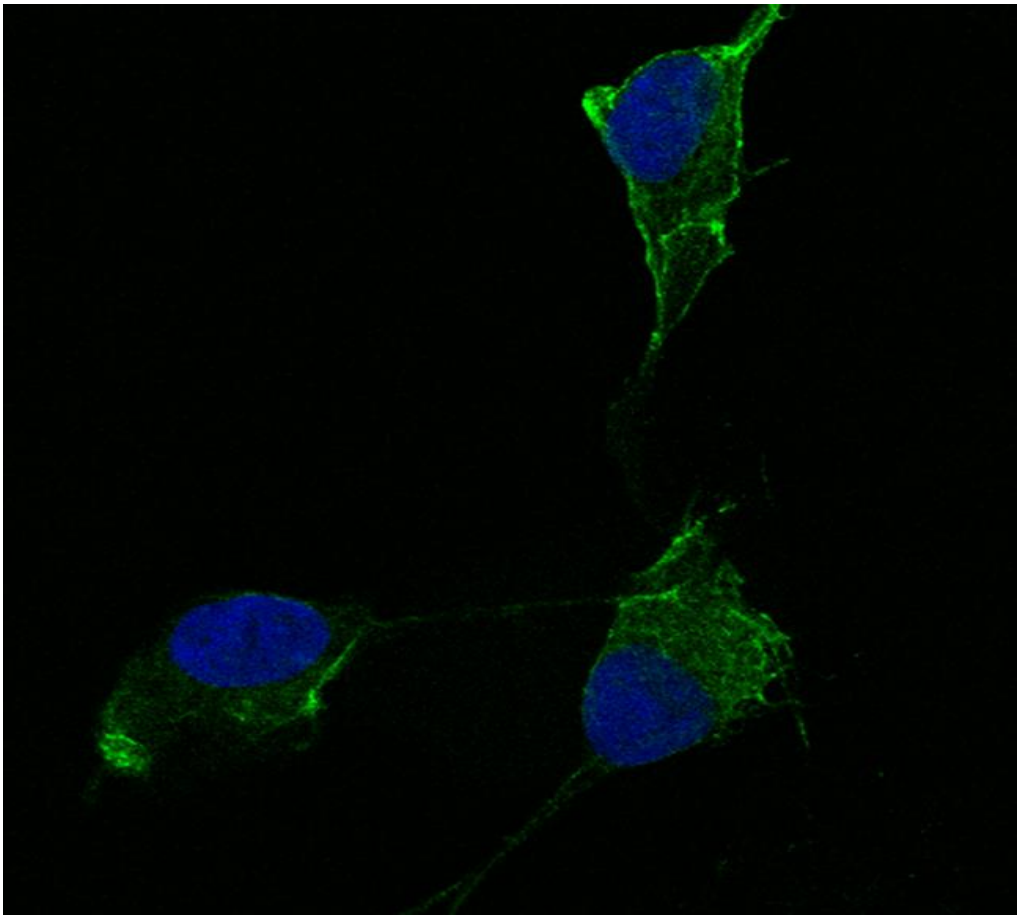


Figure 4.7: Confocal microscopy images demonstrating that CurNQ is required to be loaded onto a delivery vehicle to allow for fluorescence detection and tracking. OVCAR-5 cells treated with CurNQ for 24 hours (no MSN), nuclear DAPI staining, phalloidin 488 actin stain.

4.3.5 *Evaluating the chemotherapeutic properties of MSN_CurNQ through high content imaging*

High content imaging is an advanced technique that combines high throughput techniques and fluorescent microscopy to obtain quantitative data from complex biological systems [27]. It is a robust method utilising an automated microscope that allows for rapid, high content image acquisition and analysis [28]. Multiple independent measurements can be collected from a single cell or a single cell population. Herein, this advanced technique was employed using the CELENA® X High Content Imaging System. The high content imager was used to measure cell viability in response to MSN_CurNQ and MSN_Cur treatments; moreover, the number of nanoparticles were counted, enabling the evaluation of the effect of concentration on cell viability.

As seen in Figure 4.8, there was a dose dependent response to MSN_CurNQ and MSN_Cur treatment. With an increasing count of loaded MSN, there was a decrease in cell count, occurring in an inversely proportional manner. Therefore, treatment with MSN_CurNQ and MSN_Cur resulted in a decrease in cell viability. The visual representation with concurrent qualitative data acquired from the high content imager makes the high content imaging system a powerful tool in evaluating the anti-cancer properties of a particular system and in the drug discovery process. These results indicate the potential of MSN_CurNQ to act as a chemotherapeutic agent.

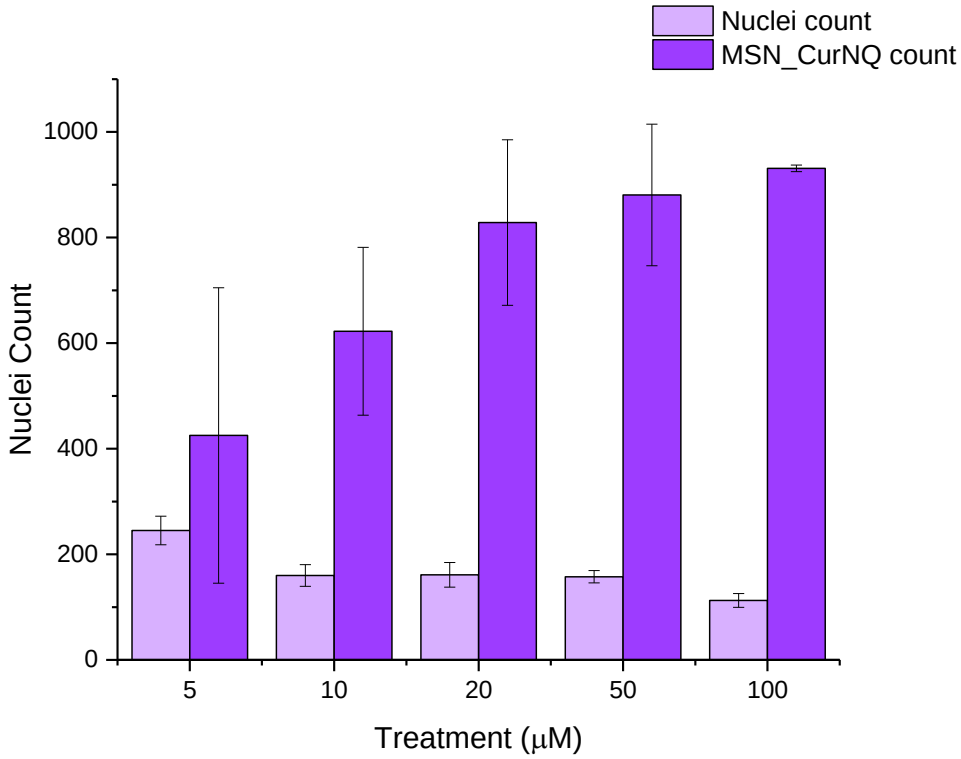


Figure 4.8: Nuclei count, and MSN count of OVCAR-5 cells treated with varying concentrations of MSN_CurNQ for 24-hours. Nuclei and MSN count were quantitatively obtained using a high content imaging system.

4.3.6 *In vitro cytotoxicity assay – MTT*

The previous research presented in chapter 3, investigated the cytotoxic effect of CurNQ on two OC cell lines and on a non-malignant fibroblast cell line. The results illustrated substantial cytotoxicity of CurNQ to the OC cell lines OVCAR-5 and SKOV3, yet low cytotoxicity to a non-malignant fibroblast cell line 3T3. This research was

promising and indicated the ability of CurNQ to potentially act as a potent anti-cancer agent. Consequently, it was of interest to investigate the cytotoxic nature of MSN_CurNQ. Moreover, owing to the novelty of the novel molecule, it was of interest if these cytotoxic effects would translate to variety of cancer cell types. To this end MTT assays were performed on 6 cancer cell lines and one non-malignant fibroblast cell line. The purpose of these MTT assays were two-fold. Firstly, it was crucial to determine if CurNQ would induce its previously observed potent anti-cancer effects whilst loaded onto the MSN delivery vehicle and secondly to evaluate if the cytotoxicity of CurNQ was translatable to a variety of cancer types.

As seen in Figures 4.9 to 4.14, the cytotoxicity of MSN_CurNQ and MSN_Cur depended greatly on the cancer cell type. Certain cancer cells such as CACO-2 and OVCAR-5 exhibited large reductions in cell viability, whereas other cancer cell lines such as HeLa experienced low overall toxicity in response to the loaded nanoparticles. Concentration administered and incubation time both affected overall cytotoxicity; however, cancer cell type was the largest determining factor.

The greatest reductions in cell viability were observed for the OVCAR-5 and CACO-2 cell lines. Cell viability dropped substantially after 48 hours of incubation for both cell lines. This aligns with Figure 4.3 which demonstrated the sustained release of CurNQ from the nanoparticles over a 96-hour period, thus the reduction in cell viability occurred once CurNQ was released. Release of CurNQ from the MSN increased drastically after 24 hours (Figure 4.3), after which it would be able to exert its effects culminating in the decline in cell viability at 48 hours. This sustained release is ideal for anti-cancer mechanisms, as it first allows for the nanoparticles to accumulate in the tumour prior to the complete release of the active compound. Additionally, this sustained release would allow for a longer detection window, in respect to the nanosystem's proposed detection applications.

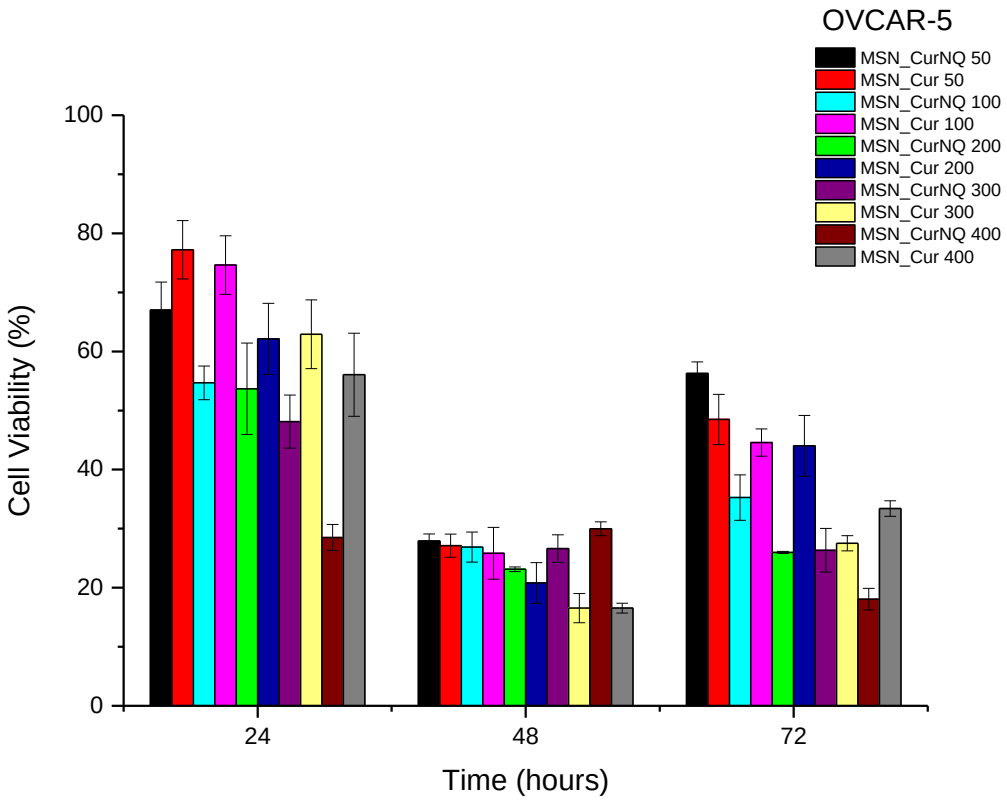
Although cell viability was reduced to the greatest extent at 48 hours, at the 24-hour incubation period, 400 ng/mL of MSN_CurNQ induced a reduction in cell viability to 28,5% in OVCAR-5 cells. This shows that this high concentration of CurNQ induced immediate cell death and this same response of immediate cell death occurred in the CACO-2 cell line. This suggests that enough CurNQ was released to induce cell death

after 24 hours on account of the high concentration administered. In the OVCAR-5 cell line, time was the most significant factor in the reduction of cell viability, as after 48 hours, all treatment concentrations induced a reduction in cell viability to below 50%. However, cell recovery was observed after 72 hours in cells receiving treatments of less than 200 ng/mL of MSN_CurNQ, whereas cell viability remained low after 72 hours in cells that received 200 ng/mL or higher of MSN_CurNQ. This same pattern of cell recovery in response to low doses of the nanosystem was observed in CACO-2 cells, with the recovery being greater; but again, treatment with 200 ng/mL or greater induced sustained reductions in cell viability. Therefore, higher concentrations of treatment are required to induce lasting cell death.

MCF-7 and CHLA cell lines demonstrated a slightly lower reduction in cell viability compared to OVCAR-5 and CACO-2, yet cell viability was still reduced to below 50%, hence MSN_CurNQ shows promise as a chemotherapeutic agent to a variety of cancer cell types. Interestingly, the MCF-7 and CHLA cell lines experienced their greatest reduction in cell viability after 24 hours, differing from the response observed for OVCAR-5 and CACO-2 cell lines. While the release from MSN peaks after 96 hours, there is not a large difference in release between 24 and 48 hours on account of the sustained release from the nanoparticles. The MCF-7 and CHLA cell lines had an immediate response to treatment, with cell viability reducing to below 50% in cells receiving 200 ng/mL or higher of MSN_CurNQ. However, MCF-7 and CHLA cells recovered subsequent to their initial reduction in cell viability, and this also occurred in cells receiving the highest concentration of MSN_CurNQ; yet cells do not recover to full viability suggesting treatment was still effective in reducing the overall cell population. Although cell viability reduction was not as high as OVCAR-5 and CACO-2, the reduction in cell viability in MCF-7 and CHLA cell lines was significantly different to the reduction observed for 3T3 cells ($p=0.000$), indicating MSN_CurNQ treatment does result in a significant reduction in cell viability to a variety of cancer types. Accordingly, it is recommended that in an *in vivo* setting, that a treatment regime is instigated, whereby a patient would receive several doses of the nanosystem, as to ensure malignant cell recovery does not occur.

There was a slight reduction in cell viability in HT-29 cells, cell viability was reduced to around 70%; and very low reductions in cell viability were observed for the HeLa cell

line. This small reduction in cell viability precludes MSN_CurNQ's chemotherapeutic application for these cancer types, as a greater reduction in cell viability are required for a system to be considered to have chemotherapeutic applications. On the contrary, MSN_CurNQ can still be applied as a detection and targeting system in these cancers. Owing to the multifaceted nature of MSN_CurNQ, its applications are not limited to a select few cancer types. Indeed, further treatment options would be required for cancer types that are not adequately treated by MSN_CurNQ; however, its application as a first line detection and targeting system is applicable.



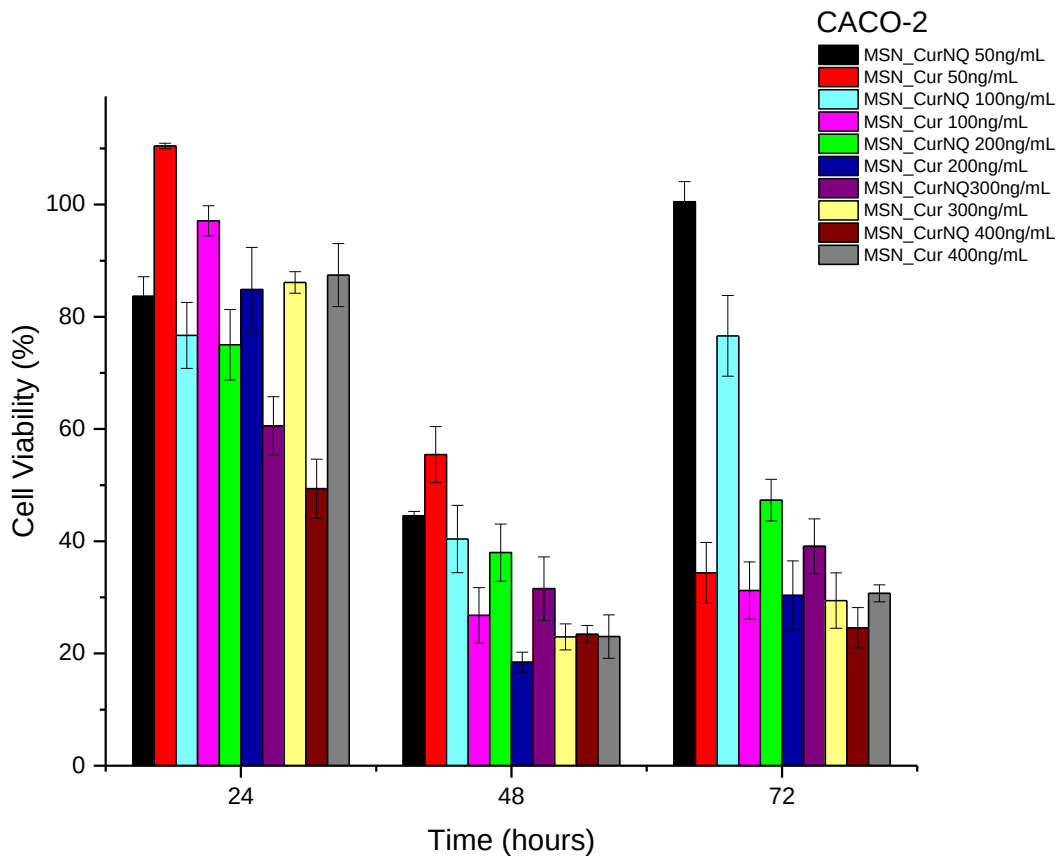


Figure 4.9: Cytotoxicity of MSN_CurNQ and MSN_Cur to OVCAR-5 and CACO-2 cell lines. MSN_CurNQ and MSN_Cur treatments were administered at a range of concentrations over a 72-hour period and the reductions in cell viability were determined through an MTT assay. Large reductions in cell viability towards MSN_CurNQ treatment were observed and cell viability reductions differed statistically significantly to 3T3 cell line ($p = 0.000$).

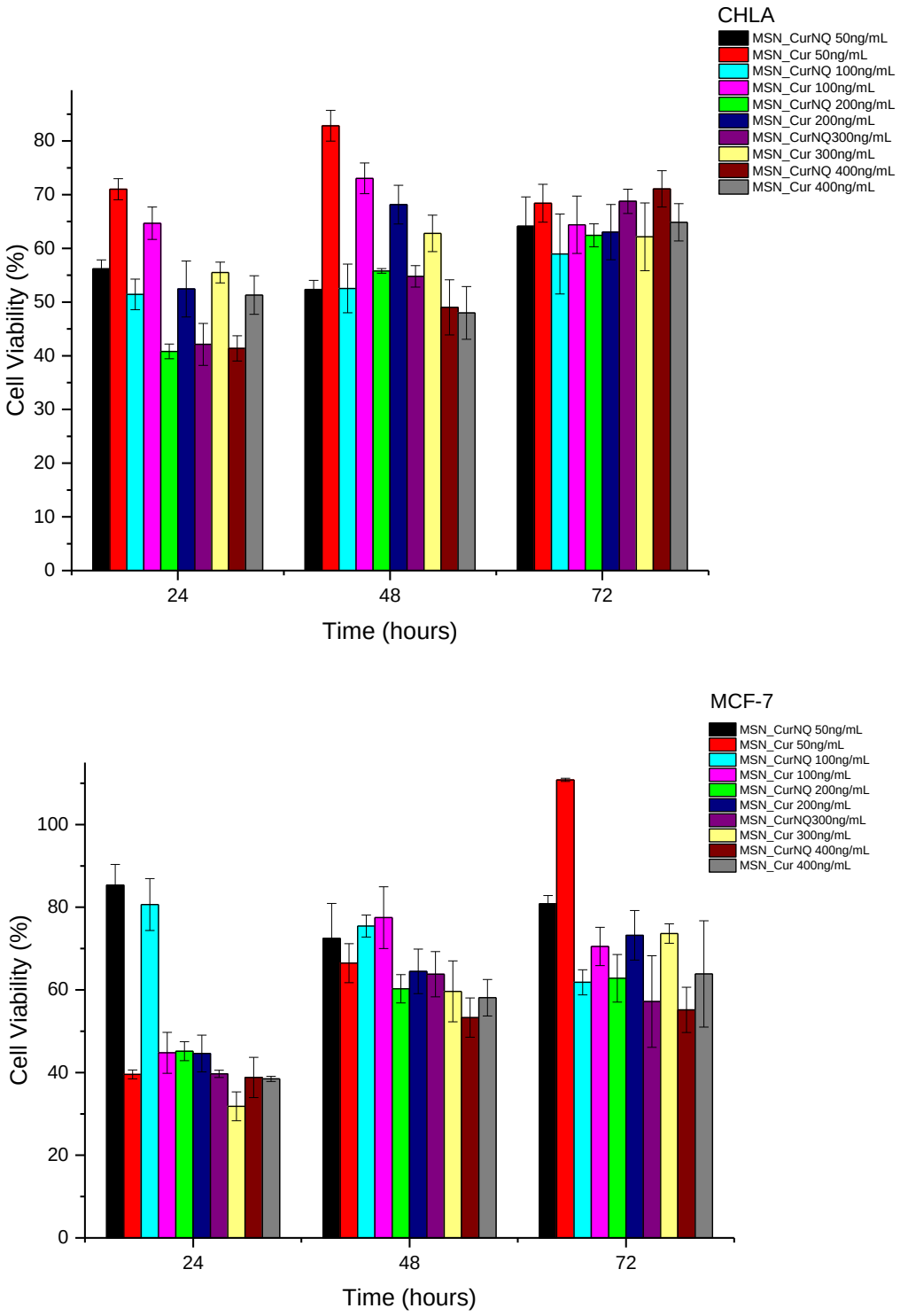


Figure 4.10: Cytotoxicity of MSN_CurNQ and MSN_Cur to MCF-7 and CHLA cell lines. MSN_CurNQ and MSN_Cur treatments were administered at a range of concentrations over a 72-hour period and the reductions in cell viability were determined through an MTT assay. Moderate reductions in cell viability towards MSN_CurNQ treatment were observed and cell viability reductions differed statistically significantly to 3T3 cell line ($p = 0.000$).

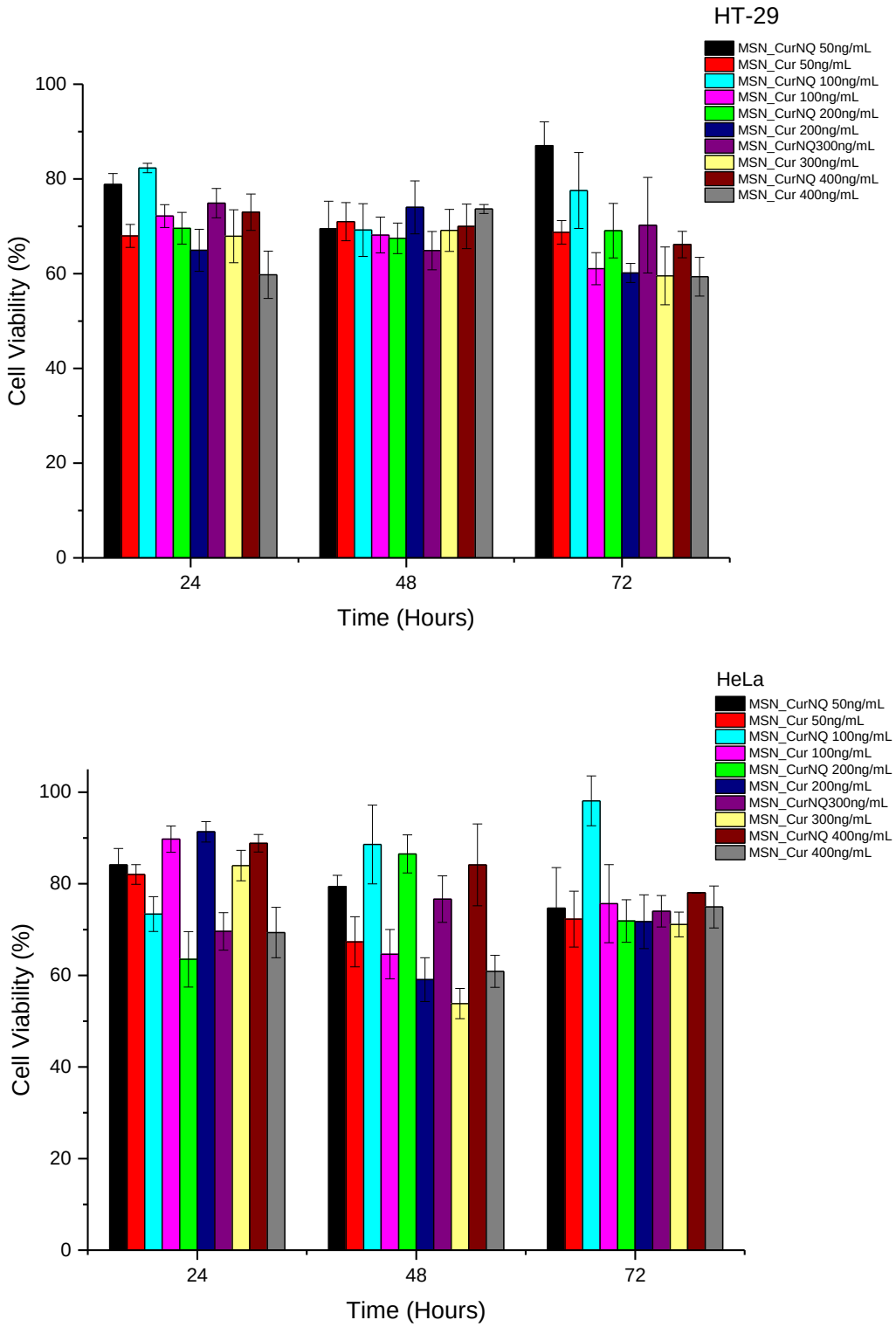


Figure 4.11: Cytotoxicity of MSN_CurNQ and MSN_Cur to HT-29 and HeLa cell lines. MSN_CurNQ and MSN_Cur treatments were administered at a range of concentrations over a 72-hour period and the reductions in cell viability were determined through an MTT assay. Low reductions in cell viability towards MSN_CurNQ treatment were observed and cell viability reductions of HT-29 differed statistically significantly to 3T3 cell line ($p = 0.004$).

Statistical analyses were performed to ascertain the effect of MSN_CurNQ and MSN_Cur on different cancer cell lines and on a healthy fibroblast cell line. Cell line was a statistically significant factor in the reduction of cell viability (p=0.0000). Administered concentration was also a statistically significant factor in cell viability reduction (p=0.0000). OVCAR-5 cells were the most responsive to MSN_CurNQ treatment, and the reduction in cell viability was significantly different to each other cell line tested (HeLa, CHLA, MCF-7, HT-29 and 3T3 p= 0.000; CACO-2 p = 0.035). Importantly, there was a significant difference in the reduction in cell viability of the healthy cell line 3T3 to all other cancer cell lines investigated, barring HeLa cells (OVCAR-5, CACO-2, MCF-7, CHLA p=0.000, HT-29 p = 0.004; HeLa p= 0.378). This means that MSN_CurNQ reduced cancer cell viability to a greater extent than it did to a healthy fibroblast cell line. The highly statistically significant p-values of 0.000 and 0.004 verify the selective toxicity of MSN_CurNQ to cancer cells, meaning MSN_CurNQ is more toxic to cancer cells than it is to a healthy cell line. This selective toxicity further extends the cancer targeting capabilities of the nanosystem and further cements its novelty and applicability in the field of cancer theranostics.

According to the obtained results a high concentration of MSN_CurNQ is required for effective and sustained reductions in cell viability. This high required dosage would not be a limiting factor to successful treatment on account of the observed cancer selective toxicity. Cell viability remained above 80% for the healthy fibroblast cell line 3T3, after treatment with 400 mg/mL of MSN_CurNQ, thereby indicating that MSN_CurNQ is nontoxic to these healthy fibroblast cells. This suggests that it would be safe to administer high concentrations of MSN_CurNQ to patients, as this should induce large reductions in cancer cell viability and a very low reduction to healthy cell viability.

MSN_CurNQ thereby offers a three-pronged approach for cancer targeting namely its pH-responsive solubility, the EPR effect and its selective toxicity towards cancer cells. This makes MSN_CurNQ a highly advanced and novel nanosystem for cancer theranostics.

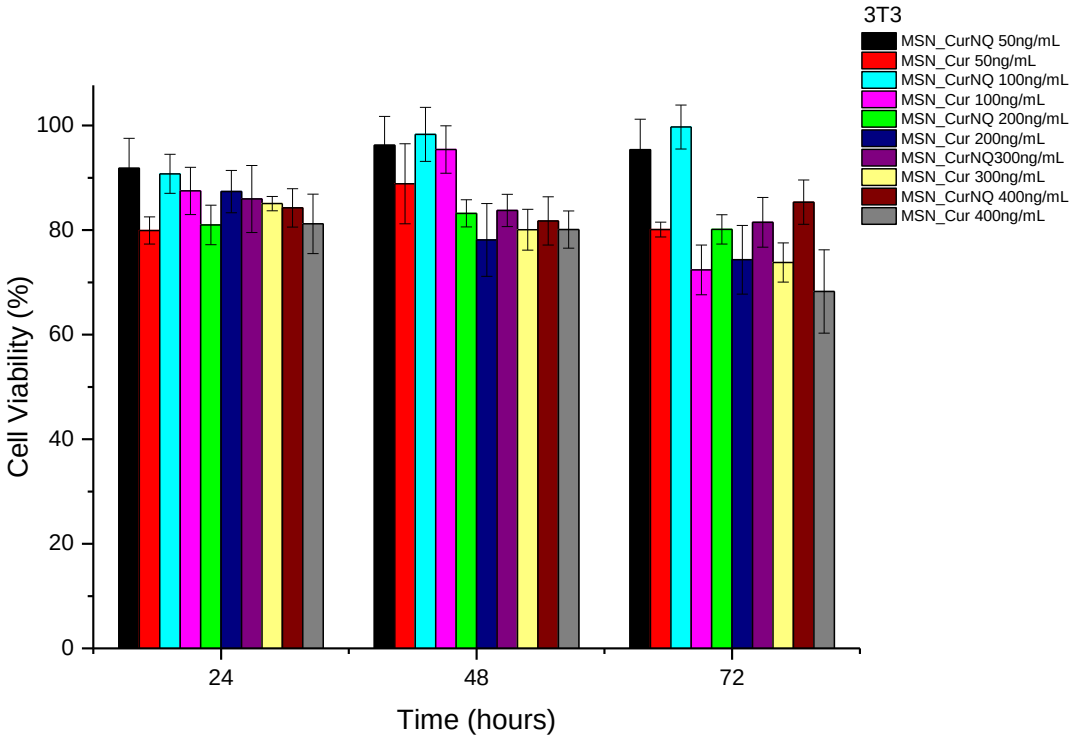


Figure 4.12: Cytotoxicity of MSN_CurNQ and MSN_Cur to the healthy fibroblast cell line 3T3. MSN_CurNQ and MSN_Cur treatments were administered at a range of concentrations over a 72-hour period and the reductions in cell viability were determined through an MTT assay. Very minor reductions in cell viability towards MSN_CurNQ treatment were observed

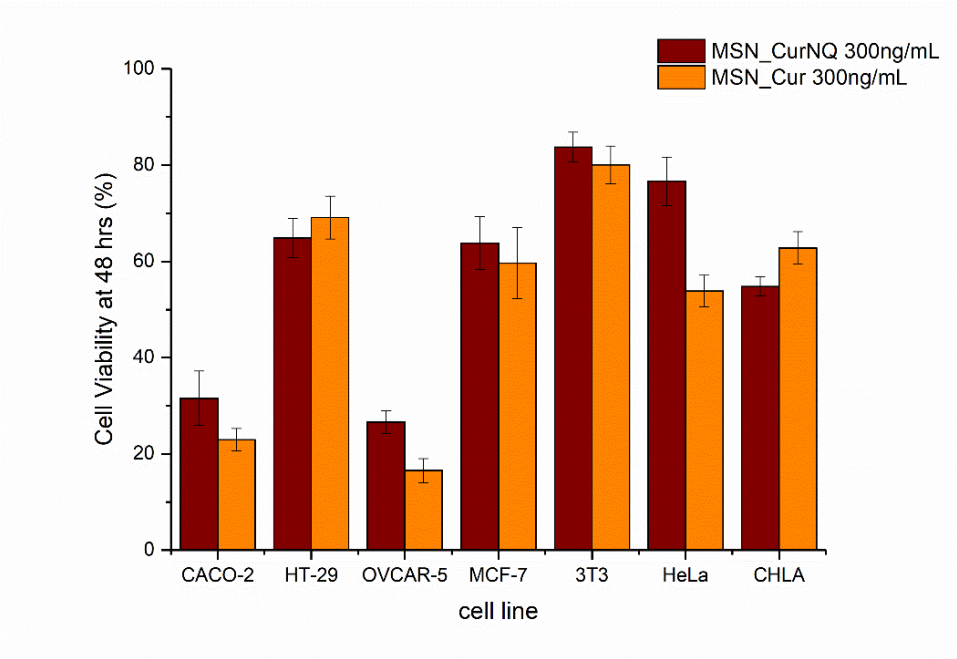


Figure 4.13: A comparative analysis of the reduction in cell viability to a variety of cell lines in response to MSN_CurNQ treatment at 300 ng/mL after 48 hours.

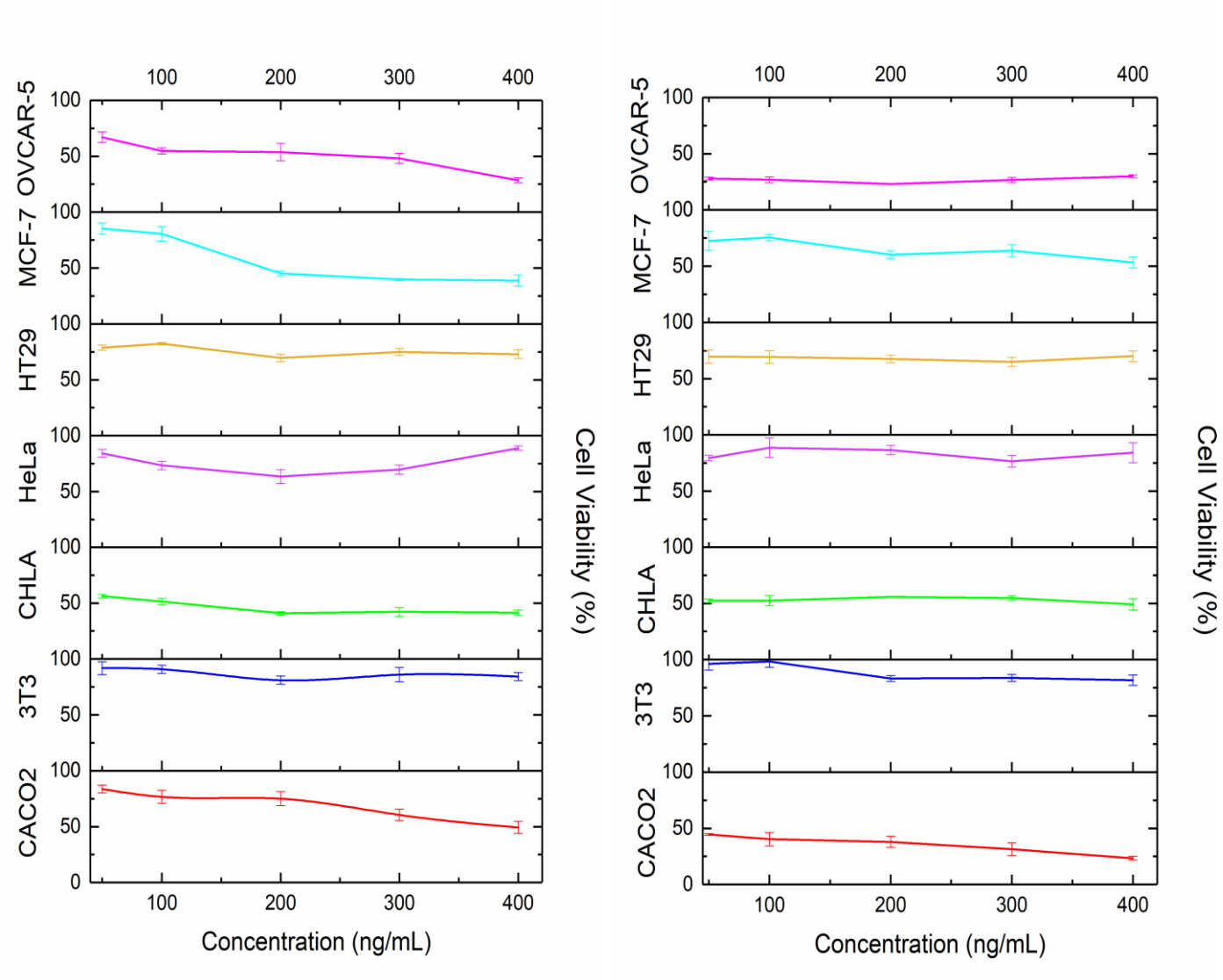


Figure 4.14: Cell viability in response to concentration of MSN_CurNQ after **A)** 24 hours and **B)** 48 hours in 6 cancer cell lines and in 1 healthy fibroblast cell line.

4.3.7 *Potential in vivo cytotoxic effects of MSN_CurNQ*

The cytotoxicity results demonstrated a reduction in cytotoxicity of MSN_CurNQ compared to CurNQ administered alone (Figure 4.15). This decrease in cytotoxicity could be owing to the limited release of CurNQ from the nanoparticle, as seen in Figure 4.3, the greatest release observed was 57% of loaded CurNQ. This limited release could account for the reduction in cytotoxicity. On the other hand, lower reduction in cell viability may be attributed to the nature of 2D cell culture. Tumour progression relies on multiple contributing factors, many of which are from the microenvironment. The tumour microenvironment is as important to tumour formation and progression as the

cancer cells themselves [29]. Cancerous tissue is not just a mass of malignant cells, but the interaction between multiple cells types, both malignant and non-malignant, as well as multiple signalling molecules and ECM components [30]. The tumour microenvironment is a highly complexed system that allows malignant cells to become rouge organs that can recruit and corrupt healthy cells [31]. Unfortunately, this complex and intricate system cannot be accurately mimicked through 2D cell culture techniques. This may explain the reduction in observed cell viability of OVCAR-5 cells to MSN_CurNQ compared to when treated with CurNQ alone. The pH change that accompanies malignancy cannot be accurately replicated in 2D cell culture, and the pH is closer to physiological conditions than the tumour microenvironment owing to the 2D nature of the cell culture techniques. Thus, the pH specific solubility and release profile of the novel nanosystem could not be observed accurately through these cell culture techniques. This obstacle was avoided when testing the cytotoxicity of CurNQ and Cur alone, as they were solubilised prior to treatment. Therefore, *in vivo* it would be expected that a greater reduction in cell viability in response to MSN_CurNQ treatment than observed in Figure 4.9-4.14. Hence, MSN_CurNQ could be a highly effective chemotherapeutic agent to a variety of cancer types when tested *in vivo*.

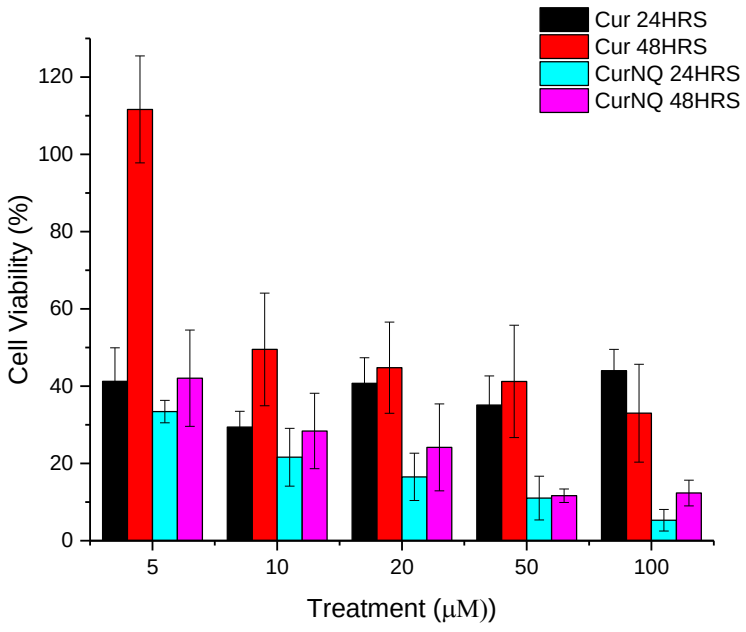


Figure 4.15: Cell viability assay of OVCAR-5 cells treated with CurNQ and Cur alone after 24-hour incubation.

Indeed, this research demonstrated that CurNQ requires to be loaded onto a nanoplatform to allow for all its theranostic capabilities to be realised. CurNQ delivered using nanotechnology results in the formation of a promising novel theranostic system allowing for potential simultaneous cancer targeting, detection and treatment.

4.4 Conclusions

The loading of CurNQ onto the MSN platform aimed to allow for enhanced delivery and enable *in vitro* and *in vivo* imaging and detection. To this end, MSN were synthesised and were impregnated with CurNQ to form the novel nanosystem MSN_CurNQ. CurNQ demonstrated pH responsive release from MSN, specific to the tumour microenvironment whereby after 96 hours 31.5% of CurNQ was released at pH 7.4 compared to 57% release at pH 6.8. This pH responsivity may allow for potential tumour targeting applications. Moreover, MSN_CurNQ exhibited high intense, clear and distinctive innate fluorescence enabling detection and possible imaging applications. Moreover, MSN_CurNQ induced cytotoxicity culminating in a reduction to below 50% cell viability in OVCAR-5, CACO-2, CHLA and MCF-7 cell lines thereby demonstrating its chemotherapeutic potential to a variety of cancer cell types. Furthermore, MSN_CurNQ treatment did not induce cytotoxicity to the healthy fibroblast cell line 3T3, demonstrating cancer selective toxicity, furthering the nanosystem's novelty and potential applications. Clearly, the novel nanosystem MSN_CurNQ has potential applications in cancer theranostics.

4.5 References

1. Shi J, Kantoff PWJ, Wooster R, Farokhzad OC. Cancer nanomedicine: progress, challenges and opportunities. Nat Rev Cancer. 2017;17(1):20–37.

2. Tran S, DeGiovanni PJ, Piel B, Rai P. Cancer nanomedicine: a review of recent success in drug delivery. Clin Transl Med. 2017;6(1):1-21.

3. Baeza A, Manzano M, Colilla M, Vallet-Regí M. Recent advances in mesoporous silica nanoparticles for antitumor therapy: Our contribution. Biomater Sci. 2016;4(5):803–13.

4. Ivey JI, Bonakdar M, Kanitkar A, Davalos RV, Verbridge SS. Improving cancer therapies by targeting the physical and chemical hallmarks of the tumor microenvironment. Cancer Lett. 2016;380(1):330–9.

5. Watermann A, Brieger J. Mesoporous silica nanoparticles as drug delivery vehicles in cancer. Nanomaterials. 2017;7(7):189.

6. Moreira AF, Dias DR, Correia IJ. Stimuli-responsive mesoporous silica nanoparticles for cancer therapy: A review. Microporous Mesoporous Mater. 2016;236:141–57.

7. Liu J, Luo Z, Zhang J, Luo T, Zhou J, Zhao X, et al. Hollow mesoporous silica nanoparticles facilitated drug delivery via cascade pH stimuli in tumor microenvironment for tumor therapy. Biomaterials. 2016;83:51–65.

9. Argyo C, Weiss V, Bra C, Bein T. Multifunctional Mesoporous Silica Nanoparticles as a Universal Platform for Drug Delivery. Chem Mater. 2013;26:435–51.

10. Mai WX, Meng H. Mesoporous silica nanoparticles: A multifunctional nano therapeutic system. Integr Biol. 2013;5:19–28.

11. Ma'mani L, Nikzad S, Kheiri-manjili H. Chemistry Curcumin-loaded guanidine functionalized PEGylated I3ad mesoporous silica nanoparticles KIT-6 : Practical strategy for the breast cancer therapy. Eur J Med Chem. 2014;83:646–54.

12. Feng Y, Panwar N, Tng DJH, Tjin SC, Wang K, Yong KT. The application of mesoporous silica nanoparticle family in cancer theranostics. Coord Chem Rev. 2016;319:86–109.

13. Haider M, Abdin SM, Kamal L, Orive G. Nanostructured Lipid Carriers for Delivery of Chemotherapeutics: A Review. Pharmaceutics. 2020;12(3):288.

14. Saroj S, Rajput SJ. Composite smart mesoporous silica nanoparticles as promising

therapeutic and diagnostic candidates: Recent trends and applications. J Drug Deliv Sci Technol. 2018;44:349–65.

15. Wicki A, Witzigmann D, Balasubramanian V, Huwyler J. Nanomedicine in cancer therapy: Challenges, opportunities, and clinical applications. J Control Release. 2015;200:138–57.

16. Hu JJ, Liu LH, Li ZY, Zhuo RX, Zhang XZ. MMP-responsive theranostic nanoplatform based on mesoporous silica nanoparticles for tumor imaging and targeted drug delivery. J Mater Chem B. 2016;4(11):1932–40.

17. Youn YS, Bae YH. Perspectives on the past, present, and future of cancer nanomedicine. Adv Drug Deliv Rev. 2018;130:3–11.

18. Yang S, Zhao L, Yu C, Zhou X, Tang J, Yuan P, et al. On the Origin of Helical Mesostructures. J Am Chem Soc Artic. 2006;128(6):10460–6.

19. Jambhrunkar S, Karmakar S, Popat A, Yu M, Yu C. Mesoporous silica nanoparticles enhance the cytotoxicity of curcumin. RSC Adv. 2014;4(2):709–12.

20. Hamilton TC, Young RC, Mckoy WM, Grotzinger KR, Green JA, Chu EW, et al. Characterization of a Human Ovarian Carcinoma Cell Line (NIH : OVCAR-3) with Androgen and Estrogen Receptors. Cancer Res. 1983;43:5379–89.

21. Warburg O. The Metabolism of Carcinoma Cells. J Cancer Res. 1925;9(1):148–63.

22. Wedege K, Dražević E, Konya D, Bentien A. Organic Redox Species in Aqueous Flow Batteries: Redox Potentials, Chemical Stability and Solubility. Sci. Rep. 2016;6, 39101

23. Kanamala M, Wilson WR, Yang M, Palmer BD, Wu Z. Mechanisms and biomaterials in pH-responsive tumour targeted drug delivery: A review. Biomaterials. 2016;85:152–67.

24. Gulzar A, Xu J, Wang C, He F, Yang D, Gai S, et al. Tumour microenvironment responsive nanoconstructs for cancer theranostic. Nano Today. 2019;26:16–56.

25. Priyadarsini KI. Photophysics, photochemistry and photobiology of curcumin: Studies from organic solutions, bio-mimetics and living cells. J Photochem Photobiol C Photochem Rev. 2009;10(2):81–95.

26. Qi Y, Huang Y, Li B, Zeng F, Wu S. Real-Time Monitoring of Endogenous Cysteine Levels in Vivo by near-Infrared Turn-on Fluorescent Probe with Large Stokes Shift. Anal Chem. 2018;90(1):1014–20.

27. Zanella F, Lorens JB, Link W. High content screening: Seeing is believing. Trends

Biotechnol. 2010;28(5):237–45.

28. Zock J. Applications of High Content Screening in Life Science Research. Comb Chem High Throughput Screen. 2009;12(9):870–6.

29. Albini A, Sporn MB. The tumour microenvironment as a target for chemoprevention. Nat Rev Cancer. 2007;7(2):139–47.

30. Bray LJ, Binner M, Holzheu A, Friedrichs J, Freudenberg U, Hutmacher DW, et al. Multi-parametric hydrogels support 3D invitro bioengineered microenvironment models of tumour angiogenesis. Biomaterials. 2015;53:609–20.

31. Balkwill FR, Capasso M, Hagemann T. The tumor microenvironment at a glance. J Cell Sci. 2012;125(23):5591–6.

Chapter 5: Preclinical studies to evaluate the safety, tolerability, toxicity and potential efficacy of CurNQ and MSN_CurNQ for cancer intervention in MF-1 nude mice

5.1 Introduction

Additionally, the cytotoxicity of MSN_CurNQ was tested on the healthy murine fibroblast cell line 3T3. The nanosystem showed no cytotoxic effect on the healthy murine cell line. From these results we assume that the nanosystem will not induce toxicity in the mice and will only affect the tumour cells.

The success of *in vitro* studies warranted the initiation of an *in vivo* preclinical trial. Previously, extensive *in vitro* assays on CurNQ and MSN_CurNQ cytotoxicity were performed on 7 cancer cell lines namely CHLA, MCF-7, HT-29, HeLa, CACO-2, SKOV3 and OVCAR-5 and on the healthy fibroblast cell line 3T3. The promising results acquired deemed it necessary to extend the research into an animal model for further investigations. To further understand the effectiveness and true theranostic potential of the nanosystem, an animal model is required. *In vitro* and computer modelling data is not sufficient to mimic *in vivo* conditions, and an *in vivo* study is required to ascertain the effectiveness of the nanosystem [1]. Animal testing is required prior to clinical trials performed on human subjects owing to ethical considerations. The safety profile, pharmacokinetic behaviour and effectiveness of the nanosystem and novel compound alone needs to be evaluated in an in vivo model prior to human testing. It has become common and standard scientific practise in cancer research to induce a human tumour in a nude mice model [1]. MF-1 nude mice were selected for this study owing to their immunocompromised nature, allowing for the growth of a human tumour in the animal model, thus providing information of how a human tumour would respond to treatment but with using an animal model.

OVCAR-5 was determined to be the most responsive cell line; accordingly, it was selected for use in the *in vivo* study through the initiation of an OVCAR-5 xenograft in female MF-1 nude mice. The experimental design was approved by the animal ethics committee prior to the initiation of the study.

A preclinical trial of CurNQ and MSN_CurNQ was performed on 25 female MF-1 nude mice. The preclinical trial was divided into two parts, part A and B. Part A aimed to determine the safety, tolerability and toxicity of CurNQ and MSN_CurNQ on a mouse model, and part B aimed to establish OVCAR-5 tumour xenografts in MF-1 nude mice and then to evaluate the potential efficacy of CurNQ and MSN_CurNQ as a chemotherapeutic agent. Part A consisted of six mice divided into 2 groups of 3 and part B consisted of 20 mice divided into 4 groups of 5. Strict ethical guidelines set out by the animal ethics committee were adhered to throughout the preclinical trial and the reduction of animal suffering was always prioritised.

5.2 Methods and Materials

5.2.1 *Materials*

Female MF-1 mice were procured from the University of Cape Town Research Animal Facility. Standard cages and commercial laboratory food were provided by the CAS of the University of the Witwatersrand. Sodium Pentobarbitone and Isoflurane were provided by the CAS of the University of the Witwatersrand and were used as received. The OVCAR-5 cell line was purchased from Cell Biolabs Inc. (San Diego, USA) and cultured using the previously described methodology (chapter 3 & 4). CurNQ and MSN_CurNQ were synthesised as previously described (chapter 3 & 4). Matrigel was purchased from Merck/Sigma Aldrich (Darmstadt, Germany) and other cell culture consumables used in the establishment of the injected OVCAR-5 cells were purchased from Thermo Fischer Scientific (Waltham, USA). Additional consumables utilised throughout the animal study were provided by the CAS of the University of the Witwatersrand.

5.2.2 *Part A -Selection of appropriate dose*

The recommended starting dose of CurNQ and MSN-CurNQ for Part A of the study was unknown owing to its novelty. Consequently, in order to select an appropriate starting dose, the IC_{50} of CurNQ in OVCAR-5 cells *in vitro* was evaluated. OVCAR-5 cells were selected as the most promising cell line owing to previous *in vitro* results and a xenograft tumour from this cell line was required to be established.

The rationale in determining an appropriate *in vivo* starting dose was to find established anti-cancer drugs that exhibit similar IC_{50} values *in vitro* to CurNQ, and through the evaluation of their effective *in vivo* doses to estimate an appropriate starting *in vivo* dose for CurNQ. The IC_{50} value of CurNQ in OVCAR-5 cells was calculated to be 4.048 µM using the software Prism-GraphPad and its graph is displayed in Figure 5.1. A search of the literature was conducted to find anti-cancer drugs demonstrating a similar IC_{50} in OVCAR-5 cells and four drugs were found matching this criteria namely: cisplatin, nimbolide, linstitinib and PF-562271 [2–8]. Their effective *in vivo* doses in nude mice range from 3 mg/kg to 33 mg/kg [2–8].

Cisplatin, a potent anti-cancer agent, is administered at a dose of 3 mg/kg; however, PF-562271, a focal adhesion kinase inhibitor that has been shown to inhibit cancer progression, has an effective dose of 33 mg/kg. Nimbolide a chemotherapeutic phytochemical is effective at 5 mg/kg but safe at 20 mg/kg, and Linsitinib, a potent small molecule demonstrating anti-tumour activity in several solid tumours is dosed at 25 mg/kg [2–8]. Thus, to select an appropriate dose for CurNQ, a median dose of the above range was selected, 10 mg/kg. It was thought 10 mg/kg would be an effective dose to ascertain the safety profile of CurNQ whilst hopefully not exceeding the LD_{50}.

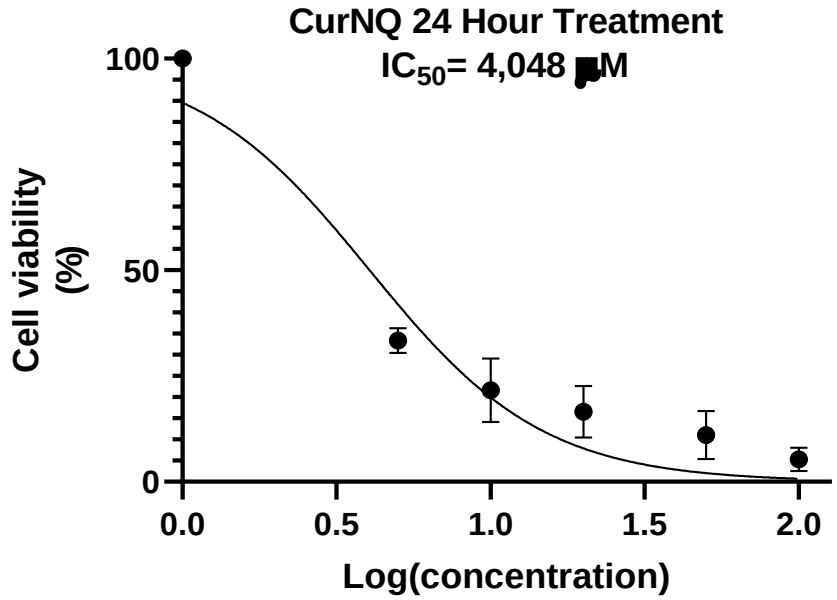


Figure 5.1: IC_{50} value of CurNQ in OVCAR-5 cells calculated using prism-GraphPad.

5.2.3 *MF-1 female nude mice*

Twenty-six female MF-1 nude mice aged 5 weeks old were procured from the University of Cape Town. Mice were transported in air filtered cages according to standard operating procedures. Once arriving at the Wits central animal services (CAS), mice were placed in individual cages in a barriered unit. Mice were kept under sterile conditions in air filtered cages under strict sterile protocols. The temperature was maintained at 22°C ±1°C, humidity 60% ±10%, with a 12-hour light/dark cycle [9]. Mice were allowed free access to water and commercial laboratory complete food and were monitored daily by veterinary personal. Habituation practises proceeded for 1 week to allow for the mice to habituate to the environment as well as to the researchers and veterinary staff.

5.2.4 *Part A - Administration of CurNQ and MSN_CurNQ, Health monitoring, Euthanasia and Histopathology*

CurNQ and MSN_CurNQ were prepared in 100 µL of saline and were administered via tail vein injection [9–11]. Stage one of this study involved three mice being allocated to each experimental group and dosing occurred on days 0, 4, 7, and 10 of the study. The experimental groups were classified as follows:

Group 1: Mice injected with a dose of 10 mg/kg CurNQ.
Group 2: Mice injected with a dose of 10 mg/kg MSN_CurNQ.

The health of the mice were monitored closely through body weight changes, the presence of infection or ascites, the impairment of grooming and movement, changes in food intake or water consumption, fur colour, and exploratory behaviour were used as indications of the overall health of the mice [11]. Additionally, a welfare monitoring score sheet was filled out to assess the health of the mice as well as to evaluate the potential side effects which present from the administration of CurNQ and MSN_CurNQ. Continuous dosing with health monitoring allowed for the safety and tolerability of CurNQ and MSN_CurNQ to be assessed. At the end of the study period, mice were euthanised through an injection with Sodium Pentobarbitone and their heart, liver, spleen, lung and kidney were collected [12]. Hematoxylin and eosin (H&E) staining was conducted on heart, liver, spleen, lung and kidney samples obtained after

euthanasia and were processed by a veterinary pathologist at Idexx laboratories. Histopathology allowed for the evaluation of toxicity.

5.2.5 *Part B -Tumour xenograft establishment*

One and a half million OVCAR-5 cells suspended in DMEM (0.2 mL) containing 50% Matrigel [12,13] were subcutaneously injected into the left lateral flank of the nude mice whilst mice were under anaesthesia induced via isoflurane. When tumours did not grow after 2 weeks, 3 million OVCAR-5 cells suspended in DMEM (0.2 mL) containing 50% Matrigel were reinjected into the left lateral flank of the nude mice [13]. Tumours then proceeded to grow. Once most of the mice developed tumours of 5 mm, the efficacy study was initiated.

5.2.6 *Part B- Evaluation of chemotherapeutic potential of CurNQ and MSN_CurNQ*

The chemotherapeutic potential of CurNQ and MSN_CurNQ were required to be evaluated in an *in vivo* animal model bearing xenograft tumours. The mice used to develop the appropriate technique for the establishment of the tumour xenograft were utilised for the efficacy study, thereby reducing the total number of animals used. Thus, 20 tumour bearing mice were allocated to this study and were divided into 4 test groups. Once tumours reached 5mm the efficacy study commenced. The test groups were allocated as follows:

Group 1: Mice injected with a dose of 10 mg/kg CurNQ.
Group 2: Mice injected with a dose of 10 mg/kg MSN_CurNQ.
Group 3: Mice injected with a dose of 25 mg MSN_CurNQ.
Group 4: Mice injected with saline (control).

The dosages were selected based on the results obtained from part A of the study. Part A demonstrated that 10 mg/kg of CurNQ and MSN_CurNQ were well tolerated and all mice survived continuous dosing during a 10-day period. Histopathology results indicated 10 mg/kg of CurNQ could result in toxicity if the dose was to be increased, thus 10 mg/kg was utilised as the dose for the efficacy study. Conversely, low toxicity was observed in mice receiving 10 mg/kg of MSN_CurNQ thus it was deemed safe to

increase this dosage to 25 mg/kg. An experimental group of 10 mg/kg MSN_CurNQ was included to offer a direct comparison to the 10 mg/kg CurNQ treatment group.

MSN_CurNQ and CurNQ were dissolved in 100 µL of saline and were sonicated prior to administration. Treatments were administered via IV tail vein injection [13]. Mice were terminated prior to the end of the study if the tumour size reached 15 mm, which was deemed as the ethical end point [14]. Treatments were administered twice per week and the study proceeded for 4 weeks after which the mice that had not previously reached the ethical end point were terminated. The tumours were measured using digital callipers biweekly and the mice were continuously weighed as a critical health measurement [15]. Health monitoring was performed twice daily, and mice were checked daily by veterinary personnel to ensure their health and that no suffering occurred.

5.3 Results and Discussion

5.3.1 *Part A – Safety Tolerability and Toxicity of CurNQ and MSN_CurNQ*

Tolerability, safety and toxicity are important measurements that are required prior to evaluating the efficacy of a novel compound. Six mice were allocated to Part A of the preclinical trial, with three mice being allocated to each experimental group. Mice were continuously monitored of any signs of ill health, pain or distress. All 6 mice survived the 10 days and showed no overt signs of ill health, pain or distress. Weight changes in the mice were used to evaluate the tolerability of CurNQ and MSN_CurNQ [16]. Mice did not experience substantial weight loss in response to either treatments (Figure 5.2). From the weight chart shown in Figure 5.2, MSN_CurNQ was better tolerated than CurNQ as the weight changes were the most stable in mice receiving MSN_CurNQ. Mice receiving CurNQ experienced weight fluctuations over the 10-day period. Behavioural changes were not observed in either group, and none of the mice were observed to have experienced discomfort or pain in response to treatment [17,18]. Thus, CurNQ and MSN_CurNQ was overall considered to be well tolerated by the mice. Moreover, all mice survived the entire length of the study and continuous dosing did not result in any outwardly observable negative side effects, thus both treatments were

considered safe at the administered dose. This was deemed a positive result for the preclinical trial.

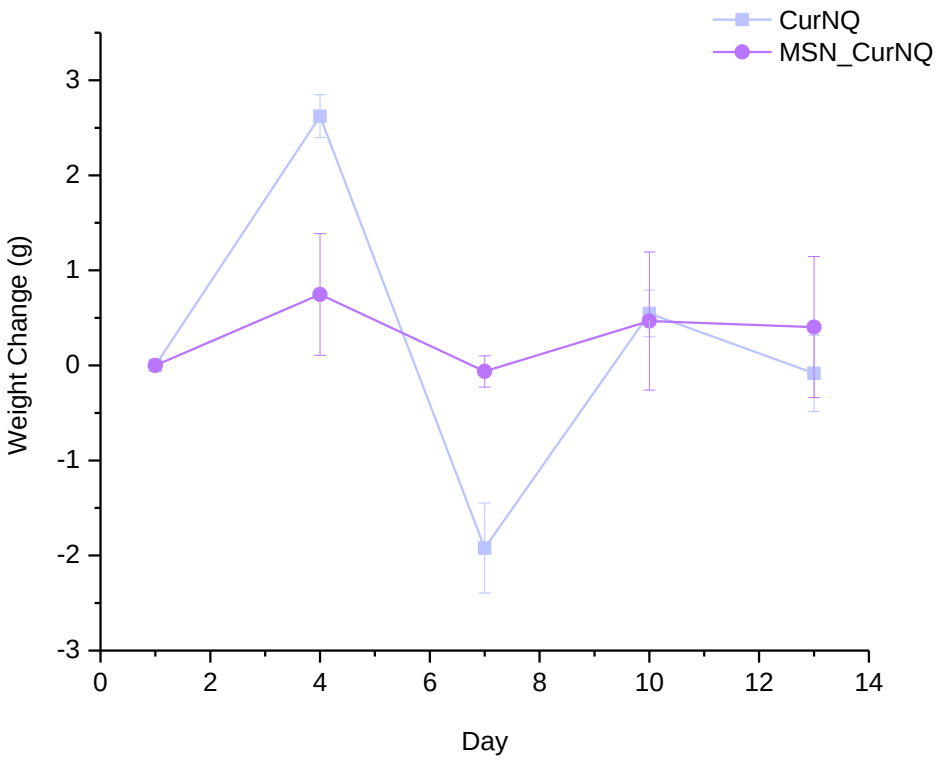


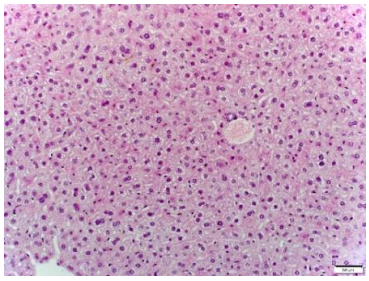
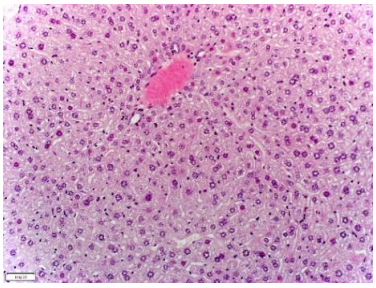
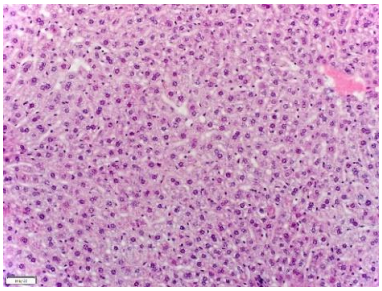
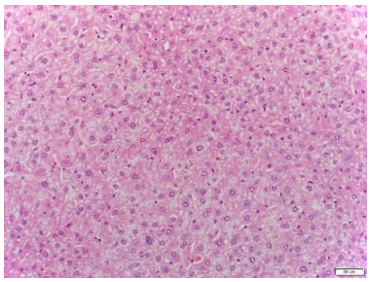
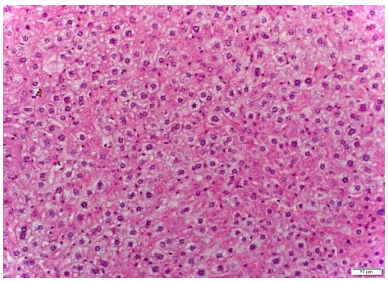
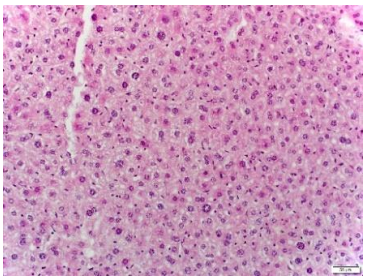
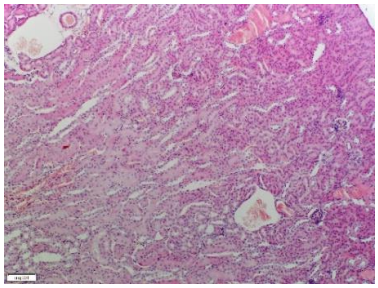
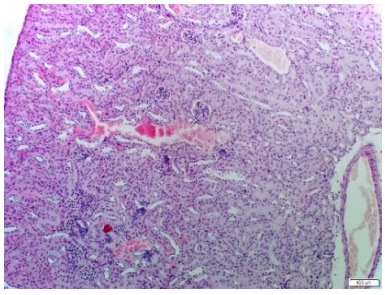
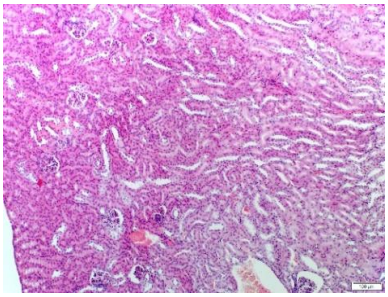
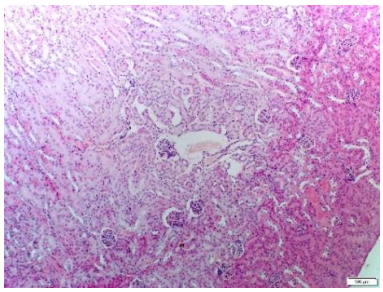
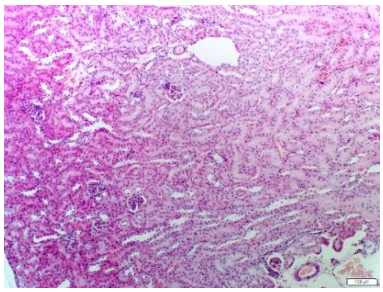
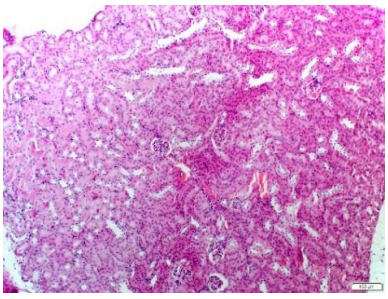
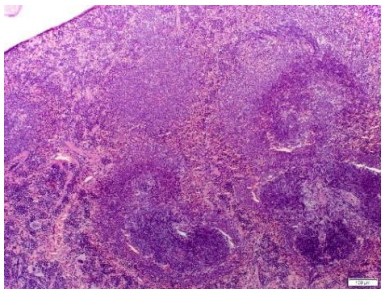
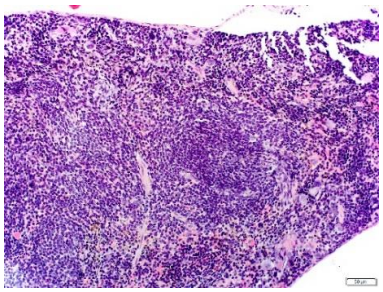
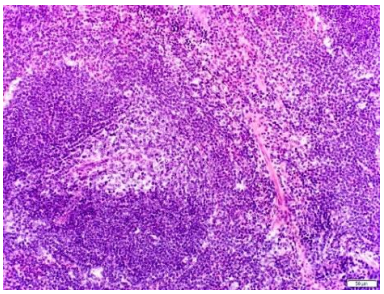
Figure 5.2: Weight changes of mice receiving CurNQ and MSN_CurNQ over Part A of the preclinical trial.

After the completion of the study, organs were sent for histopathology. Histopathology revealed the toxicity of drugs administered on the collected organs and are displayed in Table 5.1. Mice having received 10 mg/kg of CurNQ had mild to moderately swollen hepatocytes, and their cytoplasms were mildly vacuolated and granular. Hepatocyte swelling and vacuolar change is pathological in nature [19,20], however this condition was mild to moderate in these mice. Additionally, the lining tubing epithelial cells of the inner cortex of the kidney were mildly swollen in these mice. Furthermore, the white pulp follicles of the spleen were notably expanded and highly active indicating an immune response [21]. All other organs displayed an overall normal histopathology. The histopathology results taken in conjunction with the survival and weight fluctuations observed from the mice receiving CurNQ indicated CurNQ to be slightly toxic yet can be tolerated at the above dose. An increase in dose could result in greater toxicity

presenting in the form of liver and kidney damage which would likely be owing to a disruption of ATP synthesis, mitochondrial injury, free radical formation, peroxidation or perturbed cell signalling [22].

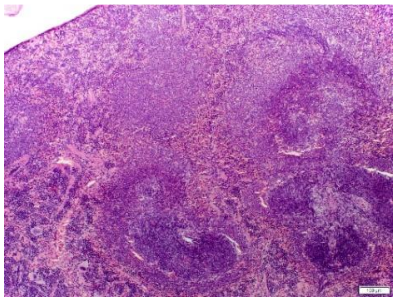
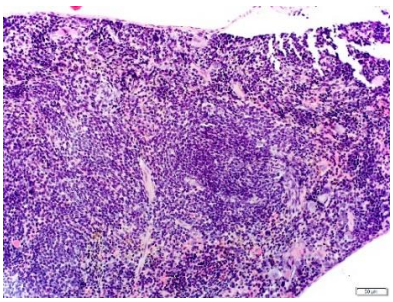
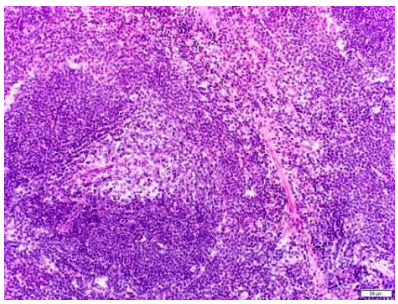
MSN_CurNQ appeared to induce less severe toxic effects than CurNQ administered alone. Here too, hepatocytes and deep cortical tubules of renal cells were slightly swollen, and a decrease in luminal diameter was observed in the deep cortical tubules. However, this swelling was less severe than mice receiving CurNQ. The white pulp follicles of the spleen were also active in group 2. The weight chart of MSN_CurNQ demonstrated that mice tolerated MSN_CurNQ better than CurNQ alone and their weights were mostly stable. Therefore, the loading of CurNQ onto the nanoplatform reduces the toxicity of CurNQ. Owing to the slight swelling of hepatocytes and renal cells, escalating doses should be closely monitored as to avoid toxicity; yet mice would likely be able to tolerate a higher dose of MSN_CurNQ.

Table 5.1: Histopathology of mice organs from preclinical trial part A. Three mice were allocated to each experimental group, and histopathology samples are presented for each mouse.

Liver CurNQ			
Liver MSN_CurNQ			
Kidney CurNQ			
Kidney MSN_CurNQ			
Spleen CurNQ			

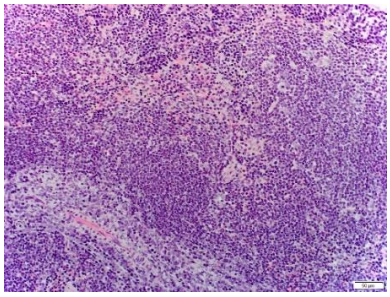
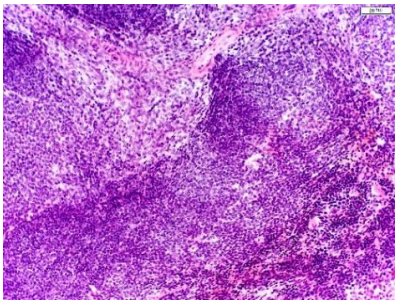
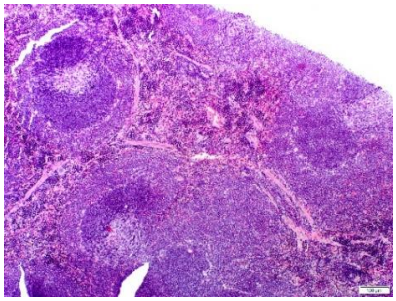
Spleen

CurNQ

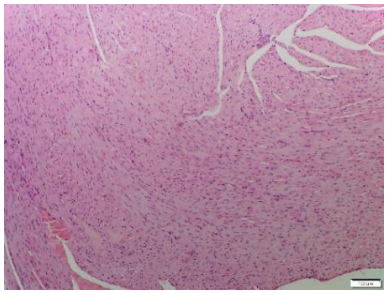
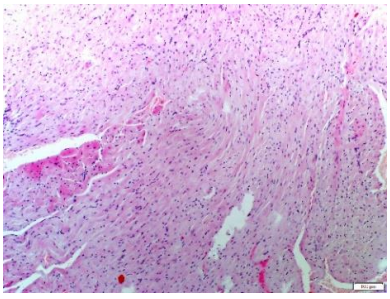
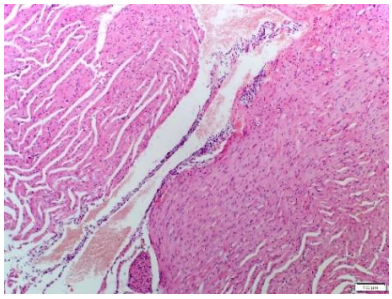
Spleen

MSN_CurNQ

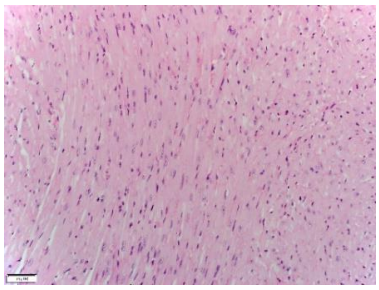
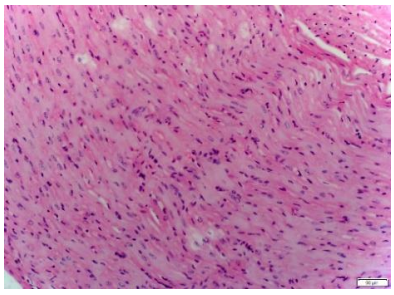
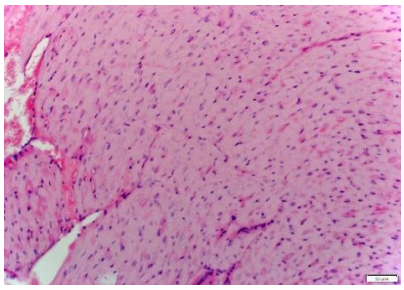
Heart

CurNQ

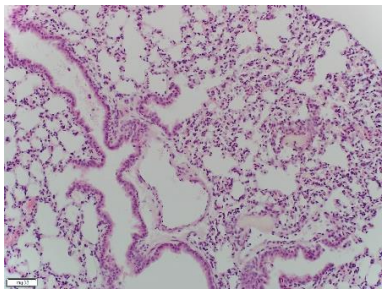
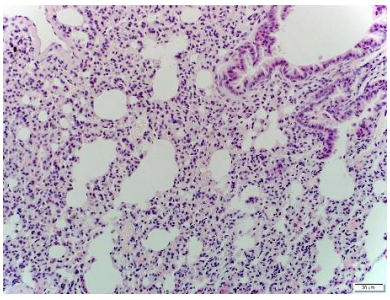
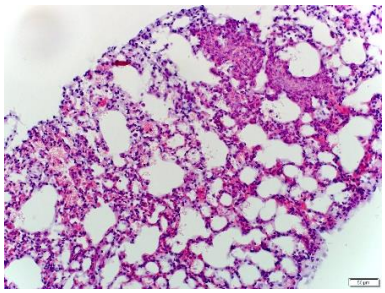
Heart

MSN_CurNQ

Lung

CurNQ

5.3.2 *Part B – OVCAR-5 tumour xenograft establishment and efficacy evaluation of CurNQ and MSN_CurNQ in MF-1 nude mice*

5.3.2.1 Establishment of tumour xenografts

Different cell lines often require different experimental techniques to successfully establish xenografts in all inoculated mice and many researchers experience difficulties in this regard [23]. Therefore, including the establishment of tumour xenograft in the preclinical trial was performed to perfect this technique and to remove future potential difficulties. Indeed, it was the case that difficulties arose in establishing a tumour xenograft. The first attempt saw the injection of 1.5 million OVCAR-5 cells into the left lateral flank of 20 mice. Two weeks later, no tumours growth was evident. This prompted a reinjection of tumour cells. The second attempt saw 3 million OVCAR-5 cells being injected into the same location. This time, care was taken to maintain the cells at 37°C for as long as possible prior to injection. Mice proceeded to grow tumours in this location, and after tumours reached about 3 mm rapid growth occurred (Figure 5.3). However, 2 mice had what appeared to be small tumours begin to appear and then after some time disappeared. These perceived tumours could have been swelling in the inoculated area that later subsided. A further 2 mice developed small tumours (2 mm), yet these tumours did not proceed to grow after the initial growth, the reason for this is unclear. Consequently, not all inoculated mice successfully developed tumours. The reason for this is unknown but other studies have reported that not all mice inoculated developed tumours [24–26]. This pilot study clarified the techniques and difficulties involved in the establishment of a human tumour xenograft. Going forward, an additional 20% of mice should be inoculated to account for the mice that do not successfully develop tumours, additionally 3 million cells should be injected at the start of the study, as this is the amount of cells required to induce tumour growth. The tumour growth pattern, mice behaviour and weights were also monitored to ascertain the effects of tumour growth on the health of the mice. The tumour growth over the 4-week period is presented in Figure 5.3. The establishment of a human tumour xenograft was therefore considered a success, and the methodology in establishing an OVCAR-5 xenograft in MF-1 mice was confirmed.

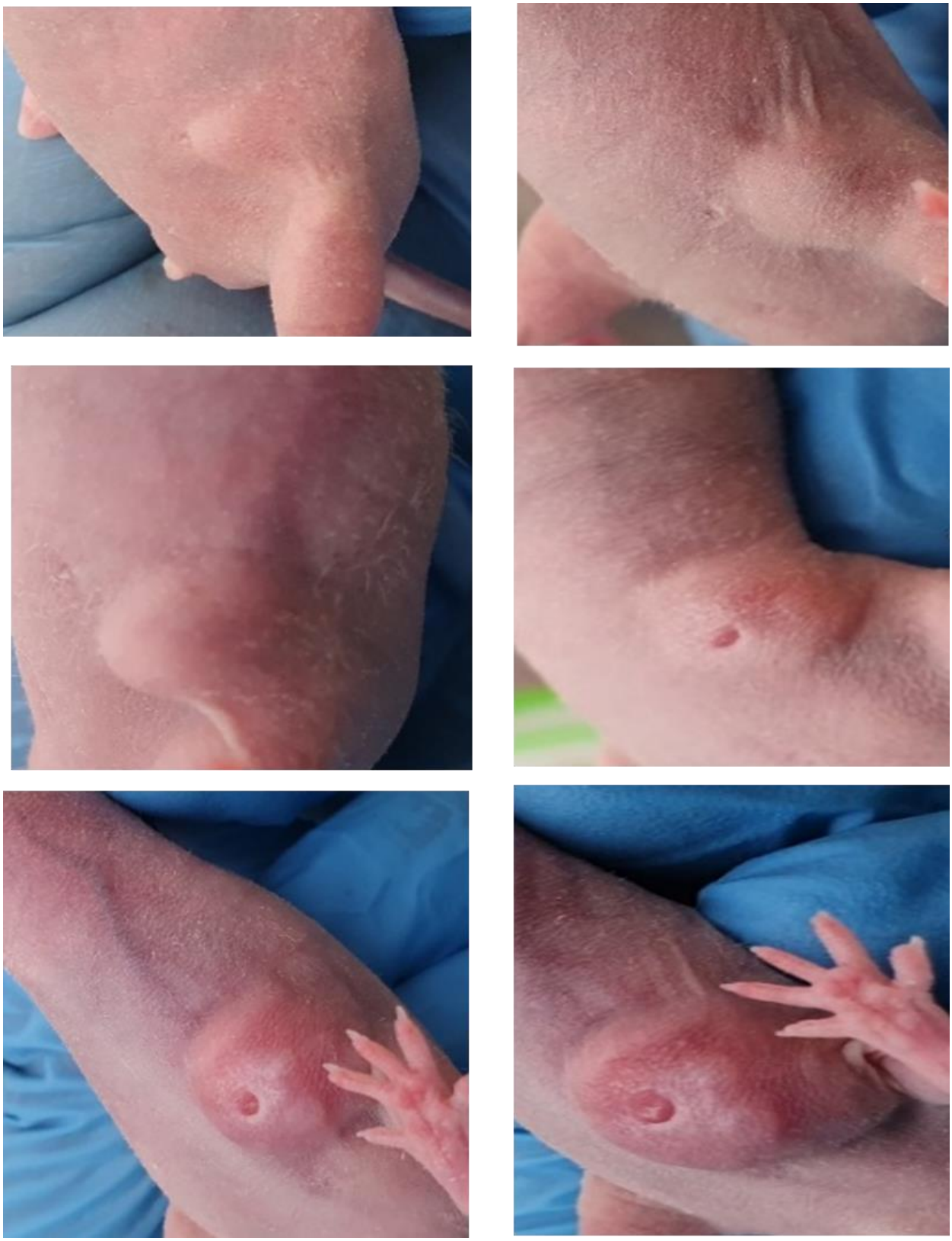


Figure 5.3: Xenograft tumour growth in nude mice over a 4-week period.

5.3.2.2 Part B – Evaluation of CurNQ and MSN_CurNQ Efficacy

The chemotherapeutic effects of CurNQ and MSN_CurNQ were required to be evaluated on an *in vivo* animal model bearing OVCAR-5 xenograft tumours [27]. The same mice used to establish the methodology for xenograft formation were utilised for the efficacy study, thereby reducing the total number of required animals. Whilst the tumours were developing, one mouse developed an unrelated skin illness and was euthanised, therefore 19 mice were utilised for the efficacy study. The 4 experimental groups were defined above. The control group was allocated 4 mice, whilst the experimental groups were allocated 5 mice per group. The 4 mice with the smallest tumours at the starting point of the efficacy study were allocated to the control group. This was done to prevent the premature termination of the study, as the control group was most likely to experience the highest rate of tumour growth resulting in the ethical end point being reached prior to the mice in the treatment group which would then not allow for an effective comparison.

At the start of the efficacy study all mice appeared to have tumours; after which tumours belonging to 2 mice allocated to the control group began to rapidly shrink and proceeded to disappear. After this occurred it was evident that these apparent tumours were in fact swelling around the injection site which later subsided. The other 2 mice allocated to the control group, had small tumours that developed slowly initially with their growth halting after reaching 2 mm. Inopportunely, these 2 events occurred after the commencement of the efficacy study and no additional unallocated mice were available. This resulted in mice in the control group bearing no tumours. Therefore, the control group was required to be excluded from the results, deeming the other obtained results inconclusive.

It was decided to see the study to completion with the remaining treatment groups to obtain preliminary results and for the study to act as a pilot study. This was considered ethically justified as to not waste the lives of the remaining 15 mice. Five mice were allocated to each experimental group and mice were administered with the allocated treatment twice a week over a period of 4 weeks. Treatments were suspended in 100 µL of saline and were administered via IV tail vein injection. The tumour size and

weights of the mice were measured biweekly. All mice survived throughout the study, further confirming the safety and non-toxicity of the administered treatments.

All tumours in the experimental groups grew throughout the study and no tumour shrinkage occurred (Figure 5.3). The average tumour growth rate was the lowest for the mice treated with CurNQ alone compared to mice treated with both doses of MSN_CurNQ. This was unexpected as it was expected for MSN_CurNQ to induce a larger response than CurNQ alone owing to the targeted and sustained release from the nanoparticles. This could indicate that the full dosage of CurNQ was not released from the MSN *in vivo*. This may be on account of the sustained release of CurNQ from MSN whereby the release peaks at 96 hours (Figure 4.3) and *in vivo* the particles may have been eliminated or cleared prior to this point, in so doing reducing the actual dose administered which correlated to a higher average growth rate.

The CurNQ treatment group resulted in the lowest average growth rate. This is promising as it suggests CurNQ may be effective in reducing the growth rate of a tumour, and if administered at the right dosage over the correct period it may have promise as an effective chemotherapeutic agent.

The growth rate of MSN_CurNQ 10 mg/kg and MSN_CurNQ 25 mg/kg were very similar; the growth rate of MSN_CurNQ 25 mg/kg was 7.6% lower than MSN_CurNQ 10 mg/kg, with the actual average tumour size being 19% lower (Figure 5.5). This indicates that an increase in administered dose does influence the tumour growth rate and size; however, this relationship between dose growth rate and tumour size is not directly proportional.

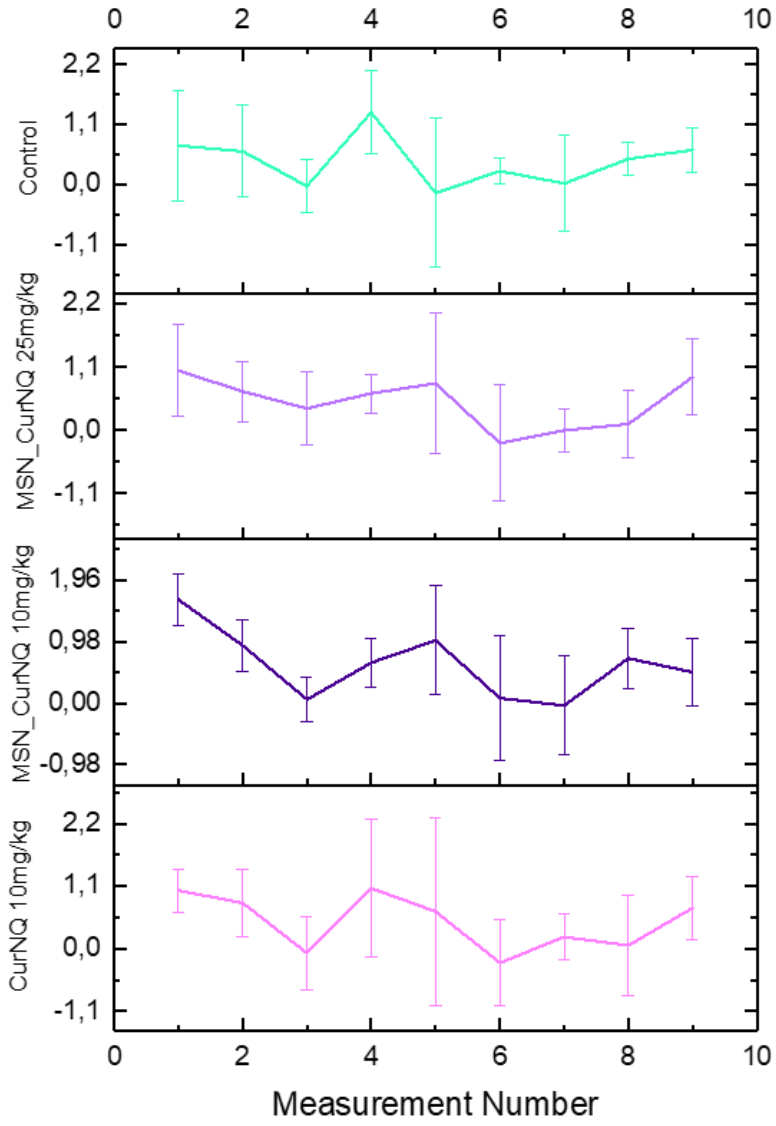
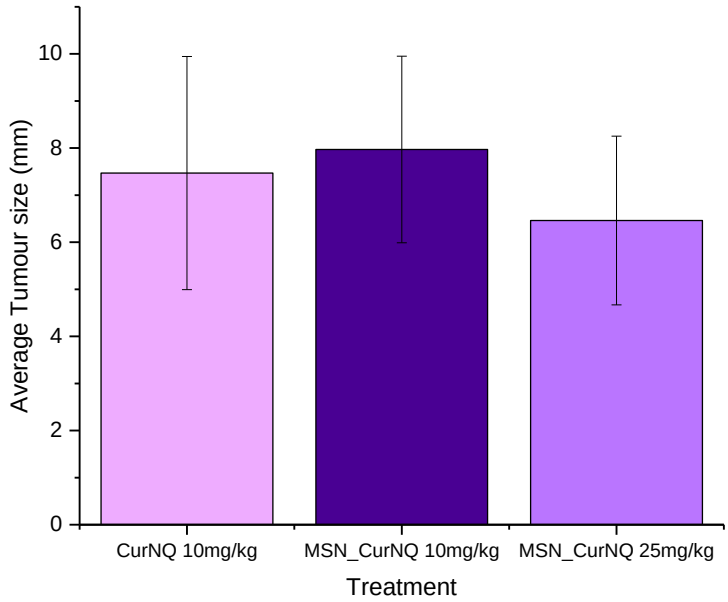


Figure 5.4: Weight changes of tumour bearing mice treated with 10 mg/kg CurNQ, 10 mg/kg MSN_CurNQ and 25 mg/kg MSN_CurNQ over part B of the preclinical trial.

A



B

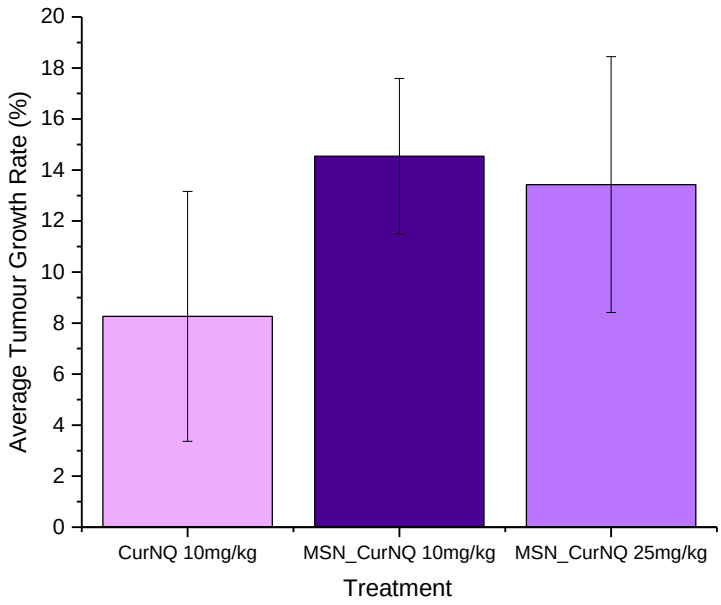


Figure 5.5 A) Average tumour size and **B)** average tumour growth rate of mice treated with 10 mg/kg CurNQ, 10 mg/kg MSN_CurNQ and 25 mg/kg MSN_CurNQ over a 4-week period. The control group was required to be excluded from the results as 2 of the mice in the control group did not develop tumours and the development of fully grown tumours did not occur in the remaining 2 mice, therefore all obtained results are considered as preliminary.

All mice demonstrated a highly similar pattern of weight changes throughout the study, and no significant differences were present between experimental groups (Figure 5.4). A decline in weights were observed for all treatment groups between measurements 3 and 6. These measurement days coincided with the initial growth of the tumours; thus, directly affecting the health of the mice and thereby their weights. All mice then experienced an improvement with their weights increasing until the termination of the study. The similar weight fluctuation pattern between all experimental groups suggests that weight changes are most likely on account of tumour growth and were not in response to the treatment administered (Figure 5.4). Moreover, the weight again observed from measurements 7 to 9 may be on account of tumour growth with the additional weight being from the tumour itself. Therefore, the weight changes alone cannot give a complete reflection on the health of the mice. Normal behaviour and eating habits were observed and no outward appearances of pain were noted; thereby indicating treatments were overall well tolerated. Furthermore, a histopathology assessment was performed on collected organs after the completion of the study. These results correlated to the histopathology results obtained from Part A of the *in vivo* study.

Mild hepatocellular swelling and vaculour changes were present in the liver samples and were observed from individuals across all treatment groups. However, these changes were mild and were determined by the veterinary anatomical pathologist to be non-pathological with mild swelling to be of metabolic origin. Mild renal changes were also present in some individuals from the CurNQ 10 mg/kg and MSN_CurNQ 25 mg/kg treatment groups. Here, the deep cortical convoluted tubules showed minimal to mild swelling of the lining epithelial cells with eosinophilic cytoplasm; however, these changes were considered mild. No other pathological changes were evident. Hence, overall CurNQ and MSN_CurNQ treatment can be considered to induce low overall toxicity.

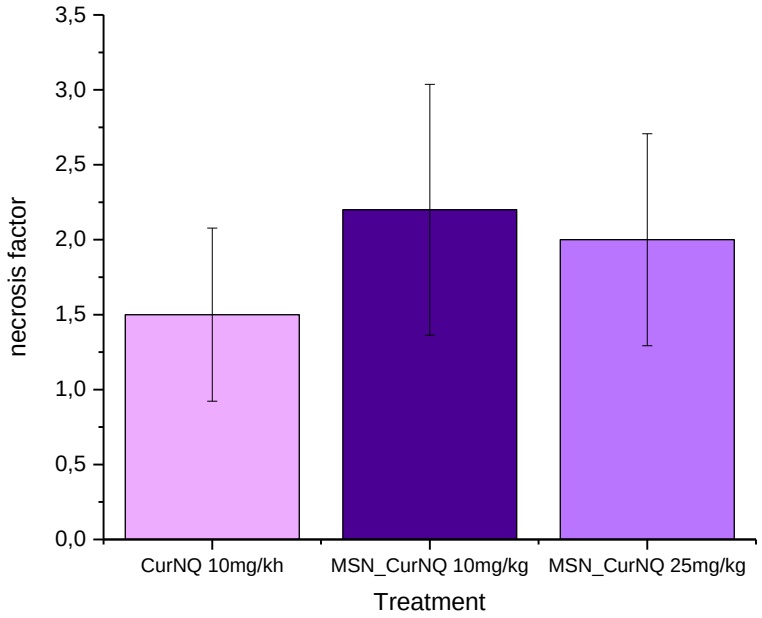


Figure 5.6: Necrosis factor of tumours in experimental groups. The necrosis factor is rated from 0 to 3, with 0 being no necrosis occurring and 3 being >50% of section viewed.

Histopathology was performed on the tumours collected at the end of the study. A histological assessment was performed to ascertain the necrosis factor and the mitotic rate of the tumours. Additionally, histology confirmed the tumours were typical of anaplastic solid epithelial neoplasia and thus correlated to the OVCAR-5 cell line used and confirmed the methodology used to induce the human tumour xenograft was successful. The necrosis factor is a measure of the degree of necrosis evident in a viewed specimen [28,29]. The necrosis factor is rated from 0 to 3, with 0 being no necrosis occurring and 3 being >50% of section viewed undergoing necrosis (Figure 5.6). The histopathological results stated that the areas of necrosis occurred in the centres of the neoplasms, thus necrosis could be drug-induced or on account of hypoxia. Higher levels of necrosis were evident in the MSN_CurNQ treatment (2.2 and 2) groups compared to the CurNQ treatment group (1.5). This suggests the nanosystem was more effective in inducing necrosis than CurNQ administered alone. Moreover, the high levels of necrosis evident in the MSN_CurNQ treatment groups is promising and indicates MSN_CurNQ may induce tumour necrosis.

The mitotic rate was also evaluated in the neoplasms and is displayed in Figure 5.7. The mitotic rate is defined as the number of mitotic cells per high power field, taken as the highest count of three high power fields. The higher the mitotic rate, the more aggressive the tumour [30,31]. As per Figure 5.7, MSN_CurNQ 25 mg/kg had the lowest mitotic rate, suggesting the higher dose of MSN_CurNQ reduced the mitotic rate of the cancer cells. This together with the higher observed necrotic factor in Figure 5.7, was a promising indication that MSN_CurNQ may reduce the mitotic rate of a tumour and induce necrosis, thus it could be effective as a chemotherapeutic.

Owing to the higher rate of necrosis and the lower mitotic rate of the mice treated with MSN_CurNQ 25 mg/kg, it was unexpected that the average growth rate was higher than that of the CurNQ treatment group. The reason for the seeming contradiction is unclear and these results remain inconclusive. It does seem evident that the higher dosage of MSN_CurNQ (25 mg/kg) was more effective than the lower dosage of MSN_CurNQ (10 mg/kg) as it resulted in a lower average tumour growth rate, and a lower mitotic rate with a similar necrosis factor. Without an experimental control group, conclusive and statistically significant results could not be drawn from the *in vivo* efficacy study and the results remain as preliminary findings. Yet, the results are promising and warrant the continuation of further *in vivo* studies as CurNQ and MSN_CurNQ may have potential as a chemotherapeutic agent.

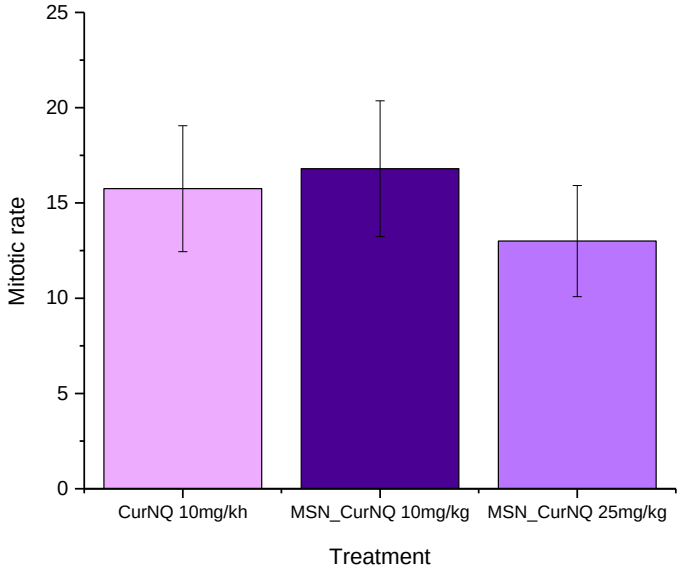


Figure 5.7: The Mitotic rate of the tumours in the three experimental groups.

5.4 Conclusions

All mice survived continuous dosing thereby deeming both treatments safe. MSN_CurNQ was better tolerated than CurNQ as less weight fluctuations occurred. Histopathology showed mild hepatocyte swelling with vacuolar changes present as well as swelling of the lining tubing epithelial cells of the inner cortex of the kidney in both treatment groups; however these histopathologist were more prominent from mice in the CurNQ treatment group and presented mildly for mice in the MSN_CurNQ treatment group. Hence, the dose of 10 mg/kg of CurNQ and MSN_CurNQ was deemed safe; however, an increased dose of CurNQ may induce liver or kidney damage. Accordingly, a maximum dose of 10 mg/kg CurNQ is recommended in future preclinical trials. The results of this preclinical trial were positive, demonstrating repeat exposure to CurNQ and MSN_CurNQ was well tolerated, safe and only resulted in mild toxicity.

OVCAR-5 tumour xenografts were successfully established in 15 mice and an efficacy study was conducted to evaluate the chemotherapeutic potential of CurNQ and MSN_CurNQ. On account of the control being excluded, conclusive and statistically significant results could not be drawn, and the acquired results are considered as preliminary findings. The 10 mg/kg CurNQ treatment group had the lowest average tumour growth rate. The 25 mg/kg MSN_CurNQ treatment appeared to be more effective as a chemotherapeutic than the lower dosage of 10 mg/kg MSN_CurNQ as it resulted in a lower average tumour growth rate, and a lower mitotic rate with a similar necrosis factor. These results suggest CurNQ and MSN_CurNQ may induce tumour necrosis and may reduce tumour growth rate; indeed, these preliminary results were promising and warrant the continuation of further *in vivo* studies as CurNQ and MSN_CurNQ may have potential as a chemotherapeutic agent.

5.5 References

1 Workman P, Aboagye EO, Balkwill F, Balmain A, Bruder G, Chaplin DJ, et al. Guidelines for the welfare and use of animals in cancer research. Br J Cancer. 2010;102(11):1555–77.

2 Roberts WG, Ung E, Whalen P, Cooper B, Hulford C, Autry C, et al. Antitumor activity and pharmacology of a selective focal adhesion kinase inhibitor, PF-562,271. Cancer Res. 2008;68(6):1935–44.

3 Subramani R, Gonzalez E, Arumugam A, Nandy S, Gonzalez V, Medel J, et al. Nimbolide inhibits pancreatic cancer growth and metastasis through ROS-mediated apoptosis and inhibition of epithelial-to-mesenchymal transition. Sci Rep. 2016;6:1–12.

4 Gupta SC, Prasad S, Sethumadhavan DR, Nair MS, Mo YY, Aggarwal BB. Nimbolide, a limonoid triterpene, inhibits growth of human colorectal cancer xenografts by suppressing the proinflammatory microenvironment. Clin Cancer Res. 2013;19(16):4465–76.

5 Sastry BS, Babu SK, Babu HT, Chandrasekhar S, Srinivas PV, Saxena AK, et al. Synthesis and biological activity of amide derivatives of nimbolide. Bioorganic Med Chem Lett. 2006;16(16):4391–4.

6 Shahin SA, Wang R, Simargi SI, Contreras A, Echavarria LP, Qu L, et al. Hyaluronic acid conjugated nanoparticle delivery of siRNA against TWIST reduces tumor burden and enhances sensitivity to cisplatin in OC. Nanomedicine Nanotechnology, Biol Med. 2018;14:1381–94.

7 Rattan R, Graham RP, Maguire JL, Giri S, Shridhar V. Metformin suppresses OC growth and metastasis with enhancement of cisplatin cytotoxicity in Vivo. Neoplasia. 2011;13(5):483–91.

8 Staffhorst RWHM, Van Der Born K, Erkelens CAM, Hamelers IHL, Peters GJ, Boven E, et al. Antitumor activity and biodistribution of cisplatin nanocapsules in nude mice bearing human ovarian carcinoma xenografts. Anti-cancer Drugs. 2008;19(7):721–7.

9 Fu C, Liu T, Li L, Liu H, Chen D, Tang F. Biomaterials The absorption, distribution, excretion and toxicity of mesoporous silica nanoparticles in mice following different exposure routes. Biomaterials. 2013;34(10):2565–75.

10 Liu T, Li L, Teng X, Huang X, Liu H, Chen D, et al. Biomaterials Single and repeated dose toxicity of mesoporous hollow silica nanoparticles in intravenously exposed mice. Biomaterials. 2011;32(6):1657–68.

11 Lu J, Liong M, Li Z, Zink JI, Tamanoi F. Efficiency of Mesoporous Silica Nanoparticles for Cancer Therapy in Animals. small. 2010;(16):1794–805.

12 Meng H, Xue M, Xia T, Ji Z, Tarn DY, Zink JI, et al. Use of Size and a Copolymer Design Feature To Improve the Biodistribution and the Enhanced Permeability and Retention

Effect of Doxorubicin- Loaded Mesoporous Silica Nanoparticles in a Murine Xenograft Tumor Model. ACS Nano. 2011;(5):4131–44.

13 Croissant JG, Zhang D, Alsaiari S, Lu J, Deng L, Tamanoi F, et al. Protein-gold clusters-capped mesoporous silica nanoparticles for high drug loading, autonomous gemcitabine/doxorubicin co-delivery, and in-vivo tumor imaging. J Control Release. 2016;229:183–91.

14 Lu J, Li Z, Zink JI, Tamanoi F. In vivo tumor suppression efficacy of mesoporous silica nanoparticles-based drug-delivery system: enhanced efficacy by folate modification. Nanomedicine Nanotechnology, Biol Med. 2012;8(2):212–20.

15 Cheng W, Nie J, Xu L, Liang C, Peng Y, Liu G, et al. pH-Sensitive Delivery Vehicle Based on Folic Acid-Conjugated Polydopamine-Modified Mesoporous Silica Nanoparticles for Targeted Cancer Therapy. ACS Appl. Mater. Interfaces. 2017; 9(22): 18462–18473.

16 Wu K, Cheng R, Zhang J, Meng F, Deng C, Zhong Z. Micellar nanoformulation of lipophilized bortezomib: High drug loading, improved tolerability and targeted treatment of triple negative breast cancer. J Mater Chem B. 2017;5(28):5658–67.

17 Vassileva V, Moriyama EH, Souza R De, Grant J, Allen CJ, Wilson BC. Efficacy assessment of sustained intraperitoneal paclitaxel therapy in a murine model of OC using bioluminescent imaging. Br J Cancer. 2008;(99):2037–43.

18 Ullman-culleré MH, Foltz CJ. Body Condition Scoring : A Rapid and Accurate Method for Assessing Health Status in Mice. Lab Anim Sci. 1999;49(3):319-23.

19 Nayak NC, Sathar SA, Mughal S, Duttagupta S, Mathur M, Chopra P. The nature and significance of liver cell vacuolation following hepatocellular injury - an analysis based on observations on rats rendered tolerant to hepatotoxic damage. Virchows Arch. 1996;428(6):353–65.

20 Kleiner DE. Drug-Induced Liver Injury: The Hepatic Pathologist's Approach. Gastroenterol Clin North Am. 2017;46(2):273–96.

21 Elmore SA. Enhanced Histopathology of the Spleen. Toxicol Pathol. 2006;34(5):648–55.

22 Mescher A. Junqueira's Basic Histology Text & Atlas. ed. 14. New York: McGraw-Hill Medical;2016.

23 Hogenesch H, Nikitin AY. Challenges in pre-clinical testing of anti-cancer drugs in cell culture and in animal models. J Control Release. 2012;164(2):183–6.

24 Braakhuis BJM, Sneeuwloper G, Snow GB. The potential of the nude mouse xenograft model for the study of head and neck cancer. Arch Otorhinolaryngol. 1984;239(1):69–79.

25 Hall DMS, Brooks SA. In Vitro Invasion Assay Using Matrigel™: A Reconstituted Basement Membrane Preparation. In Schumacher DM ed. 2. Metastasis Research Protocols Methods in Molecular Biology. New York: Springer; 2014: 1-11.

26 Shaw TJ, Senterman MK, Dawson K, Crane CA, Vanderhyden BC. Characterisation of

intraperitoneal, orthotopic, and metastatic xenograft models of human OC. Mol Ther. 2004;10(6):1032–42.

27 Jung J. Human tumor xenograft models for preclinical assessment of anti-cancer drug development. Toxicol Res. 2014;30(1):1–5.

28 Hiraoka N, Ino Y, Sekine S, Tsuda H, Shimada K, Kosuge T, et al. Tumour necrosis is a postoperative prognostic marker for pancreatic cancer patients with a high interobserver reproducibility in histological evaluation. Br J Cancer. 2010;103(7):1057–65.

29 Mitsunaga S, Hasebe T, Iwasaki M, Kinoshita T, Ochiai A, Shimizu N. Important prognostic histological parameters for patients with invasive ductal carcinoma of the pancreas. Cancer Sci. 2005;96(12):858–65.

30 Kim YJ, Ketter R, Steudel WI, Feiden W. Prognostic significance of the mitotic index using the mitosis marker anti-phosphohistone H3 in meningiomas. Am J Clin Pathol. 2007;128(1):118–25.

31 Prayson RA. Cell proliferation and tumors of the central nervous system, part II: Radiolabeling, cytometric, and immunohistochemical tecniques. J Neuropathol Exp Neurol. 2002;61(8):663–72.

Chapter 6: Conclusions and Future perspectives

6.1 Conclusions

This thesis presents the synthesis of a novel theranostic nanosystem for targeted cancer intervention, through the synthesis of a chemotherapeutic fluorescent compound, that is specifically solubilised at the pH associated with the malignant microenvironment. A novel molecule, termed CurNQ was synthesised through a Williamson ether synthesis reaction between curcumin (Cur) and lawsone. These two phytochemicals were selected for further modification owing to the abundant research that demonstrates their respective anti-cancer and fluorescent properties. However, each of these phytochemicals have several limitations precluding their clinical translation including, molecular instability, rapid degradation and poor bioavailability. Therefore, this research aimed to improve the biopharmaceutical properties of Cur and lawsone to further exploit the purported anti-cancer therapeutic properties of these two phytochemicals, by synthesizing a novel therapeutically stable molecule (CurNQ) with appropriate bioavailability, targeting capabilities and innate fluorescence.

Structural elucidation of CurNQ was performed with ^{1}H and ^{13}C NMR, HRMS-ESI and FTIR. CurNQ was demonstrated to have pH specific solubility, its saturation solubility increased from 11.15 µM at pH 7.4 to 20.7 µM at pH 6.8. This large shift in solubility coincides with the shift in pH that occurs upon malignant transformation, thereby enabling cancer targeting owing to the Warburg effect. Moreover, CurNQ displayed high intensity intrinsic fluorescence, thus once soluble a high intensity fluorescent signal would be released, enabling detection applications. Ovarian carcinoma (OC) was selected as the model cancer type for this thesis. To this end, two OC cell lines namely, OVCAR-5 and SKOV3 were utilised. The toxicity of CurNQ as well as any morphological changes that were induced through CurNQ treatment were ascertained using a high content imaging system. This high throughput imaging and screening method allowed for an in-depth analysis of the effect that CurNQ had on OC cells. Significant reductions in cell viability to below 50% occurred in response to CurNQ treatment in both OVCAR-5 and SKOV3, and no statistical difference was observed between the reduction in cell viability between these two cell lines ($p = 0.743$). Cell morphology of OVCAR-5 cells in response to varying concentrations of CurNQ was

quantified using the CELENA® X High Content Imaging System and cell eccentricity, form factor and compactness were quantified. Compactness and form factor increased, and eccentricity decreased with increasing concentrations of CurNQ. This implied DNA fragmentation, nuclear distortion and chromatin condensation was occurring and was induced in response to CurNQ treatment, all of which signify the induction of apoptosis. This sharp reduction in cell viability and induction of apoptosis observed in response to CurNQ treatment in both OVCAR-5 and SKOV3 cell lines was promising data, suggesting that CurNQ could act as a potent ovarian anti-cancer drug.

The loading of CurNQ onto a nanoplatform platform was performed to allow for enhanced delivery and enable *in vitro* and *in vivo* imaging and detection. The introduction of the nanoplatform was included to allow for advanced delivery through enhanced retention and passive tumour targeting owing to the EPR effect. Mesoporous silica nanoparticles (MSN) were synthesised and were impregnated with CurNQ thereby forming the novel nanosystem MSN_CurNQ.

CurNQ demonstrated pH responsive release from MSN, specific to the tumour microenvironment, whereby after 96 hours 31.5% of CurNQ was released at pH 7.4 compared to 57% release at pH 6.8. This equated to a 25,5% increase in release occurring in response to a 0.6 reduction in pH with the actual release of CurNQ at pH 6.8 being almost double the release at pH 7.4. This difference in release between the two pH values was highly significant with a corresponding p-value of 0.000. This highly significant p-value confirms the effects of pH on the release of CurNQ from the MSN, thus verifying the pH responsivity and specificity of the nanosystem. Moreover, this highly significant p-value emphasizes the robust nature of CurNQ pH-responsivity. Clearly, the change in pH associated with malignant transformation acts as a solubility switch for CurNQ allowing for potential cancer targeting applications.

The fluorescent nature of MSN_CurNQ was evaluated using confocal and fluorescent microscopy. The microscopy images demonstrated MSN_CurNQ to have highly precise, distinctive and high intensity fluorescence with a high target to background ratio, low fluorescent blur, a long fluorescent lifetime and fluorescent stability, all of which demonstrated MSN_CurNQ to be a potentially powerful diagnostic and imaging agent, with potential applications in cancer detection.

MTT assays were performed on 6 cancer cell lines and one non-malignant fibroblast cell line. MSN_CurNQ induced cytotoxicity culminating in a reduction to below 50% cell viability in OVCAR-5, CACO-2, CHLA and MCF-7 cell lines thereby signifying its chemotherapeutic potential to a variety of cancer cell types. Importantly, there was a significant difference in the reduction in cell viability of the healthy cell line 3T3 to all other cancer cell lines investigated, barring HeLa cells (OVCAR-5, CACO-2, MCF-7, CHLA $p=0.000$, HT-29 $p = 0.004$; HeLa $p= 0.378$). Thus, MSN_CurNQ reduced cancer cell viability to a greater extent than it did to a healthy fibroblast cell line. The highly statistically significant p-values of 0.000 and 0.004 verifies the selective toxicity of MSN_CurNQ to cancer cells. This selective toxicity further extends the cancer targeting capabilities of the nanosystem and furthers its novelty and applicability in the field of cancer theranostics. MSN_CurNQ thereby offers a three-pronged approached for cancer targeting namely its pH-responsive solubility, the EPR effect and its selective toxicity towards cancer cells. This makes MSN_CurNQ a highly advanced and novel nanosystem for cancer theranostics.

The promising *in vitro* results prompted the initiation of an *in vivo* preclinical trial utilising female MF-1 nude mice. The preclinical trial was divided into part A and part B. Part A aimed to assess the safety, toxicity and tolerability of CurNQ and MSN_CurNQ in nude mice. Part B took the form of a pilot study on tumour xenograft establishment and evaluated the potential efficacy of CurNQ and MSN_CurNQ as a chemotherapeutic.

Part A saw all mice survive continuous dosing of 10 mg/kg CurNQ and MSN_CurNQ, administered via tail vein injection thereby deeming both treatments safe. MSN_CurNQ was better tolerated than CurNQ, as less weight fluctuations occurred. Histopathology showed mild hepatocyte swelling with vacuolar changes present as well as mild swelling of the lining tubing epithelial cells of the inner cortex of the kidney in both treatment groups; however, these pathologies were more prominent from mice in the CurNQ treatment group and presented mildly for mice in the MSN_CurNQ treatment group. The results of part A of the preclinical trial were positive, demonstrating repeat exposure to CurNQ and MSN_CurNQ was well tolerated, safe and only resulted in mild toxicity.

OVCAR-5 tumour xenografts were successfully established in 15 mice and an efficacy study was conducted to evaluate the chemotherapeutic potential of CurNQ and MSN_CurNQ. Mice were administered biweekly with 10 mg/kg CurNQ, 10 mg/kg MSN_CurNQ and 25 mg/kg MSN_CurNQ via IV tail vein injection for 4 weeks. On account of the control being excluded, conclusive and statistically significant results could not be drawn, and the acquired results are considered as preliminary findings. The 10 mg/kg CurNQ treatment group resulted in the lowest average growth rate, whilst the 25 mg/kg MSN_CurNQ treatment group appeared to be more effective than the lower dosage of 10 mg/kg MSN_CurNQ as it resulted in a lower average tumour growth rate, and a lower mitotic rate with a similar necrosis factor. These preliminary results suggest CurNQ and MSN_CurNQ may induce tumour necrosis and may reduce the tumour growth rates; hence these results were promising and warrant the continuation of further *in vivo* studies.

In conclusion, MSN_CurNQ is a highly novel theranostic nanosystem with potential applications in cancer targeting, detection and treatment.

6.2 Limitations

Some limitations were encountered during the research, the most significant being the difficulty in synthesising CurNQ. Owing to the instability of Cur (discussed in chapter 3), all synthesis reactions took place in the dark. This may pose a challenge in future when scaling up synthesis of CurNQ. Certain challenges were faced during the animal study such as the difficulty in dispersing a high concentration of CurNQ in the small volume of saline that is safe for injection, thus making this injection process tricky.

6.3 Future recommendations

This thesis presents the synthesis of a novel molecule designed for cancer theranostics. Owing to the novelty of the molecule CurNQ, all information available on this molecule is limited to this thesis. Thus, this thesis is the first fundamental step and lays the groundwork for all future research. Complexities and potential limitations are still to be revealed. The novelty of the study sets the scene for multiple further research

avenues and the highly promising nature of this research warrants the initiation of multiple future studies exploring all aspects of this promising novel molecule and nanosystem.

The promising *in vivo* preliminary results from the preclinical trial warrants the continuation of animal studies. The unforeseen circumstances that resulted in the control group being excluded requires the *in vivo* efficacy study to be repeated with a control group in place. A future study should extend the preliminary *in vivo* work performed here to include a secondary double-blinded efficacy study on a variety of doses of CurNQ and MSN_CurNQ. In addition, detailed pharmacokinetic and pharmacodynamic *in vivo* studies are required as CurNQ is a novel drug compound. If CurNQ proves effective in a mice model, further animal studies should be considered to extend the preclinical trial evaluations of CurNQ as a theranostic agent. Detailed *in vivo* work fully evaluating all aspects of a novel drug compound is required prior to the commencement of clinical trials as is especially needed owing to the novelty of CurNQ. Thus, these in-depth and detailed studies should be considered for future post doctorial work. Moreover, imaging applications of nano-enabled CurNQ should be explored whereby an *in vivo* fluorescence imaging system is utilised. Successful *in vitro* imaging was demonstrated in chapter 4, thus it is of interest if these imaging applications could be translated to an animal model, which would allow for targeted tumour detection and imaging applications.

The properties of CurNQ demonstrated in this thesis highlights the complexity and multi-faceted nature of this novel molecule. It is exceptionally rare to discover a molecule with multiple potential applications, and thus research into CurNQ as a potential drug candidate is only initiated through this thesis. A far more robust understanding on CurNQ is required if it is to be propelled into clinical trials. Detailed studies on Cur's interaction and effect on multiple biochemical pathways has been discussed in literature, these same biochemical properties may stand true for CurNQ; however, this needs to be determined *in vitro* and detailed biochemical understanding on its mechanisms of actions are required. Moreover, the pharmacology of CurNQ is currently unknown and is required to be determined in detail both *in vitro* and *in vivo*. Furthermore, Cur has been cited to have applications in diseases other than cancer such as inflammation, Alzheimer's disease, inflammatory bowel disease and

cardiovascular disease. The application of CurNQ may also extend to these various diseases and this possibility should be explored. It is exciting to find a compound with the potential of such diverse applications, and all these possibilities should be explored.

Appendix A

STRICTLY CONFIDENTIAL

ANIMAL ETHICS SCREENING COMMITTEE (AESC)

CLEARANCE CERTIFICATE NO. 2018/11/55/C

APPLICANT: Ms L Freidus

SCHOOL: Pharmacy
DEPARTMENT:
LOCATION:

PROJECT TITLE: Study to evaluate the theranostic applications of the novel nanosystem MSN_CurNQ for cancer intervention in BALB/c nude mice

Number and Species

98X 6-8 weeks Female BALB/c nude mice

Approval was given for the use of animals for the project described above at an AESC meeting held on 2018/11/27. This approval remains valid until 2021/02/12.
Unreported changes to the application may invalidate the clearance given by the AESC
An annual progress report must be provided

The use of these animals is subject to AESC guidelines for the use and care of animals, is limited to the procedures described in the application form and is subject to any additional conditions listed below:

Signed: _____ (Chairperson, AESC) Date: 18/2/2019

I am satisfied that the persons listed in this application are competent to perform the procedures therein, in terms of Section 23 (1) (c) of the Veterinary and Para-Veterinary Professions Act (19 of 1982)

Signed: _____ (Registered Veterinarian) Date: 14/02/2019

cc: Supervisor: Prof V Pillay, Prof Y Choonara and Dr P Kumar
Director: CAS

Works 2000/lain0015/AESCCert.wps

Appendix B

Table S1: Preliminary reactions performed prior to the successful synthesis of CurNQ

Starting material 1	Starting material 2	Other reagents	Solvent	Reaction conditions	Outcome
Curcumin	2-Bromo-1,4-naphthoquinone	Potassium tert-butoxide	DMSO	45°C, 8 hours	Complete degradation
Curcumin	2-Bromo-1,4-naphthoquinone	Potassium tert-butoxide	DMSO	120°C, 2 hours	Complete degradation
Curcumin	2-Bromo-1,4-naphthoquinone	Copper chloride, potassium carbonate, 1-methylimidazole	Toluene	140°C, 12 hours	Product degraded
Curcumin	2-Bromo-1,4-naphthoquinone	CTAB, NaOH	Dichloromethane	60°C, 12 hours	Curcumin degradation in basic conditions
Curcumin	2-Bromo-1,4-naphthoquinone	Copper(I) iodide, Dimethylglycine, cesium carbonate	Dioxane	90°C, 6 hours	Product degradation
Curcumin	Hydrazine hydrate		Acetic acid	118°C, 8 hours	Curcumin-hydrazine was obtained.
Curcumin-hydrazine	2-Bromo-1,4-naphthoquinone	Potassium carbonate	Acetone	56°C, 12 hours	Product could not be purified completely, could not obtain clear NMR
Curcumin	2-Bromo-1,4-naphthoquinone	Potassium carbonate	Dimethylformamide (dry)	153°C, 12 hours	Curcumin degradation
Curcumin	2-Bromo-1,4-naphthoquinone	Potassium carbonate	Dimethylformamide (dry)	Room temperature, 12 hours	Curcumin degradation
Curcumin	2-Bromo-1,4-naphthoquinone	Potassium carbonate	Dimethylformamide (dry)	In the dark, room temperature, 1.5 hours	Successful

Appendix C

Preformulation reactions performed for the determination of experimental conditions required for the successful synthesis of mesoporous silica nanoparticles with favourable properties.

The following methods were performed when trying to obtain silica nanoparticles with favourable properties. These methods produced nanoparticles which were either too large, had a high polydispersity index, a negligible zeta potential or displayed poor reproducibility.

1. Two solutions were prepared:
   A) 0.5M TEOS dissolved in 15 mL pure ethanol
   B) 0.5M NH_4OH dissolved in 5 mL pure ethanol and 3 mL deionised water

Solution B was added dropwise to solution A at a rate of 0.2 mL per minute and stirred for 3 hours at room temperature. The final product was obtained through centrifugation, was then dried at 110 °C for 24 hours and milled to obtain a fine powder.

2. Pure ethanol and water were sonicated for 10 minutes. TEOS (0.8 M) was then added and sonication commenced for 2 hours. NH_4OH (1.87 M) was then added dropwise at a rate of 0.03 mL per minute and the solution was left under sonification for a further 5 hours. The solution was then allowed to dry for 24 hours after which the silica nanoparticles were collected.
3. A solution of pure ethanol (10 mL), deionised water (3 mL), TEOS (1 mL), and PEG (2.5 g) was mixed for 30 minutes. HN_4OH (1 mL) was then added dropwise. The reaction was left to stir for 2 hours. The resulting powder was dried overnight at 100 °C and the powder was then calcined at 650 °C for 1 hour.
4. Ethanol (4 M) and water were sonicated for 10 minutes after which TEOS (0.067 M) was added to the mixture. NH_4OH (14 M) was then added dropwise into the solution and sonication was continued for 60 minutes. The solution was then centrifuged, washed twice with ethanol and once with water.
5. Different concentrations of precursors were used, thereby observing the effects of concentration on particle properties. For the below mentioned concentrations, ethanol and water were sonicated for 10 minutes after which TEOS was added

to the mixture. NH_4OH was then added dropwise into the solution and sonication was continued for 60 minutes. The solution was then centrifuged, washed twice with ethanol and once with water. The silica nanoparticles were then calcined at 500 °C for 2 hours to remove unwanted surfactants.

Table S2: Preformulation reactions performed for the determination of experimental conditions required for the successful synthesis of mesoporous silica nanoparticles with favourable properties.

Attempt	TEOS (mL)	Water (mL)	NH_4OH (mL)	Ethanol (mL)	Outcome
1	0.2	3	1	5.8	Particle size too large
2	2	3	1	4	Particle size too large
3	0.8	0.2	1	8	Polydispersity index too high
4	0.8	5	1	3.2	Negligible zeta potential
5	0.8	3	0.2	6	Polydispersity index too high
6	0.8	3	4	2.2	Negligible zeta potential
7	0.7	2	1.3	9	Polydispersity index too high

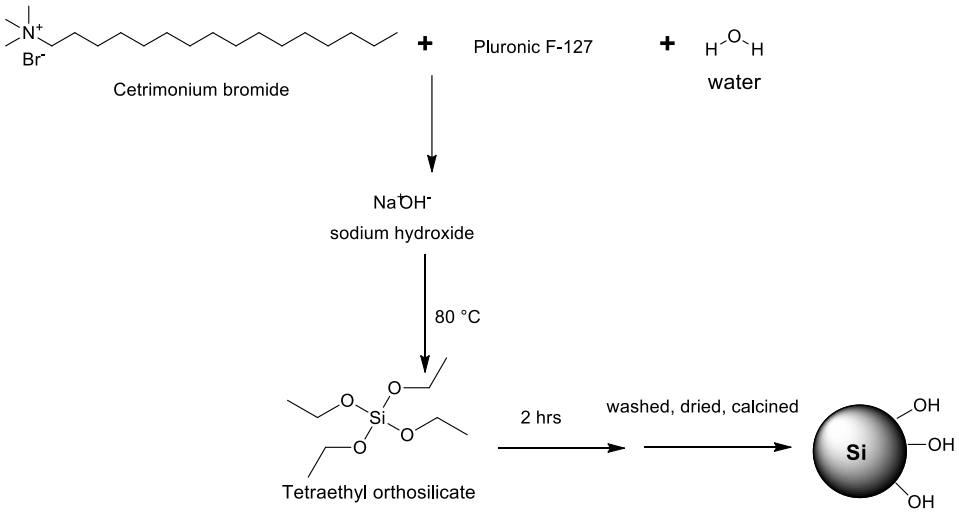
6. A reaction vessel containing ethanol (2.33 mL), water (2.52 mL) and Pluronic F-68 (10 mg) was placed in a sonicator bath. TEOS (0.15 mL) was then added to the solution and sonication was continued for 30 minutes. NH_4OH (5.4 mL) was then added to the reaction and was left to react for 1.5 hours. The particles were then collected and washed numerous times with ethanol.
7. Ethanol (5.8 mL), water (3 mL) and Pluronic F-127 (12mg) were mixed together. TEOS (0.2 mL) was then added to the solution and stirring was continued for 30 minutes. NH_4OH (5.4 mL) was then added to the reaction and was left to react

for 3 hours. The particles were then collected and washed numerous times with ethanol.

8. CTAB (1 g) was dissolved in deionised water (480 mL) until clear. To this solution, 2M NaOH (3.5 mL) was added and the temperature was raised to 80 °C. Once the temperature was constant, TEOS (5 mL) was added dropwise at a rate of 1mL/min into the solution. The reaction was left to stir for 2 hours. The precipitate was isolated by filtration and was washed numerous times with water and ethanol. The nanoparticles were then left to dry overnight at 60 °C. The particles were then calcined at 550 °C.

The final method used, adapted from Yang et al 2006, proved to produce mesoporous silica nanoparticles of 108nm, a PDI of 0.15 and a zeta potential of -42mV was as follows:

CTAB (1 g) and Pluronic F-127 (1 g) were dissolved in deionised water (480 mL) until clear. To this solution, 2M NaOH (3.5 mL) was added and the temperature was raised to 80 °C. Once the temperature was constant, TEOS (5 mL) was added dropwise at a rate of 1mL/min into the solution. The reaction was left to stir for 2 hours. The precipitate was isolated by filtration and was washed numerous times with water and ethanol. The nanoparticles were then left to dry overnight at 60 °C. The particles were then calcined at 550 °C to obtain the final product.



Scheme S1: Reaction mechanism slightly modified from Yang, et al., 2006 for the synthesis of mesoporous silica nanoparticles with desired properties.

Appendix D

Drug Discovery Today • Volume 00, Number 00 • November 2017 REVIEWS

ELSEVIER

Teaser A wide variety of alternative and novel fluorophores have been developed with wide-reaching applications in the fields of single molecule detection and molecular imaging.

Reviews • KEYNOTE REVIEW

Alternative fluorophores designed for advanced molecular imaging

Lara G. Freidus, Priyamvada Pradeep, Pradeep Kumar, Yahya E. Choonara and Viness Pillay

Wits Advanced Drug Delivery Platform Research Unit, Department of Pharmacy and Pharmacology, School of Therapeutic Sciences, Faculty of Health Sciences, University of the Witwatersrand, 7 York Road, Parktown 2193, Johannesburg, South Africa

Fluorescent molecular imaging has advanced drastically over the past decade. With the development of high-resolution microscopy techniques and the ability to visualize intracellular molecular events, there is a growing need for new fluorophores to accompany these fast-developing techniques. Therefore, there has been substantial development of alternative fluorophores for single-molecule detection and molecular imaging. These rationally designed fluorophores have infinite possibilities and novel fluorophores are constantly being produced for different applications. This review focuses on the recent developments in novel fluorophores designed for molecular imaging and single-molecule detection. Here, single-molecule imaging, smart fluorescent probes, two-photon microscopy, Förster resonance energy transfer (FRET) and super-resolution microscopy are discussed in detail.

Introduction

Molecular imaging is a technique that enables the real-time visualization and characterization of cellular structures, events and pathways in living organisms at the molecular level [1]. Molecular imaging offers the opportunity to elucidate cellular behavior at the molecular level, aiding in drug discovery, the evaluation of therapy efficacy and early diagnosis of several diseases [2–4]. Real-time *in vivo* imaging is the current goal of much research and the realization of this technique would increase medical discoveries and scientific breakthroughs that have boundless applications [5]. Molecular imaging utilizing fluorescent molecules is the focus of current molecular imaging research. The use of fluorescent molecules in imaging is advantageous because of high-resolution images, high sensitivity and precision, noninvasiveness, cost-effectiveness and no perturbation with cellular functions [6]. In recent years, the field of molecular imaging has emerged considerably, because the ability for site-specific and molecule-specific imaging enables countless applications and opportunities with wide-reaching effects [5]. The application of molecular imaging in a clinical setting requires improvements in the fluorescent dyes used in terms of background:target

Corresponding author: Pillay, V. (viness.pillay@wits.ac.za)



Lara Gaby Freidus is currently a postgraduate student at the Wits Advanced Drug Delivery Platform (WADDP), University of the Witwatersrand, Johannesburg, South Africa. Her project research areas include novel fluorophores, organic chemistry, nanotechnology, cancer research, and pharmaceutics. She has an undergraduate in molecular and cell biology and an honours degree in biochemistry (both from Wits).



Priyamvada Pradeep is currently a NRF postdoctoral research fellow at the Wits Advanced Drug Delivery Platform (WADDP), University of the Witwatersrand, Johannesburg, South Africa. She received her PhD in synthetic organic chemistry (2015) at School of Chemistry (WITS) and MS (Medicinal Chemistry) at National Institute of Pharmaceutical Education and Research (NIPER), Hyderabad, India. Her main focus of research includes multistep synthesis of poly-aromatic organic molecules and investigation of their reaction mechanisms, in silico screening and generation of therapeutic molecules, biomaterials synthesis, and drug delivery systems.



Viness Pillay, a Fulbright Scholar and Fellow of the African Academy of Sciences (AAS), is a South African NRF Research Chair in Pharmaceutical Biomaterials and Polymer-Engineered Drug Delivery Technologies hosted by the University of the Witwatersrand, funded by the Department of Science and Technology (DST) and administered by the National Research Foundation (NRF) at the Tier 1 Level. Prof. Pillay is a Personal Professor of Pharmaceutics, Head of Pharmaceutics and Director of the Wits Advanced Drug Delivery Platform (WADDP) Research Unit and Contract Research at the University of the Witwatersrand, Department of Pharmacy and Pharmacology, South Africa. He is also a Fellow of Academy of Translational Medicine Professionals. His research Unit encompasses the research, development and commercialization of innovative drug delivery systems currently under development by his research team.

1359-6446/© 2017 Elsevier Ltd. All rights reserved.
http://dx.doi.org/10.1016/j.drudis.2017.09.008

Please cite this article in press as: Freidus, L.G. et al. Alternative fluorophores designed for advanced molecular imaging, Drug Discov Today (2017), http://dx.doi.org/10.1016/j.drudis.2017.09.008

Appendix E

molecules

MDPI

Article

Synthesis and Properties of CurNQ for the Theranostic Application in Ovarian Cancer Intervention

Lara G. Freidus, Pradeep Kumar, Thashree Marimuthu, Priyamvada Pradeep, Viness Pillay and Yahya E. Choonara *

Wits Advanced Drug Delivery Platform Research Unit, Department of Pharmacy and Pharmacology, School of Therapeutic Sciences, Faculty of Health Sciences, University of the Witwatersrand, Johannesburg, 7 York Road, Parktown 2193, South Africa; lara.freidus@students.wits.ac.za (L.G.F.); pradeep.kumar@wits.ac.za (P.K.); thashree.marimuthu@wits.ac.za (T.M.); priyamvada.pradeep@wits.ac.za (P.P.); viness.pillay@wits.ac.za (V.P.)

* Correspondence: yahya.choonara@wits.ac.za; Tel.: +27-11-717-2052

Received: 17 August 2020; Accepted: 25 September 2020; Published: 29 September 2020

check for updates

Abstract: Synthesis of a novel theranostic molecule for targeted cancer intervention. A reaction between curcumin and lawsone was carried out to yield the novel curcumin naphthoquinone (CurNQ) molecule (2,2′-((((1E,3Z,6E)-3-hydroxy-5-oxohepta-1,3,6-triene-1,7-diyl)bis(2-methoxy-4,1-phenylene))bis(oxy))bis(naphthalene-1,4-dione). CurNQ's structure was elucidated and was fully characterized. CurNQ was demonstrated to have pH specific solubility, its saturation solubility increased from 11.15 µM at pH 7.4 to 20.7 µM at pH 6.8. This pH responsivity allows for cancer targeting (Warburg effect). Moreover, CurNQ displayed intrinsic fluorescence, thus enabling imaging and detection applications. In vitro cytotoxicity assays demonstrated the chemotherapeutic properties of CurNQ as CurNQ reduced cell viability to below 50% in OVCAR-5 and SKOV3 ovarian cancer cell lines. CurNQ is a novel theranostic molecule for potential targeted cancer detection and treatment.

Keywords: curcumin; lawsone; theranostics; pH responsivity; fluorescence; high content imaging

Appendix F



UNIVERSITY OF THE WITWATERSRAND, JOHANNESBURG | FACULTY OF HEALTH SCIENCES | HSRO Health Sciences Research Office

THE FACULTY OF HEALTH SCIENCES
RESEARCH DAY & POSTGRADUATE EXPO

BEST STUDENT ORAL PRESENTATION

CLINICAL SCIENCES AND THERAPEUTICS FOR HEALTH

TO

Lara Freidus

Martin Veller

PROFESSOR MARTIN VELLER
DEAN: FACULTY OF HEALTH SCIENCES

DR MARK KILLICK
RESEARCH DAY CHAIRPERSON

SEPTEMBER 2018

Appendix G

The Academy of Pharmaceutical Sciences of the Pharmaceutical Society of South Africa



congratulates

Lara Freidus

as the runner-up in the Young Scientist competition at the APSSA conference 2019

Chairman

10 October 2019

Date

Appendix H

9th CROSS-FACULTY POSTGRADUATE SYMPOSIUM

Showcasing Postgraduate Research @ WITS

WE ARE PROUD TO CONFIRM THAT

Lara Freidus

PRESENTED A PAPER AT THE 9th CROSS FACULTY POSTGRADUATE SYMPOSIUM

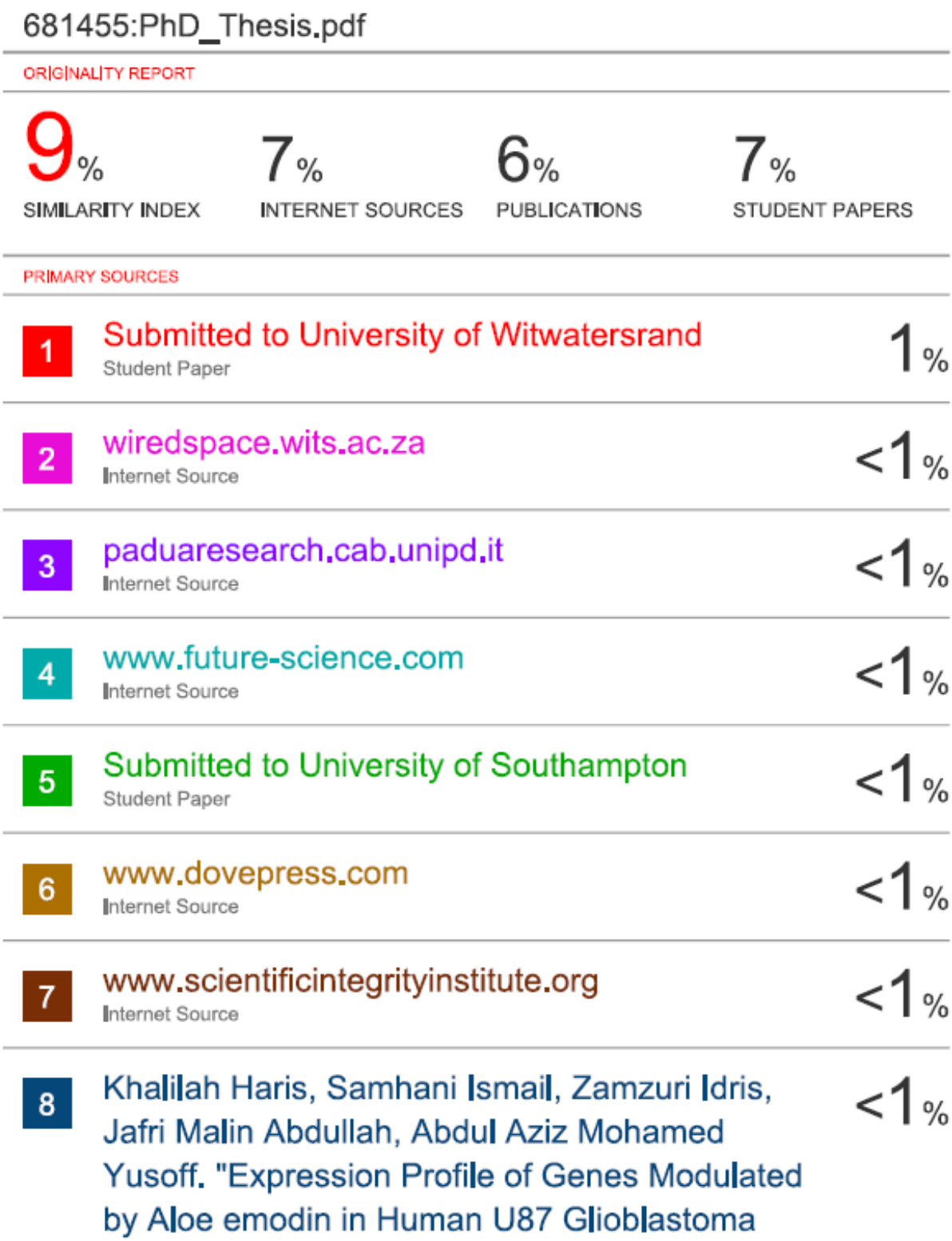
PROFESSOR NEIL COVILLE

PROFESSOR ZEBLON VILIKAZI

UNIVERSITY OF THE WITWATERSRAND, JOHANNESBURG

Postgraduate Affairs Office October 2018

Appendix I



681455:PhD_Thesis.pdf

ORIGINALITY REPORT

9%	7%	6%	7%
SIMILARITY INDEX	INTERNET SOURCES	PUBLICATIONS	STUDENT PAPERS

PRIMARY SOURCES

1	Submitted to University of Witwatersrand Student Paper	1%
2	wiredspace.wits.ac.za Internet Source	<1%
3	paduaresearch.cab.unipd.it Internet Source	<1%
4	www.future-science.com Internet Source	<1%
5	Submitted to University of Southampton Student Paper	<1%
6	www.dovepress.com Internet Source	<1%
7	www.scientificintegrityinstitute.org Internet Source	<1%
8	Khalilah Haris, Samhani Ismail, Zamzuri Idris, Jafri Malin Abdullah, Abdul Aziz Mohamed Yusoff. "Expression Profile of Genes Modulated by Aloe emodin in Human U87 Glioblastoma	<1%